Geofluids

Surveying, Monitoring, and Analysis of Hydromechanical Coupling in Geotechnical and Geological Disasters

Lead Guest Editor: Zizheng Guo
Guest Editors: Danqing Song, Wei Yuan, and Yin Xing

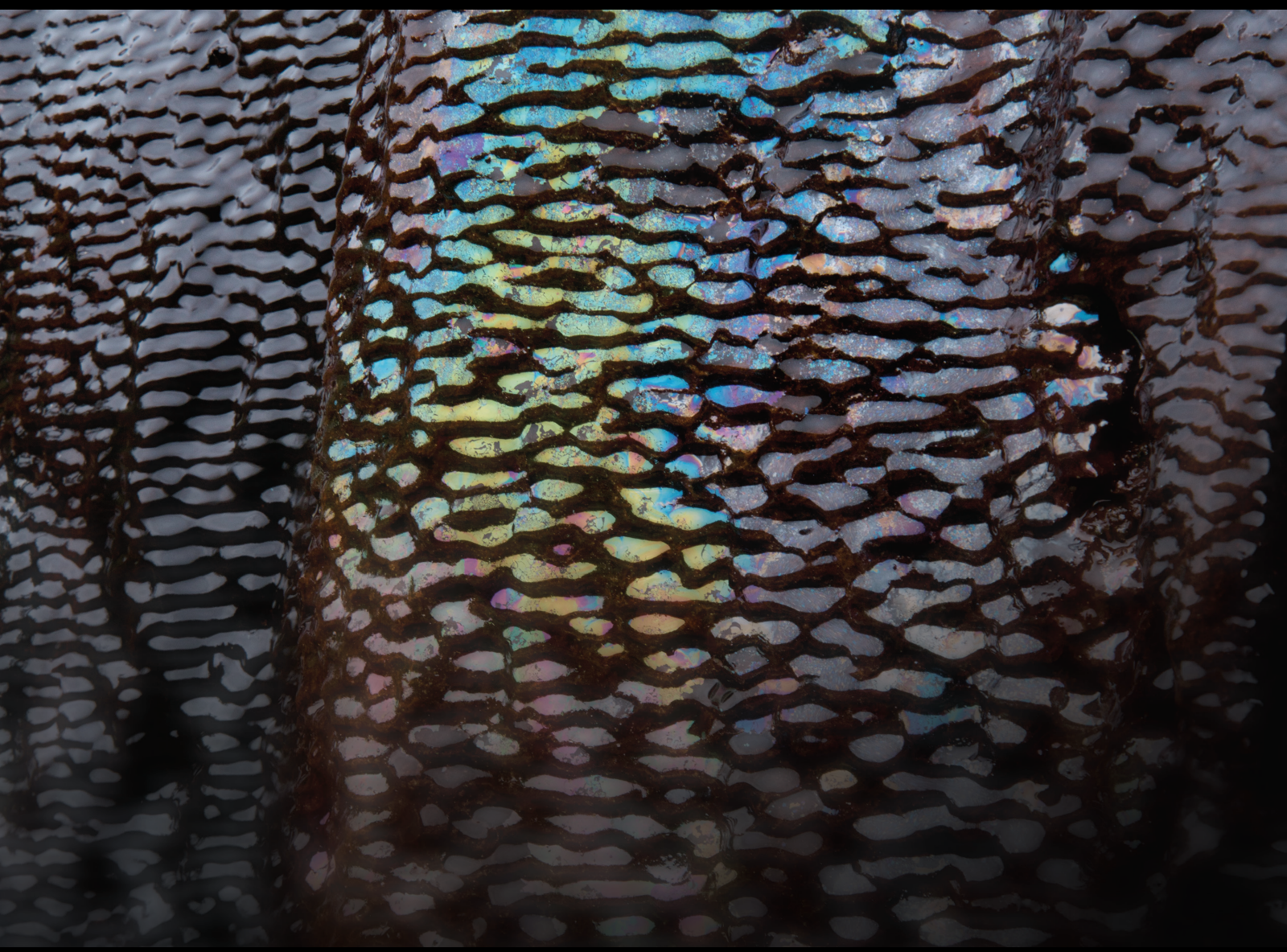

Surveying, Monitoring, and Analysis of Hydromechanical Coupling in Geotechnical and Geological Disasters

Geofluids

Surveying, Monitoring, and Analysis of Hydromechanical Coupling in Geotechnical and Geological Disasters

Lead Guest Editor: Zizheng Guo
Guest Editors: Danqing Song, Wei Yuan, and Yin Xing

Chief Editor

Associate Editors

Academic Editors

Contents

Hindawi
Geofluids
Volume 2023, Article ID 6197047, 13 pages
https://doi.org/10.1155/2023/6197047

Research Article

Degradation Characteristics and Mechanism of Black Sandy Dolomite with Fluid Added in a Mechanical Test

Xin Liao,[1,2] Qi Xu,[3] Sixiang Ling,[1,2] Angran Tian,[3] and Qiang Tang[3]

[1]*Faculty of Geosciences and Environmental Engineering, Southwest Jiaotong University, Chengdu 611756, China*
[2]*MOE Key Laboratory of High-Speed Railway Engineering, Southwest Jiaotong University, Chengdu 611756, China*
[3]*School of Rail Transportation, Soochow University, Suzhou 215131, China*

Correspondence should be addressed to Angran Tian; gangguo@126.com and Qiang Tang; tangqiang@suda.edu.cn

Received 8 March 2022; Revised 20 June 2023; Accepted 2 August 2023; Published 30 August 2023

Academic Editor: Chris Harris

Sandy dolomite, being a soluble rock, is prone to dissolution and erosion caused by groundwater, leading to the formation of underground caves and fractures. This may result in geological disasters such as ground subsidence and collapse. In this paper, the changes and mechanical properties of black sandy dolomite after hydrochemistry are studied. A semi-immersion test with different concentrations of iron sulfate solution was carried out to simulate the water-rock interaction in different water environments. After that, scanning electron microscope (SEM) results could reflect the dissolution and pore development of rock by the effect of water-rock interaction from the microscopic. Water-rock interaction enlarges cracks in rocks and dissolves pyrite, carbonate minerals, and other components, reducing the cementation between particles. The change in the mechanical properties of black sandy dolomite under water-rock chemical interaction was revealed by uniaxial compression test. The mechanical properties of the samples exhibit varying degrees of deterioration, with strain increased ranging from 4.96 to 29.58%. The brittleness index modified (BIM) values for each sample ranged from 5.20 to 6.20%, all of which are larger than 4.70% in the natural state.

1. Introduction

Sandy dolomite, a sedimentary rock primarily composed of dolomite (a calcium magnesium carbonate mineral) and sand-sized particles [1], is known for its abundant presence of pores and fissures, making it susceptible to erosion and dissolution by groundwater [2, 3]. This rock type is frequently utilized in geology as a significant layer for underground water storage and transportation purposes [4]. However, its solubility and fissure characteristics also render it prone to geological hazards, including ground subsidence, collapse, and damage [5]. In the context of preventing and controlling geological hazards in mountainous regions, investigating the characteristics and mechanisms of sandy dolomite holds great significance for the mitigation of landslides and rock collapses [6, 7].

With increasing concerns regarding engineering construction issues associated with sandy dolomite strata, the investigation of degradation caused by water-rock interaction has emerged as a forefront topic in the field of engineering geology. During the weathering process, sulfide minerals and organic matter present in sandy dolomite undergo oxidation in an oxygen-rich water environment, resulting in the formation of a complex acidic water environment [8, 9]. Consequently, water dissolution leads to the depletion of certain minerals, while the formation of new minerals occurs in their original positions, thereby altering the distribution of pores and stress within the rocks [10]. This aqueous environment further accelerates the weathering of primary minerals, leading to the rapid disintegration of rocks and subsequent modifications to their composition and structure [11]. Ultimately, the chemical weathering of

the rock mass can result in the deterioration of its physical and mechanical properties.

Sandy dolomite contains a significant amount of organic matter and sulfide minerals, particularly pyrite, which plays a crucial role in water-rock interaction. Pyrite surfaces do not achieve automatic charge compensation, leading to the formation of polar surfaces with excess charges. These polar surfaces exhibit instability and high surface activity. They readily form bonds with ions or molecules in the surrounding medium to compensate for the excess charges in the suspension, resulting in surface oxidation reactions [12, 13]. In an acidic environment, the oxidation reaction of pyrite can be expressed as follows:

$$\begin{aligned} &FeS_2 + \frac{7}{2}O_2 + 2H_2O \longrightarrow Fe^{2+} + 2H^+ + 2SO_4^{2-} \\ &Fe^{2+} + \frac{1}{4}O_2 + H^+ \longrightarrow Fe^{3+} + \frac{1}{2}H_2O \\ &Fe^{3+} + 3H_2O \longrightarrow +Fe(OH)_3 + 3H^+ \\ &FeS_2 + 7Fe_2(SO_4)_3 + 8H_2O \longrightarrow 15FeSO_4 + 8H_2SO_4 \end{aligned} \quad (1)$$

The reactions involved in water-rock interaction continue to cycle, resulting in intensification. Research indicates that Fe^{3+} ions, rather than O_2, are the most significant oxidizing agents in the process of pyrite oxidation [14, 15]. Aqueous solutions containing ferric ions can accelerate the oxidation of pyrite, leading to an increased concentration of hydrogen ions in the water environment of the rock and subsequent acidification [16]. Therefore, investigating iron ions, which are among the primary factors influencing the water-rock interaction of rock strata, holds theoretical importance in exploring the degradation patterns of the mechanical properties of sandy dolomite strata.

By applying the energy mechanism, the process of energy absorption, transformation, and release in rocks can be studied more effectively, leading to a more comprehensive understanding of the degradation process of rocks. Previous studies have systematically explained the process of rock deformation and failure and the characteristics of energy transformation [17, 18]. The energy absorbed and transformed from the outside is divided into dissipative energy and releasable elastic energy. Dissipated energy can be used to describe the new plastic deformation and internal damage of rock mass, which is the main cause of rock strength loss [19, 20]. The releasable elastic strain energy can be released during unloading.

In this paper, the effect of water-rock interaction on the deterioration of sandy dolomite was studied, taking black sandy dolomite as the research object. Semi-immersion tests were conducted under various ferric sulfate concentrations to simulate the effects of different water environments. Subsequently, uniaxial compression tests were performed to determine the changes in the mechanical properties of the samples due to the chemical effects of water-rock interaction. Based on the energy mechanism, the energy changes of rocks under uniaxial compression were analyzed.

2. Materials and Methods

2.1. Sampling and Preparation. The rock samples studied in this paper were selected from the lower Cambrian black rock in Chengkou County, Chongqing, China. Due to the high levels of rainfall and hot summer temperatures in the local area, the rock strata distributed in the study area have strong water-rock interaction. As a result of abundant rainfall, the surface of the rock mass was visibly fractured and denuded. The rock mass was coated with a yellow substance, which was speculated to be the oxide formed by the replacement of iron ions due to the water-rock interaction.

The black sandy dolomite rock blocks were selected and prepared into standard cylindrical samples with dimensions of φ50 mm × 100 mm, following the *ASTM D4543* standard [21]. Using ultrasonic velocity measurement, eight samples with uniform internal structure were chosen. In order to provide an objective assessment of the sample properties, three samples were selected for the determination of their physical and chemical properties.

The mineral analysis results obtained through X-ray diffraction (XRD) measurements are presented in Table 1 and Figure 1, providing valuable insights into the mineral composition of the tested black sandy dolomite samples. The dominant minerals observed in the samples are dolomite, accounting for 46.60-52.40% of the composition, and quartz, comprising 31.70-36.80% of the mineral content. Additionally, minor constituents such as pyrite (3.60-4.60%), plagioclase (1.60-2.90%), and illite (1.91-3.59%) were identified. The samples also contain trace amounts of chlorite (0.36-0.59%), kaolinite (0.37-0.59%), and other unidentified minerals.

The chemical composition analysis of the black sandy dolomite samples was conducted using PW2424 X-ray fluorescence spectrometer (XRF), and the results are presented in Table 2. The chemical composition of the samples is mainly SiO_2 (32.00-36.37%), followed by CaO (16.45-18.55%), with MgO content of 11.55-12.95%. The contents of Al_2O_3, SO_3, and Fe_2O_3 are 2.17-3.30%, 2.25-2.80%, and 1.39-1.47%, respectively. Other chemical compositions are relatively low. This indicates that there are some pyrite contained in the black sandy dolomite samples as well. The loss on ignition (LOI) is 25.64-28.98%, indicating that there is high content of inorganic carbonate in the rock.

2.2. Experiments

2.2.1. Semi-immersion Test. After drying and vacuuming the rock samples, they were immersed in solutions of $Fe_2(SO_4)_3$ at different concentrations for this study. Acid-proof plastic boxes were used as containers, with four groups consisting of two soaking samples per group. The immersion solution in the simulation test consisted of deionized water and sulfuric acid, with Fe^{3+} concentrations of 1 g/L, 1.5 g/L, 2 g/L, and 2.5 g/L, labeled as A, B, C, and D, respectively, in ascending order of concentration. The semi-immersion experiment is shown in Figure 2.

According to the empirical formula of the oxidation rate of bulk pyrite, the concentration of Fe^{3+} produced during

Table 1: Mineral composition of the samples.

Sample	Quartz	Plagioclase	Pyrite	Dolomite	Illite	Kaolinite	Chlorite	Others
1	31.70	2.20	4.60	52.40	1.91	0.46	0.36	6.38
2	36.80	2.90	5.30	46.60	3.02	0.34	0.59	4.45
3	33.80	1.60	3.60	51.80	3.59	0.46	0.46	4.69
Average	34.10	2.23	4.50	50.27	2.84	0.42	0.47	5.17

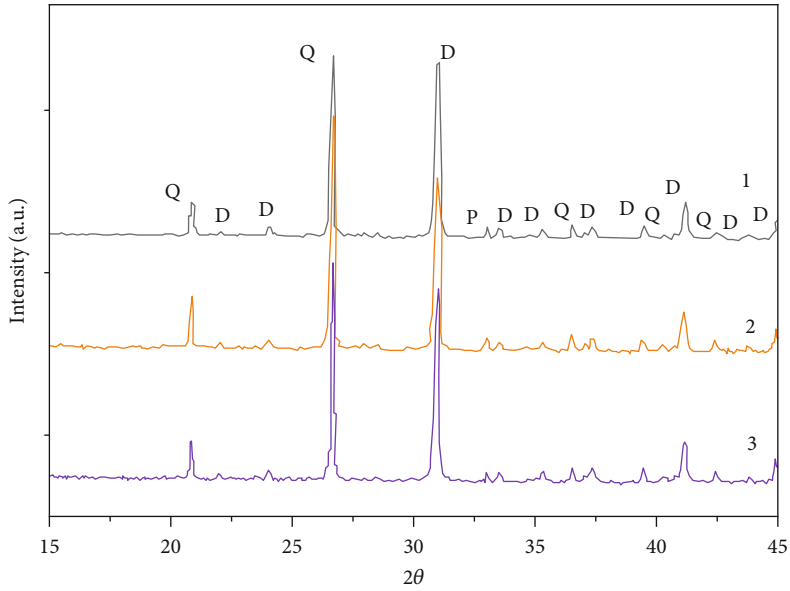

Figure 1: X-ray diffraction results of the samples. D: dolomite; Q: quartz; P: pyrite.

Table 2: Chemical composition of the samples.

Sample	SiO_2	TiO_2	Al_2O_3	K_2O	MgO	Fe_2O_3	CaO	P_2O_5	Na_2O	SO_3	Cr_2O_3	BaO	LOI
1	32.83	0.13	2.17	0.52	12.85	1.44	18.30	0.06	0.16	2.27	<0.01	0.03	28.54
2	36.37	0.18	3.30	0.87	11.55	1.47	16.45	0.09	0.27	2.80	<0.01	0.05	25.64
3	32.00	0.14	2.22	0.58	12.95	1.39	18.55	0.09	0.16	2.25	<0.01	0.02	28.98
Average	33.73	0.15	2.56	0.66	12.45	1.43	17.77	0.08	0.20	2.44	<0.01	0.03	27.72

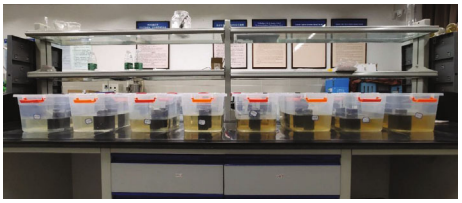

Figure 2: Semi-immersion experiment.

the oxidation and acid erosion process of black sandy dolomite differs by four orders of magnitude from the Fe^{3+} concentration in the immersion solution. This difference has a weak impact on the test process and can be ignored [22–24]. Therefore, the chosen iron ion concentrations in the immersion solution for this paper are reasonable and feasible.

Before the test, the rock samples underwent vacuum freeze-drying for one hour using a vacuum freeze-dryer. This process created a negative pressure within the rock mass, ensuring that the soaking liquid entered the rock mass through the cracks. The initial pH value of the precipitate was approximately 2.2, so the pH value of the immersion solution was set to 2.

During the test, the electronic conductivity and pH of each group of solutions were periodically measured. Initially, measurements were taken three times a day at 6-hour intervals, and subsequently, measurements were taken twice a day at 12-hour intervals. After the semi-immersion test, the samples were removed for the mechanical test.

2.2.2. Scanning Electron Microscopy Analysis. The rock samples were initially cleaned to eliminate surface impurities. Subsequently, they were processed into small pieces of approximately 1 cm^3 using a cutting machine. The surfaces of these samples were then polished to obtain smooth flakes suitable for argon ion polishing. These samples were polished in a LEICA EM RES102 argon ion polishing instrument. The polished samples were thoroughly cleaned with deionized water and dried for 24 h in a drying box with the temperature set at 60°C. After the rock sample was polished by argon ions, they were fixed on the surface of the coin to ensure the smooth placement of the rock sample on the scanning electron microscope platform, and then, the rock sample was observed and analyzed by scanning electron microscopy (QUanta-Fec250). Lastly, a platinum coating was applied to the surface of the rock samples observed under the scanning electron microscope. This was accomplished by placing the samples into a platinum deposition instrument, ensuring optimal electrical conductivity through a platinum injection time of 60 seconds.

2.2.3. Uniaxial Compression Experiment. After 41 days of soaking in different ferric sulfate solutions, the samples underwent uniaxial compression testing using a YZW-Y series microcomputer-controlled electrohydraulic servo pressure testing machine, with a loading rate of 0.5 MPa/s. The test was conducted until the sample was completely destroyed, and the stress-strain parameters of each sample were recorded.

3. Results and Discussion

3.1. Oxidation-corrosion morphology of the samples. The change of the samples at four different concentrations is similar. Typical changes in the process of immersion are described as follows.

The rock samples were immersed in a liquid solution with the top surface positioned approximately 1 cm above the water level. Upon immersion, bubbles were observed in the lower portion of the solution at all concentrations. After 3 days, a slight cloudiness was noticeable in the soaking solution compared to its initial state. By the fourth day, the sample with a concentration of 1 g/L exhibited an increased pH value, accompanied by additional precipitation at the bottom of the solution. Precipitation in the form of white substances was observed in the wetted regions above the liquid level for all rock samples, consistently appearing at the boundary between the wet and dry areas surrounding the rock samples.

After 14 days, the height of the immersion solution within the rock samples had increased by approximately 1 cm due to capillary action, and an increased amount of flocculent or needle-like white precipitates was observed. Some of the precipitates transitioned from white to a yellow-brown color. At the 20-day mark, the soaking solution further penetrated the internal pores of the rock samples, resulting in significant precipitation from the immersed regions. Approximately half of the white precipitates turned yellow-brown in alignment with the direction of solution infiltration. Over time, noticeable dissolution phenomena occurred within the wetted portions of the rock samples.

By the 34th day, the wetted regions of the rock samples displayed the appearance of yellow-brown material, with the coverage area gradually expanding. As more precipitates migrated through the pores in the direction of the solution, the surface exhibited undulations, and a few instances of exfoliation and discrete particles could be observed at the bottom of the solution. After 41 days, no visible precipitate was observed on the immersed surface of the rock samples. However, the portion above the liquid level was coated with a yellow-brown precipitate. Figure 3 provides a depiction of the typical etching characteristics observed in the samples.

3.2. pH and Electric Conductivity. Electric conductivity (EC) is a measure of solution conductivity and is influenced by the properties of ions present in the solution. The observed increase in conductivity can be attributed to the ongoing oxidation of pyrite, resulting in the production of various ions. Simultaneously, the hydrogen ions generated during the oxidation process react with other minerals within the rock sample, causing their dissolution and the formation of additional soluble ions. Consequently, the conductivity value is further elevated. The augmentation of electrical conductivity exhibits a positive correlation with the extent of water-rock interaction.

The relationship curves of EC and pH values of the samples in hydrochemical solutions with different concentrations with experimental time are shown in Figure 4. The data shown in the figure are the average values of the two samples in each experiment group. The EC changes in different concentrations of aqueous chemical solution in different time periods were consistent. In the early stage of the test, the soaking solution directly contacted the surface of the rock sample, and the soaking fluid entered the sample along with the pores. The water-rock reaction was severe, and rock-forming minerals and cementation were dissolved. Soluble minerals in the rock sample begin to decompose, producing ions into the immersion solution, such as Fe^{2+} and Mg^{2+}. Macroscopically, the conductivity of the soaking fluid increased. With the passage of oxidation acid etching time, the conductivity of the soaking solution increased gradually, and when it increased to a certain value, the increasing rate decreased to different degrees and finally tended to a certain stable value.

To ensure that the pH value was kept within a stable range during the test, when the pH value rose to 2.3, an appropriate amount of sulfuric acid solution was added to the soaking solution to adjust the pH value to the initial value of 2. The EC and pH values increased and decreased rapidly in the early stage in group A. At 25 h, the EC value reached a maximum of 6.8 mS/cm, and the pH value reached a minimum of 1.6. Then, the EC value began to decrease with partial fluctuation, and the pH value began to rise. In groups B, C, and D, the trends of both were similar; the EC value increased slowly, and the pH value decreased slowly. After 25 h, EC and pH fluctuated occasionally but

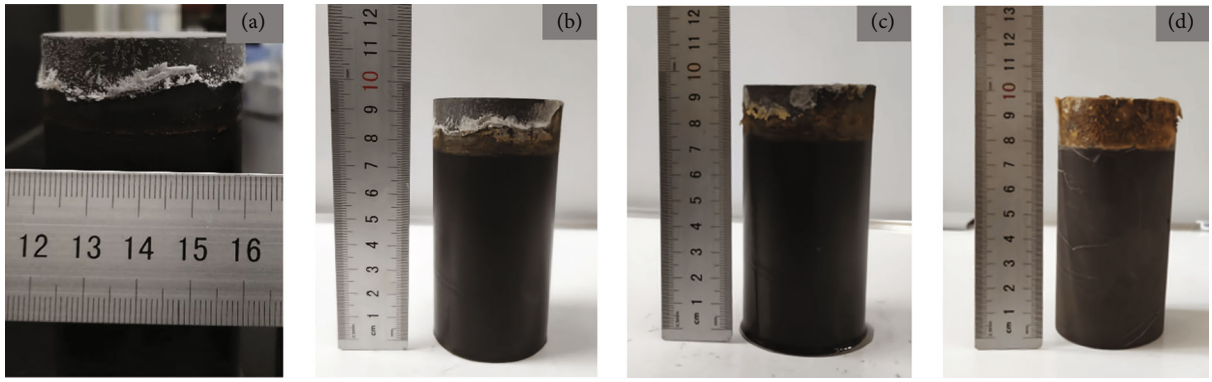

Figure 3: Group A oxidation acid etching characteristics: (a) day 4; (b) day 20; (c) day 34; (d) day 41.

generally tended to be stable, and the conductivity stabilized at approximately 3.3, 5.1, and 6.2 mS/cm, respectively.

After 500 hours of testing, the EC value and pH value of the soaking solution in the test groups were stable. It is speculated that pyrite in the rock is completely dissolved and the chemical reactions reach equilibrium. The conductivity of the four groups increased from 3.2 to 9.8 mS/cm, 2.7 to 8.2 mS/cm, 4.0 to 9.2 mS/cm, and 4.6 to 9.1 mS/cm, respectively. The pH values of the four groups were kept at about 2.0, 2.1, 2.1, and 2.0, while the electrical conductivity increased with growth rates of 206%, 203%, 130%, and 97%, respectively. The change in conductivity decreases with increasing immersion concentration. This indicates that with the increase in the concentration of Fe^{3+} in the soaking solution, the water-rock chemical interaction weakens in the same period. The rate of ion generation is also slow, which makes the change range of EC smaller, leading to less consumption of H^+ and a smaller rise rate of pH. It is speculated that the complexes formed by Fe^{3+} with water and dissolved oxygen cover the surface of rock samples in the form of thin films, which inhibit the dissolution rate of diagenetic minerals. This prevents further chemical reactions, giving the rock some protection [25, 26]. The control group with the same concentration of iron ions and different immersion heights showed a similar change trend in EC, indicating that the immersion height has little effect on the water-rock interaction of black sandy dolomite.

3.3. Characteristics of Microstructure after Water-Rock Interaction. The samples of black sandy dolomite were analyzed by scanning electron microscopy after soaking in solutions for 41 days. Pores and fissures in the black sandy dolomite were observed, as well as the microstructure and the cementation between the mineral particles.

The internal microstructure before water-rock interaction of the sample is shown in Figure 5(a). The overall structure of the black sandy dolomite is closely connected, and the main frame is jointly constructed of dolomite and quartz. The overall structure of the rock and the clay minerals is layered.

Figure 5(b) shows the internal pore diagram of black sandy dolomite in natural state. The size and shape of microscopic particles are irregular, and the structure between particles is loose. Inside the rock, there are many pores of different sizes with irregular shapes (red arrows). The pores are a few microns in diameter, much smaller than the minerals in the rock sample. At the same time, honeycomb aggregates were observed, which were inferred to be pyrite by X-ray energy-dispersive spectrometry. Pyrite on the surface of rock samples is easily dissolved into fine particles, which are further decomposed into ions to improve the conductivity of the solution.

Erosion and fissures occurred in the samples, as shown in Figure 5(c), resulting in mineral loss and disintegration. Pore water carries the ions released by minerals to move into the cracks of rock mass. After the ion concentration reaches saturation in the open area of the cracks, mineral redeposition will occur. During this process, the concentration of ions in the solution increases, resulting in the increase of EC value. Chemical dissolution in the narrow fissure widens the opening, changes the cementation between mineral particles, and reduces the mechanical properties. In acidic environments, all the samples have strong dissolution phenomena, mainly manifested as dissolution and expansion along the intergranular pores and all kinds of cracks and cavities, and finally connected to a certain extent. After these reactions, the solution pores and gaps are beaded. Figure 5(d) shows that the pyrite particles are eroded away and the original structure turns into holes after water-rock interaction.

Scanning electron microscopy analysis reveals that the microdissolution process of dolomite primarily occurs along the dolomite grains, crystalline pores, and crystal interfaces. Dissolution initially takes place at crystal cleavage fissures, contact points between dolomite crystals, and within and around sand patches. This results in a gradual deterioration of the internal structure of dolomite. The pores gradually enlarge and extend as the dissolution progresses. Crystal detachment during the process weakens the interconnection between dolomite crystals, leading to a loosening of the structure and the eventual formation of a powdery substance. Thus, water-rock interaction has a significant impact on the micromorphological characteristics of the rock samples.

3.4. Uniaxial Compression Experiment Results. The results of the uniaxial compression test indicate that the failure mode of the rock samples is brittle failure. The stress-strain curve

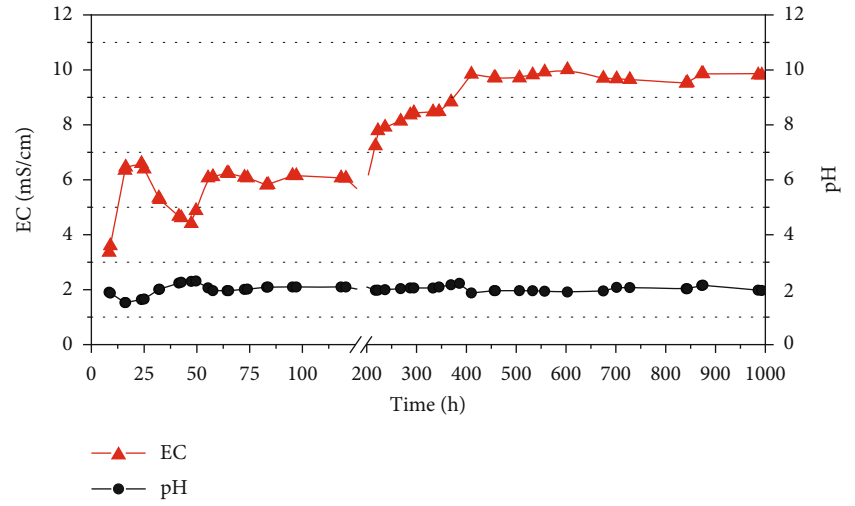

(a)

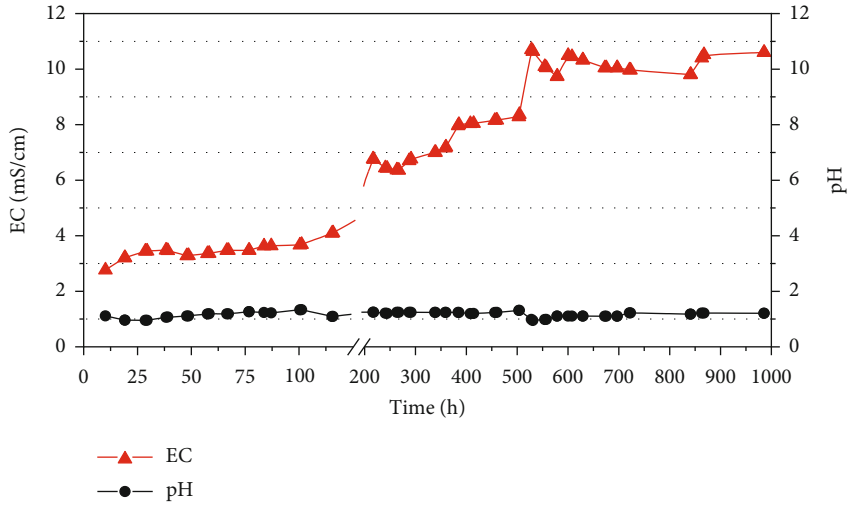

(b)

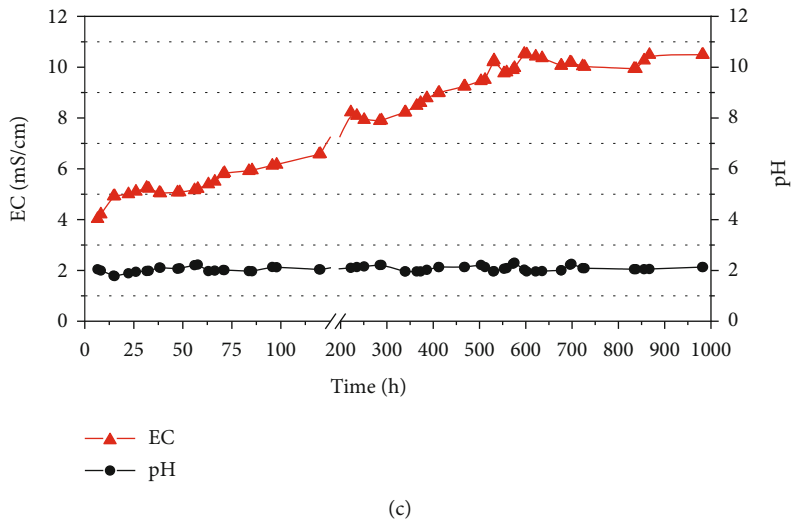

(c)

Figure 4: Continued.

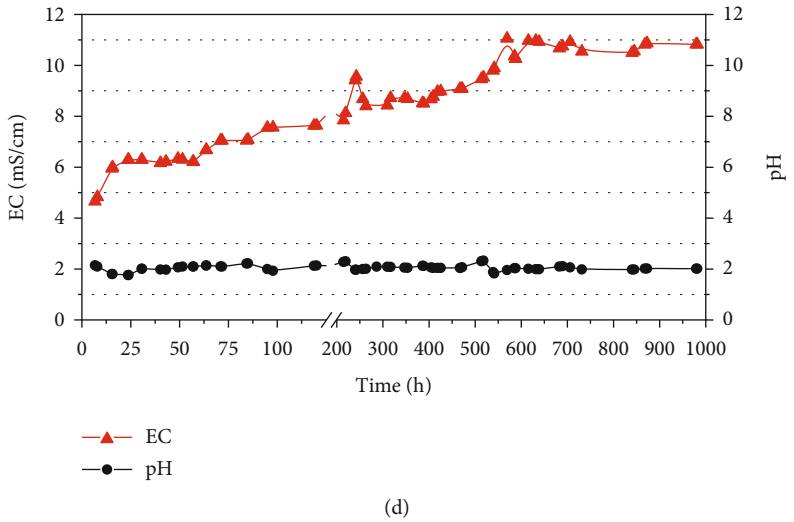

(d)

Figure 4: Conductivity and pH value of the samples: (a) group A; (b) group B; (c) group C; (d) group D.

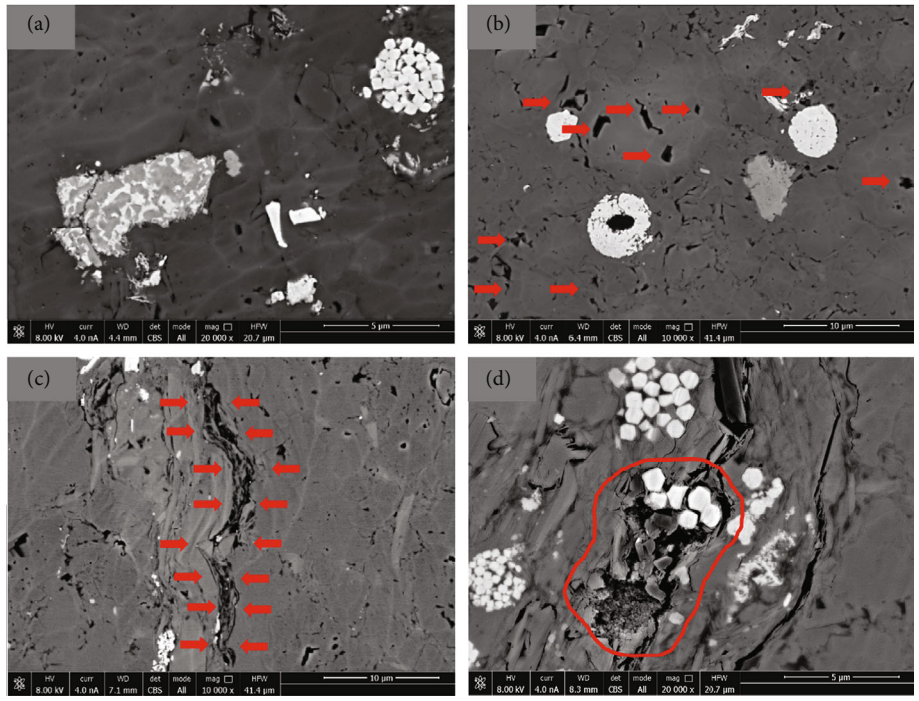

Figure 5: SEM images of the samples before and after water-rock interaction. Before water-rock interaction: (a) overall structure and (b) internal pores. After water-rock interaction: (c) enlargement of pores and (d) pyrite corrosion.

of the samples after acid etching with different concentrations of Fe^{3+} is shown in Figure 6.

The initial compression section of the uniaxial compression stress-strain curve of a rock sample displays an upward concave shape, and its length is indicative of the sample's internal defects and void development. After chemical corrosion, the upward concave section of the sample is lengthened. The length and degree of the upper sag can reflect the pore development of rock. The compaction section of the sample increased obviously. The softening effect of the chemical solution significantly impacts the elastic and yield stages of the curve, with the elastic stage being shorter after chemical corrosion than under natural conditions.

At the stage of plastic deformation, the peak point strain can reflect the amount of deformation when the rock is damaged. The mechanical and deformation parameters of specimens obtained by uniaxial compression test are shown in Table 3. With the increase in acidity of the chemical solution. The axial strain increases when the peak point is reached. After soaking in chemical solution, the axial strain

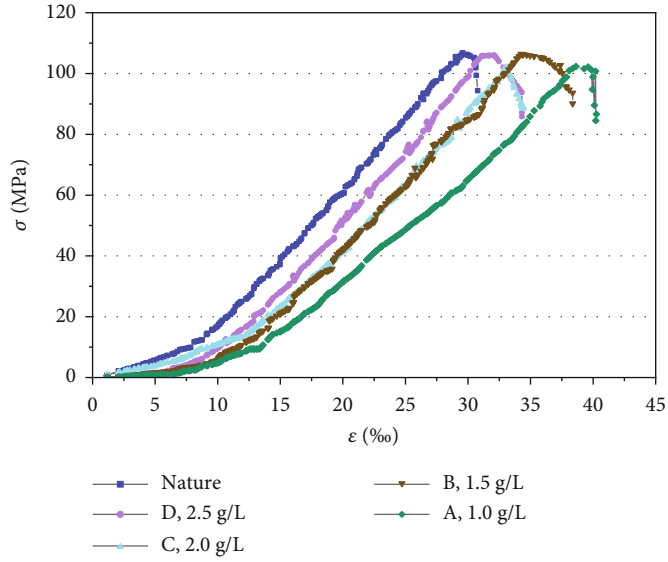

Figure 6: Stress-strain curves of the samples.

at the peak point of each sample is greater than that in the natural state.

The degradation of mechanical indexes of the sample under different Fe^{3+} ion concentrations is as follows: compared with the unsoaked samples, the peak strength of groups A, B, C, and D decreased by 4.18%, 0.19%, 2.93%, and 0.64%; the peak strain increased by 29.58%, 14.11%, 12.42%, and 4.96%; and the elastic modulus decreased by 16.00%, 2.96%, 6.98%, and 1.88%, respectively. Different concentrations of immersion solution have different corrosion effects on the samples. With increasing Fe^{3+} ion concentration, the degradation rate of the strength parameter decreased. If the concentration of Fe^{3+} increases, Fe^{3+} forms a film on the surface of the sample, the contact surface between sample and solution was reduced, and the dissolution rate is inhibited [27–29].

4. Energy Mechanism under Uniaxial Compression

In the process of the uniaxial compression test, the rock deforms until it is destroyed by an external load. It is assumed that there is no heat exchange in the process of deformation, and the external force works on the rock with input energy U. That includes the elastic strain energy released at the time of failure and the dissipated energy of the rock [25].

$$U = U^{e} + U^{d}, \tag{2}$$

where U^{e} is the releasable elastic strain energy and U^{d} is the dissipated energy.

The relationship between dissipative energy U^{d} and releasable elastic energy U^{e} is shown in Figure 7. The dissipated energy of damage and plastic deformation U^{d} in the forming element is numerically equal to the area formed by the stress-strain relationship curve and the unloading elastic modulus. The area of the shaded part represents the value of the releasable elastic strain energy U^{e}, which is the elastic strain energy released by the rock mass after unloading.

Table 3: Strength and deformation parameters of the samples under uniaxial conditions.

Group	Peak strength (MPa)	Peak strain (‰)	Elasticity modulus (GPa)
A	102.16	38.54	3.87
B	106.41	33.94	4.47
C	103.50	33.44	4.28
D	105.94	31.22	4.52
Nature	106.62	29.75	4.60

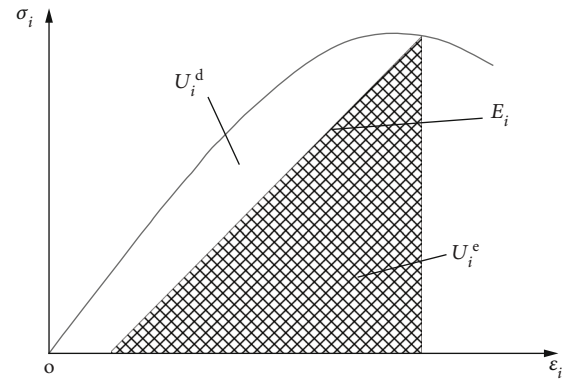

Figure 7: Quantitative relationship between U^{e} and U^{d}.

Table 4: Average plastic deformation and BIM.

Group	A	B	C	D	Nature
Concentration (g/L)	1.0	1.5	2.0	2.5	/
BIM (%)	6.20	5.60	5.90	5.20	4.70
U_p (mm)	1.22	1.02	0.93	0.78	0.65

The energy of each part in the principal stress space can be represented as [26]

$$\begin{aligned} U &= \int_0^{\varepsilon_1} \sigma_1 d\varepsilon_1 + \int_0^{\varepsilon_2} \sigma_2 d\varepsilon_2 + \int_0^{\varepsilon_3} \sigma_3 d\varepsilon_3, \\ U^e &= \frac{1}{2}\sigma_1 d\varepsilon_1^e + \frac{1}{2}\sigma_2 d\varepsilon_2^e + \frac{1}{2}\sigma_3 d\varepsilon_3^e, \\ U^d &= U - U^e. \end{aligned} \tag{3}$$

In this formula, U is the work done by the principal stress in the direction of the principal stress; ε_i $(i = 1, 2, 3)$ is the strain in three principal stress directions; ε_i^e $(i = 1, 2, 3)$ is the elastic strain in three principal stress directions.

In practical engineering applications, the releasable elastic strain energy can be written as follows [30, 31]:

$$U^e = \frac{\sigma_1^2 + \sigma_2^2 + \sigma_3^2 - 2\mu(\sigma_1\sigma_2 + \sigma_2\sigma_3 + \sigma_3\sigma_1)}{2E_u}, \tag{4}$$

where E_u is the unloading elastic modulus.

At present, a large number of studies show that the initial elastic modulus E_0 is generally used to replace the unloading elastic modulus E_u in calculating the elastic strain energy that can be released [32–34]. In the uniaxial compression test, only the axial stress ε_1 works on the sample, and the principal stress in the other directions is 0. Therefore, the above formula can be written as

$$U = \int_0^{\varepsilon_1} \sigma_1 d\varepsilon_1, \tag{5}$$

$$U^e = \frac{1}{2}\sigma_1 d\varepsilon_1^e, \tag{6}$$

$$U^d = U - U^e = \int_0^{\varepsilon_1} \sigma_1 d\varepsilon_1 - \frac{\sigma_1^2}{2E_0}. \tag{7}$$

The amount of plastic deformation can be expressed by the value of the brittleness index modified (BIM) [35, 36]:

$$\mathrm{BIM} = \frac{U^d}{U^e}, \tag{8}$$

where U^d and U^e represent the dissipated energy and releasable elastic energy of the sample at the peak stress.

The total plastic deformation of the sample in the progressive failure process under uniaxial compression can be calculated by the formula below [37]:

$$U_p = L\left(\varepsilon - \frac{\sigma}{E}\right), \tag{9}$$

where U_p is the total plastic deformation of the sample, L is the length of the sample, ε is the axial strain, E is the elastic modulus, and σ is the axial compressive stress.

According to Equations (8) and (9), the average plastic deformation amount and brittleness correction index value of the sample at the peak stress before failure can be obtained, as shown in Table 4.

As shown in Table 4, the BIM of the sample in the natural state is 4.70%, while those of the samples after soaking are 6.20%, 5.60%, 5.90%, and 5.20%. That is greater than the value of the rock in the natural state and decreases with the increase in the concentration of solution. This indicates that after oxidizing acid corrosion, the samples softened, the ductility enhanced and brittleness weakened. The degree of softening decreased with increasing aqueous chemical solution concentration. The average plastic deformation of groups A, B, C, and D is 1.22 mm, 1.02 mm, 0.93 mm, and 0.78 mm, which are larger than the average plastic deformation of the natural rock (0.65 mm). This demonstrates that the variation law of BIM is the same as the average plastic deformation, so the energy mechanism can be used to characterize the chemical corrosion of rock. The larger the brittleness correction index value is, the deeper the mechanical properties of the sample deteriorate under the effect of chemical corrosion.

According to Equation (5)-Equation (7), the curves of the relationship between the strain energy of each part and axial strain can be obtained, which were affected by chemical corrosion at different concentrations, as shown in Figure 8.

It can be seen intuitively from Figure 8 that the accumulation and transformation patterns of the absorbed strain energy in various components are generally consistent in black sandstone limestone specimens in their natural state and after chemical corrosion. However, the evolution of energy in the process of deformation and failure of the black sandy dolomite samples in the hydrochemical solution corrosion is still obviously different from that in the natural state. The increase rates of absorbed total strain energy and releasable elastic strain energy in the saturated state after chemical corrosion are lower than those in the natural state. With the same axial strain, the strain energy U and the released elastic strain energy U^e are both larger than those after chemical corrosion, indicating that the chemical solution has a significant effect on them. After the peak value

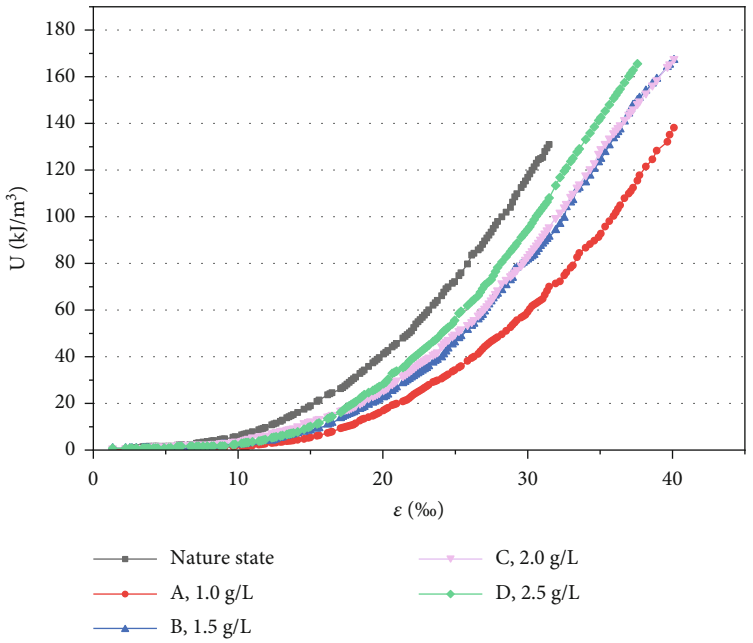

(a)

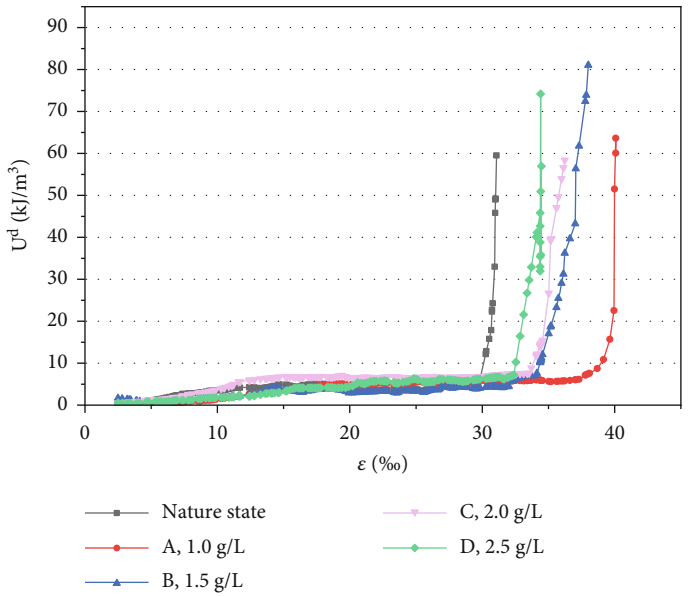

(b)

Figure 8: Continued.

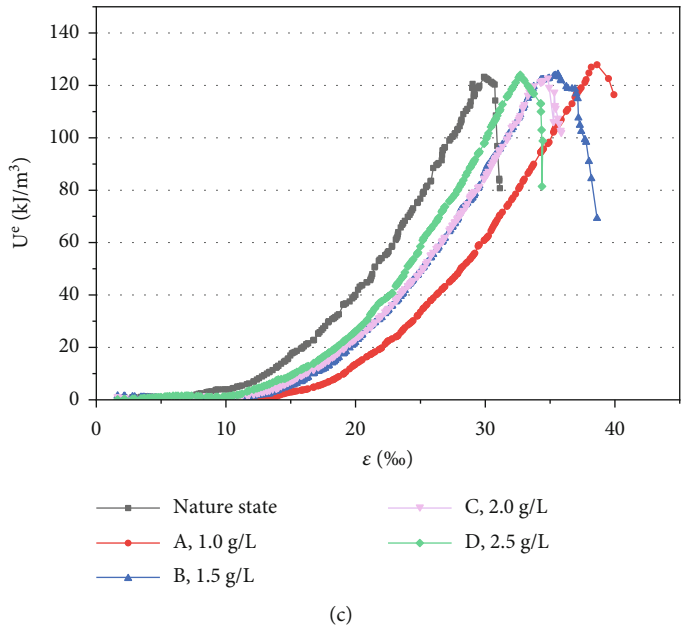

(c)

Figure 8: Curves of axial strain and energy: (a) total strain energy; (b) dissipation energy; (c) releasable energy.

point, the energy absorption from the external environment decreases to varying degrees for both natural corrosion and chemical corrosion, but the decrease is more significant under chemical corrosion.

5. Conclusions

The semi-immersion test and uniaxial compression test of black sandy dolomite at different concentrations were carried out, and the mechanical properties of rock under different chemical damage states were analyzed combined with the energy mechanism. The specific results are as follows:

(1) The morphological characteristics of oxidizing acid erosion of black sandy dolomite were obtained through the semi-immersion test of chemical solutions with different Fe^{3+} concentrations. Results showed that water-rock interaction was more significant when the concentration of iron ions was low. The electrical conductivity (EC) value increased rapidly in 1 g/L solution and reached its maximum after approximately 25 hours, earlier than other concentrations. Moreover, the hydrogen ion consumption capacity is weak, and the pH value increases more slowly

(2) Through uniaxial compression tests of the samples corroded by chemical solutions of different concentrations, the stress-strain relationship curves of the whole process were obtained. Under the natural state of rock in water after chemical etching, the peak strength of the samples decreased to varying degrees, and the peak strain increased to different extents, with a decreasing trend as the concentration of Fe^{3+} increased. The maximum increasement of strain reached 29.58% at a concentration of 1 g/L iron ions, and the minimum was 4.96% at 2.5 g/L

(3) The variations in mechanical properties of the rock under uniaxial compression have been derived from an energy-based perspective by analyzing the stress-strain curves. With increasing chemical solution concentration, the strain energy of each characteristic point of the rock sample decreases, and the U_d/U value, brittleness correction index, and average plastic deformation also decrease. BIM reaches the highest value of 6.20% at 1 g/L, and U_p also reaches the maximum value of 1. The variation range of the elastic strain energy (U_e) value is small, suggesting that the elastic properties of the rock have not changed significantly during the process of energy absorption

Data Availability

The data used to support the findings of this study are available from the corresponding authors upon request.

Conflicts of Interest

The authors declare that they have no competing interests.

Acknowledgments

We would like to thank the Analytical and Testing Center of Southwest Jiaotong University for the XRD and XRF analyses. The research presented here is supported by the National Natural Science Foundation of China (52078317), Natural Science Foundation of Sichuan Province for Young Scholars (2022NSFSC1117), Natural Science Foundation of Jiangsu

Province for Excellent Young Scholars (BK20211597), Project from Bureau of Housing and Urban-Rural Development of Suzhou (2021ZD02 and 2021ZD30), Bureau of Geology and Mineral Exploration of Jiangsu (2021KY06), China Tiesiju Civil Engineering Group (2021-19), CCCC First Highway Engineering Group Company Limited (KJYF-2021-B-19), Innovative Practice Bases of Geological Engineering and Surveying Engineering of Southwest Jiaotong University (YJG-2022-JD04), CCCC Tunnel Engineering Company Limited (8gs-2021-04), Key R&D Program of Sichuan (2019YFG0460 and 2019YFG0001), Major Systematic R&D Project of China Railway Corporation (P2018G047), and Key R&D Program of China (2016YFC0802206).

References

[1] M. Wang, W. Xu, H. Mu, J. Mi, Y. Wu, and Y. Wang, "Study on construction and reinforcement technology of dolomite sanding tunnel," *Sustainability*, vol. 15, p. 9217, 2022.

[2] P. Zhou, Y. Fan, F. Zhou, F. Wu, Y. Yong, and Z. Wang, "Disaster mechanism of tunnel face with large section in sandy dolomite stratum," *Engineering Failure Analysis*, vol. 131, article 105905, 2022.

[3] V. Chander, D. Tewari, V. Negi, R. Singh, and L. Aleya, "Structural characterization of Himalayan black rock salt by SEM, XRD and in-vitro antioxidant activity," *Science of the Total Environment*, vol. 748, article 141269, 2020.

[4] Y. Jiang, P. Zhou, F. Zhou et al., "Failure analysis and control measures for tunnel faces in water-rich sandy dolomite formations," *Engineering Failure Analysis*, vol. 138, article 106350, 2022.

[5] R. Attia and G. Awny, "Leaching characterisations and recovery of copper and uranium with glycine solution of sandy dolomite, Allouga area, South Western Sinai, Egypt," *International Journal of Environmental Analytical Chemistry*, pp. 1–14, 2021.

[6] X. Liao, X. Wu, B. Zhu, and F. Jun, "Study on the characteristics of black strata geochemical weathering and its disaster-causing mechanism," *Disaster Advances*, vol. 5, no. 4, pp. 1558–1562, 2012.

[7] L. Li, C. Xu, X. Yao et al., "Large-scale landslides around the reservoir area of Baihetan hydropower station in Southwest China: analysis of the spatial distribution," *Natural Hazards Research*, vol. 2, no. 3, pp. 218–229, 2022.

[8] O. Farkas, S. Siegesmund, T. Licha, and Á. Török, "Geochemical and mineralogical composition of black weathering crusts on limestones from seven different European countries," *Environmental Earth Sciences*, vol. 77, no. 5, pp. 175–184, 2018.

[9] M. W. Saaltink, C. Domenech, C. Ayora, and J. Carrera, "Modelling the oxidation of sulphides in an unsaturated soil," *Geological Society, London, Special Publications*, vol. 198, no. 1, pp. 187–204, 2002.

[10] J. Srodo, J. Szulc, and A. Anczkiewicz, "Weathering, sedimentary and diagenetic controls of mineral and geochemical characteristics of the vertebrate-bearing Silesian Keuper," *Clay Minerals*, vol. 49, no. 4, pp. 569–594, 2014.

[11] X. Liao, M. Chigira, Y. Matsushi, and X. Wu, "Investigation of water–rock interactions in Cambrian black shale via a flow-through experiment," *Applied Geochemistry*, vol. 51, pp. 65–78, 2014.

[12] E. Forbes, L. Smith, and M. Vepsalainen, "Effect of pyrite type on the electrochemistry of chalcopyrite/pyrite interactionsm," *Physicochemical Problems of Mineral Processing*, vol. 54, no. 4, pp. 1116–1129, 2018.

[13] M. Berta, F. Dethlefsen, M. Ebert, K. Gundske, and A. Dahmke, "Surface passivation model explains pyrite oxidation kinetics in column experiments with up to 11 bars p (O_2)," *Environmental Earth Sciences*, vol. 75, no. 16, pp. 1–13, 2016.

[14] Y. Liu, Z. Dang, P. Wu, J. Lu, X. Shu, and L. Zheng, "Influence of ferric iron on the electrochemical behavior of pyrite," *Ionics*, vol. 17, no. 2, pp. 169–176, 2011.

[15] C. O. Moses, D. K. Nodstrom, and J. S. Herman, "Aqueous pyrite oxidation by dissolved oxygen and by ferric iron," *Geochimica et Cosmochimica Acta*, vol. 51, no. 6, pp. 1561–1571, 1987.

[16] Y. Huai, C. Plackowski, and Y. Peng, "The effect of gold coupling on the surface properties of pyrite in the presence of ferric ions," *Applied Surface Science*, vol. 488, pp. 277–283, 2019.

[17] T. Zhou, Y. Qin, Q. Ma, and J. Liu, "A constitutive model for rock based on energy dissipation and transformation principles," *Arabian Journal of Geosciences*, vol. 12, no. 15, pp. 1–14, 2019.

[18] Y. Wen, C. Xin, X. Zhang et al., "The stability analysis of tunnel lining structure with seismic excitation based on the energy evaluation principle," *Shock and Vibration*, vol. 2021, Article ID 9995682, 17 pages, 2021.

[19] J. Chen, Y. Xuanyuan, and Y. Dai, "Expressions of stored and dissipated energy densities," *Optik*, vol. 207, no. 4, 2020.

[20] F. Gu, D. Presti, M. Heitzman, B. Powell, and V. Allison, "Feasibility of using more polishable aggregates in dense-graded asphalt surface mixture: case study of dolomite," *Construction and Building Materials*, vol. 342, article 127915, 2022.

[21] D. Shiozawa, T. Inagawa, T. Washio, and T. Sakagami, "Accuracy improvement in dissipated energy measurement by using phase information," *Measurement Science and Technology*, vol. 28, 2017.

[22] L. Li, C. Polanco, and A. Ghahreman, "Fe (III)/Fe (II) reduction-oxidation mechanism and kinetics studies on pyrite surfaces," *Journal of Electroanalytical Chemistry*, vol. 774, pp. 66–75, 2016.

[23] Y. Ramprakash, D. Koch, and R. Woods, "The interaction of iron species with pyrite surfaces," *Journal of Applied electrochemistry*, vol. 21, pp. 531–536, 1991.

[24] E. C. Dos Santos, D. Cecí Lia, and H. A. Duarte, "Pyrite oxidation mechanism by oxygen in aqueous medium," *Journal of Physical Chemistry*, vol. 120, no. 5, pp. 2760–2768, 2016.

[25] M. Salamon, "Energy considerations in rock mechanics: fundamental results," *Journal of the Southern African Institute of Mining and Metallurgy*, vol. 84, no. 8, pp. 233–246, 1984.

[26] E. Fjær and H. Ruistuen, "Impact of the intermediate principal stress on the strength of heterogeneous rock," *Journal of Geophysical Research: Solid Earth*, vol. 107, no. B2, 2002.

[27] A. Arisoy and B. Beamish, "Mutual effects of pyrite and moisture on coal self-heating rates and reaction rate data for pyrite oxidation," *Fuel*, vol. 139, pp. 107–114, 2015.

[28] H. Wang, P. A. Dowd, and C. Xu, "A reaction rate model for pyrite oxidation considering the influence of water content and temperature," *Minerals Engineering*, vol. 134, pp. 345–355, 2019.

[29] S. Kaviani, M. Izadyar, and M. R. Housaindokht, "A DFT study on the complex formation between desferrithiocin and metal ions (Mg^{2+}, Al^{3+}, Ca^{2+}, Mn^{2+}, Fe^{3+}, Co^{2+}, Ni^{2+}, Cu^{2+}, Zn^{2+})," *Computational Biology & Chemistry*, vol. 67, pp. 114–121, 2017.

[30] B. G. Tarasov and T. R. Stacey, "Features of the energy balance and fragmentation mechanisms at spontaneous failure of class I and class II rocks," *Rock Mechanics and Rock Engineering*, vol. 50, no. 10, pp. 2563–2584, 2017.

[31] P. Li and M. Cai, "Energy evolution mechanism and failure criteria of jointed surrounding rock under uniaxial compression," *Journal of Central South University*, vol. 28, no. 6, pp. 1857–1874, 2021.

[32] S. Souissi, E. Hamdi, and H. Sellami, "Microstructure effect on hard rock damage and fracture during indentation process," *Geotechnical and Geological Engineering*, vol. 33, no. 6, pp. 1539–1550, 2015.

[33] J.-A. Wang and H. D. Park, "Comprehensive prediction of rockburst based on analysis of strain energy in rocks," *Tunnelling and Underground Space Technology*, vol. 16, no. 1, pp. 49–57, 2001.

[34] M. Aubertin, D. Gill, and R. Simon, "On the use of the brittleness index modified (BIM) to estimate the post-peak behavior of rocks," *Rock Mechanics*, pp. 945–952, 1994.

[35] H. Munoz, A. Taheri, and E. K. Chanda, "Rock drilling performance evaluation by an energy dissipation based on rock brittleness index," *Rock Mechanics and Rock Engineering*, vol. 48, no. 8, pp. 3343–3355, 2016.

[36] M. Jarrahi, G. Blöcher, C. Kluge, and H. M. Holländer, "Elastic–plastic fracture propagation modeling in rock fracturing via punch through shear test," *Rock Mechanics and Rock Engineering*, vol. 54, no. 6, pp. 3135–3147, 2021.

[37] S.-i. Karato and H.-R. Wenk, *Plastic Deformation of Minerals and Rocks (Vol. 51)*, Walter de Gruyter Gmb H & Co KG, 2002.

Hindawi
Geofluids
Volume 2022, Article ID 6277553, 10 pages
https://doi.org/10.1155/2022/6277553

Research Article

Study on Strength Attenuation Characteristics of Residual Expansive Soil under Wetting-Drying Cycles and Low Stress and Its Relationship with Shallow Landslide

Jin Chang[1,2] **Jieling Ma**[3] **and Xianyuan Tang**[3]

[1]*College of Civil Engineering, Changsha University, Changsha 410022, China*
[2]*Shanghai Key Laboratory for Digital Maintenance of Buildings and Infrastructure, Department of Civil Engineering, Shanghai Jiao Tong University, Shanghai 200240, China*
[3]*School of Architecture and Traffic Engineering, Guilin University of Electronic Technology, Guilin 541004, China*

Correspondence should be addressed to Xianyuan Tang; thy1188@126.com

Received 18 May 2022; Accepted 18 August 2022; Published 14 September 2022

Academic Editor: Zizheng Guo

The rapid development of expansive soil fissures and the attenuation of strength under the action of repeated atmospheric wetting-drying cycles have a very adverse impact on the shallow stability of expansive soil slope. In this study, shear strength test and fissure observation test were performed on typical residual expansive soil specimens at various wetting-drying cycles and low stress. The results show that the shear strength index of residual expansive soil should be obtained according to the high and low stress sections, respectively. The cohesion of the three residual expansive soils decreased to a similar low value range (0~5 kN) at multiple wetting-drying cycles and low stress; the attenuation of cohesion is the main cause of shallow slope collapse. The fissure rate of the specimen surface increases with the increasing number of wetting-drying cycles, and increasing the dry density can significantly inhibit the development of fissures. The repeated wetting-drying cycles leads to the rapid development of slope fissures from the surface to the inside, destroys the internal natural structure of undisturbed expansive soil, reduces the cementation between soil particles, and leads to the decrease of soil cohesion. For slope stability analysis of residual expansive soil, the strength parameters of the specimens with multiple wetting-drying cycles and internal fissure network should be selected according to the overburden pressure of the slope sliding surface. The research results provide a theoretical basis for the stability analysis of shallow landslide of expansive soil slope and slope protection design.

1. Introduction

Expansive soil is widely distributed in China. More than 300 million people live in expansive soil distribution areas. The geological environment in these areas is fragile, and the economic loss caused by expansive soil landslide disaster exceeds tens of billions of yuan every year [1–3]. Due to the existence of montmorillonite clay minerals with strong hydrophilicity, the expansive soil is extremely sensitive to humidity and heat change. The numerical analyses could be inconsistent with the actual stability of the slope as the uncertainties of its strength contribute to the slope instability in practice [4, 5].

Many researchers almost study the slope stability of expansive soil from the two aspects of shear strength parameters and the development of fissures [6–11]. Li et al. [12] believe that for expansive soil embankment, the influence of wetting-drying cycles on residual strength parameters should be properly considered when selecting strength parameters. Cheng et al. [13] emphasized that the shear strength parameters measured under low stress conditions should be selected to analyze the slope stability in order to obtain reasonable calculation results, but it did not closely link the strength attenuation with the wetting-drying cycle effect. Xiao et al. [14, 15] carried out indoor direct shear and triaxial tests and found that after multiple wetting-drying cycles, the saturated slow shear strength of expansive soil is very small or even tends to zero in the low stress section. Selecting the strength parameters under this condition to analyze the slope

stability can get more practical results. There are also some differences in the simulation methods of wetting-drying cycles process in the shear strength test of expansive soil carried out by previous researchers [16–20]. Considering that the actual sliding surface of expansive soil slope is under different overlying pressure conditions, there must be a difference between the deformation of expansive soil after moisture absorption and its expansion without load. Therefore, it is considered that the simulation of moisture absorption conditions in the preparation of expansive soil specimens should be changed to the loaded state. The actual overburden pressure at the shallow sliding surface of expansive soil slope is generally less than 50 kPa, which does not match the overburden pressure that can be applied by the conventional direct shear test, so the shear application conditions in the shear test need to be improved accordingly.

The influence of fissures must be considered in the stability analysis of expansive soil slope [21] .Yin et al. [22] believe that the existence of fissures makes the shear strength of slope soil clear, the fissure depth will be stable at a certain value after repeated wetting-drying cycles, the strength of soil within the fissure development depth will be reduced, while the deeper soil has no fissures and the strength is higher. Therefore, it is proposed that the slope stability analysis should be replaced by corresponding strength parameters in layers to obtain the collapse failure results of expansive soil slope. Secondary fissure refers to the newly generated fissure affected by climate change such as weathering and dry wet cycle, which has a significant impact on the strength of expansive soil. The shallow secondary fissure surface and deep primary fissure surface constitute the unstable sliding surface of expansive soil slope [23] . Moreover, researchers initially treated expansive soil slope as ordinary cohesive soil slope, and the results obtained by limit equilibrium method are quite different from the actual situation. For example, the average slope of Nanyang expansive soil slope in China is 1 : 2, and the calculated stability coefficient is 2.7, but there are still landslides. Some even slow down the slope to 1 : 4, and the landslide phenomenon still exists [24].

This highlights the complexity and uncertainty of the selection of strength parameters in the stability analysis of expansive soil slope. In addition, there are few existing studies to discuss the selection of expansive slope stability analysis parameters combined with the strength attenuation and fissures development of expansive soil under the action of atmospheric wetting-drying cycles. Therefore, studying the strength attenuation and fissures development characteristics of expansive soil under dry wet cycle and low stress conditions are of great significance to clarify the causes of frequent shallow collapse of slope and determine the reasonable value of slope stability analysis parameters and effective engineering treatment measures.

Nanning, Baise, Shangsi, and other places in Guangxi Zhuang Autonomous Region are typical distribution areas of residual expansive soil in China. The properties of residual expansive soil in these areas are complex and bring many engineering disasters.

In order to study the relationship between strength attenuation and fissure development of residual expansive soil and explore the selection of soil parameters in Shallow Stability Analysis of expansive soil slope, the representative residual expansive soil specimens from Nanning, Baise, and Shangsi in Guangxi Zhuang Autonomous Region are selected for shear strength test under wetting-drying cycles and low stress. Moreover, the Baise residual expansive soil is selected for fissure observation test.

2. Materials and Test Methods

2.1. Soil for Test. Three representative residual expansive soil specimens of Nanning, Baise, and Shangsi in Guangxi Zhuang Autonomous Region were selected for experimental research. The basic soil property test indexes of the three soils are shown in Table 1.

2.2. Specimen Preparation. In this test, remoulded soil was used for specimen preparation. Three types of soil taken from the three selected areas were dried by natural air, crushed, and screened for 2 mm and then mixed into wet soil to achieve a natural moisture content of 17.0%. After 24 hrs of stuffing, the soil specimens were prepared by static pressure method. The dry density of the specimens was maintained at 1.70 g/cm^3, and the test errors of moisture content and dry density were limited within ±0.5% and ±0.02 g/cm^3, respectively, to ensure that the initial state of each soil specimen was basically the same before the implementation of the wetting-drying cycles. In addition, Baise expansive soil specimens with dry densities of 1.5 g/cm^3, 1.6 g/cm^3, and 1.7 g/cm^3 were prepared according to the above methods as fissure observation specimens.

2.3. Wetting-Drying Cycles Methods. The selected numbers of wetting-drying cycles were 0, 2, 4, and 6. Four groups of soil specimens were prepared, and one group of eight specimens was tested with load wetting-drying cycles. A total of 32 specimens were prepared. Filter paper and permeable stone were used to cover the upper and lower sides of each specimen so as to prevent the soil particles on the surface from scattering after water absorption and specimen expansion, respectively. Five specimens from each group were placed in the water tank, and vertical loads of 5, 15, 30, 50, and 75 kPa were applied, as shown in Figure 1. In the moisture absorption process, in order to simulate the critical state that the soil is completely saturated by moisture absorption in the process of rainfall infiltration, the saturated moisture content is controlled above 97%. The tank was filled with water to the same level as the permeable stone on the specimen. The specimen was left standing for 3-4 days for water absorption and saturation. The other three specimens in each group were humidified via vacuum pumping for 24 hrs, and the volume of each specimen was controlled to be constant during the saturation process according to the expansion force of the specimen. The saturations of the specimens obtained by the two methods were basically the same which is equal or more than 97%. Then, the weights of the specimens were determined. In the dehumidification process, in order to simulate the extreme high temperature of the natural environment, the temperature in the control

Table 1: Characteristic Indexes of Residual Expansive Soil.

Expansive soil	Bulk density [g/cm^3]	Liquid limit w_L [%]	Plastic limit w_p [%]	Plasticity index I_P	Particle composition [%]				Montmorillonite content [%]	Free expansion rate δ_{ef} [%]	Properties of water-soaked disintegrated material of dry rock mass
					>0.075 mm	0.075–0.005 mm	<0.005 mm	<0.002 mm			
Nanning expansive Soil	2.075	46.04	23.77	22.27	0.30	56.14	43.56	42.29	11.78	62	"Slice" muddy
Baise Expansive soil	2.092	56.26	21.37	34.89	0.10	52.02	47.88	45.20	16.58	82	"Clastic" muddy
Shangsi Expansive soil	2.032	55.33	25.19	30.14	0.09	47.87	52.04	48.6	15.05	51	"Debris" muddy

Figure 1: Wetting-drying cycles saturation with loading.

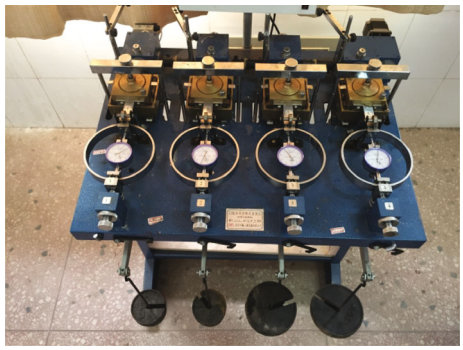

Figure 2: Strain controlled direct shear apparatus.

box is 40 °C, and the sample is taken out for weighing in time during the dehumidification process, and the moisture content of dehumidification is controlled to 13% of the shrinkage limit moisture content of the sample.

2.4. Direct Shear Test. After unloading the water saturated specimens with the proposed number of wetting-drying cycles, they were loaded into the shear box. The test instrument was a four-way direct shear instrument produced by Nanjing Soil Instrument Factory (see Figure 2). The corresponding vertical pressure was applied to minimize the impact of the unloading and loading process by conducting the test quickly. The shear strength of each group was measured with slow shearing, with a shearing rate of 0.02 mm/min. For a group of eight specimens, 5, 15, 30, 50, 75, 100, 200, and 300 kPa of corresponding moisture absorption loads were applied. In order to reduce the deviation of test results, three samples are selected as a group for parallel test in this shear strength test. The average value of the test results of the three samples is taken as the final result, and the test results are accurate to 0.01 kpa. The whole test process is carried out in strict accordance with the requirements of Chinese specification highway geotechnical test specification (JTG 3430-2020) [25].

2.5. Fissure Observation Test. After unloading the load on the saturated specimen that has completed the proposed number of wetting-drying cycles, the permeable stone and specimen are put into a 50 °C incubator to continue dehumidification. The specimen is weighed to monitor its humidity change. The fissure changes of different dehumidified specimens were photographed by a camera, and the fissure observation tests of specimens under wetting-drying cycles for 1, 2, 3, 5, and 6 times were completed.

3. Results and Discussion

3.1. Analysis of Shear Strength Test Results

3.1.1. Peak Shear Stress Results. The final shear data of the residual expansive soil measured in slow shear tests are listed in Table 2.

3.1.2. Effect of Vertical Load on Shear Strength. The absolute attenuation rate of the strength of the expansive soil is used as follows to facilitate the quantitative analysis of the attenuation law of the shear strength of soil specimens under different loads relative to the number of wetting-drying cycles:

$$\Delta_{i,\sigma} = \frac{\left|\tau_{i,\sigma} - \tau_{0,\sigma}\right|}{\tau_{0,\sigma}} \times 100. \quad (1)$$

In Equation (1), i is the number of wetting-drying cycles, σ denotes the vertical load, $\tau_{i,\sigma}$ is the shear strength after i wetting-drying cycles (kPa), and $\tau_{0,\sigma}$ is the shear strength of expansive soil without wetting-drying cycles under vertical load σ (kPa).

For the convenience of research, only the measured values of the three groups of soil specimens in Table 2 under the level 4 vertical load of 5, 50, 100, and 300 kPa are selected for analysis. The results calculated by substituting the corresponding data into Equation (1) are listed in Table 3. When the vertical load is fixed, the absolute attenuation rate of the strength of the three types of expansive soil gradually increases with the increasing number of wetting-drying cycles. However, after every two wetting-drying cycles, the attenuation rate gradually decreases, thus indicating the considerable impact of the initial wetting-drying cycles on the strength attenuation. When a number of wetting-drying cycles are the same, the greater the vertical load of the same soil specimen is, the smaller the absolute attenuation rate of the strength is. Therefore, increasing the overburden pressure can reduce the influence of the wetting-drying cycles on the strength attenuation of the expansive soil. It indicates that the load can effectively inhibit the strength attenuation of expansive soil during the wetting-drying cycles [26, 27].

3.1.3. Determination of Shear Strength Parameters. Many experiments have been pointed out that the shear strength line of expansive soil measured under the condition of low stress is nonlinear, which is dominant when the overburden pressure is smaller [28, 29]. The more significant the overburden pressure is, the larger the volume expansion is and the smaller the corresponding maximum shear stress is. However, if the direct shear test is carried out according to the method specified in the code and only the shear force under the condition of high stress is measured and analyzed, then the true value of shear strength at the shallow sliding surface of the expansive soil slope cannot be obtained.

In view of the characteristics of the shallow failure of expansive soil slope, the effective approach is to take the

Table 2: Results of Shear Strength Tests.

Vertical stress during shearing [kPa]	The peak shear stress of Nanning expansive soil [kPa] Number of cycles				The peak shear stress of Baise expansive soil [kPa] Number of cycles				The peak shear stress of Shangsi expansive soil [kPa] Number of cycles			
	0	2	4	6	0	2	4	6	0	2	4	6
5	12.09	7.85	5.46	4.10	12.56	6.32	5.66	5.12	11.27	6.62	5.48	4.86
15	15.84	13.60	13.42	12.74	25.30	17.22	14.63	12.10	15.17	12.05	11.14	10.01
30	26.74	22.12	20.46	19.15	29.05	19.47	18.16	16.43	25.91	21.01	18.65	16.94
50	35.41	31.68	29.80	28.01	42.15	33.01	28.48	26.73	36.72	30.10	27.21	25.29
75	45.14	40.57	37.34	36.65	49.91	45.27	40.24	38.96	48.78	40.42	36.90	34.72
100	55.08	50.29	47.37	47.03	60.35	55.84	53.97	51.83	57.25	47.86	43.32	41.05
200	94.14	89.68	86.13	83.93	99.02	94.69	89.26	84.34	96.09	88.21	83.36	79.35
300	139.28	131.70	128.26	127.40	127.06	118.44	116.72	110.94	130.25	120.33	113.67	110.92

Table 3: Shear strength reduction ratio of expansive soil with different wetting-drying cycles and loadings.

Vertical load [kPa]	Nanning soil [%]				Baise soil [%]				Shangsi soil [%]			
	Δ_0, σ	Δ_2, σ	Δ_4, σ	Δ_6, σ	Δ_0, σ	Δ_2, σ	Δ_4, σ	Δ_6, σ	Δ_0, σ	Δ_2, σ	Δ_4, σ	Δ_6, σ
5	0	34.70	54.24	65.43	0	49.22	54.38	58.67	0	41.25	51.38	56.88
50	0	10.43	15.69	20.70	0	21.48	32.11	36.22	0	18.03	25.90	31.13
100	0	8.61	13.86	14.48	0	7.41	10.45	13.98	0	16.40	24.33	28.30
300	0	5.39	7.83	8.44	0	6.71	8.05	12.56	0	7.62	12.73	14.84

high-stress and low-stress sections into consideration separately obtain the strength parameters in different sections. Five measuring points of 5, 15, 30, 50, and 75 kPa and four measuring points of 75, 100, 200, and 300 kPa are divided into two sections. As shown in Figure 3(a), straight-line fitting is carried out, and the corresponding c and φ values are shown in Table 4. For the convenience of comparison, a single straight-line strength line is also drawn in Figure 3(b). The correlation coefficient R^2 of each soil specimens fitting segmented strength line is greater than 0.94, which indicates that expressing the shear strength of expansive soil with either a single line or a double line is reasonable and feasible. However, the c value of a single line is much larger than that of a double line for the low-stress section. Therefore, in the stability analysis of expansive soil slope, the c and φ values should be, respectively, varied according to the possible sliding surface depth, and the corresponding index of the stress section can help obtain practical results.

3.1.4. Test Results of c and φ. According to the data in Table 4, regardless of the type of expansive soil and its high-stressor low-stress sections, the cohesion c value decreases continuously with the increasing number of wetting-drying cycles. However, the change range of the internal friction angle φ is relatively small. To further explore the change rule of the cohesion c value, the number of wetting-drying cycles is designated as the abscissa, and the cohesion is designated as the ordinate for curve fitting in the high- and low-stress sections, respectively, and the analysis results are shown in Figure 4.

The attenuation curve of the c value in Figure 4 is fitted numerically, and the attenuation of cohesion of the three types of soil with the increasing number of wetting-drying cycles is an exponential-type relationship. The correlation for the high-stress section is high, and the correlation coefficient is larger than 0.9. The correlation coefficient of the low-stress section of Nanning soil is greater than 0.95, and that of Baise soil is the lowest of 0.91. In summary, the relationship between the strength index c of expansive soil and the number of wetting-drying cycles N can be expressed as $c = ae^{-bN}$ (where a *and* b are constant).

Under the condition in which the internal friction angle φ does not decrease significantly with the increasing number of wetting-drying cycles, the average values of the four internal friction angles of each group of specimens under several wetting-drying cycles are taken in high-stress and low-stress sections, which are shown in Figure 5. The variation of the measured internal friction angle in five places is relatively small especially in Nanning soil and Baise soil, except for the low-stress section of Shangsi soil (see Figure 5). The deviation of the low-stress section of Shangsi soil is because that the measured internal friction angle of the soil specimen is relatively large when it is not subjected to the wetting-drying cycles. The difference may also be related to the small maximum dry bulk density of the soil. Therefore, within the test error, the value of the internal friction angle of each type of soil under the condition of low stress is replaced by the average value, which should meet the requirements of engineering applications.

3.2. Analysis of Fissure Observation Test Results

3.2.1. Change of Apparent Fissure of Specimen under Wetting-Drying Cycles. Figure 6 shows the photos of apparent fissure development of Baise expansive soil with dry

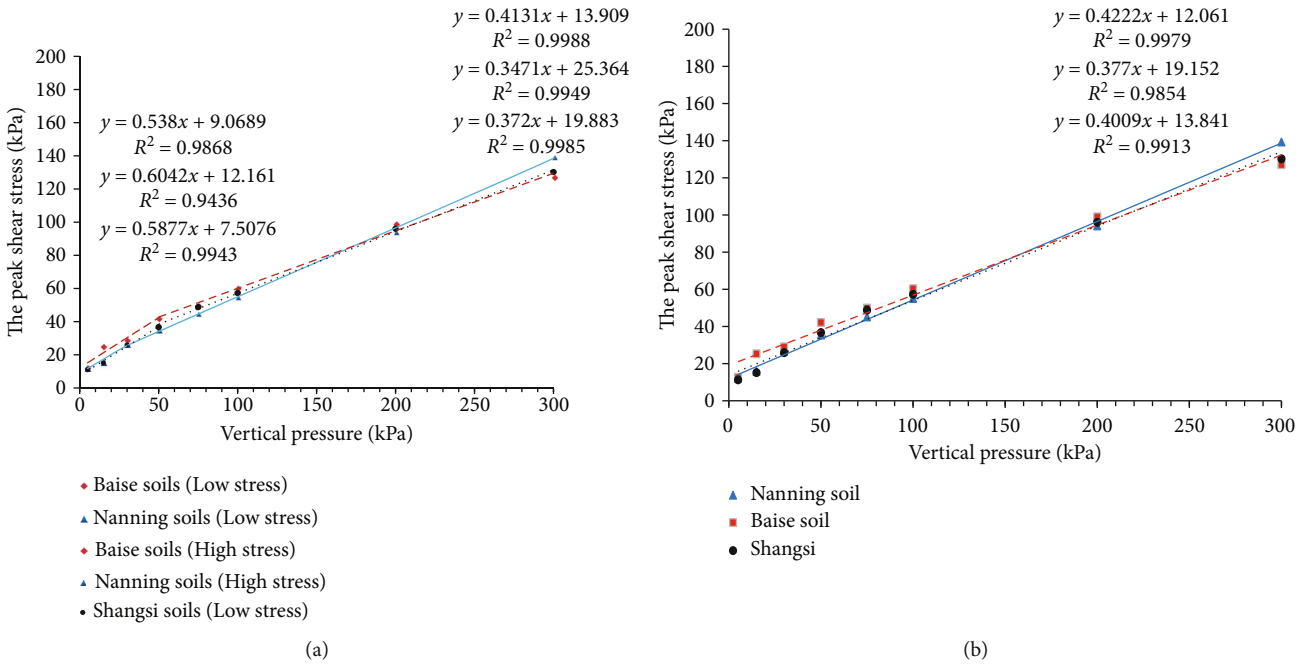

Figure 3: Line of shear strength of expansive soil with 0 wetting-drying cycles.

Table 4: Shear strength parameters of high and low stresses.

Stress interval	Parameters of strength	Nanning soil specimen under dry-wet conditions Number of cycles				Baise soil specimen under dry-wet conditions Number of cycles				Shangsi soil specimen under dry-wet conditions Number of cycles			
		0	2	4	6	0	2	4	6	0	2	4	6
High stress	φ [°]	22.58	22.00	21.90	21.76	19.02	18.18	18.51	17.46	20.07	19.88	19.26	19.07
	c [kP]	13.17	9.82	6.97	6.32	22.30	14.33	10.71	9.83	21.44	13.18	10.33	8.19
Low stress	φ [°]	25.78	25.13	24.03	24.13	26.90	27.96	25.20	25.16	28.79	25.81	24.02	23.01
	c [kP]	10.12	6.72	5.67	4.44	14.02	5.64	4.95	3.41	8.34	5.11	4.28	3.50

density of 1.5 g/cm^3, 1.6 g/cm^3, and 1.7 g/cm^3 under the action of wetting-drying cycles (n = 2, 3, 4, 5, and 6).

According to the Figure 6, under the same dry density, the apparent fissure development of the specimen becomes more intense with the increase of the number of wet dry cycles, and the depth of fissure development also gradually increases. The above findings are broadly consistent with the previous results reported in the literature (e.g., Luo et al. [30] and Xu et al. [31]).

This is because when the tensile force generated under the wetting-drying cycles exceeds the tensile force of the soil, the specimen surface will crack. Even if the fissure heals with water, the tensile strength of the soil cannot be fully restored with the healing of the fissure, so this place becomes the weak place of the soil. In the next dehumidification process, the weak place is easy to produce stress concentration and small tension, resulting in cracking. Therefore, with the increasing number of wetting-drying cycles, the fissure of the specimen continues to expand in the original weak position, gradually forming a fissure with larger area and deeper fissure depth until it is connected. However, the larger the dry density of the specimen, the slower the development of the apparent fissure under the same wetting-drying cycles conditions, which shows that increasing the dry density can significantly inhibit the development of the specimen fissure [32] .The dry density of the actual expansive soil slope soil increases gradually with the increase of soil depth, and the development of the apparent fissure also slows down from the surface to the inside under the action of atmospheric wetting-drying cycles, which is just consistent with the conclusion of the test.

In order to quantitatively analyze the influence of dry cycle action on the fissure development of Baise expansive soil specimen, the image pro plus image processing software is used to obtain the characteristic parameters of the apparent fissure of Baise expansive soil specimen, and the variation curve of the fissure area ratio of the specimen with the number of wetting-drying cycles is drawn (see Figure 7). The formula for calculating the fissure area ratio of the specimen is written as

$$S = \sum_{i=1}^{k} A_i / A_w, \tag{2}$$

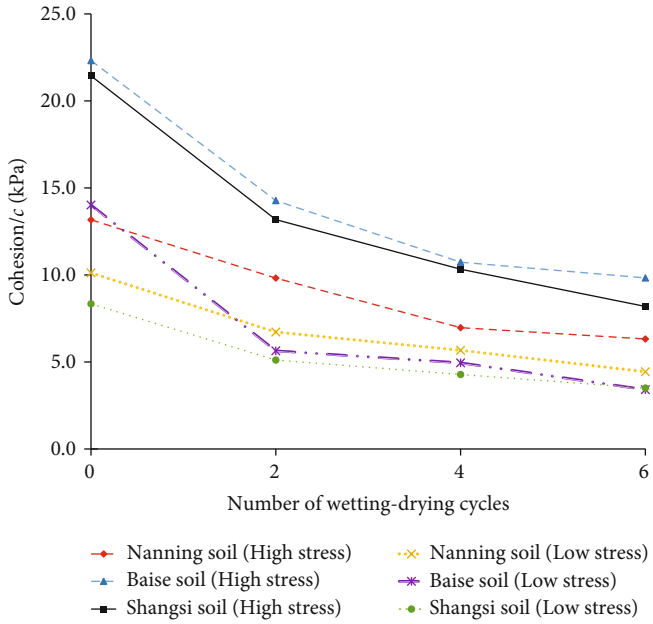

Figure 4: Curve fitting of c reduction with three types of expansive soil.

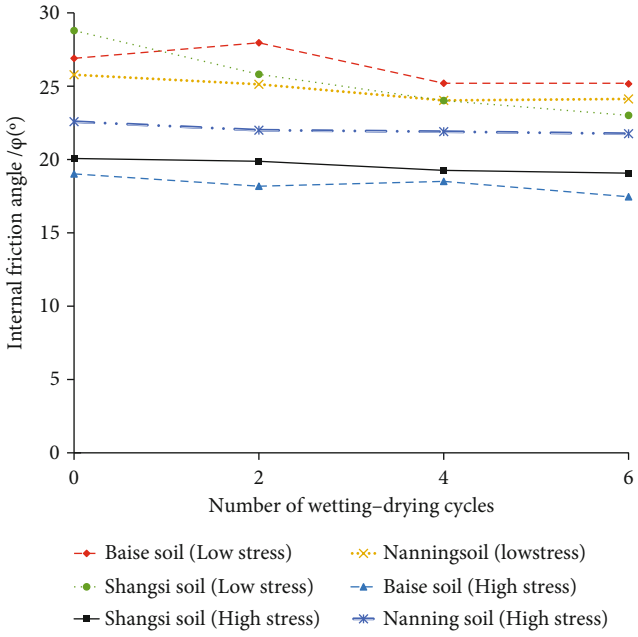

Figure 5: φ range of three types of expansive soil.

where S is the fissure area ratio; A_w is the area of the specimen when the humidity is w; A_i is the area of the i fissure; and k is the total number of fissures in the specimen.

It can be seen from Figure 7 that the fissure area ratio of the specimen increases with the increase of the number of wetting-drying cycles and finally tends to be stable. When the dry density is 1.5 g/cm3 and $N = 1 \sim 6$ times, the fissure area ratio are 0.00%, 0.26%, 3.38%, 4.43%, 5.50%, and 5.88%, respectively. The largest increase in the fissure area ratio of the specimen occurs in $n = 3$, which is 12 times that of $n = 2$. The fissure area ratio of $n = 6$ is only 6.9% higher than that of $n = 5$. The increase of specimens with higher dry density is more gentle than those with lower dry density, and the fissure area ratio is also smaller after six wetting-drying cycles. When $n = 6$, the fissure area ratio of the specimen with dry density of 1.7 g/cm^3 is 1.68%, which is only 29% of that of the specimen with dry density of 1.5 g/cm^3.

4. Discussion

4.1. The Relationship between Strength Attenuation of Expansive Soil and Fissure Development. Expansive soil is a typical clayey soil with many fissures. One of its typical characteristics is that the swelling shrinkage deformation is much larger than that of ordinary clayey soil. The swelling and shrinkage deformation of newly excavated expansive soil slope occurs continuously under the action of dry and wet cycle. The wetting-drying cycles leads to the generation and development of fissures in the slope and finally forms a chaotic fissure network after repeated times, especially in the high-temperature, humid, and hot areas in the south. The internal natural structure and initial integrity of undisturbed expansive soil are damaged due to the development of fissures, which immediately has a significant impact on the shear strength of soil. Therefore, the fissure factor in expansive soil cannot be ignored when analyzing the causes of shear strength attenuation.

From the perspective of fissure, the reason for strength attenuation is mainly the repeated expansion and contraction of soil specimens under the action of wetting-drying cycles. When the tensile force exceeds the tensile force of soil, the soil surface will crack [33]. However, the tensile strength of soil is a function of effective cohesion and matrix suction. The cohesion of soil will gradually decrease with the progress of wet dry cycle and finally tend to be stable. At this time, the tensile strength of soil is a function of matrix suction. In

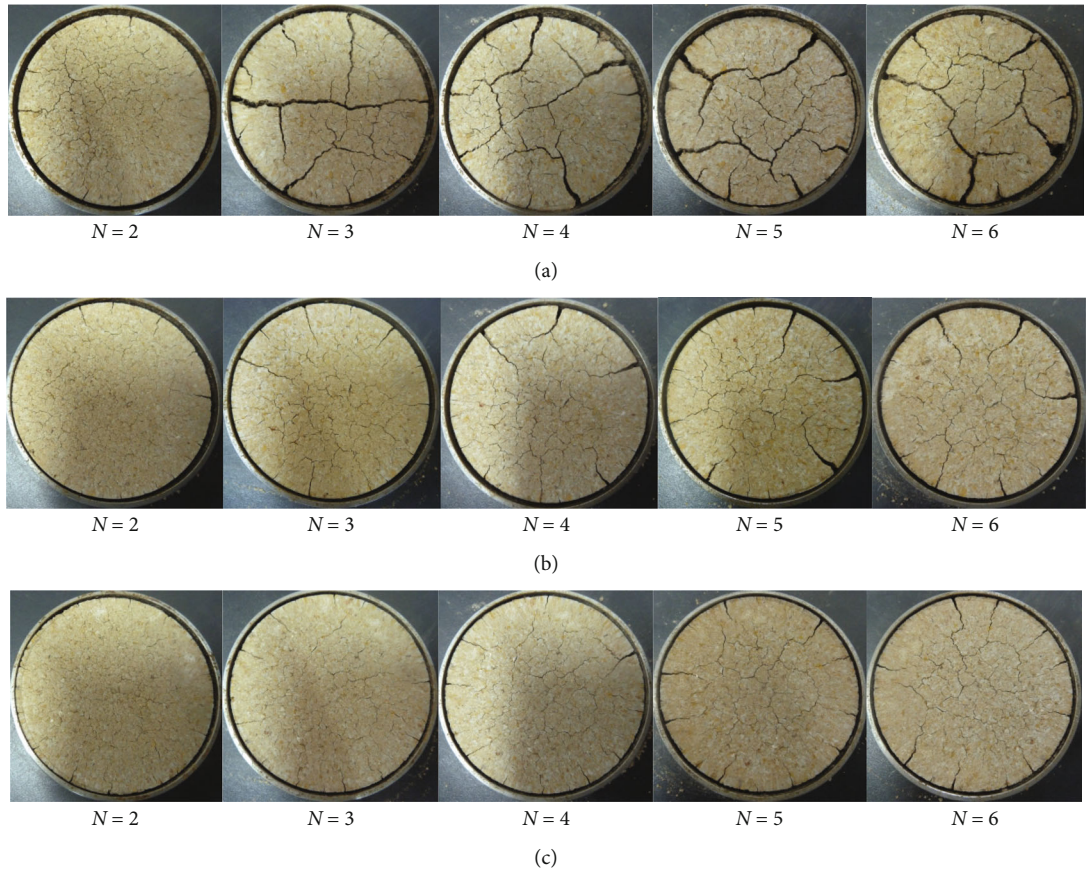

Figure 6: Apparent fissure images of Baise expansive soil specimens with different dry densities (N represents the number of wetting-drying cycles).

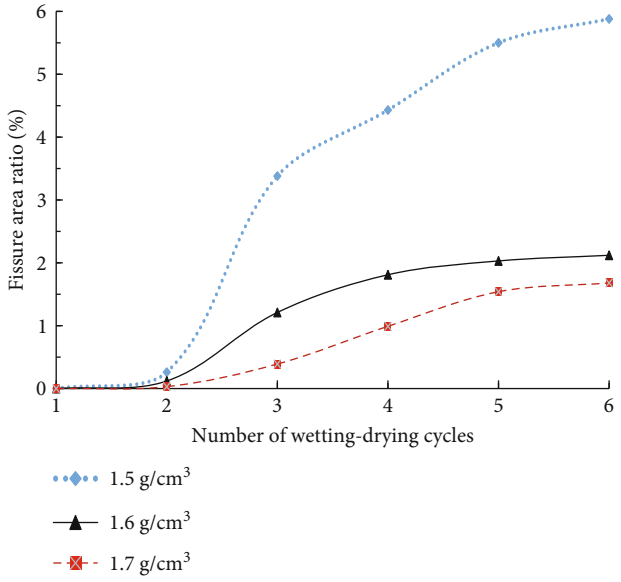

Figure 7: The fissure area ratio of specimen under wetting-drying cycles.

addition, matrix suction is mainly affected by water content [34] .With the increase of fissure depth, the distance between soil particles increases and the viscosity decreases after wet dry cycle. As a result, the moisture in the lower part is easier to evaporate, the moisture content gradient of the shallow surface soil of the specimen gradually decreases, the tensile strength decreases, and the fissures continue to develop and form a network inside. The continuously expanding and penetrating fissures reduce the cementation ability between soil particles, greatly reduce the cohesion, and aggravate the damage to the integrity of soil specimens, resulting in the reduction of its shear strength.

4.2. Suggestions on Strength Value during Stability Analysis of Expansive Soil Slope. Shallow collapse is a common geological problem faced by exposed expansive soil slopes in Southwest China, especially in Guangxi Zhuang Autonomous Region. Practice has shown that it has a certain relationship with the types and causes of expansive soil, but the severity of its damage is more closely related to the local atmospheric dry and wet cycle. In order to explore the main cause of shallow collapse of slope, the final shear strength of expansive soil must be determined.

Due to the remarkable characteristics of high peak strength and low residual strength of expansive soil, some scholars believe that the change process of expansive soil slope from stability to failure is from the peak of shear strength to the attenuation of residual strength [35]. The residual strength value of expansive soil is recommended

for slope stability checking calculation. However, residual strength is the stress drop after reaching the peak value. It is proposed for ordinary cohesive soil slope, which is suitable for analyzing the progressive failure of slope. Expansive soil is a special clay which is particularly sensitive to the external water temperature. Its strength variation characteristics are mainly determined by its own expansion and contraction properties, and its actual attenuation reason is not directly related to the residual strength. Liu et al. [36] concluded that the residual strength of expansive soil is not equal to the strength after wetting-drying cycles by using the specific data obtained from the test. The repeated change of the volume of expansive soil reduces the compactness of the soil, and the fissure development affects the initial integrity of the soil. The existence of small fissures leads to the reduction of strength, and large fissures directly disconnect the soil without strength.

The three soil specimens selected in this study are typical and representative expansive soils in Guangxi. After six wetting-drying cycles, the cohesion of residual expansive soil specimens in Nanning, Baise, and Shangsi in the low stress section (representing the shallow layer of the slope) is 4.48 kpa, 3.44 kpa, and 1.60 kpa, respectively. According to the rapid development of apparent fissures of the specimen with dry density of 1.5 g/cm^3 (representing the shallow soil of the slope) under the action of six wetting-drying cycles, it is not difficult to find that the strength of the sliding surface is also in the extremely low strength range of 0 ~ 5 kpa when the shallow soil of the expansive soil slope is damaged. Therefore, according to the actual environment, the strength index value of specimens with fissure network after many wetting-drying cycles should be used in the stability calculation of expansive soil slope.

In the construction of slope in expansive soil area, the shallow protection of expansive soil slope should be strengthened. In particular, for some cutting slopes disturbed by excavation, timely covering and water sealing measures should be taken to delay the development of secondary fissures on the slope, so as to avoid shallow damage of exposed expansive soil on the excavated expansive soil slope caused by atmospheric dry wet cycle for a long time.

5. Conclusion

(1) The shear strength parameters (cohesion) of the soil in the shallow layer (less than 50 kPa) and deep layer (100~200 KPa) of the expansive soil slope are very different. Generally, the slope stability analysis based on the deep soil strength parameters obtained from the conventional shear test will overestimate the stability of the actual expansive soil slope

(2) Although the expansion and shrinkage grades of expansive soil are different, as long as they are placed under the same climatic environment and load conditions (less than 50 kPa), the final shear strength will fall to a similar low value range (0~5 kN) after multiple wetting-drying cycles and low stress, which is also the key reason for the shallow collapse of slope in expansive soil area

(3) The strength decline of expansive soil under wetting-drying cycles is closely related to the development of fissures in the soil. The continuous development of fissures reduces the cementation ability between soil particles, greatly reduces the cohesion, and intensifies the damage to the integrity of soil specimens, resulting in the reduction of its shear strength. The strength index value of specimens with fissure network after many wetting-drying cycles should be used in the stability calculation and protection design of expansive soil slope

(4) The object of this study is the residual expansive soil in Guangxi Zhuang Autonomous Region of China. The general adaptability of its conclusion needs to be further verified by relevant tests of different expansive soils in other regions

Data Availability

The data used to support the results of this study are available from the corresponding authors upon request.

Conflicts of Interest

The authors declare that they have no conflicts of interest.

Authors' Contributions

Jin Chang contributed to the methodology and writing-original draft. Jieling Ma contributed to the conceptualization and revision. Xianyuan Tang contributed to the data curation and language editing.

Acknowledgments

This research was financially supported by the National Key R&D Program of China (Grant no. 2019YFC1509800), the National Natural Science Foundation of China (42107166), and the Hunan Provincial Natural Science Foundation (2021JJ40632).

References

[1] H. P. Yang, J. L. Zheng, and R. Zhang, "Addressing expansive soils," *Civil Engineering Magazine*, vol. 77, no. 3, pp. 62–69, 2007.

[2] Y. F. Xu, Y. Cheng, and H. H. Tang, "Instability characteristics of expansive soil slope and standardization of its prevention technology," *Journal of Central South*, vol. 53, no. 1, pp. 1–20, 2022.

[3] G. L. Yang, Z. A. Chen, H. R. Zhang, J. Y. Duan, X. P. Xia, and Y. L. Lin, "Study on instability and failure mechanism of gentle expansive soil slope under dry wet cycle," *Journal of Central South University*, vol. 53, no. 1, pp. 95–103, 2022.

[4] Z. L. Cheng, B. W. Gong, and H. Bo, "Shear strength of expansive soil and its test method," *Chinese Journal of Geotechnical Engineering*, vol. 37, no. S1, pp. 11–15, 2015.

[5] J. Xiao, H. P. Yang, H. F. Li, and X. Y. Tang, "Shallow failure stability analysis of expansive soil slope," *Journal of Transportation Engineering*, vol. 14, no. 2, pp. 21–27, 2014.

[6] H. P. Yang, X. Z. Wang, and J. Xiao, "Influence of wet-dry cycles on strength characteristics of Nanning expansive soils," *Chinese Journal of Geotechnical Engineering*, vol. 36, no. 5, pp. 949–954, 2014.

[7] C. S. Tang, B. Shi, and C. Liu, "Study on shrinkage cracking characteristics of expansive soil," *Journal of engineering geology*, vol. 5, pp. 663–6735, 2012.

[8] Y. L. Zhao, Y. X. Wang, W. J. Wang, L. M. Tang, Q. Liu, and G. Cheng, "Modeling of rheological fracture behavior of rock cracks subjected to hydraulic pressure and far field stresses," *Theoretical and Applied Fracture Mechanics*, vol. 101, pp. 59–66, 2019.

[9] Y. L. Zhao, L. Y. Zhang, J. Liao, W. J. Wang, Q. Liu, and L. M. Tang, "Experimental study of fracture toughness and subcritical crack growth of three rocks under different environments," *International Journal of Geomechanics*, vol. 20, no. 8, 2020.

[10] Y. L. Zhao, Q. Liu, C. Zhang, J. Liao, H. Lin, and Y. Wang, "Coupled seepage-damage effect in fractured rock masses: model development and a case study," *International Journal of Rock Mechanics and Mining Sciences*, vol. 144, article 104822, 2021.

[11] H. Yang, H. Lin, Y. Chen et al., "Influence of wing crack propagation on the failure process and strength of fractured specimens," *Bulletin of Engineering Geology and the Environment*, vol. 81, no. 1, p. 71, 2022.

[12] X. M. Li, L. W. Kong, K. Mu, Y. Liu, and X. D. Liu, "Experimental research on shear strength of expansive soil under wetting-drying cycles based on wrapping method," *Rock and Soil Mechanics*, vol. 35, no. 3, pp. 675–682, 2014.

[13] Z. L. Cheng, Q. Y. Li, X. L. Guo, and B. W. Gong, "Study on the stability of expansive soil slope," *Journal of Yangtze River Scientific Research Institute*, vol. 28, no. 10, pp. 102–111, 2011.

[14] J. Xiao, H. P. Yang, J. Zhang, and X. Tang, "Properties of drained shear strength of expansive soil considering low stresses and its influencing *factors*," *Journal of Civil Engineering*, vol. 16, no. 10, pp. 1389–1398, 2018.

[15] J. Xiao, H. P. Yang, J. S. Lin, G. Y. Chen, J. Chang, and X. Ni, "Triaxial test of expansive soil simulating dry wet cycle and low confining pressure," *Chinese Journal of Highway*, vol. 32, no. 1, pp. 21–28, 2019.

[16] S. J. Wang, Y. Han, X. Li, L. J. Shi, Y. Q. Zhang, and Z. H. Chen, "CT triaxial test study on strength and deformation characteristics of expansive soil with cylindrical hole damage," *Geotechnical mechanics*, vol. 34, no. 10, pp. 2763–2768, 2013.

[17] X. H. Hu, K. Y. Zhang, M. J. Nie, and R. Y. Pan, "Influence of dry wet cycle conditions on strength index of expansive soil," *Journal of Central South University*, vol. 53, no. 1, pp. 269–279, 2022.

[18] J. Xiao, H. P. Yang, H. F. Li, and X. Y. Tang, "Shear strength test of Nanning expansive soil with different density under low stress condition," *Chinese Journal of Highway*, vol. 26, no. 6, pp. 15–21, 2013.

[19] Q. F. Gao, L. Zeng, Z. N. Shi, and R. Zhang, "Evolution of unsaturated shear strength and microstructure of a compacted silty clay on wetting paths," *International Journal of Geomechanics*, vol. 21, no. 12, 2021.

[20] S. P. Zhang, R. Y. S. Pak, and J. Zhang, "Three-dimensional frequency-domain Green's functions of a finite fluid-saturated soil layer underlain by rigid bedrock to interior loadings," *International Journal of Geomechanics*, vol. 22, no. 1, 2022.

[21] Z. Z. Yin, J. P. Yuan, J. Wei, X. S. Cao, H. Q. Liu, and B. Xu, "Influences of fissures on slope stability of expansive soil," *Chinese Journal of Geotechnical Engineering*, vol. 34, no. 12, pp. 2155–2161, 2012.

[22] Z. Z. Yin and B. Xu, "Phylogenetic reconstruction of Chirita and allies (Gesneriaceae) with taxonomic treatments," *Chinese Journal of Geotechnical Engineering*, vol. 49, no. 1, pp. 50–64, 2011.

[23] B. W. Gong, Z. L. Cheng, B. Hu, and L. Zhao, "Study on engineering characteristics of fissures in expansive soil," *Geotechnical Mechanics*, vol. 35, no. 7, p. 7, 2014.

[24] M. Y. Wang, H. Xu, H. Yang, and X. H. Zhou, "Failure mechanism and stability analysis of unsaturated expansive soil slope," *South to North Water Diversion and Water Conservancy Science and Technology*, vol. 6, no. 1, pp. 151–153, 2008.

[25] Ministry of Transport of PRC, *Test methods of soil for highway engineering*, China Communications Press, Beijing, China, 2020.

[26] S. H. Liu, Y. S. Wang, K. S. Zhu, and J. Wu, "Experimental study on strength characteristics of Nanyang expansive soil under loading and its application," *Journal of Hydraulic Engineering*, vol. 41, no. 3, pp. 361–367, 2010.

[27] H. P. Yang, X. Y. Tang, X. Z. Wang, J. Xiao, and X. Ni, "Basic characteristics of shear strength of different expansive soils under loaded dry wet cycle," *Geotechnical Mechanics*, vol. 39, no. 7, p. 7, 2018.

[28] J. J. Li, L. W. Kong, and K. Mu, "In-situ borehole shear test on expansive soil and its strength characteristics," *Rock and Soil Mechanics*, vol. 38, no. 2, pp. 453–461, 2017.

[29] J. Xiao, H. P. Yang, X. Z. Wang, and X. Y. Tang, "Analysis of nonlinear characteristics of shear strength of Nanning expansive soil and its influencing factors," *China Journal of Highway and Transport*, vol. 27, no. 10, pp. 1–7, 2014.

[30] Z. G. Luo, S. J. Wang, and Z. B. Yang, "Evolution and quantitative analysis of wet dry expansion shrinkage cracks in expansive soil," *Geotechnical Mechanics*, vol. 41, no. 7, p. 11, 2020.

[31] X. C. Xu, W. Zhou, and S. X. Chen, "Analysis on crack characteristics and influencing factors of expansive soil in the whole process of dehumidification in Nanyang remodeling," *Geotechnical Mechanics*, vol. 36, no. 9, 2015.

[32] X. C. Xu, W. Zhou, and S. X. Chen, "Study of cracking characteristics and influencing factors for remolded Nanyang expansive soil in dehydration process," *Rock and Soil Mechanics*, vol. 36, no. 9, 2015.

[33] Z. Z. Yin, J. P. Yuan, J. Wei, X. S. Cao, H. Q. Liu, and B. Xu, "On the influence of cracks on the stability of expansive soil slope," *Journal of Geotechnical Engineering*, vol. 34, no. 12, pp. 2155–2161, 2012.

[34] P. H. Morris, J. Graham, and D. Williams, "Cracking in drying soils," *Canadian Geotechnical Journal*, vol. 29, no. 2, pp. 263–277, 1992.

[35] H. H. Xie, Z. H. Xu, Q. B. Liu, and G. Y. Hu, "Study on the evolution of peak and residual strength of weakly expansive soil under dry wet cycle path," *Geotechnical Mechanics*, vol. 40, no. S1, pp. 245–252, 2019.

[36] H. Q. Liu and Z. Z. Yin, "Experimental study on the influence of cracks on the shear strength index of expansive soil," *Geotechnical Mechanics*, vol. 31, no. 3, pp. 727–731, 2010.

Hindawi
Geofluids
Volume 2022, Article ID 2891029, 14 pages
https://doi.org/10.1155/2022/2891029

Research Article

Development of Modified LSTM Model for Reservoir Capacity Prediction in Huanggang Reservoir, Fujian, China

Bibo Dai,[1,2,3] Jiangbin Wang,[4] Xiao Gu,[5] Chunyan Xu,[4] Xin Yu,[6] Haosheng Zhang,[6] Canming Yuan ,[3,5] and Wen Nie [3,5,6]

[1]*School of Resources and Civil Engineering, Northeastern University, Shenyang 110819, China*
[2]*Geomechanics Research Center, Northeastern University, Shenyang 110819, China*
[3]*State Key Laboratory of Safety and Health for Metal Mines, Maanshan 243000, China*
[4]*The Water Resources Allocation Center of Shanmei Reservoir in Quanzhou, Quanzhou 362000, China*
[5]*School of Resources and Environmental Engineering, Jiangxi University of Science and Technology, Ganzhou 341000, China*
[6]*Quanzhou Institute of Equipment Manufacturing, Haixi Institutes, Chinese Academy of Sciences, Quanzhou 362000, China*

Correspondence should be addressed to Canming Yuan; 3187805991@qq.com and Wen Nie; wen.nie@fjirsm.ac.cn

Received 1 April 2022; Revised 13 June 2022; Accepted 23 June 2022; Published 23 July 2022

Academic Editor: Zizheng Guo

The Huanggang Reservoir capacity is affected by a variety of factors. In order to accurately understand the Huanggang Reservoir capacity change, we develop a new hydrological prediction model based on the LSTM (Long-Short-Term Memory) method, which is used to predict the capacity of the reservoir. In this modified model, we choose to input multidimensional factors, two fully connected layers, selecting the optimal number of the hidden neurons, the optimizer, and adding the attention mechanism. The result of using the Developed LSTM and usual LSTM shows that the prediction curve of the Developed LSTM model can fit the true value better than the usual LSTM model, and the mean relative error of the Developed LSTM model decreased by 1.15%-3.82%, comparing with the usual LSTM model. Thus, we realize that the Developed LSTM model can make accurately prediction in some reservoir capacity estimations.

1. Introduction

Reservoir, a water conservancy project, which plays an important role in agricultural irrigation, flood control during flood season, hydroelectric power generation, and water supply [1–3]. Therefore, the safety of reservoirs will directly affect economic development and people's livelihood. With the environment changing, extreme weather occurring frequently, the probability of reservoir safety hazards has greatly increased [4–6].

With climate change and the country's emphasis on water conservancy projects, the prediction of reservoir capacity has become a hot research spot in recent years. To clarify the changes in reservoir water volume, a large number of fruitful studies have been carried out. There are three commonly used methods of reservoir volume forecasting: (1) Reservoir volume prediction based on the principle of reservoir flood regulation calculation; (2) Hydrodynamic methods; (3) Artificial Neural Networks predict the complex nonlinear reservoir capacity [7]. The first method is to estimate the water level using the principle of reservoir flood regulation calculation. The principle of reservoir flood regulated calculation was used widely and predicted the water level of the reservoir initially. If the reservoirs' inflow is back-calculated by the balance equation, the errors would occur [8]. The second method depends on the hydrodynamic method. An excellent hydrological model can simulate the water level pretty well. However, the hydrodynamic model requires amounts of data, and the exactitude of the input factors will determine the accuracy of the model. In addition, the hydrodynamic process is complex and changeable, which could increase the difficulty of reservoir capacity simulation.

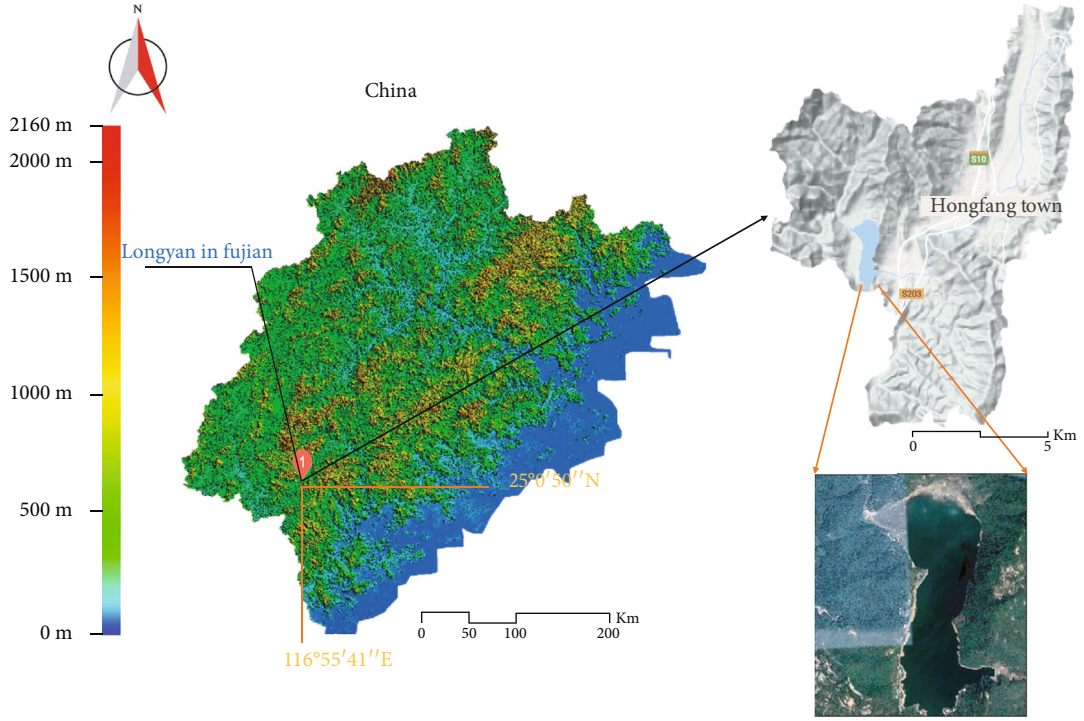

Figure 1: Location of Huanggang Reservoir.

These factors limit the development of this hydrodynamic model [9, 10]. For the third method, the reservoir capacity prediction depends on the Artificial Neural Networks. With the continuous development of various monitoring and forecasting technologies [11–14], especially the emergence of the LSTM (Long Short-term Memory) neural network, it stores historical information by cyclic feedback and has a strong ability to solve time series problems. It has attracted attention in the prediction of hydrological time series problems [15, 16]. Lin [17] et al. compared the LSTM algorithm with the hydrological physical model who found the LSTM model is better than the traditional physical model; Mich [18] et al. compared the accuracy of several different neural network algorithms in water level prediction; Chen [19] Compared the water level prediction with LSTM and SVM models, it found that LSTM has advantages over general neural networks; Gu [20] et al. used LSTM to predict the water level of Poyang Lake by using 7 lakes' data. The accuracy of predicting the water level of Poyang Lake based on the amount of rivers' data that is much better than one single river 's. The traditional LSTM model mainly focuses on the prediction of time series of hydrological information, while external factors are often ignored. Factors, which are closely related to the prediction, are usually not involved in the structure of the model. This ignorance directly made the model prediction have a large deviation from the real when the correlation factor changes greatly. Therefore, considering the influence of the correlation factor on the model, we optimize the LSTM model for the prediction of reservoir capacity.

In the study area, Huanggang Reservoir capacity (Fujian, China) has many influence factors which are complex nonlinear changing. LSTM model usually predicts the storage capacity only by one input factor (historical reservoir capacity). We use the multiple inputting factors of developed LSTM including historical storage capacity and rainfall. In addition, an attention mechanism is introduced in the developed LSTM model, which can give different weights to different factors in the process of LSTM decoding and coding, so that the calculation results are more accurate. In the following, we explore whether they can improve the accuracy of the model in reservoir capacity prediction.

2. Materials and Methods

The study area is located in the upper reaches of the Jiulong River water system, which belongs to Longyan City, Fujian Province, China. The city has a population of 300,000, a land of about 150,000 acres, many industrial and mining enterprises [21]. Huanggang Reservoir is an important reservoir that is mainly used for irrigation, combined with comprehensive utilization of flood control, power generation, and aquaculture [22, 23]. The study area is affected by a subtropical monsoon climate with sufficient rainfall throughout the year. Sufficient water flow, typhoons, heavy rainfall, and other extreme weather usually occur in summer [24]. The total storage capacity of the reservoir area reaches 28.6 million m^3 [25, 26], and the location map of Huanggang Reservoir is shown in Figure 1.

2.1. Research data. The daily hydrological data of the Huanggang Reservoir from 2001-to 2019 was obtained from the Longyan Reservoir Management Center. These data

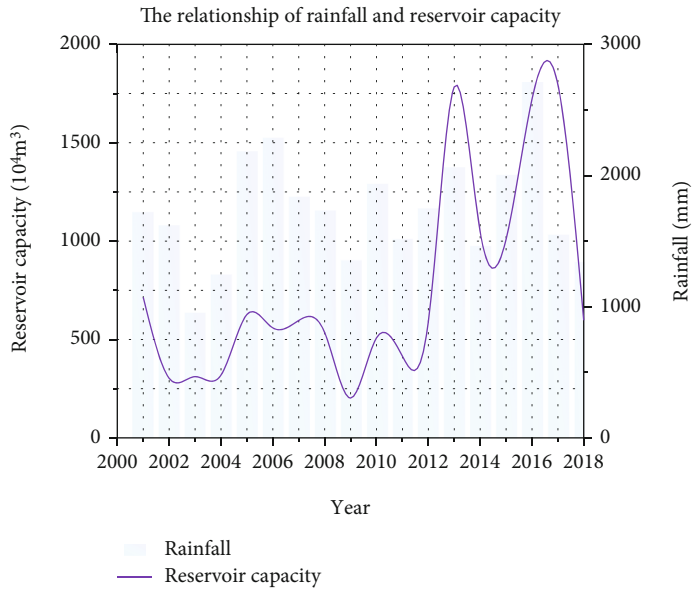

Figure 2: The data of reservoir capacity and rainfall from 2001 to 2019.

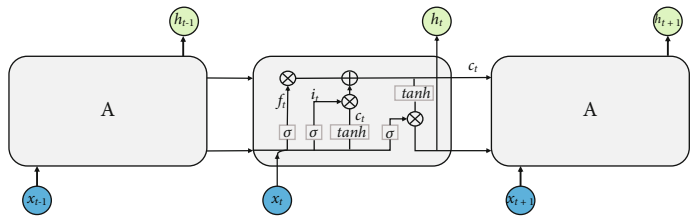

Figure 3: LSTM model structure [27].

included the historical storage capacity of the reservoir and the rainfall value around Huanggang Reservoir. The relationship between rainfall and reservoir capacity from 2001-to 2019 is shown in Figure 2.

2.2. Basic principles of LSTM. LSTM is a special deep learning neural network that is based on RNN, which makes up for the problem of gradient disappearance and explosion in the process of long sequence training (Figure 3). In the hydrological prediction of long time series, the LSTM model has been widely used [27]. Compared with other algorithm models, it has some significant advantages and the simulation effect is excellent in hydrological prediction [28].

The long-short-term memory neural network is composed of memory cells. Its key is the state of these memory cells and the structure of the "gate" in the process. The cell state transmits the information in the time series that likes a conveyor belt and then passes through three gates: the input gate, the forget gate, and the output gate. The input gate determines how much input data of the network at the current moment is saved in the unit state; the forget gate determines how much of the unit state at the previous moment is saved to the current moment; the output gate

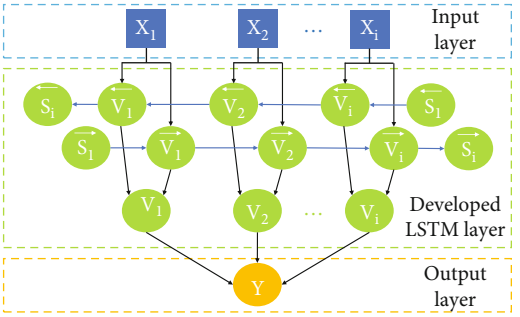

Figure 4: Developed LSTM model structure diagram.

determines the number of the control unit state which is outputted to the current output value of LSTM.

The basic process of LSTM neural network information transmission is as follows (only one neural network node is used as an example to illustrate): (1) The forget gate controls the input information through the sigmoid function to determine which information can enter the current cell state unit; (2) A candidate value that can be added to the current cell state unit is generated by the tanh layer, and then the

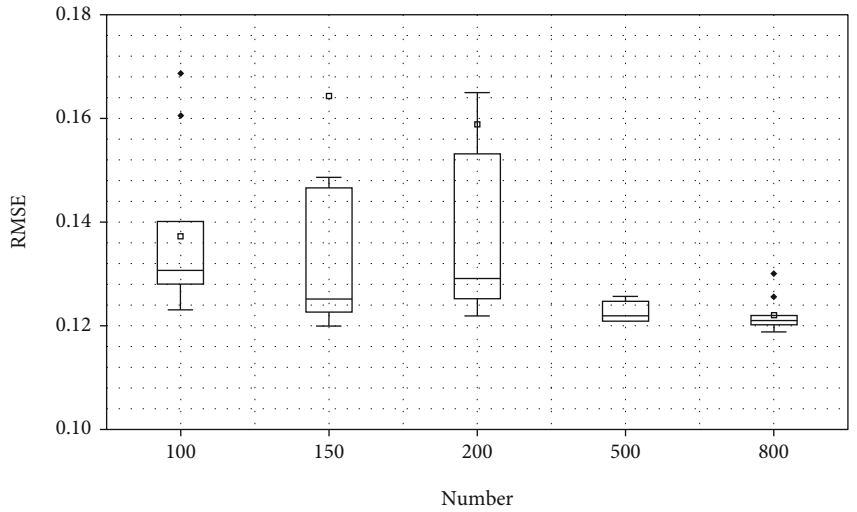

Figure 5: Hidden Neuron box plot.

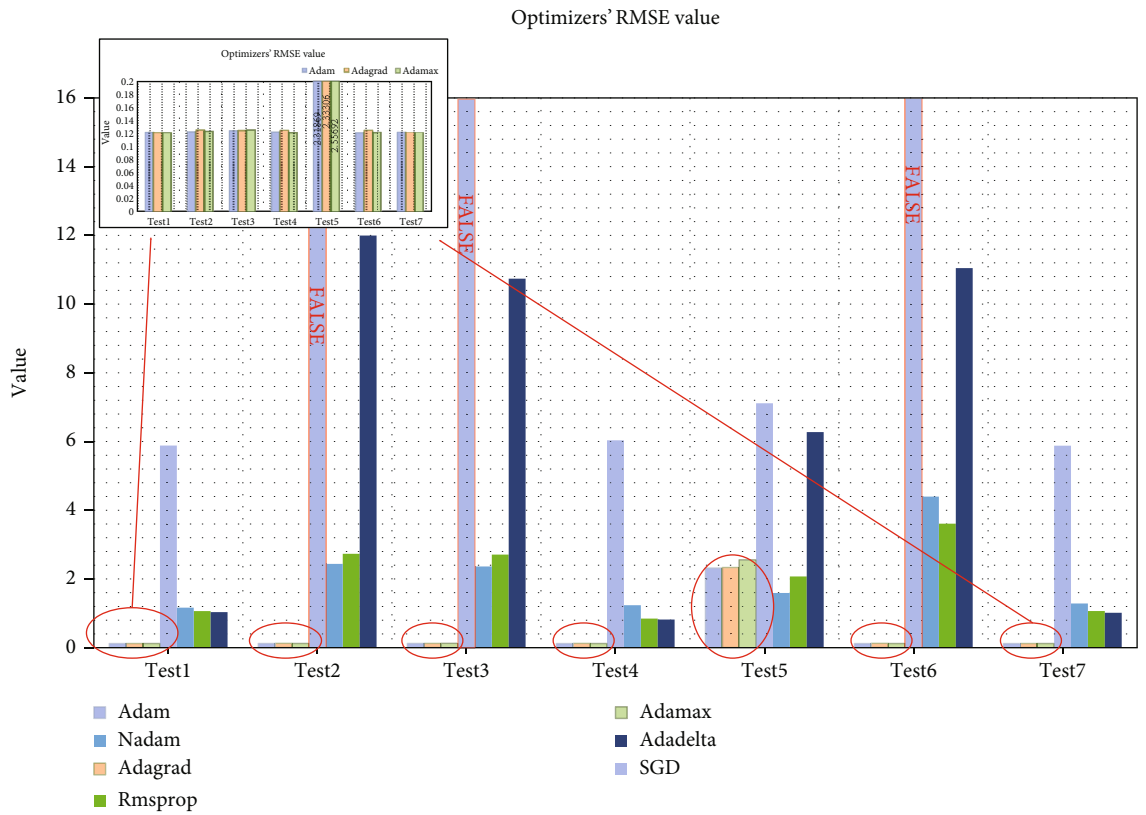

Figure 6: Optimizers' RMSE value.

candidate value, the input information of the previous step, and the cell unit state of the previous moment are bitwise operated to obtain a new cell unit state value; (3) After obtaining the initial output information through the sigmoid function, the tanh layer is used to process the new cell unit state value to make it between -1 and 1. The information of the initial output and the state value of the processed cell unit are calculated and output.

$$\begin{aligned} it &= \sigma(Wxixt + Whiht - 1 + bi) \\ \mathrm{ft} &= \sigma(Wxfxt + Whfht - 1 + bf) \\ ot &= \sigma(Wxoxt + Whoht - 1 + bo) \\ ct &= \mathrm{ft} \times ct - 1 + it \times \tanh(Wxcxt + Whcht - 1 + bc) \\ ht &= ot \times \tanh(ct) \end{aligned} \tag{1}$$

Table 1: Hyperparameters of LSTM.

Experimental objects	Huanggang Reservoir		Hejiapo Reservoir	
	Single-factor	Two-factor	Single-factor	Two-factor
Number of hidden layers	2	2	2	2
Number of neurons in hidden layer 1	500	500	100	100
Number of neurons in hidden layer 2	500	500	20	20
Activation function of hidden layer 1	tanh	tanh	tanh	tanh
Activation function of hidden layer 2	relu	relu	linear	linear
Optimizer	adam	adam	adam	adam
Training times	200	60	500	240

it - the output value of the hidden layer at the previous moment in the input gate and the value of the input value at the current moment processed by the sigmoid function; ft - the output value of the hidden layer at the previous moment in the forget gate and the value of the input value at the current moment processed by the sigmoid function; ot - the output value of the hidden layer at the previous moment in the output gate and the value of the input value at the current moment processed by the sigmoid function; ct - the state value of the cell unit after the update at the current moment; ht - the output value of the hidden layer at the current moment; σ and tanh - cyclic activation functions; ht-1 - the output value of the hidden layer at the previous moment; xt - the input value at the current moment; W - different weight matrices; b—different bias parameters.

2.2.1. LSTM neural network backpropagation. The LSTM neural network model finds the optimal solution by continuous optimization and making the model converge. The Loss function is used to compare the true value and the prediction and it is an important indicator for evaluating the quality of models. The Loss function, which reaches an infinitely close to 0 degree, determines the pros and cons of the model. The neural network backpropagation algorithm uses gradient descent to iteratively update the weight value of the neural network:

$$\text{Loss} = \frac{1}{m}\sum_{i=1}^{m}(y_i - \bar{y}_i)^2 \tag{2}$$

In the formula, Loss is the Loss function, y_i and $\hat{y}_i$ are the true value and predicted value at the time i, respectively.

2.3. Data processing method. We got the Developed LSTM model multidimensional inputting factors historical reservoir capacity and rainfall that are from 2001 to 2018. Due to the unusual characteristics of the original data (the historical reservoir capacity and rainfall), we processed the original data, deleted outliers, supplemented missing values, and minimized the abnormal samples of the data that had a large negative impact on the calculation results, such as the model calculation does not converge, the expected effect of the model is worse and other phenomena. To ensure that the data are in the same dimension, we normalize the data as eq (3):

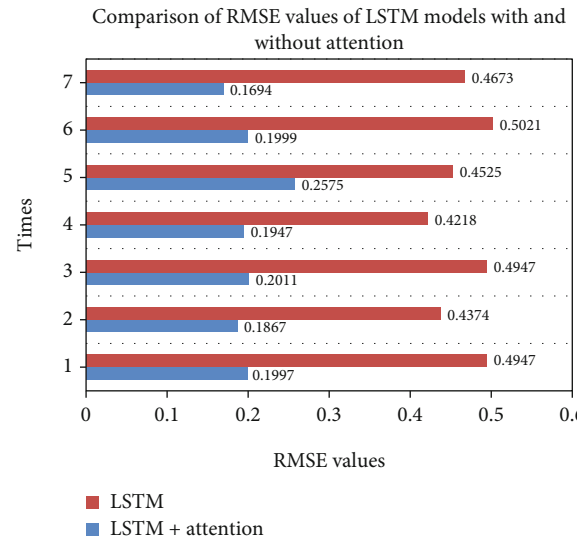

Figure 7: Comparison plot of RMSE values of LSTM models with and without attention.

$$X^* = \frac{X - X_{min}}{X_{max} - X_{min}} \tag{3}$$

Here we adopt the Min-Max Normalization method. In the formula, X_i is the normalized result, X is the original data, X_{max} is the maximum value in the original data, and X_{min} is the minimum value in the original data.

3. Developed LSTM model structure

In the Developed LSTM structure, we considered a variety of correlation factors as the model inputting, getting the optimal number of hidden neurons and the best type of the optimizer in the LSTM model, and the introduction of attention mechanism in the model.

3.1. Model structure. The model was structured by using a both way two-layer fully connected layer and multi-factor inputting parameter optimized. We selected the two factors including Huanggang reservoir capacity and the rainfall data as the input factor from 2013-2018. The data from 2013-2016 was training set, while the data of 2017-2018 was used

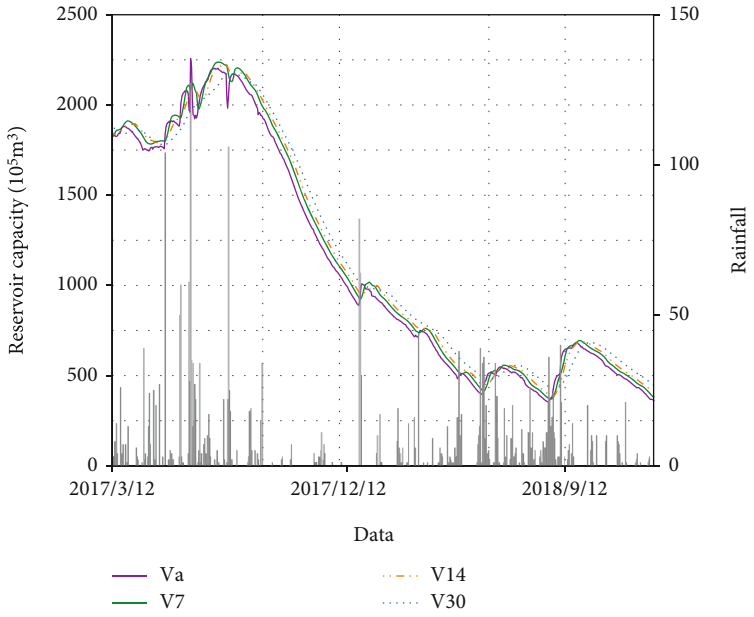

(a) Single-factor input LSTM model

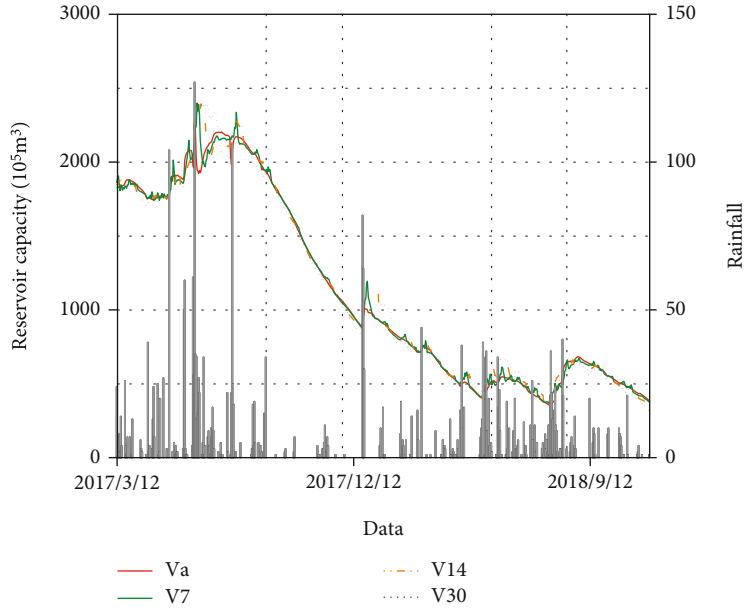

(b) Two-factor input LSTM model

Figure 8: Continued.

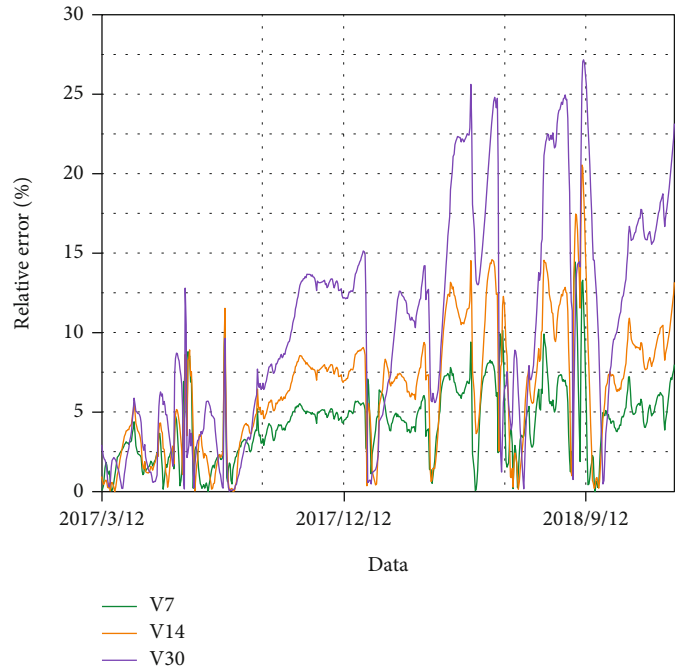

(c) Single-factor input LSTM relative error curve

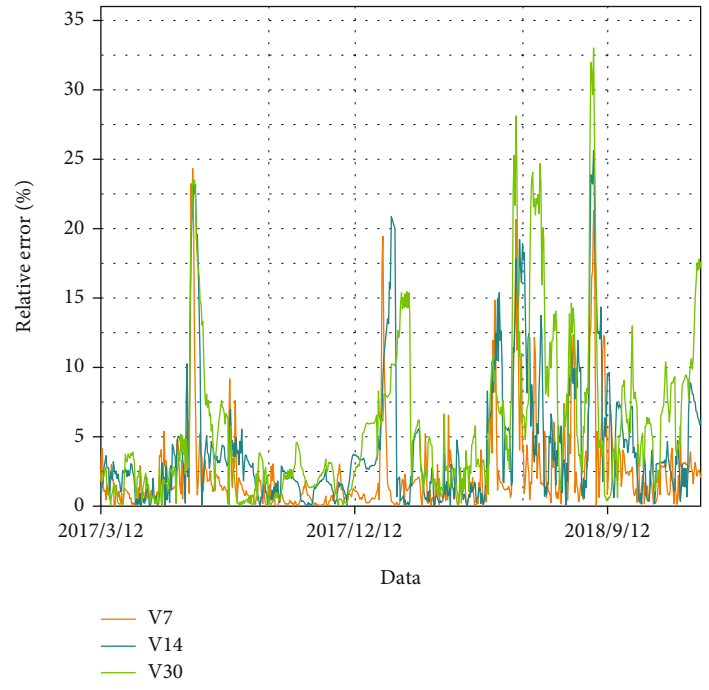

(d) Two-factor input LSTM relative error curve

FIGURE 8: The prediction of reservoir capacity and the relative error of both models. V_a represents the actual reservoir capacity, V_7, V_{14} and V_{30} represent the predicted reservoir capacity for 7, 14, and 30 days.

as the test data to predict the changes in reservoir capacity for 7days, 14 days, and 30 days, respectively. The developed LSTM neural network model structure is shown in Figure 4. x_i is the inputting factor. It changes the dimension of the x_i matrix, $x_i = \{a_i, c_i\}$, a_i=storage capacity, c_i=rainfall, to realize multi-factor input; $\overleftarrow{V_i}$ stands for data to participate in forward operation; $\overrightarrow{V_i}$ stands for data to participate in opposite operation; $\overleftarrow{S_i}$, $\overrightarrow{S_i}$ represents the value of the hidden layer in forward and opposite operation; V_i is the value after attention processing; Y is the prediction result in Developed LSTM model.

3.2. Model parameter optimization. In the model parameter optimization processing, we selected optimal number of

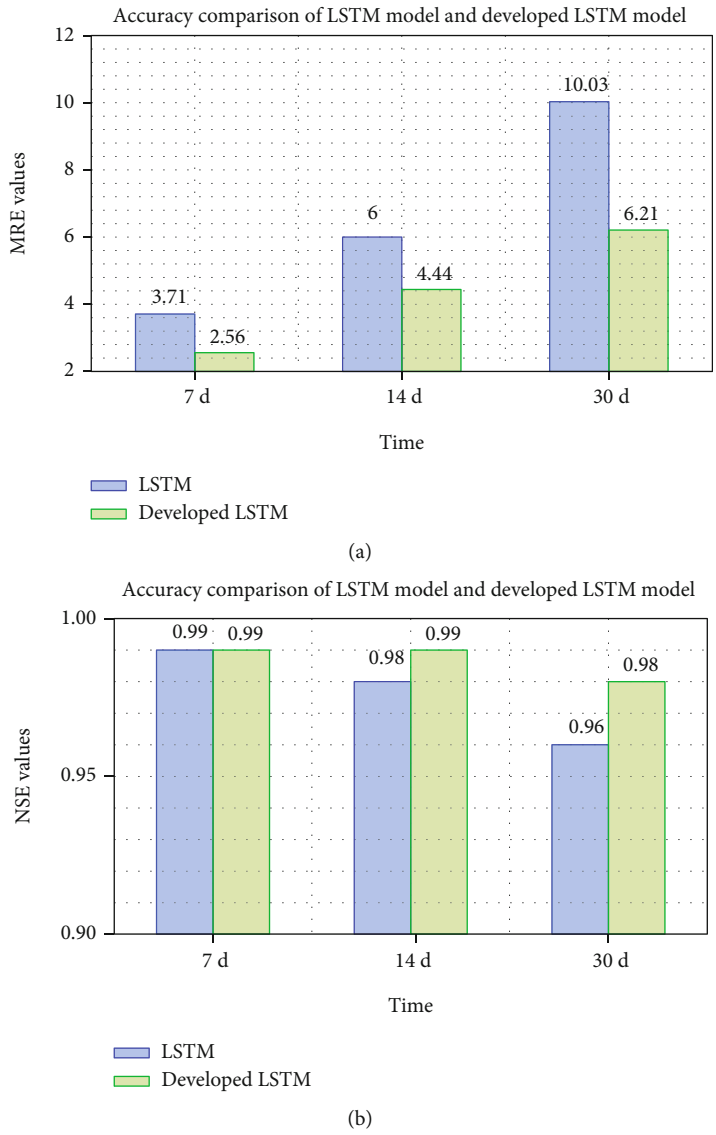

Figure 9: Comparison plot of accuracy between LSTM model and developed LSTM model.

hidden neurons, the activation function, the optimizers and introduced the attention mechanism in the LSTM model.

3.2.1. The influence of the number of hidden neurons. The LSTM algorithm has high requirements for the number of hidden neurons [28]. The number of hidden neurons is one of the most important factors that affect the accuracy of the LSTM model. If only few neurons were used in the hidden layer, the model could not be fully trained; while too many hidden neurons would cause a time-consuming training, which may lead the model to take a phenomenon of non-convergence or over-fitting.

Finding the appropriate number of neurons had an important impact on the quality of model training. We took a total of 10 kinds of neural network numbers (1, 10, 20, 30, 50, 100, 150, 200, 500, 800) to predict the future reservoir capacity by inputting the historical storage capacity and rainfall of the Huanggang Reservoir. It found that the RMSE value of the 1, 10, 20 items varies from 1 to 7. And the RMSE value of 30 and 50 items ranges from 0.975 to 0.27 and the results have great fluctuations (in the box plot would have a negative effect). Thus, the result of 100-800 items are only considered as shown in Figure 5.

With the number of neurons increase, the RMSE value of the model becomes smaller and gradually stabilizes, and the number of abnormal points decreases. When the number of neurons exceeds 500 to 800, the increased neurons number has a small effect on the model and the number of outliers becomes more, so we finally use 500 hidden neurons.

3.2.2. The influence of choosing a good optimizer. The optimizer plays a vital role in improving the speed of model training and accelerating model convergence to find the optimal solution [29–31]. Increasing of complex neural networks directly lead to huge model parameters. A good

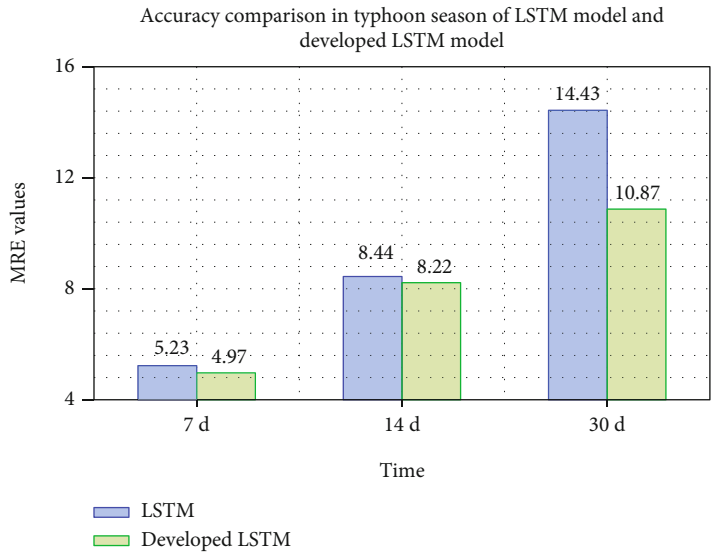

Figure 10: Comparison plot of accuracy of the LSTM model and the developed LSTM model in typhoon season.

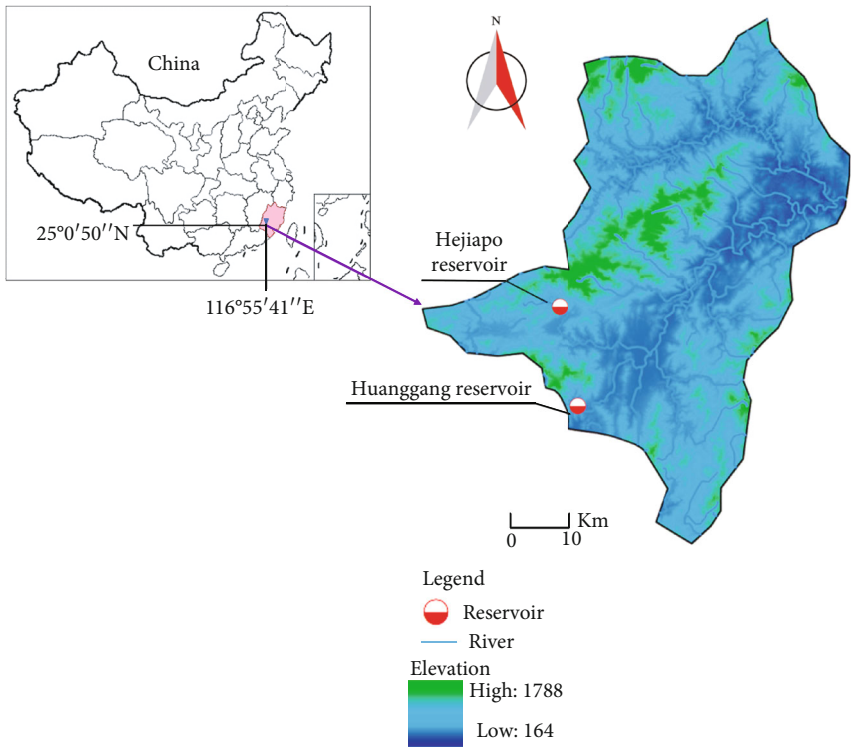

Figure 11: Location of Hejiapo Reservoir.

optimizer can speed up the update and calculate the network parameters output of the model so that the model can approximate and find the optimal solution. We randomly selected 7 kinds of functions ("adam", "adagrad", "adamax", "SGD", "Nadam", "Rmsprop", "Adadelta" 7 kinds of optimizers), run 7 times under random conditions, and recorded the RMSE generated in each operation (Figure 6).

The running results of 7 kinds of optimizers shows that the "SGD" optimizer was the worst since there are many failures to converge. Although the results of the "Adadelta" and "Nadam" optimizers have converged, the RMSE was too large. The result greater than 1 means the effect is very poor. The effect of the remaining three optimizers is well, and the value of RMSE is less than 1. The calculation result of "Adam" is more stable and works better by comparing with the other two optimizers, so the suitable optimizer is "Adam".

According to the description of hyperparameters in sections 3.2.1 and 3.2.2, and combined with the experimental

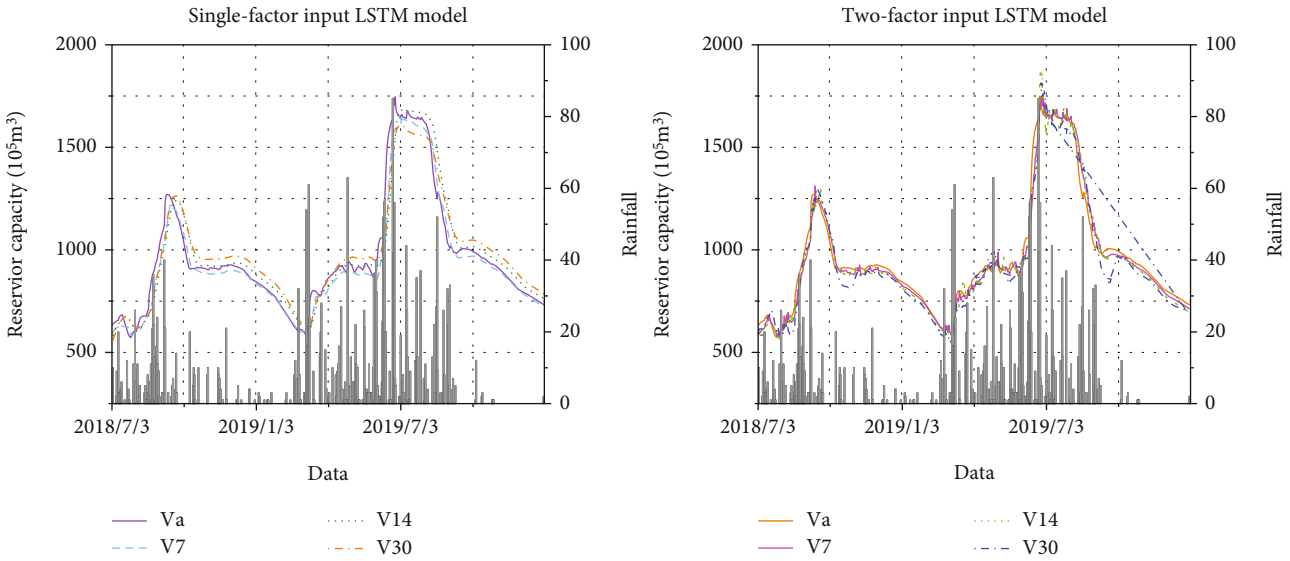

FIGURE 12: The prediction of reservoir capacity. V_a represents the actual reservoir capacity of the reservoir, V_7, V_{14}, and V_{30} represent the predicted reservoir capacity of the 7, 14 and 30 days, respectively, and Rainfall is the rainfall in the reservoir area.

objects (Huanggang Reservoir and Hejiapo Reservoir), we set appropriate hyperparameters to train each model to convergence. The final hyperparameter selections are shown in Table 1.

3.2.3. Introduction of attention mechanism. In the LSTM model, the same vector is assigned to each input unit during the decoder decoding process [31]. In the encoder process, the output is the same fixed-length semantics. In the long-short-term prediction process of the model, these factors directly limit the model's accuracy, so we considered adding the attention mechanism into LSTM. The attention mechanism comes from the human learning process, in which a certain part of our learning always appears to be the most important content. To speed up learning efficiency and improve accuracy, we focus our attention on that part of the information and suppress other irrelevant information in the re-learning process. The weights, which are assigned by the attention mechanism to the input sequence, can determine the most relevant aspects that affect the prediction data, thus improving prediction accuracy. The attention mechanism can effectively improve the situation in which the LSTM loses information because of long sequences, and simultaneously replace the original method of randomly assigning weights with that of assigning probabilities [32, 33]. Firstly, the attention machine value obtains a proportion by calculating the similarity between each output and input. Then, the mechanism accumulates all the inputs based on these factors' proportion. By comparing the LSTM model with the attention and without the attention, we run 7 times under the same initial conditions and recorded the RMSE (Figure 7). We find that input of the attention mechanism in LSTM has a significant improvement than the LSTM without attention.

4. Result

4.1. Model evaluation criteria. For judging the prediction effect of the model, we used the most common indicator of hydrological models: the Nash-Sutcliffe Efficiency (NSE) [34] and the Mean Relative Error (MRE) [35]. As an important indicator of hydrological model evaluation, NSE is used to verify the quality of the hydrological model simulation. The value range is from negative infinity to 1. The closer of value is to 1, the better quality and reliability of the hydrological model.

$$\mathrm{NSE} = 1 - \frac{\sum_{i=1}^{N}\left(Q_{sim,i} - Q_{obs,i}\right)^2}{\sum_{i=1}^{N}\left(Q_{obs,i} - \bar{Q}_{obs}\right)^2} \tag{4}$$

In the formula, $Q_{sim,i}$ is the true value of the reservoir capacity, $Q_{obs,i}$ is the predicted value of the reservoir capacity, and $\bar{Q}_{obs}$ is the total average of the true value of the reservoir capacity.

MRE is used to measure the average relative error between the true value and the predicted value, and then to judge the pros and cons of the model fitting.

$$\mathrm{MRE} = \frac{1}{n}\sum_{i=1}^{n}\left|x_i - x_{vi}\right| \tag{5}$$

In the formula, n represents the total number of validation set data, and x_i represents the reservoir monitoring capacity of a reservoir on the i day. x_{vi} represents the reservoir capacity predicted by the model on the i-th day, and i represents 1, 2, 3, ..., n.

4.2. Model accuracy comparison. Previously, we have optimized the model parameters by selecting the model

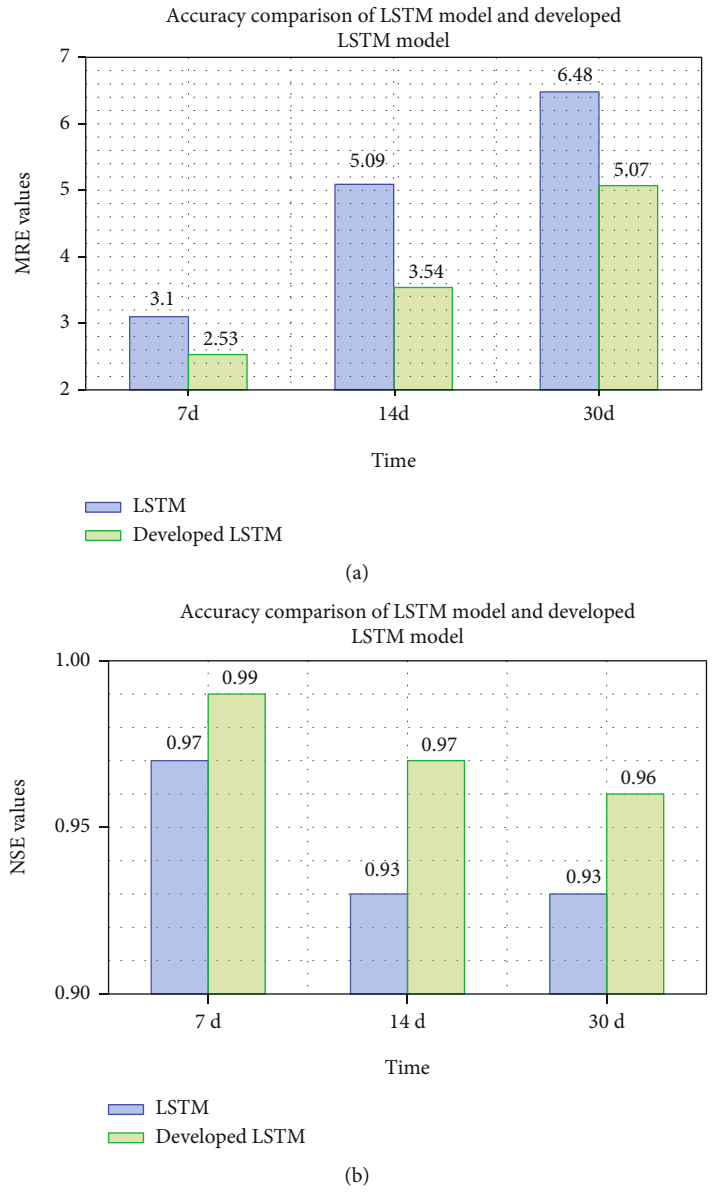

Figure 13: Two models' accuracy comparison.

structure with excellent effects. And considering the relevant factors in the reservoir capacity change, we have established a Developed LSTM model. We would verify whether the developed LSTM model had an improvement compared with the traditional LSTM model in predicting the change of reservoir capacity. We selected the Huanggang Reservoir data from 2013 to 2018, and used 70% of the data as the model training set and the rest 30% for model validation. LSTM model considers inputting the single-factor (historical reservoir capacity), while the developed LSTM model considers inputting the two-factors (historical reservoir capacity and rainfall) and introduction of attention mechanism. We used the model to predict the Huanggang Reservoir's capacity change in 7days, 14days, and 30days, respectively. The prediction of reservoir capacity and the relative error of both models are as shown in Figure 8. (The relative error described in this article refers to the value obtained by multiplying the ratio of the absolute error caused by the measurement to the true value of the measurand multiplied by 100%.)

The result of Figure 8 shows that developed LSTM model with inputting the two-factor (historical reservoir capacity and rainfall) fits measurement data higher than the LSTM model with inputting single-factor (historical reservoir capacity). The two-factor input prediction model has few deviations between the predicted reservoir capacity and the real reservoir capacity only at a few points while at other points the prediction are well. NSE is an important indicator for hydrological model evaluation. The value is closer to 1 means that a model has a higher credibility. MRE is an indicator to judge the degree of agreement between the predicted value and the true value. We can see the NSE and MRE

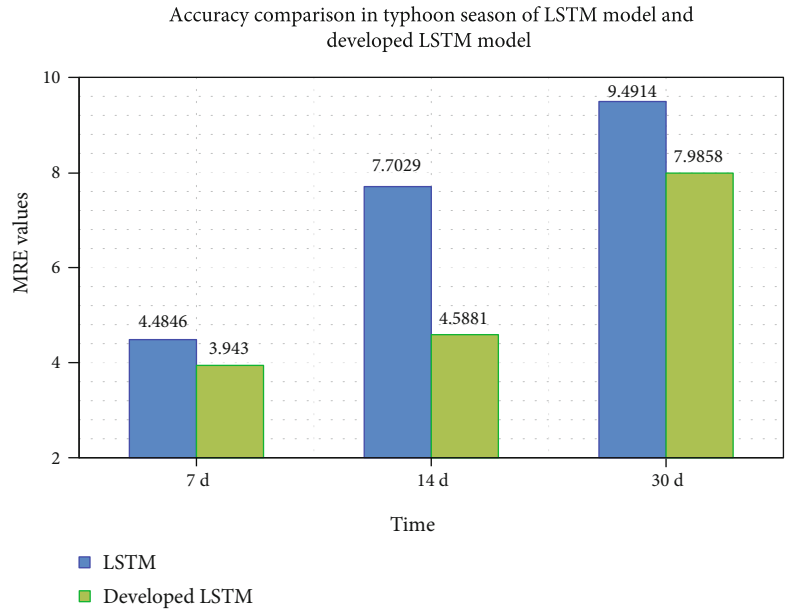

Figure 14: Two models' accuracy comparison in typhoon season.

values of developed LSTM model are better than that of the LSTM model for predictions of 7-day, 14-day, and 30-day. In addition, as the increase of prediction period (from 7, 14 to 30 days), the increase of error is obviously slow for the developed LSTM model than LSTM model (Figure 9). We also test the performances of these models during the typhoon season, which shows the similar results (Figure 10).

5. Discussion

In this section, two aspects of the developed LSTM model will be discussed: the inputting influence factors of LSTM model, and the further applicability of model.

5.1. Influence factors of LSTM model. For multi-factors input, we considered that the influencing factors of reservoir capacity are often diverse rather than one-single. Thus, physically it is impossible to make good predictions for considering only one factor (reservoir capacity) input. Considering the impact of multi-correlation factors, the model can make good adaptability for some predictions of mutation. The input of multi factors is not blind, and the influencing factors need to have sufficient correlation. If the input influencing factors are irrelevant or negatively related to the reservoir capacity prediction, it will directly lead to the reduction of the accuracy of the model. Specially, one factor of historical reservoir capacity is used in the LSTM model. It considers this single factor containing the previous information of rainfall and drainage which mainly affect the balance of reservoir capacity. In two factors inputting consideration, besides the historical reservoir capacity, we regards the time-series rainfall, the most important factor to improve the reservoir capacity, as the one independent factor.

5.2. Application of model in another case. In order to further illustrate the applicability of the developed LSTM model, we obtained the reservoir data of Hejiapo in Longyan City. The data contained the Hejiapo historical reservoir capacity and the historical rainfall from 2015 to 2019 (Figure 11). By using the data of 2015-2017 as the training set and the data of 2018-2019 as the validation set, we used the Developed LSTM model and the LSTM model for the prediction of the reservoir capacity of the Hejiapo (7 days, 14 days, and 30 days) (Figure 12).

The Figure 13 indicates that the developed two-factor LSTM model has a lower MRE and a higher NSE values than the LSTM model for 7-day, 14-day, and 30-day.

Comparing the MRE of the single-factor LSTM model and the two-factor developed LSTM model during the typhoon season, the Figure 14 shows that the developed LSTM model makes a more accurate predictions in extreme weather.

6. Conclusions

(1) This study verified the better performance of the developed LSTM model than the LSTM model for the Huanggang Reservoir capacity prediction for 7-day, 14-day, and 30-day. In addition, the Developed LSTM model was well applied to the Hejiapo Reservoir capacity estimation, which also shows an accurate prediction

(2) The prediction accuracy of the LSTM neural network model based on two-factor input has a great relationship with the parameter settings. Different parameter settings of the same model could produce different results. The input of multi factors is not blind, and the influencing factors need to have sufficient correlation. If the input influencing factors are irrelevant or negatively related to the reservoir

capacity prediction, it will directly lead to the reduction of the accuracy of the model

(3) Due to the limitation of data collected in this study, the developed LSTM only considers two factors. There could be more factors related to the change of reservoir capacity. The question that with the increasing of number of factors, whether the prediction accuracy of the model continually improves will be investigated in our future work

Data Availability

The data used to support the findings of this study are available from corresponding authors upon request.

Conflicts of Interest

The authors declare that there are no conflicts of interest regarding the publication of this paper.

Acknowledgments

The work was supported by the National Natural Science Foundation of China (No. 52130403) and the Transportation Science and Technology Project Foundation of Fujian Provincial (No.201911).

References

[1] J. Tan, "The role of reservoir regulation in responding to natural disasters," *Express Water Resources*, vol. 39, no. 7, pp. 22-23, 2019.

[2] P. Yang, "Research on Improving Reservoir Sedimentation by Using Density Current in Extreme Weather," *Environment and Development*, vol. 30, no. 7, pp. 225–227, 2018.

[3] J. Li, "Talking about the role of reservoirs and river dikes in flood control and drought resistance and construction management countermeasures," *Sichuan Water Resources*, vol. 41, no. 3, 2020.

[4] W. Wang, G. Cao, Y. Li et al., "Experimental Study of Dynamic Characteristics of Tailings With Different Reconsolidation Degrees After Liquefaction," *Frontiers in Earth Science*, vol. 10, article 876401, 2022.

[5] D. Anghiler, N. Voisin, A. Castelletti, F. Pianosi, B. Nijssen, and D. P. Lettenmaier, "Vaule of long-term streamflow forecasts to operations for water supply in snow-dominated river catchments," *Water Resources Research*, vol. 52, no. 6, pp. 4209–4225, 2016.

[6] A. D. Tiwari and V. Mishra, "Prediction of Reservoir Storage Anomalies in India," *Indian Institute of Technology Gandhinagar*, vol. 124, no. 7, pp. 3822–3838, 2019.

[7] C. Deng, P. Liu, W. Chaohui, and W. Chen, "Research on Early Warning Model of Reservoir Water Level," *Journal of Water Reseources Research*, vol. 3, no. 1, pp. 62–65, 2014.

[8] P. Zhao and Y. Ma, "Study of Flood Routing Method in Connectivity Dual Reservoirs," *Guangdong Water Resources and Hydropower.*, no. 1, pp. 13–16, 2015.

[9] Z. Liu, Q. Wang, and X. Jijun, "Application of one-dimensional hydrodynamic model to predict the storage level of the Three Gorges library," *Journal of Yangize River Scientific River Scientific Research*, vol. 28, no. 8, pp. 22–26, 2011.

[10] Y. Sun, *Study on the dynamic law of watershed hydrological model parameters under changing environment*, Tsinghua University, Beijing, 2015.

[11] W. Nie, M. Krautblatter, K. Leith, K. Thuro, and J. Festl, "A modified tank model including snowmelt and infiltration time lags for deep-seated landslides in alpine environments (Aggenalm, Germany)," *Natural Hazards and Earth System Sciences*, vol. 17, no. 9, pp. 1595–1610, 2017.

[12] Q. Li, D. Song, C. Yuan, and W. Nie, "An image recognition method for the deformation area of open-pit rock slopes under variable rainfall," *Measurement*, vol. 188, p. 110544, 2022.

[13] S.-S. Back and J. Pyo, "Prediction of water level and water quality using a CNN-LSTM combined deep learning Approach," *Water*, vol. 12, no. 12, p. 3399, 2020.

[14] N. Bezak and B. Zeng, "Daily runoff forecasting using a cascade long short-term memory model that considers Different Variables," *Management*, vol. 35, no. 4, pp. 1167–1181, 2021.

[15] Z. Tang, D. Zhang, and J. Lin, "Reservoir operation simulation based on cyclic neural network algorithm," *Water Resources and Power*, vol. 39, no. 5, 2021.

[16] H. C. Kilinc and B. Haznedar, "A Hybrid Model for Streamflow Forecasting in the Basin of Euphrates," *Water.*, vol. 14, no. 1, p. 80, 2022.

[17] H. Fan, M. Jiang, L. Xu, H. Zhu, J. Cheng, and J. Jiang, "Comparison of Long Short Term Memory Networks and the Hydrological Model in Runoff Simulation," *Water*, vol. 12, no. 1, 2020.

[18] M. Sapitang, W. M. Ridwan, K. F. Kushiar, A. N. Ahmed, and A. El-Shafie, "Machine Learning Application in Reservoir Water Level Forecasting for Sustainable Hydropower Generation Strategy," *Sustainability*, vol. 12, no. 15, p. 6121, 2020.

[19] C. Liang, H. Li, M. Lei, and Q. Du, "Dongting Lake Water Level Forecast and Its Relationship with the Three Gorges Dam Based on a Long Short-Term Memory Network," *Water*, vol. 10, no. 10, p. 1389, 2018.

[20] Y. Guo and X. Yan, "Water level Prediction of Lake Poyang Based on Long Short-term Memory Neural Network," *Journal of Lake Sciences*, vol. 32, no. 3, pp. 865–876, 2020.

[21] Y. Wang, T. Sun, X. Liang, and H. Xie, "Prediction of river water volume and level based on EMD-LSTM model," *Hydraulic Science and Technology*, vol. 40, no. 6, pp. 40–47, 2020.

[22] Y. Chen, *Study on Water Quality Analysis and Status Quo Evaluation of Urban Drinking Water Sources*, JiMei University, 2013.

[23] Y. Luo, "Application of high-pressure shotcrete technology in culvert plugging of dam of Huanggang Reservoir," *Hydraulic Science And Technoligy*, vol. 2, pp. 24–26, 2017.

[24] Y. Wang, *Huanggang Reservoir Reinforcement Project Passed Acceptance*, Minxi Daily, 2010.

[25] Y. Zou, D. Ye, Y. Lin, and A. Liu, "A Quantitative Method for Assessment of Regional Heavy Rainfall Intensity," *Journal of Applied Meteorological Science*, vol. 25, no. 3, pp. 360–364, 2014.

[26] G. Hou, "Analysis of Huanggang Reservoir Tourism Development Status," *International Journal of Education and Economics.*, vol. 1, no. 2, 2018.

[27] F. A. Gers, J. Schmidhuber, and F. Cummins, "Learning to Forget: Continual Prediction with LSTM," *Neural Computation*, vol. 12, no. 10, pp. 2451–2471, 2000.

[28] Y. Yang, R. Liu, Y. Hong et al., "Development of Modified Tank Model for Reservoir Storage Prediction: Case Study of Huanggang Reservoir, Fujian, China," *Journal of Hydrologic Engineering*, vol. 26, no. 7, 2021.

[29] C. Dang, H. Chen, K. Chen et al., "Application of Long Short-term Memory Neural Network in Precipitation-Runoff Simulation in Seasonal Snowmelt Basin," *Journal of North China University of Water Resources and Electric Power(Natural Science Edition)*, vol. 41, no. 5, 2020.

[30] C. Liang, *Research on Dongting Lake Water Level Prediction Based on Long and Short-term Memory Networks and the Impact of the Three Gorges Project on Dongting Lake Water Level*, WuHan University, WuHan, 2019.

[31] K. K. Chandriah and R. V. Naragnahalli, "RNN / LSTM with modified Adam optimizer in deep learning approach for automobile spare parts demand forecasting," *Multimedia Tools and Applications*, vol. 80, no. 17, pp. 26145–26159, 2021.

[32] Y. Zhu, Y. Gao, Z. Wang et al., "A Tailings Dam Long-Term Deformation Prediction Method Based on Empirical Mode Decomposition and LSTM Model Combined with Attention Mechanism," *Water*, vol. 14, no. 8, p. 1229, 2022.

[33] W. Xie, W. Nie, P. Saffari, L. F. Robledo, P.-Y. Descote, and W. Jian, "Landslide hazard assessment based on Bayesian optimization–support vector machine in Nanping City, China," *Natural Hazards*, vol. 109, no. 1, pp. 931–948, 2021.

[34] J. E. Nash and J. V. Sutcliffe, "River flow forecasting through conceptual models part I – A discussion of principles," *Journal of Hydrology*, vol. 10, no. 3, p. 282, 1970.

[35] S. M. Vicente Serrano, J. I. López-Moreno, S. Beguería, J. Lorenzo-Lacruz, C. Azorin-Molina, and E. Morán-Tejeda, "Accurate Computation of a streamflow drought index," *Journal of Hydrologic Engineering*, vol. 17, no. 2, pp. 318–332, 2012.

Hindawi
Geofluids
Volume 2022, Article ID 9167573, 13 pages
https://doi.org/10.1155/2022/9167573

Research Article

Experimental Investigation of the Influence of the Anchor Cable Inclination Angle on the Seismic Response Characteristics of Anchored Piles

A. Fa-you,[1,2] **Xue-gang Dai**,[1] **Peng ZHang**,[1] **Ming-chang Hei**,[3] **and Shi-qun Yan**[1]

[1]*Faculty of Land Resource Engineering, Kunming University of Science and Technology, Kunming, Yunnan 650093, China*
[2]*Key Laboratory of Geohazard Forecast and Geoecological Restoration in Plateau Mountainous Area, Ministry of Natural Resources of the People's Republic of China, Kunming, Yunnan 650000, China*
[3]*State Key Laboratory of Hydraulics and Mountain River Engineering, College of Water Resource and Hydropower, Sichuan University, Chengdu Sichuan 610065, China*

Correspondence should be addressed to A. Fa-you; afayou@163.com

Received 13 April 2022; Revised 27 May 2022; Accepted 6 June 2022; Published 24 June 2022

Academic Editor: Zizheng Guo

Studies show that prestressed anchor cable antislide piles have good antiseismic characteristics. As an important parameter in the design of anchor-cable piles, the effect of anchor-cable inclination on the seismic response of the anchor-cable pile system has been rarely studied so far. In the present study, the seismic response characteristics of the anchor-pulled pile under different cable inclinations are studied using a large-scale seismic model test platform and numerical methods. The obtained results show that the inclined angle of the anchor cable has a great influence on the seismic response of the pile-anchor system. It is found that under the same seismic conditions, the axial force of the anchor cable becomes smaller as the anchor dip angle increases, while the pile top displacement becomes larger. The dynamic earth pressure behind the pile changes from the sliding surface to the pile top, indicating that the earth pressure near the sliding surface and the pile top is of active and passive earth pressure types, respectively. This pressure decreases with the increase of the anchor dip angle, thereby affecting the performance of the antisliding pile.

1. Introduction

Antislide piles can be mainly divided into composite and noncomposite piles according to the combination form with other structures. A noncomposite pile generally refers to a single pile, independent of other structures. On the other hand, a composite pile, such as a prestressed anchor cable antislide pile, refers to a single pile combined with other structures. As a common slope reinforcement measure, the prestressed anchor cable antislide pile has superior characteristics, including low cost and quick construction, so it has been widely used in large-scale and extra-large slopes and reinforcement of landslide optimization [1–7]. Analyzing the damages of Wenchuan earthquake showed that the slope reinforced by a prestressed anchor cable antislide pile has promising antiseismic capabilities [8, 9].

With the rapid development of industrialization, numerous investigations from different aspects have been carried out on the seismic behavior of antislide piles. In order to investigate the seismic characteristics of noncomposite piles, Valsangkar et al. [10] performed shaking table tests on the seismic response of partially supported single piles and achieved earlier research time, accordingly. Moreover, Makris and Badoni [11] studied the nonlinear seismic response of single piles. He et al. [12] studied the three-dimensional limit analysis of seismic displacement of slope reinforced by piles. Sáez et al. [13] studied the seismic response of pile-supported excavation in the Santiago gravel stratum. Qu et al. [14] analyzed the seismic response characteristics of the antislide pile using the elastic-plastic theory. Li et al. [15] performed shaking table tests and studied the seismic response of landslides reinforced by minipiles. Zhang et al.

[16] carried out large-scale shaking table tests to study the seismic behavior of the pile-foundation slope of the antislide pile-reinforced bridge. It is worth noting that the seismic analysis of these noncomposite piles provides a basis to study composite piles. To study the seismic characteristics of the combination of anchor-pull piles, Su and Zhang [17] studied the influence of rock excavation blasting vibration on the prestressed anchor cable on the high and steep slope of the diversion tunnel of the Zipingpu project. Then Yang et al. [18] analyzed the dynamic response characteristics of anchor cables under a blasting load. However, further investigations revealed that there are essential differences between blasting vibration and earthquake. Accordingly, the abovementioned analyses cannot be applied to the seismic design of the prestressed anchor cable. Ye et al. [19] carried out shaking table tests of slope reinforced by single-row antislide pile and prestressed anchor cable under the earthquake action. Lederer et al. [20] studied the interaction between embedded an antislide pile and a prestressed anchor frame beam. Qu et al. [21] studied the earth pressure distribution on different parameters, including the seismic response characteristics of the pile displacement, prestress of the anchor cable, dynamic characteristics and acceleration amplification effect of the reinforced slope, and seismic response of an antislide pile with anchor cable. Zhou et al. [22] and Yan et al. [23] analyzed the ultimate strength and anchorage characteristics of prestressed anchor cable in bedding rock slope. Fu et al. [24] carried out the shaking table test and studied the seismic response of slope reinforced by a pile-cable support structure. Furthermore, Chen et al. [25] studied the influence of earthquake characteristics on the seismic performance of anchored sheet pile quay with barrette piles. Lin et al. [26] studied the seismic response of beam-sheet-pile walls with anchor frames numerically and experimentally. Huang et al. [27] simulated the seismic response and failure mode of slope reinforced by the pile-anchor structure. It should be indicated that although the seismic study of these composite structures with anchor-pull piles provides a theoretical basis for the seismic design of composite structures, the influence of anchor cable inclination angle on the seismic response of anchor-pull pile composite structures is often neglected in the calculations, thereby affecting the accuracy of the results.

Reviewing the literature indicates that as an important parameter in the design of anchor-cable pile, the effect of anchor-cable inclination on the seismic response of the anchor-cable pile system has not yet been studied so far. More specifically, most investigations in this area only consider the influence of static action on the prestressed anchor-cable inclination [1, 2, 7]. Accordingly, it is of great theoretical value to study the seismic response of antislide piles with different inclination angles by performing shaking table tests and provide a scientific basis to improve and develop the aseismic design method of the anchor cable antislide pile.

2. Model Design

2.1. Similarity Principle. According to similarity criteria, the similarity of physical variables can be mainly divided into three categories, including general geometric similarity, dynamic similarity, and kinematic similarity. General geometric similarity refers to elementary geometric similarity wherein the unit length is generally considered the dimension of physical variables. Combining similar characteristics of various physical systems, the positions and significances of three categories can be described as that if any two systems are similar in geometry, dynamics, and kinematics, then the two systems have similar performances [28]. It is worth noting that among the three similarity criteria, the geometric similarity is easier to be achieved while reaching both the geometric and dynamic similarity is required to have the kinematic similarity. Accordingly, it is a challenge to reach the kinematic similarity in complicated engineering problems. Any solution obtained from the dynamic similarity under the condition of geometric similarity should satisfy the requirements of the kinematic similarity.

In the present study, the geometric and dynamic similarity of the anchor-pull pile supporting landslides is used as the basic conditions. Due to limited data on the properties of the prototype materials, including the standard values of the characteristic parameters, it is an enormous challenge to achieve complete similarity between the model materials and the prototype materials. Consequently, it is a challenge to reach an agreement between the test results and the prototype results. Aiming at resolving this problem, the main objective of the present study is to study the similarity laws in the test model.

2.2. Experimental Equipment. In the present study, tests are performed on the large shaking table (Yunnan Institute of Engineering Aseismic, China). The table size was 4 m × 4 m and has 3 degrees of freedom. The table can supply a maximum of 30 tons of load in the test. The maximum displacement and velocity along the X and Y directions are 250 mm and 0.8 m/s, respectively. Moreover, the maximum acceleration along the X and Y directions with a load of 20 and 30 tons is 1 g and 0.8 g, respectively. The operating frequency is 0~100 Hz, and the maximum overturning moment is 300 KN m.

Numerous materials, including landslide material, model box, retaining plate, antislide pile, anchor cable, and concrete, are involved in the test. The landslide model consists of three parts, including the sliding bed, sliding surface, and sliding body. Silty clay is used as soil. The sliding-bed soil is compacted before the test. To prepare the sliding surface, the soil is first screened with a 2 mm sieve. The screened soil is then dried; impurities are picked out and mixed with 50% fine sandy soil. The prepared sliding surface soil is evenly distributed over the sliding bed with a thickness of 5 cm. Natural-grade silty clay is used as the sliding soil. Instead of sieving, drying, and tamping, the silty clay is stacked above the sliding surface and leveled evenly. The bedrock of the anchoring section of the antislide pile is made of C40 concrete. Table 1 shows the physical and mechanical parameters of the test material.

A 60 cm long wooden antislide pile with a cross-section of 80 mm × 80 mm is used in the tests. The bottom is

Table 1: Physical and mechanical parameters of the test material.

Material	r kN/m^3	Es MPa	μ	Cohesion c kPa	Internal friction angle φ °
Sliding body	19	20	0.30	8	12
Sliding surface	18.8	20	0.30	10	8
Sliding bed	21	35	0.25	15	14
C40	24.4	3.25E4	0.2	Elastic material	

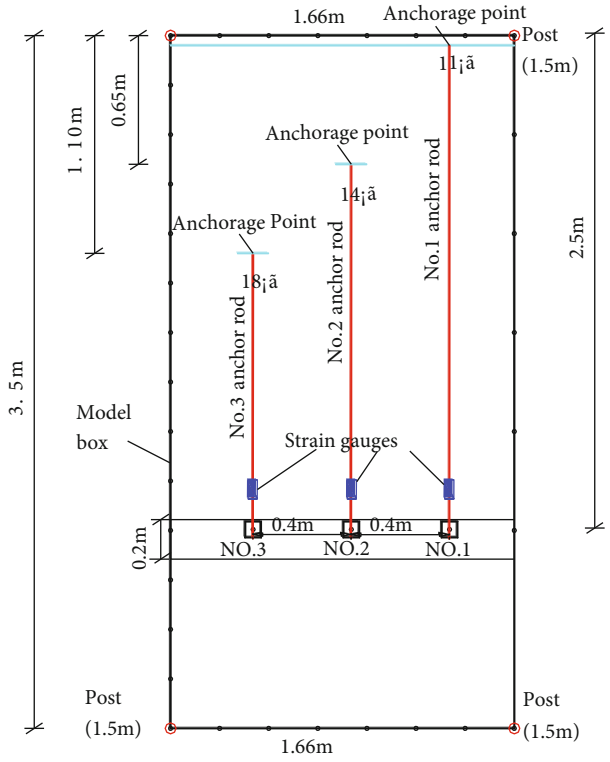

Figure 1: Top view of the physical model.

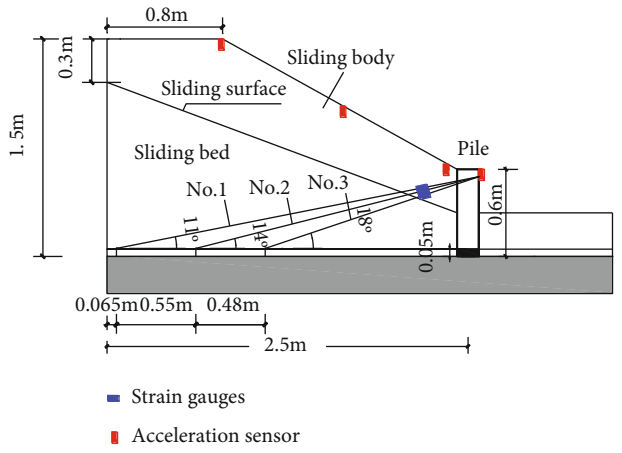

Figure 2: Schematic of the physical model.

Figure 3: Assembly of the acceleration sensors.

embedded in the concrete cast in a steel channel as the rock-socketed depth of the antislide pile. Each antislide pile has a 15 mm diameter hole at 5 cm from the pile top to place anchor rods. The retaining plate is 1.66 m long, 1.5 cm thick, and 45 cm high. According to the experience, the dip angle of the bolt should be 15°-25° and should not be less than 10°. Accordingly, the dip angle of the bolt was set to 11°, 14°, and 18°. The anchorage cable No. 1, 2, and 3 with a diameter of 14 mm and a total length of 2.65 m, 2.12 m, and 1.68 m is connected to the antislide pile with an anchor cable angle of 11°, 14°, and 18°, respectively. One end of all bolts is connected to the bottom of the model box for anchorage, and the prestressing force applied on each bolt is 0.5 kN. The height, length, and width of the model box are 1.5 m, 3.5 m, and 1.66 m, respectively. The top view of the physical model is shown in Figure 1.

An acceleration sensor is arranged on the top of each pile to measure the acceleration and to convert the displacement of the pile top to electrical signals. Furthermore, strain gauges are arranged on four sides of the anchor cable 8 cm from the retaining plate to measure the applied axial force. Figures 2 and 3 show the assembly layout of acceleration sensors.

The studied seismic wave in this experiment is an El Centro wave as shown in Figure 4. Since the first seismic wave successfully records the whole process data, the El

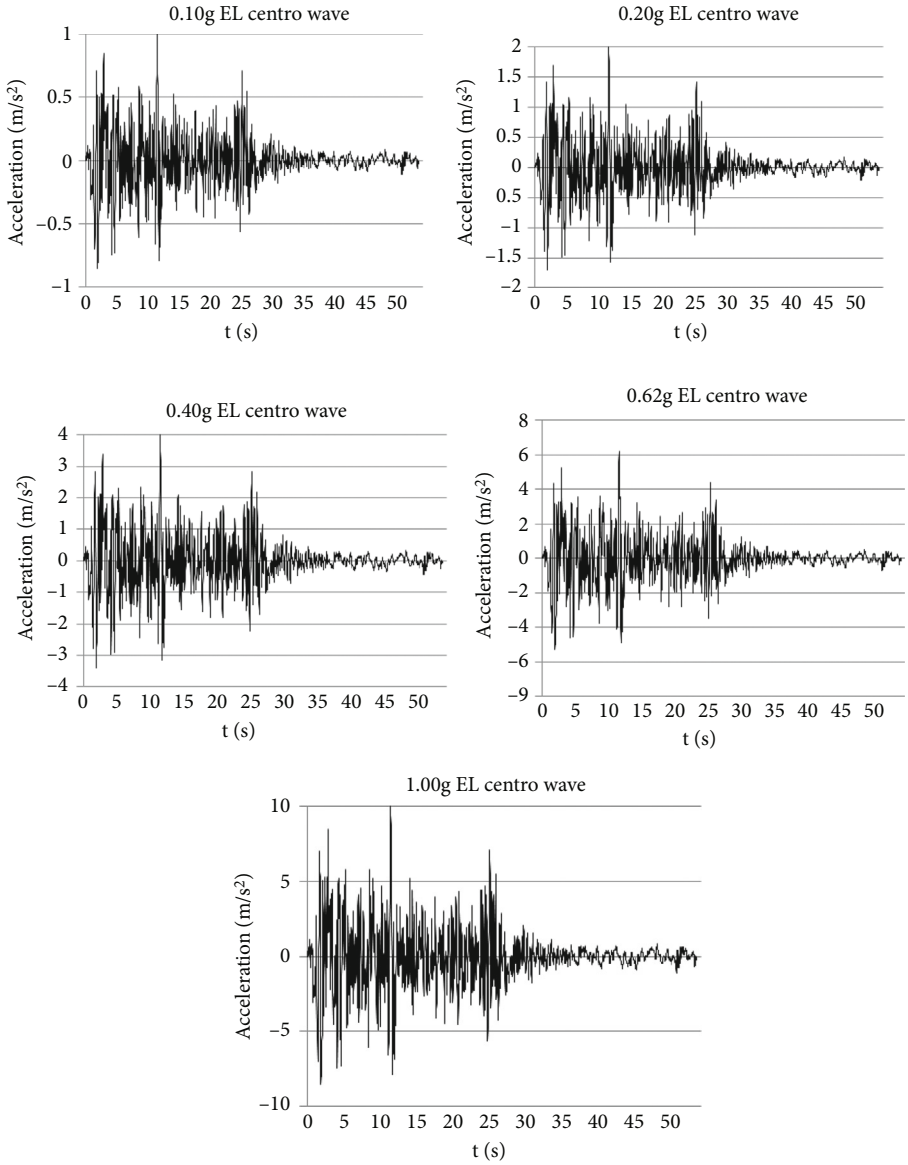

Figure 4: El Centro wave under five sets of conditions.

Centro wave is extensive and representative. In this regard, studies show that the horizontal component of the seismic wave is the fundamental force that causes the crack propagation, failure of the landslide, and its retaining structure. In the present study, five seismic conditions, including 7-degree medium earthquake, 8-degree medium earthquake, 8-degree large earthquake, 9-degree large earthquake, and over 9-degree earthquake, were designed. The control peak of the horizontal acceleration of these conditions is 0.10 g, 0.20 g, 0.40 g, 0.62 g, and 1.00 g, respectively. The data of slope acceleration, pile tip displacement, and anchor shaft force are collected in the test.

3. Analysis of the Test Results

3.1. Seismic Displacement Response. In the whole vibration process, the sensor monitoring data were analyzed mainly because the slope has been supported and no deformation failure occurred. Acceleration sensors A1, A2, and A3 were installed on the top of each antislide pile to measure the seismic acceleration response of the pile top under the action of the earthquake and obtain the time-history curves of pile top displacement under five working conditions. Figure 5 shows the displacement peaks of the pile top under pile-anchor system No. 1, 2, and 3. It is observed that as the earthquake power increases, the displacement of the pile top increases, and the response intensifies. Moreover, it is found that the displacement of the pile top increases rapidly before the acceleration of the seismic wave reaches 0.62 g, and then it increases slowly. The obtained results show that the aseismic effect of the anchor pile is remarkable.

Figure 6 shows the displacement of the pile top with different anchorage dip angles under the same seismic condition. It is observed that the displacement of the pile top

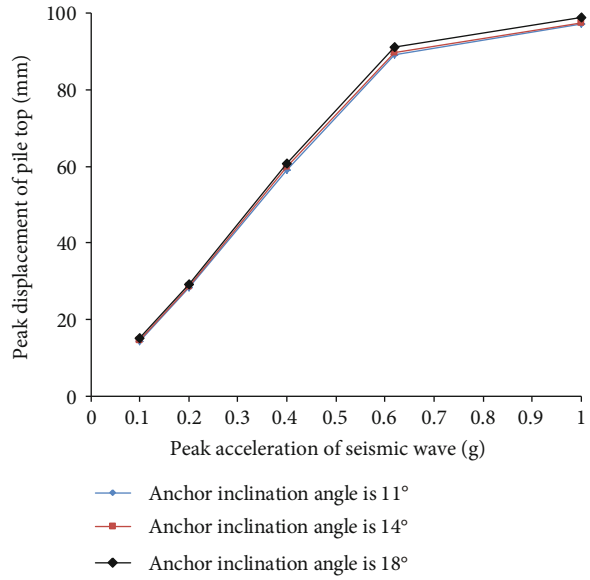

Figure 5: Peak displacement of the pile top under different working conditions.

with an 18° anchorage dip angle under the same seismic condition is larger than that of the pile top with a 14° anchorage dip angle. Meanwhile, the displacement of the pile top with a 14° anchorage inclination is always larger than that with an 11° anchorage inclination. It is concluded that as the anchorage angle increases, the corresponding displacement of the pile top increases too.

3.2. Axial Force Response of the Anchor Rod. The axial force peak values of three anchor cables with different inclination angles under different working conditions are presented in Figure 7.

Figure 7 shows that the axial force peak value of the anchor cable increases with the input seismic acceleration peak value, and the slope of the broken line of the axial force of each anchor cable becomes larger, indicating that the axial force grows faster and the response of the axial force intensifies.

The comparison of the axial force of the anchor cable under the same seismic condition with different inclination angles reveals that as the inclination angle increases, the corresponding axial force reduces continuously.

Table 2 shows the statistical tables of the peak values of the axial force and displacement of the anchor cable under the combined support of different pile-anchor systems. It is found that the axial force of the anchor cable is related to the displacement of the antislide pile under the pile-anchor combined support system. Figure 8 shows that under the same seismic conditions, the axial force of anchor rod No. 1 is greater than that of anchor rod No. 2 and 3, but the displacement of the pile top is just the opposite.

From the theoretical mechanics' viewpoint, the experimental results are in agreement with the theoretical ones. It is found that the angle between the pile and the anchor cable decreases with the increase of the inclination of the anchor cable and the decrease of the angle between the pile and the anchor cable. In this case, the seismic component of the anchor cable decreases, and the axial force of the anchor cable reduces, thereby weakening the pulling effect of the anchor cable and increasing the pile top displacement.

4. Validation of the Numerical Simulation

In this section, the flac3D software, which is a widely adopted software in geotechnical engineering, is applied to carry out numerical simulations. In this regard, three models are established, and each model has three antislide piles. The inclination angles of the three models are 11°, 14°, and 18°, respectively. In each model, the antislide pile in the middle position was selected for data analysis to avoid the influence of boundary conditions.

To increase the calculation accuracy and efficiency, the retaining plate, antislide pile, and anchor cable are treated as elastic materials. Table 3 shows the physical and mechanical parameters of model materials. Figure 9 shows that the established model is meshed using 5,634 elements and 9,789 nodes.

4.1. Analysis of the Displacement Response of the Pile Top. Three antislide piles are established in each model, and the time-history curve of the top displacement of middle antislide piles is selected for analysis. Figure 10 shows the distribution of the peak displacement of the pile top. It is observed that under the same seismic condition, the largest and smallest peak displacements of the pile top occur at an inclination angle of 18°and 11°, respectively. Furthermore, Figure 10 reveals that the peak displacement of the pile top increases with the increase of the anchor cable inclination. This is consistent with the obtained results from the shaking table test.

4.2. Analysis of the Axial Force Response of the Anchor Cable. Figure 11 shows the time-history curve of the axial force of the anchor cable at the same position at different anchor

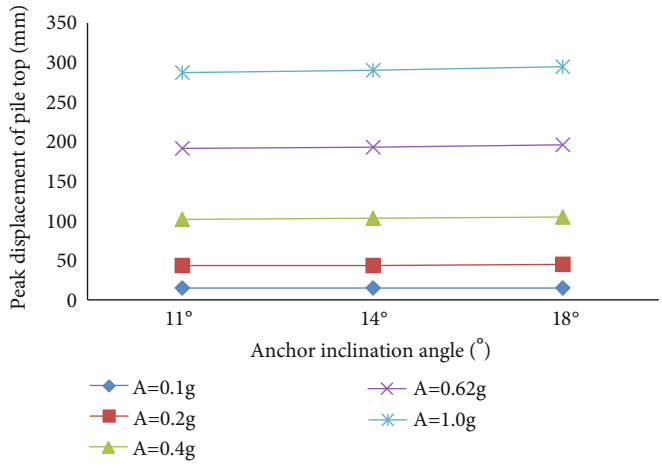

Figure 6: Distribution of the peak displacement of the pile top against the anchor inclination angle under the same working conditions.

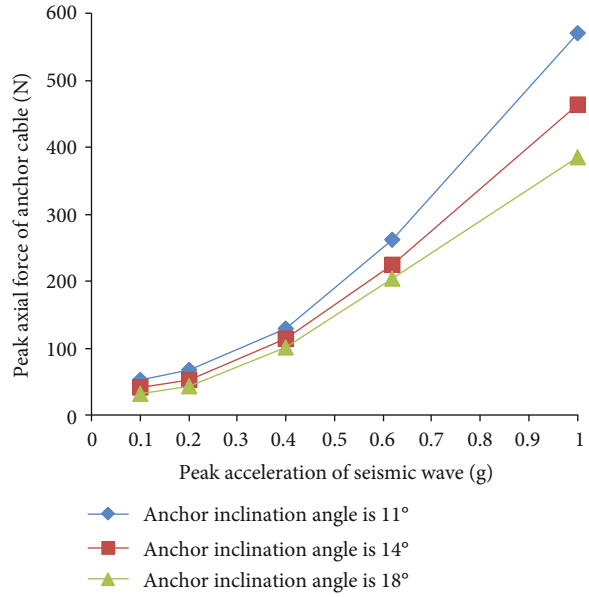

Figure 7: Peak axial force of the anchor cable under different working conditions.

Table 2: Axial force and peak displacement of anchor piles under different working conditions.

Working conditions	Peak acceleration (g)	No. 1		No. 2		No. 3	
		Axial force (N)	Peak displacement (mm)	Axial force (N)	Peak displacement (mm)	Axial force (N)	Peak displacement (mm)
1	0.1	51.73	14.42	40.33	14.61	31.41	15.03
2	0.2	67.43	28.45	53.27	28.69	42.18	29.22
3	0.4	129.01	59.09	114.23	59.79	100.99	60.78
4	0.62	261.41	89.16	224.15	89.75	204.75	91.29
5	1	571.15	97.09	464.01	97.38	384.88	98.99

inclination angles. It is observed that as the anchor inclination angle increases, the corresponding axial force decreases, which is in good agreement with the test results. It is also consistent with the theoretical deduction that the higher the inclination of the anchor cable, the lower the intersection angle between the pile and the anchor cable, the smaller the seismic component of the anchor cable, the lower the axial force of the anchor cable, and the weaker the anchor cable.

4.3. Response Analysis of Dynamic Earth Pressure behind the Pile. In this section, the dynamic earth pressure along the x-axis behind the anchored pile is monitored. During the

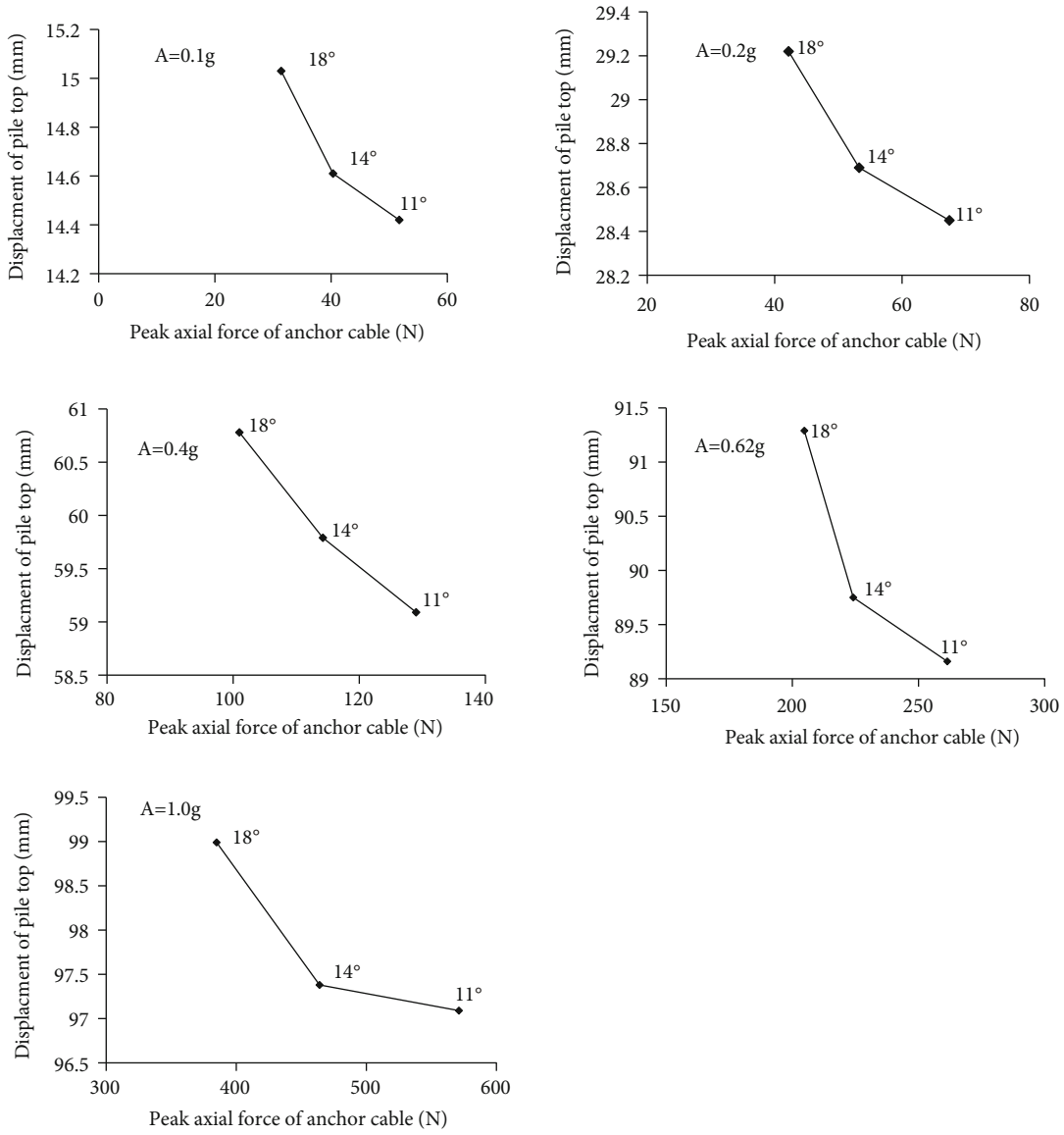

Figure 8: Distribution of axial force of the anchor cable against the pile top displacement.

Table 3: Physical and mechanical parameters of model materials.

Material	r kN/m^3	Es MPa	μ	Notes
Retaining plate	22	1.2*E*3	0.35	
Antislide pile	23	3.0*E*3	0.30	Elastic material
Anchor rod	78	2.0*E*4	0.20	

analysis, the earth pressure increased in the process of earthquake action, without considering the earth pressure under static action. Therefore, monitoring points are set after the initial balance to monitor the variations of the earth pressure behind the antislide piles when applying seismic waves. In this simulation, a total of 9 monitoring points are set up, and 3 points are set after each pile. Figure 12 shows that the monitoring points are set at 20 cm intervals above the sliding surface.

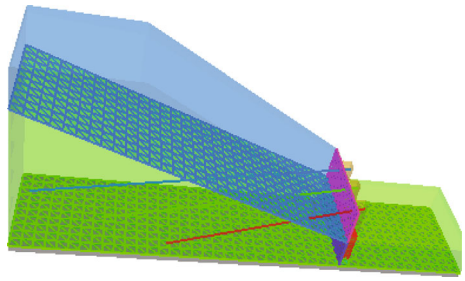

Figure 9: Three-dimensional model of the anchor pile.

In this analysis, 0.35 g El Centro waves are considered as the input seismic waves. Figures 13–15 show the time-history curves of the dynamic earth pressure behind the piles detected at W1, W2, and W3 of antislide piles No. 1, 2, and 3, respectively.

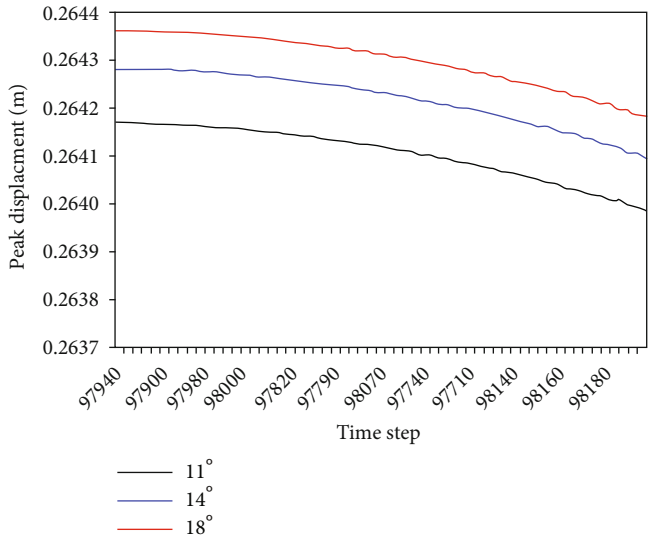

Figure 10: Distribution of the maximum displacement peak against the calculation time step.

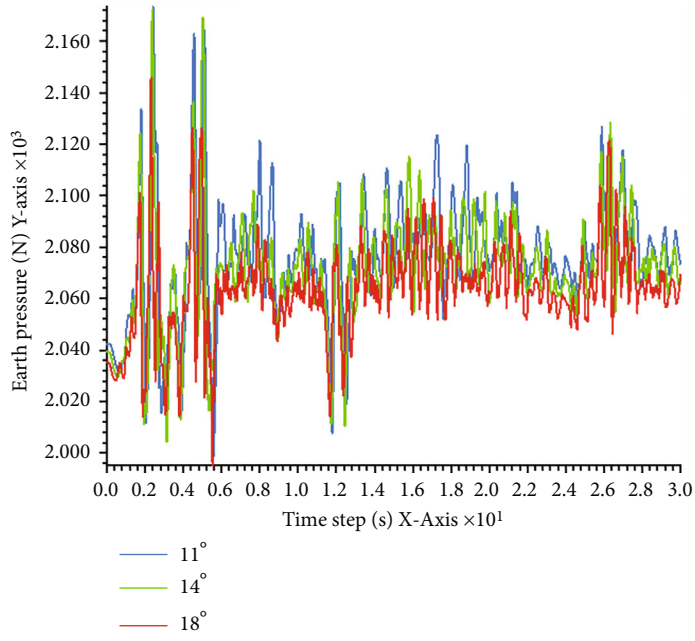

Figure 11: Distribution of the anchor cable axial force under different anchor angles.

The comparison of time-history curves of the dynamic earth pressure at different heights after three antislide piles indicates that the properties of the dynamic earth pressure behind piles change from the sliding surface to the top of the pile. More specifically, the dynamic earth pressure near the sliding surface (W1) is active, while the dynamic earth pressure near the pile top (W2, W3) is passive. This is because W1 is located near the sliding surface, so it is subjected to a large thrust of the sliding body of the pile, while W2 and W3 are subjected to the reverse pressure on the soil because of the anchor pulling action. Meanwhile, W3 is near the pile top, where the largest anchor pulling action and the biggest passive earth pressure occur.

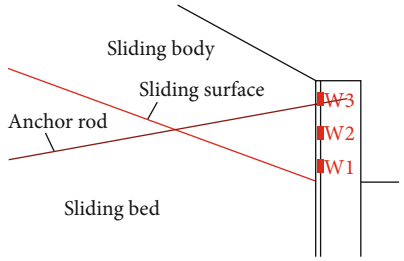

Figure 12: The monitoring points of dynamic earth pressure at postpile.

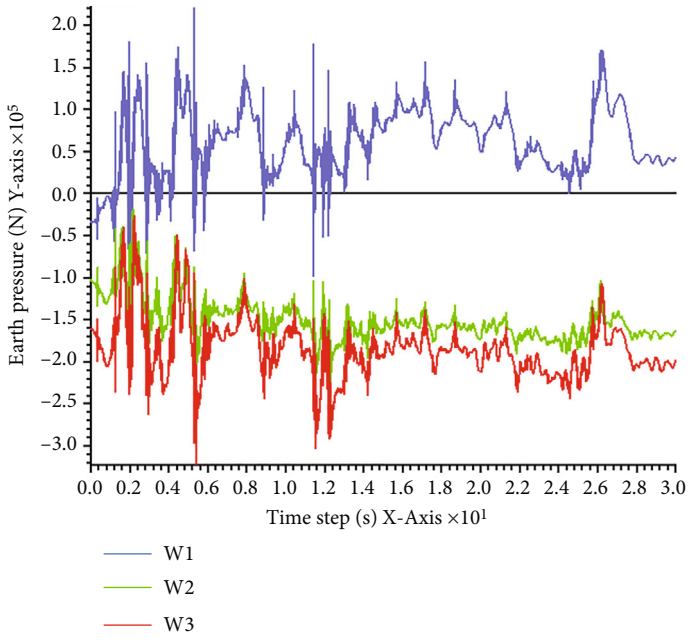

Figure 13: The time-course curve of the earth pressure behind the antislide pile No. 1.

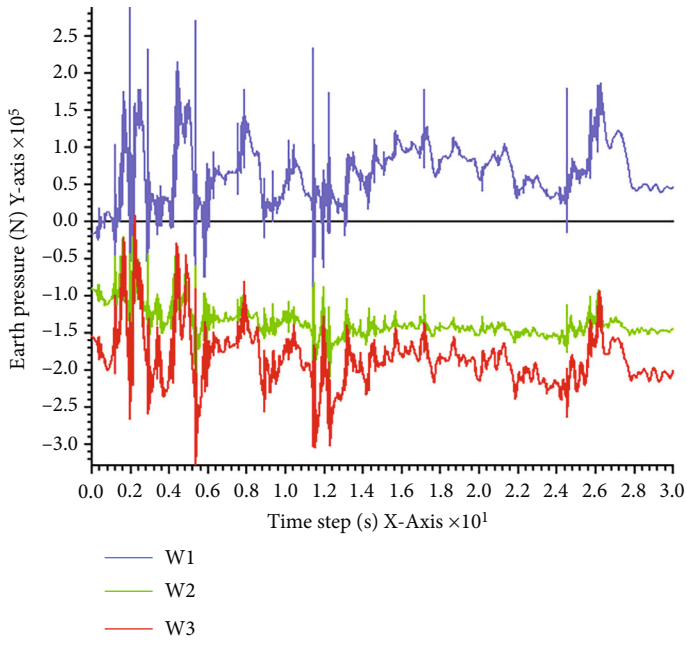

Figure 14: The time-course curve of the earth pressure behind the antislide pile at No. 2.

The distributions of the earth pressure behind the pile at the same location with different anchorage angles are shown in Figures 16–18. It is observed that variations of different anchor inclination angles at the same position are basically the same. It is found that as the anchorage angle increases, the active earth pressure increases, and the passive earth pressure decreases near the pile top. This is because as the inclined angle of the anchor cable increases, the intersection angle of the pile and the anchor cable decreases, the seismic component of the anchor cable reduces, the effect of the anchor cable weakens, and the passive earth pressure of the pile on the soil reduces. The obtained results verify the relationship between the displacement of the pile top and the anchorage dip angle.

5. Conclusion

In the present study, a large-scale model test platform was used to investigate the seismic response characteristics of anchor piles with different slope angles of anchor cables. Based on the obtained results, the main achievements can be summarized as follows:

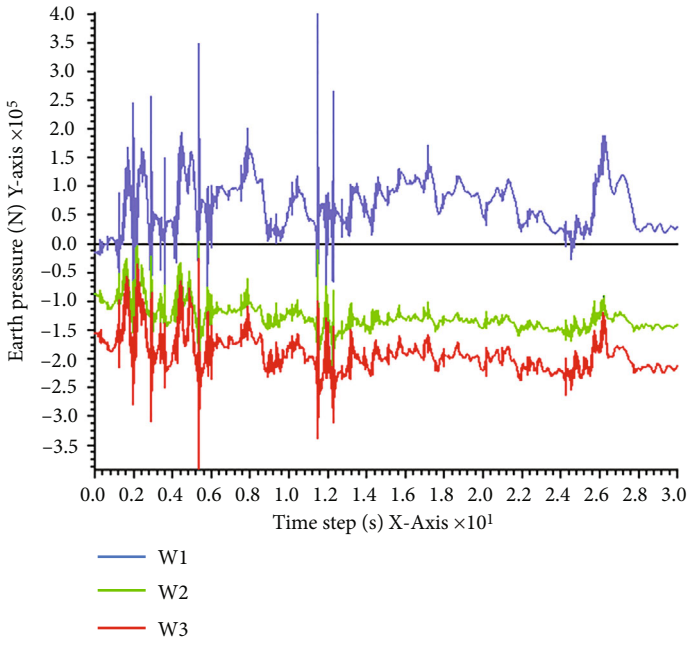

Figure 15: The time-course curve of the earth pressure behind the antislide pile No. 3.

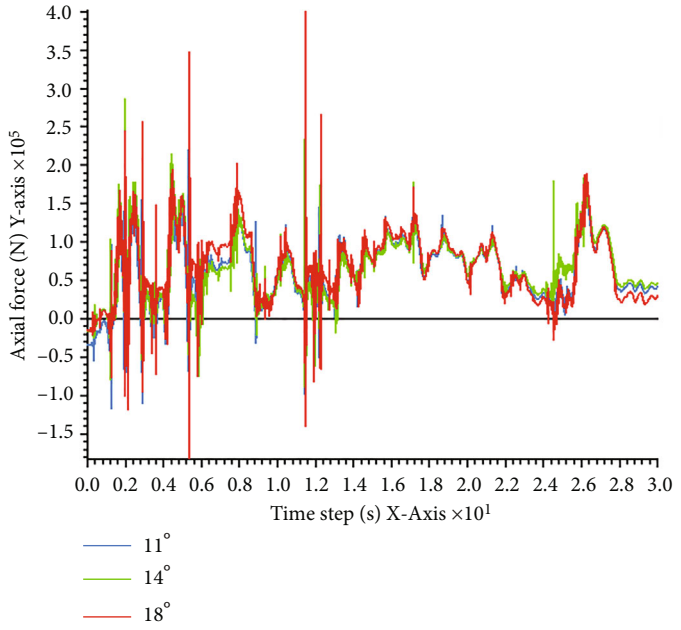

Figure 16: Distribution of dynamic earth pressure at W1 under different anchor angles.

(1) The inclined angle of the anchor cable has a great influence on the seismic response of the pile-anchor system. As the inclined angle of the anchor cable increases, the axial force of the seismic response decreases while the displacement of the pile top increases. Moreover, as the inclination of the anchor cable increases, the intersection angle of the pile and the anchor cable decreases, the seismic component of the anchor cable decreases, the axial force of the anchor cable decreases, the effect of the anchor cable on the piles weakens, and the pile top displacement increases

(2) With the increase of the earthquake power, the peak displacement of the pile top and the axial force of the anchor cable increase, and the seismic response

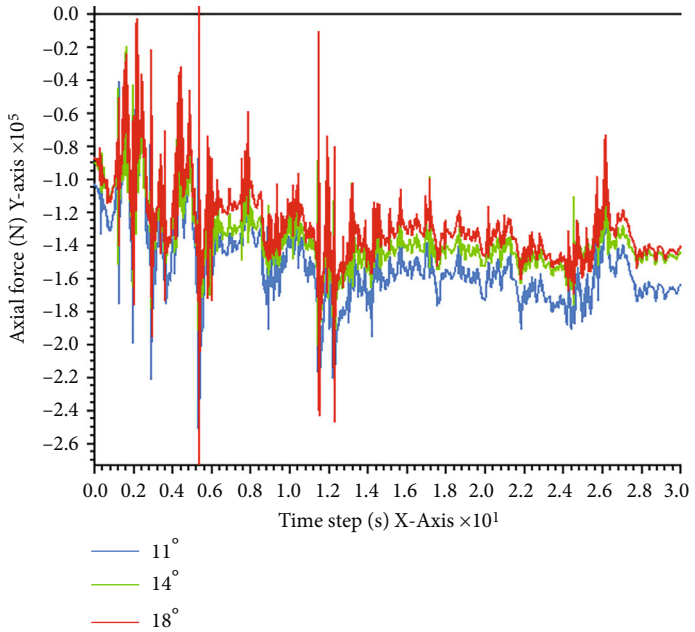

Figure 17: Distribution of dynamic earth pressure at W2 under different anchor angles.

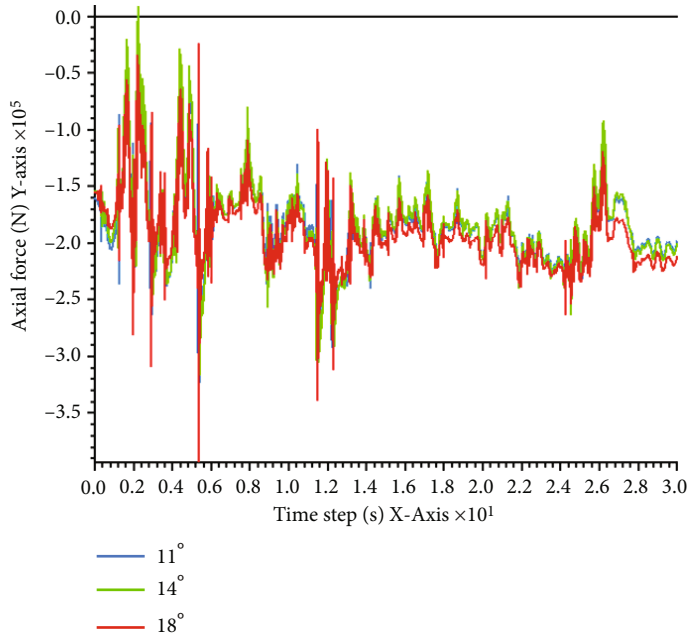

Figure 18: Distribution of dynamic earth pressure at W3 under different anchor angles.

intensifies. Accordingly, when the acceleration of the seismic wave is less than 0.62 g, the pile top displacement increases rapidly. However, when the earthquake power exceeds 0.62 g, the displacement increases slowly

(3) The performed numerical simulation shows that the dynamic earth pressure of anchor piles is active near the sliding surface and increases with the increase of the anchor dip angle. Moreover, it is passive at the pile top and decreases with the increase of the anchor dip angle. This is because with the increase of the inclined angle of the anchor cable, the intersection angle of the pile and the anchor cable decreases, the seismic component of the anchor cable reduces, the effect of the anchor cable weakens, and the passive earth pressure of the pile to the soil reduces. Accordingly, the correlation between the pile top displacement and the angle of the anchor cable is verified

Data Availability

The data used to support the findings of this study are included within the article.

Conflicts of Interest

The authors declare that they have no conflicts of interest.

Authors' Contributions

A.Fayou and Xue-gang Dai contributed equally to this work.

Acknowledgments

The authors acknowledge the National Natural Science Foundation of China (Grant: 41562016), the General Project of Yunnan Applied Basic Research Plan (Grant: 2017FB070), and the Key Research and Development Program of Yunnan Province in 2022 (the technology and application of integrated risk assessment for major earthquake disasters and their disaster chains in Yunnan).

References

[1] B. M. Das and V. K. Puri, "Holding capacity of inclined square plate anchors in clay," *Soils and Foundations*, vol. 29, no. 3, pp. 138–144, 1989.

[2] P. K. Basudhar and D. N. Singh, "A generalized procedure for predicting optimal lower bound break-out factors of strip anchors," *Geotechnique*, vol. 44, no. 2, pp. 307–318, 1994.

[3] D. K. Keefer, "Statistical analysis of an earthquake-induced landslide distribution – the 1989 Loma Prieta, California event," *Engineering Geology*, vol. 58, no. 3-4, pp. 231–249, 2000.

[4] G. A. O. Da-shui and Z. E. N. G. Yong, "Monitoring analysis of pre-stress state of anchor cable of high slope in the TGP permanent ship locks," *Chinese Journal of Rock Mechanicsand Engineering*, vol. 20, no. 5, pp. 653–656, 2001.

[5] L. I. Ning, Z. Peng, and Y. Chong, "Research on stability of left abutment slope of Jinping hydro-power station and reinforcement measurements of pre-stressed anchorage cable," *Chinese Journal of Rock Mechanics and Engineering*, vol. 26, no. 1, pp. 36–42, 2007.

[6] P. Bhattacharya, "Pullout capacity of shallow inclined anchor in anisotropic and nonhomogeneous undrained clay," *Geomechanics & Engineering*, vol. 13, no. 5, pp. 825–844, 2017.

[7] P. Bhattacharya and S. Sahoo, "Uplift capacity of horizontal anchor plate embedded near to the cohesionless slope by limit analysis," *Geomechanics & engineering*, vol. 13, no. 4, pp. 701–714, 2017.

[8] D. P. Zhou, J. J. Zhang, and Y. Tang, "Seismic damage analysis of road slopes in Wenchuan earthquake," *Chinese Journal of Rock Mechanics and Engineering*, vol. 29, no. 3, pp. 565–576, 2010.

[9] Z. H. E. N. G. Tong, L. I. U. Hongshuai, Y. U. A. N. Xiaoming, and Q. I. Wenhao, "Experimental study on seismic response of anti-slide piles with anchor cables by centrifugal shaking table," *Chinese Journal of Rock Mechanics and Engineering*, vol. 35, no. 11, pp. 2276–2286, 2016.

[10] A. J. Valsangkar, J. L. Dawe, and K. A. Mita, "Shake hake table studies of seismic response of single partially supported piles," in *6TH Canadian Conf on Earthquake Engineering*, Toronto, Canada, June 1991.

[11] N. Makris and D. Badoni, "Nonlinear seismic response of single piles," in *7th International Conference on Soil Dynamics and Earthquake Engineering (SDEE 95)*, Crete, Greece, May 1995.

[12] H. Yi, H. Hemanta, Y. Noriyuki, H. Zheng, and L. Yang, "Three-dimensional limit analysis of seismic displacement of slope reinforced with piles," *Soil Dynamics & Earthquake Engineering*, vol. 77, pp. 446–452, 2015.

[13] E. Sáez, G. S. Pardo, and C. Ledezma, "Seismic response of a pile-supported excavation on Santiago gravel," *Soil Dynamics and Earthquake Engineering*, vol. 76, pp. 2–12, 2015.

[14] Q. Honglue, L. Ying, H. Luo Hao, and H.,. H. Qindi, "Seismic response characteristics of stabilizing pile based on elastic-plastic analysis," *Shock & Vibration*, vol. 2018, pp. 1–15, 2018.

[15] L. Nan, Y. Me, Y. Liqun, W. Banqiao, L. Jun, and L. Xueling, "Seismic response of micropiles-reinforced landslide based on shaking table test," *Geomatics, Natural Hazards and Risk*, vol. 10, no. 1, pp. 2030–2050, 2019.

[16] C. Zhang, G. Jiang, L. Su, W. L. Da Lei, and Z. Wang, "Large-scale shaking table model test on seismic performance of bridge-pile-foundation slope with anti-sliding piles: a case study," *Bulletin of Engineering Geology & the Environment*, vol. 79, no. 3, pp. 1429–1447, 2020.

[17] S. Hua-you and Z. Ji-chun, "Analysis of blastingvibration effect on pre-stressed cable of high slope in Zipingpu project," *Chinese Journal of Rock Mechanics and Engineering*, vol. 22, no. 11, pp. 1916–1918, 2003.

[18] S. H. Yang, B. Liang, J. C. Gu, J. Shen, and A. M. Chen, "Research on characteristics of prestress change of anchorage cable in anti-expulsion model test of anchored cavern," *Chinese Journal of Rock Mechanics and Engineering*, vol. 25, no. S2, pp. 3749–3756, 2006.

[19] H. L. Ye, Y. R. Zheng, A. H. Li, and X. Du, "Shaking table test studies of pre-stressed anchor cable of slope under earthquake," *Chinese Journal of Rock Mechanics and Engineering*, vol. 31, no. S1, pp. 2847–2854, 2012.

[20] J. Xu, Y. Zheng, and F. Wu, "Research on interaction between the embedded anti-slide piles and the frame beam with pre-stressed anchors," in *2014 Geo Shanghai International Congress: Advances in Soil Dynamics and Foundation Engineering*, Shanghai, China, May 2014.

[21] H. Qu, J. J. Zhang, and F. Wang, "Seismic response of pre-stressed anchor sheet pile wall from shaking table tests," *Chinese Journal of Geotechnical Engineering*, vol. 35, no. 2, pp. 313–320, 2013.

[22] W. Zhou, L. I. Hai-bo, and Y. Liu, "Pseudo-dynamic analysis of anchored characteristics of layered rock slopes subjected to seismic loads," *Chinese Journal of Rock Mechanics and Engineering*, vol. 35, no. S2, pp. 3570–3576, 2016.

[23] Y. Min-jia, X. Yuan-you, and L. Ting-ting, "Limit analysis of bedding rock slopes reinforced by prestressed anchor cables under seismic loads," *Rock and Soil Mechanics*, vol. 39, no. 7, pp. 2091–2698, 2018.

[24] X. Fu, J. Zhang, W. Liao, L. Cao, and G. Fan, "Shaking table test on seismic response of slopes reinforced by pile-cable retaining structure," *Yanshilixue Yu Gongcheng Xuebao/Chinese Journal*

of Rock Mechanics and Engineering, vol. 36, no. 4, pp. 831–842, 2017.

[25] C. Fumao, T. Huiming, C. Jia, and J. Zhibin, "Influences of earthquake characteristics on seismic performance of anchored sheet pile quay with barrette piles," in *15th International Coastal Symposium (ICS)*, Busan, South Korea, May 2018.

[26] L. Yu-liang, C. Xue-ming, and Y. Guo-lin, "Seismic response of a sheet-pile wall with anchoring frame beam by numerical simulation and shaking table test," *Soil Dynamics and Earthquake Engineering*, vol. 115, pp. 352–364, 2018.

[27] Y. Huang, X. Xi, and L. Junji, "Centrifuge modeling of seismic response and failure mode of a slope reinforced by a pile-anchor structure," *Soil Dynamics & Earthquake Engineering*, vol. 131, article 106037, 2020.

[28] L. Xianqi and G. Xiurun, *Theory and Application of Model Test and Landslide*, China Waterpower Press, Beijing, China, 2008.

Hindawi
Geofluids
Volume 2022, Article ID 4042418, 9 pages
https://doi.org/10.1155/2022/4042418

Research Article

Experimental and Numerical Studies on Flowing Properties of Grouting Mortar Based on the Modified MPS Method

Ailifeila Aierken[1,2] **Shilin Luo**[1,3] **Jianqing Jiang**[1] **Linlin Chong**[1,2] **Jin Chang**[1] **Rui Zhang**[1] **and Xiangchao Zhang**[1,2]

[1]*College of Civil Engineering, Changsha University, Changsha 410022, China*
[2]*Innovation Center for Environmental Ecological and Green Building Materials of CCSU, Changsha University, Changsha 410022, China*
[3]*College of Civil Engineering and Geomatics, Chang'an University, Xi'an 710064, China*

Correspondence should be addressed to Shilin Luo; rosilynn@cqu.edu.cn

Received 16 April 2022; Accepted 2 June 2022; Published 22 June 2022

Academic Editor: Zizheng Guo

Grouting mortar has widespread application in engineering because of the advantages of good durability, low cost, and environmental friendliness. To study the flowing properties of grouting mortar, laboratory minislump tests taking different rheological parameters of grouting mortar into consideration were conducted to obtain the flow time and flow pattern of grouting mortar. A modified MPS method (moving-particle semi-implicit method) introduced two sections of Bingham rheological, and segregation was proposed. The effects of the plastic viscosity on the flow state of mortar were studied, and the relationship between the plastic viscosity and the flowing time was established. The numerical results show that the modified MPS method can be used to predict the flow time and flow pattern of mortar in the template, and plastic viscosity has a great influence on the flow time of concrete, and with the increase of plastic viscosity, the time to flow to the specified area also increases. Moreover, the analysis of the rheological parameters can provide the basis for the design of mix ratio in the construction practice.

1. Introduction

In a variety of seismic reinforcement methods for concrete structures, the steel plate lining method is widely used to reinforce existing bridge piers or columns. In this method, the properties of grouting materials must be carefully controlled to fill the narrow gap between the steel plate and the structure. Otherwise, the reinforcement will not perform the expected strength in the design. Among the properties of grouting materials, fluidity and segregation-resistance are the most important properties to control the filling process.

From a computational point of view, choosing the right strategy for the simulation is an important issue, and several approaches have been tried to simulate the flow of these approaches in previous studies [1–3]. The CFD software is usually employed to simulate the pipe flow to predict the velocity distribution and pressure loss. However, fresh concrete is considered a single-phase fluid in CFD methods, it is unable to provide information about the dynamic segregation of concrete in the pipe for predicting blockage [4–6]. Recently, the meshless particle method, such as Smoothed Particle Hydrodynamics (SPH) method [7], has been increasingly used in the flow simulation of fluid, which represents the fluid with particles. The meshless particle method has the potential to numerically discuss aggregate segregation [8]. The SPH method has been proved to be applied to the flow simulation of fresh concrete [9–12]. There is no doubt that accurate calculation of pressure is important for the grouting mortar simulation. However, since the magnitude of the time step is limited in the SPH, the accuracy and efficiency

of calculation are greatly reduced. For analyzing the incompressible fluid problem, Koshizuka and Oka [13] developed a new meshless method named moving-particle semi-implicit method (MPS). The MPS has been successfully used in the simulation of multiphase flows under high pressure [14], and the flow simulations of fresh cementitious fluid [15, 16], and has special advantages in simulating flow and filling behavior. Li et al. [17] and Jing-jun et al. [18] used the MPS method to simulate the flow characteristics of SCC and RFC in the L-box test. The results show that this method can simulate the flow process of SCC in rock-filled bodies, predict the compactness of RFC, and ultimately provide a reference for the design and construction practice of RFC engineering [19–21]. The MPS method was also used to investigate the geohazard mechanism [22, 23] and flow performances of concrete [24, 25]. Thus, the numerical simulation method including MPS has been widely used in many geotechnical applications, such as mining engineering, tunnel engineering, and slope engineering [26–32].

This paper was aimed at extending the MPS approach to simulate the flow of grouting mortar in a minislump test. This methodology provided a thorough understanding of whether a minislump test can satisfy the self-compatibility criterion of passing ability through narrow gaps beside the flowability criterion. The result is compared with the flow time and flow pattern of the minislump test in the laboratory. By using this method, the effects of the plastic viscosity on the flow state of mortar in the minislump test are studied. The relationship between the plastic viscosity, the flowing time, and the density of mortar which is calculated as the ratio of mass to volume of the test is established. On this basis, the material segregation constitutive model is proposed. The distribution of aggregates in the mixes will also be tracked during the simulation to check whether or not they are homogeneously distributed after the flow has stopped. Simultaneously, it can provide a reference basis for the design and construction practice of cement mortar in engineering.

2. Methodology

2.1. Experimental Method

2.1.1. Material Preparation. In this study, grouting mortar was chosen as a grouting material and used minislump test to measure the flow properties. Three kinds of mix proportions of grouting mortar were presented according to the rational mix design method proposed in [19, 20]. All of the mix designation, cement, water, fine aggregate, and natural river sand among these three schemes were unchanged, which is 0.4, 969, 388, 621, and 156, respectively. The variations of rheological parameters of grouting mortar were changeable and controlled by different mix proportions of thickening agent and polycarboxylate superplasticizer. The detailed compositions of all mixes were given in Table 1. It should be noted that only W/C ratio of 0.4 was selected in this paper because we want to test the feasibility of the modified MPS method. Next step, we will try to simulate the flow pattern of mortar and concrete under different mix proportions.

Table 1: Mix proportion of grouting mortar, kg/m^3.

No	Mix designation	Cement	Water	FA[a]		VMAS[b]	HRWR[c]
				FA*	FA**	(W × %)	(C × %)
1	0.4	969	388	621	156	0.0	0.9
2						0.45	2.0
3						0.1	0.7

[a]Fine aggregate <2.5 mm (note: a part of the fine aggregate is the coarser fraction of the limestone powder, FA*125 μm–1.2 mm, whereas FA** refers to natural river sand ≥1.2 mm). [b]Thickening agent. [c]Polycarboxylate superplasticizer.

2.1.2. Testing Apparatus. The minislump flow test is widely used in laboratories and construction sites for detecting grouting mortar flow characteristics. In this work, the slump cylinder was placed on the wet plate, and the mortar was injected into the cylinder, size, and shape of the cylinder as shown in Figure 1. The linear scraper was used to smooth the upper surface of the mortar, and sector scraper was adapted to remove the residual mortar dripping on the glass plate. Dampen the cylinder mold and place it on a flat moist glass plate, fill the mold with mortar, and remove the mold immediately by raising it in a vertical direction after striking off the surface by screeding. Measure the time when the mortar reach 250 mm, the diameter of the two right angles was measured with a ruler, and the average value was obtained as the flow value. The volume of the mix in the mold is 1.96×10^5 mm^3 with a diameter and height of 50 mm and 100 mm, respectively.

2.2. Modified MPS Method. The accurate prediction of the mortar flowing behavior is not a simple task, particularly in the presence of a complex formwork shape. In this regard, the indispensable and inexpensive approach offering considerable potential is the numerical simulation of grouting mortar. MPS method applies a prediction–correction semi-implicit computation algorithm, which calculates external force and viscous term in the prediction step and calculates pressure term in the correction step. Since the MPS method has been brought forward for only two decades, it is considered one promising but immature method. Some drawbacks still exist with the MPS method, particularly in the investigation of the flowing properties of grouting mortar with different viscosity coefficients. Thus, a modified MPS method introduced two sections of Bingham rheological and segregation was developed. Actually, through the comparison between the numerical simulation and the experimental results by using modified MPS method, it is found that the simulation accuracy was improved. Simultaneously, it can provide a reference basis for the design and construction practice of cement mortar in engineering.

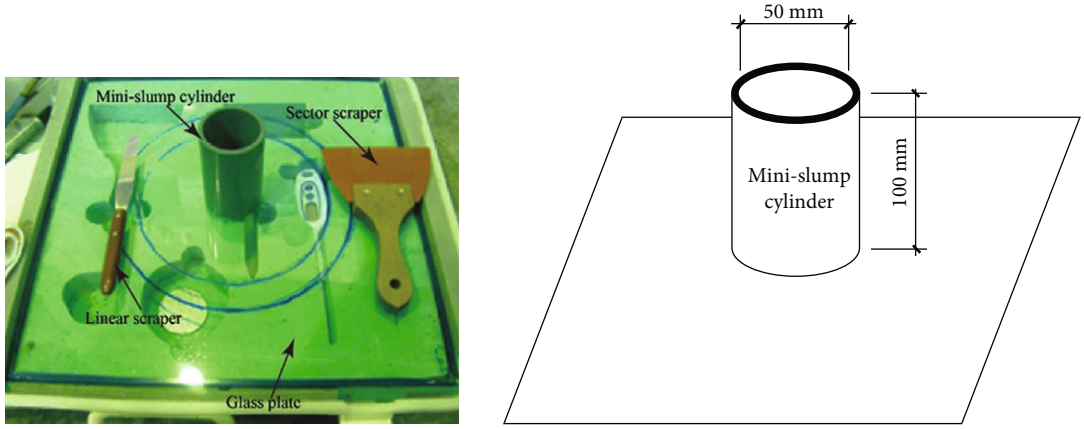

Figure 1: Size and shape of the minislump test.

2.2.1. Governing Equations. The governing equations for incompressible viscous flows are the mess conservation and Navier-Stokes equations:

$$\frac{D_\rho}{D_t} = 0, \tag{1}$$

$$\frac{D_u}{D_t} = -\frac{1}{\rho}\nabla P + \upsilon\nabla^2 u + g, \tag{2}$$

where ρ is the density, t is the time, u is the velocity vector, P is the pressure, υ is dynamic viscosity, and g is the acceleration due to gravity.

In the MPS method, the density and pressure increase when particles come close to each other and vice versa. The interaction between particles uses the weight function:

$$w(r_{ij}) \begin{cases} \dfrac{r_e}{r_{ij}} - 1 & (0 < r_{ij} < r_e), \\ 0 & (r_e \le r_{ij}), \end{cases} \quad \text{Otherwise,} \tag{3}$$

where r_{ij} is the distance between particle i and j, and r_e is the effective radius. r_e is chosen as $2.1r_{ij}$ [13]. All the forms of the weight function satisfy that the weight values are nonzero in the region of effective radius and the weight function increases as r_{ij} decreases and vice versa. It means that the r_{ij} will increases when the distance between particles is closer than r_e and becomes zero when the distance is farther than r_e.

The particle number density, which is proportional to the mass density, at the position of the particle i is defined as

$$n_i = \sum_{j\neq i} w(|r_j - r_i|), \tag{4}$$

where r_i and r_j are the position vector of the *i th and j th* particles, respectively, and n_i is the particle number density of the ith particle.

The discretization models of MPS method are derived from the Taylor expansion, and the gradient and Laplacian models in the MPS method are given as

$$\langle\nabla\varnothing\rangle_i = \frac{\boldsymbol{d}}{\boldsymbol{n^0}}\sum_{\boldsymbol{j\neq i}}\left[\left(\frac{(\varnothing_j - \varnothing_i)}{|\overrightarrow{r_j} - \overrightarrow{r_i}|^2}|\overrightarrow{r_j} - \overrightarrow{r_i}|\right) w(|\overrightarrow{r_j} - \overrightarrow{r_i}|)\right],$$
$$\langle\nabla^2\varnothing\rangle_i = \frac{\boldsymbol{2d}}{\boldsymbol{\lambda n^0}}\sum_{\boldsymbol{j\neq i}}(\varnothing_j - \varnothing_i) w(|\overrightarrow{r_j} - \overrightarrow{r_i}|), \tag{5}$$

where $\varnothing_j$ and $\varnothing_i$ are the quantities possessed by particles i and j, respectively, n^0 is the constant particle number density, d is the number of spatial dimensions, and λ is the Laplacian model coefficient, which is defined as

$$\lambda = \frac{\sum_{j\neq i}\boldsymbol{w}(|r_j - r_i|)|r_j - r_i|^2}{\sum_{j\neq i}\boldsymbol{w}(|r_j - r_i|)}. \tag{6}$$

This parameter adjusts the increase in the variance caused by the Laplacian model to that of the analytical solution. The gradient and Laplacian models are substituted into their corresponding operators in Equation (2). and the pressure, velocity, and position can be obtained. Substitute the velocity and pressure of each particle into the Lagrangian model. The source term of pressure can be represented by

$$\langle\nabla^2 P\rangle_i = \frac{2d}{\lambda n^0}\sum_{j\neq i}[(P_j - P_i) w(|r_j - r_i|)], \tag{7}$$

where P_j and P_i is the pressure of the ith and jth fluid particles, respectively. Substitute the pressure of particles into the gradient model. The pressure gradient model can be obtained

$$\langle\nabla P\rangle_i = \frac{2d}{n^0}\sum_{j\neq i}\frac{P_j - \widehat{P}_i}{|r_j - r_i|}(r_j - r_i)\, w(|r_j - r_i|), \tag{8}$$

where $\widehat{P}_i$ is the minimum pressure within the effective radius r_e. The purpose of replacing pressure P_i with $\widehat{P}_i$ is

to enforce repulsive force on all particles to stabilize the simulation.

2.2.2. Derivation of MPS. The semi-implicit scheme is adopted in MPS method. The Navier-Stokes equation is solved in two steps:

$$\left[\frac{D_{\boldsymbol{u}}}{D_t}\right]^{k+1} = \left[-\frac{1}{\rho}\nabla P\right]^{k+1} + \left[\upsilon\nabla^2 u\right]^k + [g]k. \tag{9}$$

The superscript k represents the kth time step, and the $k+1$ represents the $(k+1)-$th time step. The left side of Equation (9) can be divided into two parts

$$\left[\frac{D_{\boldsymbol{u}}}{D_t}\right]^{k+1} = \frac{u^{k+1}-u^*}{\Delta t} + \frac{u^*-u^k}{\Delta t}. \tag{10}$$

The explicit process is conducted. The intermediate velocity is only calculated by viscosity and gravity term.

$$u^* = u^k + \Delta t\left[\upsilon\nabla^2 u\right]^k + \Delta t[g]k. \tag{11}$$

The intermediate position can be ascertained by

$$r^* = r^k + u^*\Delta t. \tag{12}$$

Then, the incompressible condition is enforced in the MPS method, namely, the particle number density must remain constant, as

$$n_i = n^0 \tag{13}$$

where n_i is the particle number density of the ith fluid particle.

The following Poisson equation is derived, and the pressure of particles is implicitly evaluated using this equation

$$\langle\nabla P\rangle_i^{k+1} = -\frac{\rho}{\Delta t}\frac{n_i^*-n^0}{n^0}, \tag{14}$$

where n_i^* is the temporary particle number density calculated after the explicit step. After calculating the pressure of particles, the gradient of pressure is computed by Equation (8). The velocity of the next time step is corrected by

$$u^{k+1} = u^* - \Delta t\left[-\frac{1}{\rho}\nabla P\right]^{k+1}. \tag{15}$$

The position of particles at the $(k+1)-$th time step can be calculated

$$r^{k+1} = r^* + \left(u^{k+1}-u^*\right)\Delta t. \tag{16}$$

The Dirichlet boundary condition is enforced in the Poisson equation on the free surface. The pressure of particles is set to zero when the particle number density satisfies the equation

$$n_i^* < \beta n^0, \tag{17}$$

where β is a parameter for surface detection and $\beta = 0.97$ is adopted in this study.

The solid wall boundary condition is represented by fixed boundary particles which are composed of one layer of boundary particles and several layers of dummy particles.

The flow chart of the MPS method is shown in Figure 2.

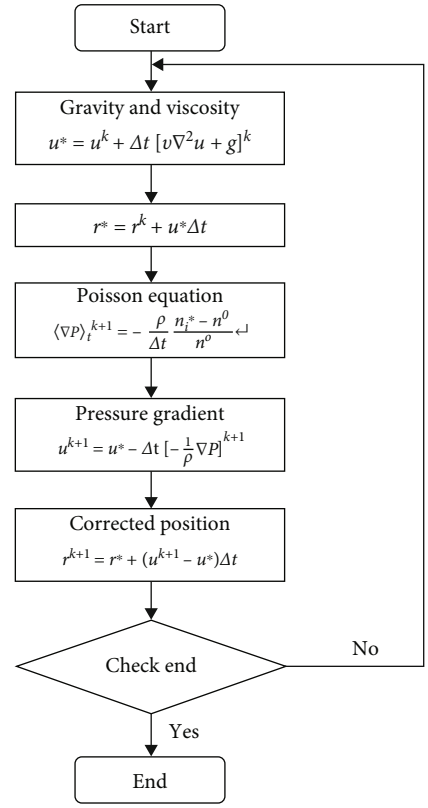

Figure 2: Flow chart of the MPS method.

2.2.3. Biviscosity Section. The behavior of the mortar in the flow test was simulated using MPS numerical method. The governing equation is the momentum equation of the Bingham fluid. The non-Newtonian viscosity of a biviscosity model is used in this study. The momentum equation for the ***ith*** direction is as follows:

$$\begin{aligned}\frac{\boldsymbol{Du_i}}{\boldsymbol{Dt}} = \boldsymbol{F_i} + \frac{\boldsymbol{1}}{\boldsymbol{\rho}}\Bigg\{&-\boldsymbol{\nabla P} + \left(\boldsymbol{\eta} + \frac{\boldsymbol{\tau_y}\left(\boldsymbol{1}-\boldsymbol{e}^{-\boldsymbol{m}\sqrt{\boldsymbol{II}}}\right)}{\sqrt{\boldsymbol{II}}}\right)\boldsymbol{\nabla^2 u_i} \\ &+ \boldsymbol{2\dot{\varepsilon}_{ij}}\frac{\boldsymbol{\partial}\left(\boldsymbol{\tau_y}\left(\boldsymbol{1}-\boldsymbol{e}^{-\boldsymbol{m}\sqrt{\boldsymbol{II}}}\right)/\sqrt{\boldsymbol{II}}\right)}{\boldsymbol{\partial x_j}}\Bigg\},\end{aligned} \tag{18}$$

where F_i represents the body forces (N/m^3), ρ is the density of mortar (kg/m^3), P is the pressure (Pa), η is the plastic viscosity (Pa·s), τ_y is the yield value (Pa), m is the fitting

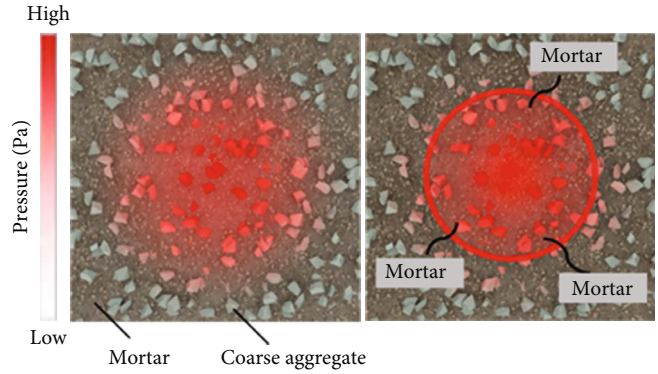

Figure 3: Conceptual diagram of the segregation model.

index [6], $\dot{\varepsilon}_{ij}$ is the strain rate, and $\sqrt{II} = \sqrt{2\dot{\varepsilon}_{ij}\dot{\varepsilon}_{ij}}$.

$$\dot{\varepsilon}_{ij} = \frac{1}{2}\left[(\nabla u) + (\nabla u)^T\right]. \tag{19}$$

Velocity gradient of ith particle at time level k is calculated using the following gradient model

$$\langle \nabla \boldsymbol{u} \rangle_{\boldsymbol{i}}^{\boldsymbol{k}} = \frac{\boldsymbol{d}}{\boldsymbol{n^0}} \sum_{\boldsymbol{j \neq i}} \frac{\left(\boldsymbol{u_j^k} - \boldsymbol{u_i^k}\right)\left(\boldsymbol{r_j^k} - \boldsymbol{r_i^k}\right)}{\left|\boldsymbol{r_j^k} - \boldsymbol{r_i^k}\right|^2} \boldsymbol{w}\left(\left|\boldsymbol{r_j^k} - \boldsymbol{r_i^k}\right|\right), \tag{20}$$

where d is the number of space dimensions.

The viscosity coefficient is calculated between the particles i and j and average of particle i and particle j.

$$\begin{aligned} \mu_{ij} &= \eta + \frac{\tau_y\left(1 - e^{-m\sqrt{II}}\right)}{\sqrt{II}}, \\ \nu_{ij} &= \frac{\mu_i + \mu_j}{2\rho}. \end{aligned} \tag{21}$$

When calculating viscous items after calculating the viscous coefficient, the formulas for viscous terms are discretized using the Laplacian model as

$$u_i^* = u_i^k + \Delta t \frac{2d}{\lambda n^0} \sum_{j \neq i} \nu_{ij}^k \left(u_j^* - u_i^*\right) w\left(\left|r_j^* - r_i^*\right|\right). \tag{22}$$

2.2.4. Segregation Section. According to the model of the previous studies proposed [33–37], segregation of material occurred because the pressure force from the difference of fresh concrete caused the mortar flows from a high-pressure area to low pressure area is used to simulate in this paper as shown as Figure 3.

$$\begin{aligned} M_i^{t+\Delta t} &= M_i^t + \left(\alpha \times \frac{\sum_{j \neq i}\left(\left|P_j - P_i\right|\right) w\left(\left|r_j - r_i\right|\right)}{\sum_{j \neq i} w\left(\left|r_j - r_i\right|\right)} \times M_i^t\right) \times \Delta t\left(P_j > P_i\right), \\ M_i^{t+\Delta t} &= M_i^t - \left(\alpha \times \frac{\sum_{j \neq i}\left(\left|P_j - P_i\right|\right) w\left(\left|r_j - r_i\right|\right)}{\sum_{j \neq i} w\left(\left|r_j - r_i\right|\right)} \times M_i^t\right) \times \Delta t\left(P_j < P_i\right), \end{aligned} \tag{23}$$

where t is the time, M_i^t is the mix-proportion of point i, and $M_i^{t+\Delta t}$ is the proportion of mortar. α is the material segregation resistance coefficient, which is based on the change of the rheological constant assumed by this study.

The maximum and minimum of mix-proportion need to be set. The maximum of mix-proportion was set as 0.99, and minimum of mix-proportion was set as (1 ~ solid content in aggregate/100) in this paper. The mortar no longer flows into central area when the mix-proportion of point $\boldsymbol{i}$ reaches the maximum value, and the mortar will no longer flows out when the mix-proportion of point $\boldsymbol{i}$ reaches the minimum.

3. Experimental Results

The plastic viscosity coefficient reflects the flow properties of concrete. Generally, the higher the plastic viscosity, the slower the mortar flow. As listed in Table 2, the plastic viscosity for three kinds of mix proportions of grouting mortar was 2.14, 5.00, and 2.82 Pa·s, the mortar flow value within 5 seconds recorded by the camera was 245, 195, and 226 mm, respectively. The segregation resistance index y and segregation resistance coefficient α was described as Equations (24) and (25). The relationship between flow value and time with different plastic viscosity of minislump tests was shown in Figure 4. At the same time before the flow stops, with the increase of plastic viscosity, the flow distance of grouting mortar becomes shorter. The flow time with different plastic viscosity at the same distance and the flow velocity of mortar also increases with the decrease of plastic viscosity, which is a negative correlation trend. It also directly shows that plastic viscosity is an important factor affecting the flow velocity of a cement-based material.

4. Numerical Results and Discussions

4.1. The Effects of Viscosity Coefficient on Flow Value. The purpose of slump flow simulation is to verify the implementation of the Bingham model for non-Newtonian rheology. The numerical model has a total number of particles of 121,107. The density of the fluid is 2133 kg/m^3, 2156 kg/m^3, and 2140 kg/m^3. The rheological parameters (plastic viscosity and yield stress) of the sample were measured by viscometer as listed in Table 2. The

Table 2: Measured data of minislump test.

No	ρ (kg/m^3)	η_p (Pa·s)	τ_0 (Pa)	Flow* (mm)	y	α
1	2133	2.14	22.6	245	1.23	6.1×10^{-4}
2	2156	5.00	35.18	195	1.57	7.9×10^{-4}
3	2140	2.82	26.75	226	1.32	6.6×10^{-4}

*Flow value of minislump test in 5 s (flow pattern of mortar was recorded by the camera during the test).

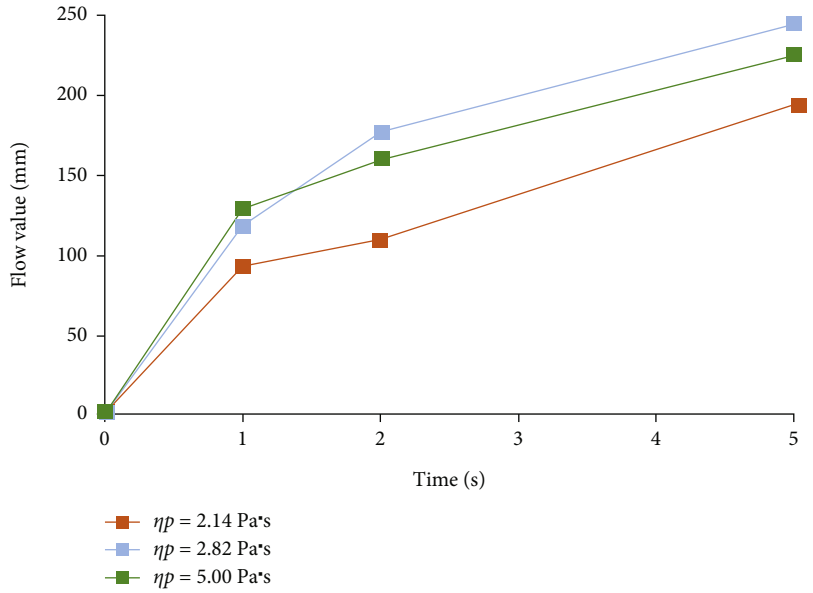

Figure 4: Relationship between flow value and time with different plastic viscosity.

computational time step is 0.00002 seconds, and the total computational time is 5.0 seconds.

Figure 5 shows the numerical simulation of the minislump flow process by using the modified MPS method when the plastic viscosity is 2.14 Pa·s. As illustrated in this plot, the flow value presents an increasing tendency with the rise of time. The flow value at time of 0.5 s, 1.0 s, 2.0 s, and 5.0 s was 0.085, 0.120, 0.181, and 0.241 m, respectively. Figure 6 manifests the comparison of simulation and test results. It can be seen from Figure 6 that the simulated value is in good agreement with the experimental value, but in the early stage of flow, the experimental value is smaller than the simulated value. This is caused by the delay in the lifting time of the slump cone under the test state, and the numerical simulation can achieve the ideal state of the instant lifting of the slump cone.

All of the above indicate that the flow time and pattern are affected by the rheological constant.

4.2. Assessment of Segregation Section. The numerical simulation of flow is a powerful tool for understanding the rheological behavior of flow patterns. In order to verify the availability of the segregation model depending on the rheological properties and pressure, the simulation results of the flow test are validated with the measured data. The parameters used in the calculation are shown in Table 2.

The material segregation resistance coefficient is used in this paper, which is based on the regression analysis of the material segregation resistance index and rheological constant as shown in Table 2.

$$y = 0.072\eta + 0.011\tau + 0.827, \tag{24}$$

where y is the segregation resistance index, η is the plastic viscosity, and τ is the yield value. According to this formula, it can be known that y increases with the increase of η and τ. In addition, the segregation resistance index y represents the index of the tendency of material segregation resistance in the experiment. In addition, the material factor alpha-factor used in the analysis indicates the proportion of concrete moving in unit time and the value of segregation resistance is consistent with the tendency of segregation resistance index. Therefore, the segregation resistance index y obtained by the heavy regression equation is used as the coefficient of w ($w = 5.0 \times 10^{-4}$), which is used as the material segregation resistance coefficient α (Table 2).

$$\alpha\left(\eta_m^p, \tau_y\right) = wy. \tag{25}$$

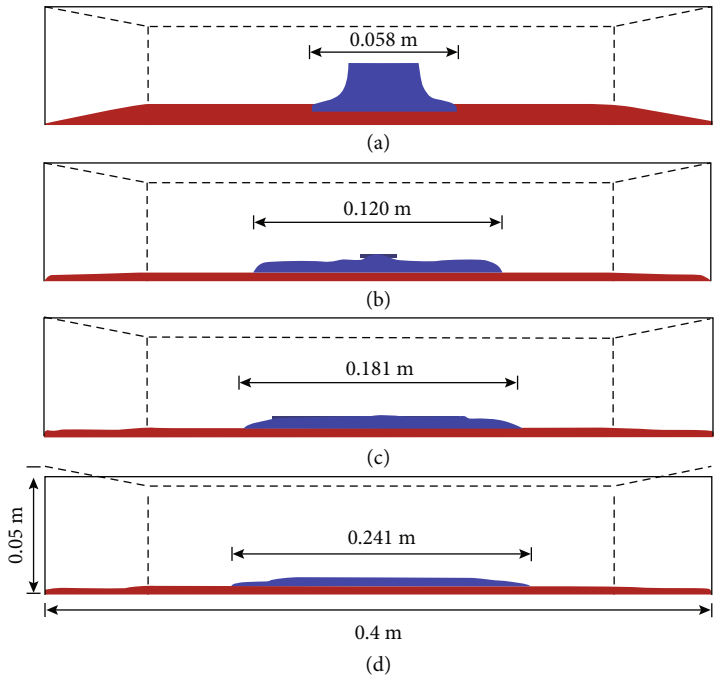

Figure 5: Snap shots of 3D minislump test at time of 0.5 s (a), 1.0 s (b), 2.0 s (c), and 5.0 s (d).

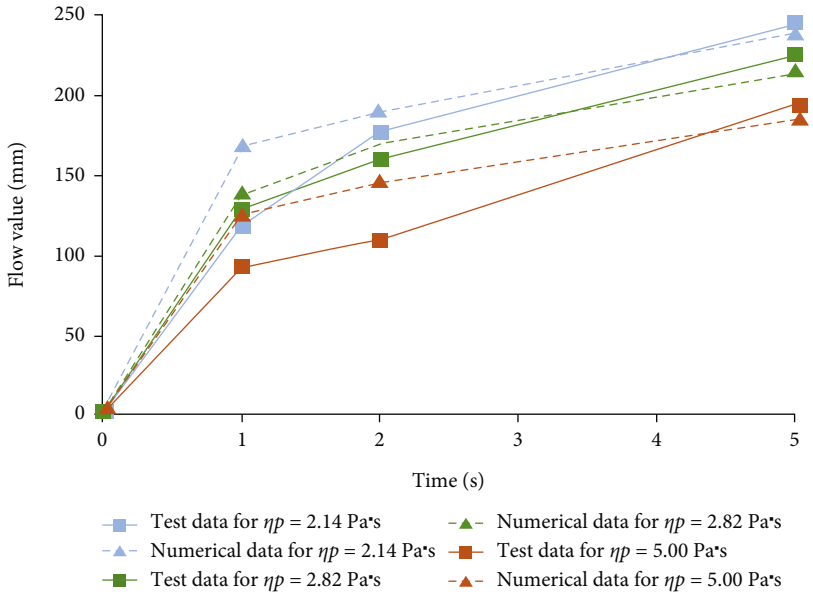

Figure 6: Comparison between simulation results and experiment results.

There is no unified test method for quantitative measurement of segregation of material. Therefore, from the perspective of numerical simulation, this paper verifies the feasibility of segregation section of mortar.

Numerical simulation is carried out for different test conditions, and the test flow value and simulated flow value are compared and analyzed. The errors of the two are shown in Table 3, where T_e is the test result, T_s is the simulation result, and E is the error rate. The results show that the maximum error of the simulation results is 5.1%, which shows that the segregation section established in this paper has a

Table 3: Accuracy of simulation.

No	(T_e/s)	(T_s^*/s)	$(E_1/\%)$	(T_s^{**}/s)	$(E_2/\%)$
1	245	233	5.0	240	2.0
2	195	179	8.2	185	5.1
3	226	211	6.6	215	4.9

T_s^*/s: Simulation result by modified MPS method without segregation section. T_s **/s: Simulation result by modified MPS method with segregation section.

certain accuracy and can provide a reference basis for the flow state of mortar and concrete described by the Bingham rheological model.

5. Conclusions

Based on the results obtained in the experiment and the numerical simulation, it is clear that plastic viscosity and yield stress have the great influence on the flow time of mortar, and with the increase of plastic viscosity, the time to flow to the specified area also increases.

A good agreement between numerical and experimental data was found in the comparison of the final shape of the sample. It can be known that the modified MPS method in this paper is feasible for the flow simulation of grouting mortar and has high accuracy. The investigated results indicate that the modified MPS method by setting reasonable particle spacing can simulate and predict the flow process of non-Newtonian fluid with a free surface. The effectiveness of the segregation section depending on the rheological properties and pressure proposed in this paper was verified. Through the comparison between the numerical simulation and the experimental results, it is found that the simulation accuracy was improved from 91.8% to 94.9%, which showed that the segregation section was suitable for the simulation of the grouting mortar.

Data Availability

All data, models, and code generated or used during the study are available from the corresponding author by request.

Disclosure

A preprint has previously been published [38].

Conflicts of Interest

The authors declare that they have no conflicts of interest.

Authors' Contributions

Ailifeila Aierken contributed to the methodology and writing-original draft. Shilin Luo contributed to the conceptualization and revision. Jianqing Jiang contributed to the data curation and language editing. Linlin Chong and Jin Chang contributed to the algorithm analysis. Rui Zhang and Xiangchao Zhang contributed to the software and validation.

Acknowledgments

This work was supported by the Hunan Provincial Natural Science Foundation (Nos 22021JJ40632, 2021JJ30758 and 2022JJ40521), Scientific Research Project from the Education Department of Hunan Province (Nos 21C0740, 21C0753, and 21B0773), and Changsha Municipal Natural Science Foundation (Nos kq2007089, kq2202065, and kq2202063).

References

[1] J. Wu and C. Shu, "An improved immersed boundary-lattice Boltzmann method for simulating three- dimensional incompressible flows," *Journal of Computational Physics*, vol. 229, no. 13, pp. 5022–5042, 2010.

[2] O. Švec, J. Skoček, H. Stang, M. R. Geiker, and N. Roussel, "Free surface flow of a suspension of rigid particles in a non-Newtonian fluid: a lattice Boltzmann approach," *Journal of Non-Newtonian Fluid Mechanics*, vol. 179-180, pp. 32–42, 2012.

[3] F. P. T. Baaijens, "A fictitious domain/mortar element method for fluid-structure interaction," *International Journal for Numerical Methods in Fluids*, vol. 35, no. 7, pp. 743–761, 2001.

[4] E. Secrieru, J. Khodor, C. Schröfl, and V. Mechtcherine, "Formation of lubricating layer and flow type during pumping of cement-based materials," *Construction and Building Materials*, vol. 178, pp. 507–517, 2018.

[5] M. Choi, C. F. Ferraris, N. S. Martys, D. Lootens, V. K. Bui, and H. R. T. Hamilton, "Metrology needs for predicting concrete pumpability," *Advances in Materials Science and Engineering*, vol. 2015, 10 pages, 2015.

[6] M. S. Choi, Y. J. Kim, and S. H. Kwon, "Prediction on pipe flow of pumped concrete based on shear-induced particle migration," *Cement and Concrete Research*, vol. 52, pp. 216–224, 2013.

[7] G. R. Liu and M. B. Liu, *Smoothed Particle Hydrodynamics*, World Scientific Publishing Co, Pte Ltd, 2003.

[8] Z. Li, Z. Xu, and R. Yoshioka, *Flow Simulation of Fresh Concrete Using SPH Method with Consideration of Geometry of Particles, in: Sixth Int*, Conf. Constr. Mater, Fukuoka, Japan, 2020.

[9] G. Cao, Z. Li, and Z. Xu, "A SPH simulation method for opening flow of fresh concrete considering boundary restraint," *Construction and Building Materials*, vol. 198, pp. 379–389, 2019.

[10] W. S. Alyhya, S. Kulasegaram, and B. L. Karihaloo, "Simulation of the flow of self-compacting concrete in the V-funnel by SPH," *Cement and Concrete Research*, vol. 100, pp. 47–59, 2017.

[11] G. Cao and Z. Li, "Numerical flow simulation of fresh concrete with viscous granular material model and smoothed particle hydrodynamics," *Cement and Concrete Research*, vol. 100, pp. 263–274, 2017.

[12] M. S. Abo Dhaheer, S. Kulasegaram, and B. L. Karihaloo, "Simulation of self-compacting concrete flow in the J-ring test using smoothed particle hydrodynamics (SPH)," *Cement and Concrete Research*, vol. 89, pp. 27–34, 2016.

[13] S. Koshizuka and Y. Oka, "Moving-particle semi-implicit method for fragmentation of incompressible fluid," *Nuclear Science and Engineering*, vol. 123, no. 3, pp. 421–434, 1996.

[14] Y. Shimizu, H. Gotoh, and A. Khayyer, "An MPS-based particle method for simulation of multiphase flows characterized by high density ratios by incorporation of space potential particle concept," *Computers & Mathematcs with Applications*, vol. 76, no. 5, pp. 1108–1129, 2018.

[15] Z. Xu, Z. Li, G. Cao, and F. Jiang, "Comparison of SPH and MPS methods for numerical flow simulations of fresh mortar," *Proceeding of the Japan concrete institute*, vol. 41, pp. 1127–1132, 2019.

[16] Z. Xu, Z. Li, and F. Jiang, "The applicability of SPH and MPS methods to numerical flow simulation of fresh cementitious

materials," *Construction and Building Materials*, vol. 274, p. 121736, 2021.

[17] J. Li, L. Tian, L. Qiu, and H. Yu, "Numerical simulation of self-compacting concrete flow based on MPS method," *Journal of Building Materials*, vol. 23, no. 2, pp. 309–316, 2020.

[18] L. I. Jing-jun, T. I. A. N. Lei, and Q. I. U. Liu-chao, "Numerical simulation for the filling of RFC based on MPS method," *Journal of Building Materials*, vol. 23, no. 6, pp. 1357–1365, 2020.

[19] Y. Zhao, C. Zhang, Y. Wang, and H. Lin, "Shear-related roughness classification and strength model of natural rock joint based on fuzzy comprehensive evaluation," *International Journal of Rock Mechanics and Mining Sciences*, vol. 137, article 104550, 2021.

[20] Y. Zhao, Q. Liu, C. Zhang, J. Liao, H. Lin, and Y. Wang, "Coupled seepage-damage effect in fractured rock masses: model development and a case study," *International Journal of Rock Mechanics and Mining Sciences*, vol. 144, article 104822, 2021.

[21] D. Sun, H. Wen, J. Xu, Y. Zhang, D. Wang, and J. Zhang, "Improving geospatial agreement by hybrid optimization in logistic regression-based landslide susceptibility modelling," *Frontiers in Earth Science*, vol. 9, no. 8, pp. 117–129, 2021.

[22] Y. C. Jin, K. Guo, Y. C. Tai, and C. H. Lu, "Laboratory and numerical study of the flow field of subaqueous block sliding on a slope," *Ocean Engineering*, vol. 124, no. 15, pp. 371–383, 2016.

[23] E. Harada, H. Ikari, T. Tazaki, and H. Gotoh, "Numerical simulation for coastal morphodynamics using DEM-MPS method," *Applied Ocean research*, vol. 117, article 102905, 2021.

[24] Z. Xu, Z. Li, and F. Jiang, "Numerical approach to pipe flow of fresh concrete based on MPS method," *Cement and Concrete Research*, vol. 152, article 106679, 2022.

[25] P. Yu, Y. H. Duan, Q. X. Fan, and S. W. Tang, "Improved MPS model for concrete creep under variable humidity and temperature," *Construction and Building Materials*, vol. 243, article 118183, 2020.

[26] Y. Pan, H. Wang, Y. Zhao, Q. Liu, and S. Luo, "Numerical analysis of the mud inflow model of fractured rock mass based on particle flow," *Geofluids*, vol. 2021, Article ID 5599748, 16 pages, 2021.

[27] Y. Z. Q. Liu, J. Lian, Y. Wang, and L. Tang, "Theoretical and numerical models of rock wing crack subjected to hydraulic pressure and far-field stresses," *Arabian Journal of Geosciences*, vol. 13, no. 18, p. 926, 2020.

[28] J. Liao, Y. Zhao, L. Tang, and Q. Liu, "Experimental studies on cracking and local strain behaviors of rock-like materials with a single hole before and after reinforcement under biaxial compression," *Geofluids*, vol. 2021, Article ID 8812006, 15 pages, 2021.

[29] L. Tang, Y. Zhao, J. Liao, and Q. Liu, "Creep experimental study of rocks containing weak interlayer under multi-level loading and unloading cycles," *Frontiers in Earth Science*, vol. 8, article 519461, 2020.

[30] Y. Zhao, Y. Wang, W. Wang, W. Wan, and J. Tang, "Modeling of non-linear rheological behavior of hard rock using triaxial rheological experiment," *International Journal of Rock Mechanics and Mining Sciences*, vol. 93, pp. 66–75, 2017.

[31] H. Lin, D. Lei, C. Zhang, Y. Wang, and Y. Zhao, "Deterioration of non-persistent rock joints: a focus on impact of freeze-thaw cycles," *International Journal of Rock Mechanics & Mining Sciences*, vol. 135, article 104515, 2020.

[32] F. Miao, Y. Wu, Á. Török, L. Li, and Y. Xue, "Centrifugal model test on a riverine landslide in the Three Gorges Reservoir induced by rainfall and water level fluctuation," *Geoscience Frontiers*, vol. 13, no. 3, p. 101378, 2022.

[33] S. Hirano, Y. Yamada, H. Nishi, and K. Sakihara, "rheological constants measurement of mortar that fluidity is evaluated by slump and analysis of slump and slump flow of mortar by MPS method," *Journal of Structural and Construction Engineering (Transactions of AIJ)*, vol. 85, no. 774, pp. 993–1003, 2020.

[34] Y. Higashifunamichi and Y. Yamada, "Study on the rheological constants estimation method of cement paste by flow test," *Journal of Structural and Construction Engineering (Transactions of AIJ)*, vol. 86, no. 784, pp. 860–870, 2021.

[35] P. Xie, H. Wen, S. Ma et al., "The bearing capacity analysis of limestone strata roof containing a shallow-buried cylinder Karst cave," *Mechanics of Advanced Materials and Structures*, vol. 12, no. 33, pp. 1–8, 2021.

[36] Y. Yamada, Y. Uehara, K. Sakihara, and S. Urano, "Slump flow simulation of high fluidity concrete by MPS method," *Journal of Structural and Construction Engineering (Transactions of AIJ)*, vol. 85, no. 771, pp. 663–672, 2020.

[37] Z. Xu and Z. Li, "Numerical method for predicting flow and segregation behaviors of fresh concrete," *Cement and Concrete Composites*, vol. 123, p. 104150, 2021.

[38] A. Aierken, *Study on Flow Properties and Segregation-resistance Performance on Filling Behavior of Grout Mortar, [Ph.D. thesis]*, Tokyo Metropolitan University, Tokyo, 2018.

Hindawi
Geofluids
Volume 2022, Article ID 9253324, 12 pages
https://doi.org/10.1155/2022/9253324

Research Article

Relationships among Seepage, Water Level, and Rainfall of a Fill Dam by Decision Tree Analysis

Seong-Kyu Yun,[1] **Jiseong Kim**,[2] **Eun-Sang Im**,[3] **and Gichun Kang**[4]

[1]*Engineering Research Institute, Gyeongsang National University, Jinju 52828, Republic of Korea*
[2]*Department of Cadastre & Civil Engineering, Vision College of Jeonju, 235 Cheonjam-ro, Wansan-gu, Jeonju, Jeollabuk-do 55069, Republic of Korea*
[3]*Water Energy & Infrastructure Research Center, K-water, 1689 Yuseongde-ro, Yuseong-gu, Daejeon 34045, Republic of Korea*
[4]*Department of Civil Engineering, College of Engineering, Gyeongsang National University, 501 Jinjudero, Jinju, Gyeongsangnam-do 52828, Republic of Korea*

Correspondence should be addressed to Gichun Kang; gkang@gnu.ac.kr

Received 12 May 2022; Revised 7 June 2022; Accepted 7 June 2022; Published 16 June 2022

Academic Editor: Zizheng Guo

This study is to present acceptable measurement values through decision tree analysis for the seepage, which is an important measuring item of the fill dam. The seepage of the dam under study increases rapidly when rainfall occurs, when the direct inflow of rainfall from the downstream slope and both sides occur. Therefore, the allowable seepage of fill dam considering rainfall and water level is required. Decision tree analysis was conducted for one domestic fill dam by setting the seepage as a response variable and setting rainfall and water level as explanatory variables. At this time, in order to analyze the effects of rainfall on the seepage more closely, the data subject was classified into two groups consisting of a rainfall-free group and a rainfall-occurring group. Group A, which is a rainfall-free group, had 97.7% of the seepage data distributed under the conditions of 98.50 mm/day of the antecedent 5-day rainfall selected as the first explanatory variable. The average seepage of the group was between 12.01 L/min and 26.35 L/min. Group B, which is a rainfall-occurring group, had 85.7% of the water leakage data distributed under conditions of 38.50 mm/day of daily rainfall selected as the first explanatory variable, with an average of 23.70 L/min.

1. Introduction

In Korea, about 20,000 dams serve an important function of industrial infrastructure. However, recently, the aging of dams, the increasing frequency of earthquakes, and weather fluctuations have threatened the stability of dams, and the development and improvement of design, construction, and maintenance technologies to secure the stability of dams is urgently required. In particular, the need for repair and reinforcement is emerging as multipurpose dams, which have been constructed in Korea since the 1960s and are gradually aging. Among the 37 multipurpose dams and water supply dams in Korea, about 30% have passed more than 30 years, and more than 50% of the 14 water supply dams have passed about 30 to 60 years. Problems with these dams are thought to not only cause water disasters but also negatively affect the nation's water supply. Therefore, various kinds of measuring instruments such as water seepage meter, pore pressure meter, seismometer, earth pressure gauge, clinometer, and settlement gauge are buried and installed in the dam and used for stability analysis through real-time or manual monitoring [1]. And the data obtained from these various instruments is critical as basic data for maintenance or research of dams [2]. In particular, the amount of seepage flowing through the dam is important for understanding the motion and mysterious symptoms of the dam, and accurately identifying them is a prerequisite for dam management [3]. As shown in Figure 1, the dam is referred to as stage 1 until it reaches normal high-water level for the first time after the commencement of

impoundment, and it is referred to as stage 2 from the first normal high-water level to the time when the dam's movement reaches a safe state. And after the dam's movement has reached a stable state, it is called stage 3. As shown in Figure 1, the seepage is typically at its peak in stage 1 and stabilizes over time with a gradual decrease in the seepage, resulting in a constant value in stage 3.

According to the US Committee on Large Dams [5], 77 cases of collapse of fill dams in the US (accidents that occurred until the 1980s) were analyzed, and the destruction caused by leaks and piping through dam body or foundation ground accounted for 44%. Seepage water meter of the fill dam is an important measuring item that can monitor this type of destruction. In addition, it is necessary for seepage measurement management to establish an acceptable measurement, which means a safe level for the observed values, and to evaluate the stability of the dam by comparing the current measurement with the acceptable measurement. It is important to establish the decision of the acceptable measurement considering many assumptions or environmental conditions included in the design [6]. However, there is an actual difference in the predicted seepage in the design and the measurement of the seepage of the dam considering the surrounding environmental conditions. Therefore, the dam shall analyze test impoundment and the measurement data of operation period to check the normal range of the dam and establish the acceptable measurement based on it. However, it is common to establish acceptable measurements of seepage by using measurements obtained during operation of the dam due to no implementation of test impoundment, absence of instruments, and deterioration of reliability due to the inflow of rainfall.

For the dam measurements, Kuperman et al. [7] considered the behavior of the dam to be normal if the measurements measured from the same instrument are within a certain range under conditions such as water levels similar to the past. Lee [8] calculated the upper and lower limits by methods of the Shewhart control chart method and linear regression analysis according to the aging characteristics within the normal range of dam behavior and presented it as the management criteria. Ryan [9], Lewis et al. [10], and Myers and Montgomery [11] conducted studies on many measurements that did not follow a normal distribution and found that measured values by dam measuring instruments often exhibited asymmetric distributions that did not follow a normal distribution. In addition, Park and Park [12] said that using Shewhart control chart based on normality assumption for control chart of measured values following asymmetric distributions is less efficient in managing measure variability and increases the probability of making errors as asymmetry increases, proposing a quartile control chart as an alternative to this problem. In fact, however, many fill dams have limitations in introducing the method above as the water catchment wall is located at the bottom of the downstream slope and the seepage increases due to the direct inflow of rainfall through the downstream slope.

Decision tree analysis is easy to understand the classification structure of the data and can explain the reasons for the decision-making so that the effect of water levels and rainfall, which are highly correlated with the water seepage of the dam, can be considered [4]. In this study, the seepage is determined as a response variable for one fill dam, while rainfall and water level are set as explanatory variables. At this time, in order to analyze the effects of rainfall on the seepage more closely, the decision tree analysis was conducted by classifying measured data into two groups consisting of a rainfall-free group and a rainfall-occurring group, using the daily rainfall and antecedent 5-day rainfall as explanatory.

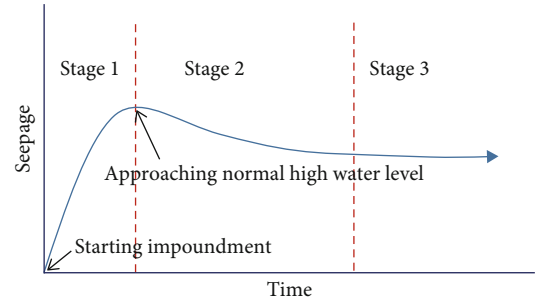

Figure 1: Management stage of fill dams [4].

Table 1: Summary of the dam for study.

Dam type	Center-cored rockfill dam
Dam crest elevation (m)	44
Dam crest wide (m)	8
Upstream slope	1 : 2.2
Downstream slope	1 : 1.8
Dam crest length (m)	108
Dam height (m)	35.2
Dam volume (m^3)	153,000

2. Target Dam for Research

The dam subject to the research is a central core rockfill dam, and the cross section of the dam is constructed in order of filter and rockfill, with the core installed on the axis of the dam and directed upstream and downstream. The main dimensions of the dam are shown in Table 1. The dam was completed in 2007 and has been around 13 years since impoundment (Figure 2).

2.1. Installation Status of Water Seepage Measuring Instruments. The water seepage measurement instrument of the dam under research was installed to identify the changes in the amount of water penetrating through the dam body and the foundation ground and to understand the soundness of the barrier function of the dam. First of all, a barrier water catchment wall is installed at the lower fore-end of the dam, and the wall is connected by a seepage measurement room and an induction pipe. The water seepage of the fill dam to be studied is measured in real time (1 time/hr). Figure 3 shows V-notch, a seepage measurement

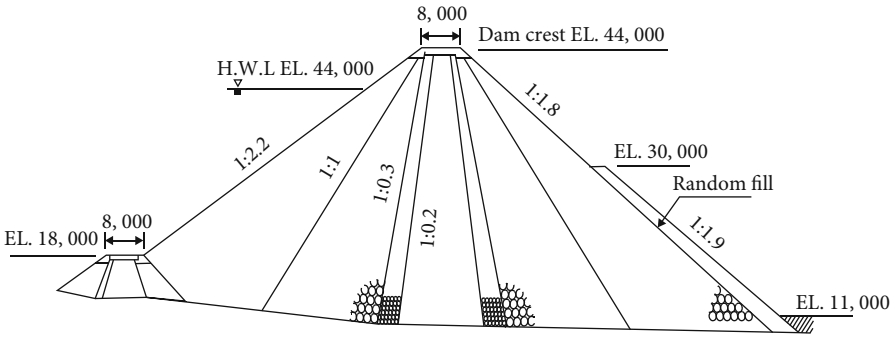

Figure 2: Cross-sectional plan (unit: mm).

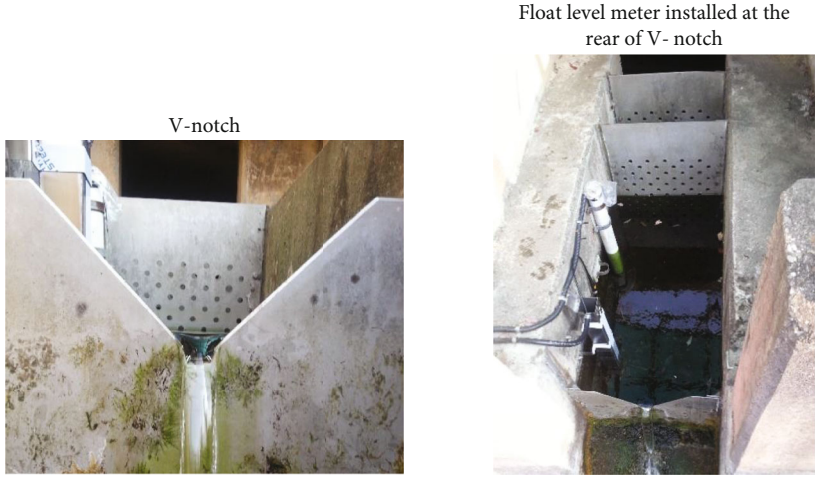

(a) V-notch (b) Float level meter installed at the rear of V-notch

Figure 3: Instruments for measuring seepage of a fill dam.

instrument installed in the dam, and a water gauge. The dam has one seepage water meter installed, with bottom width of waterway (B) of 0.5 m and height from the bottom of the waterway to the bottom of the V-notch (D) of 0.3 m. The depth (h) and angle (a) of the V-notch are 0.2 m and 90 degrees, respectively. To measure the seepage, a float type water gauge is installed at the entrance of seepage water to automatically measure the height flowing over the V-notch (h) and calculate it by converting it to the rate of flow. In the case of the dam studied, it was installed in the specifications suggested by the International Organization for Standardization ISO [13] so that its accuracy has already been verified [14].

3. Measurement Status

3.1. Storage Level and Rainfall. Figure 4 shows changes in water level and rainfall over time. The water level, which is an important factor in dam management and operation, has an excellent data management with missing rate of 0% within the data collection period. As shown in the figure, a surge in rainfall indicates a rise in the water level. The average water level is EL.35.68 m, and the standard deviation is 2.97 m. For statistical analysis of water levels and rainfall, the measured results from June 1st, 2009 to June 10th, 2019 were used. The average daily rainfall of the reservoir in the dam was 3.27 mm/day, and the maximum daily rainfall was approximately 234 mm/day, which occurred on October 05, 2016.

Another explanatory variable, the antecedent 5-day rainfall, is shown in Figure 5. The reason for the application of the antecedent 5-day rainfall is that the inflow of rainfall usually lasts for several days after rainfall, and the rainfall, which is the standard of the Antecedent Soil Moisture Content (AMC) applied in hydrological flood simulations, is the antecedent 5-day rainfall [15]. The average of the antecedent 5-day rainfall was 16.31 mm/day, and the maximum antecedent 5-day rainfall was approximately 354 mm/day, which occurred on September 18th, 2012.

3.2. Seepage of Water. For statistical analysis of seepage quantities, water levels and rainfall measurement results at the same time were utilized. The average missing rate of seepage during the data collection period was 21.6% (792 days/3,662 days). Also, since the barrier wall is located in the fleet of the downstream, the seepage of water of the fill

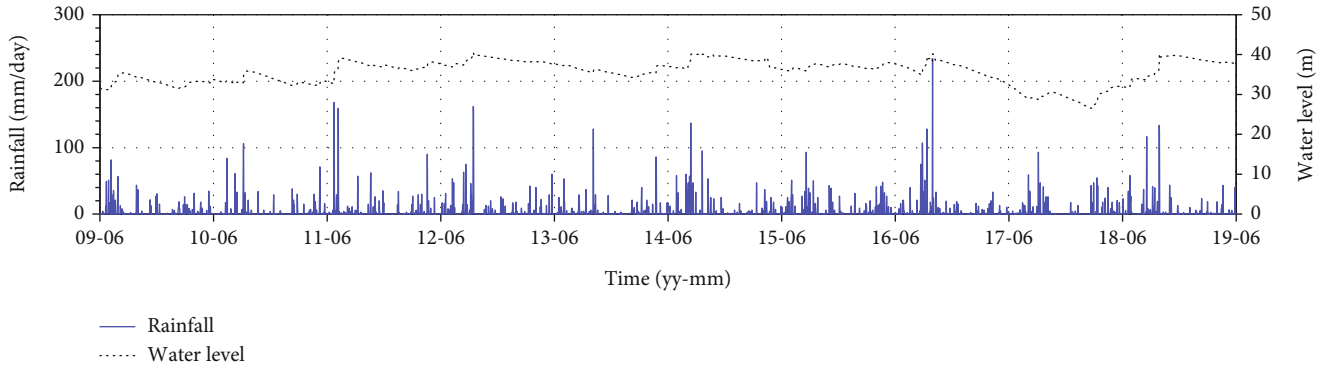

Figure 4: Water level and daily rainfall.

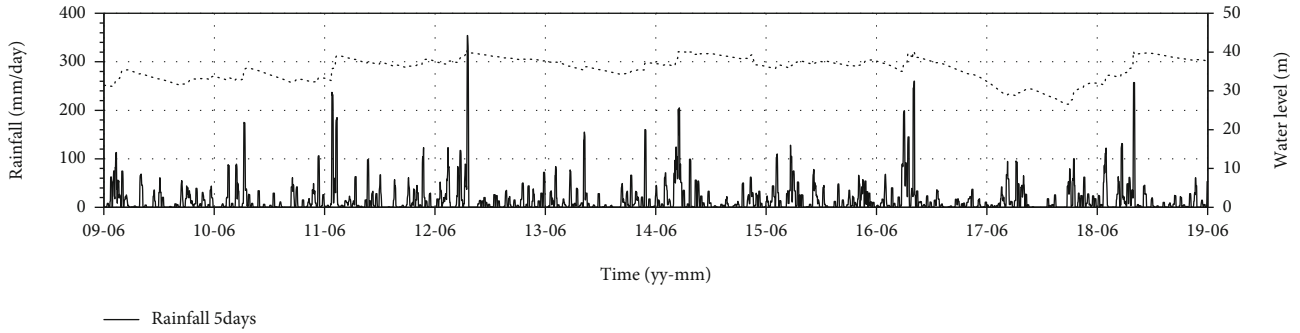

Figure 5: Water level and antecedent 5-day rainfall.

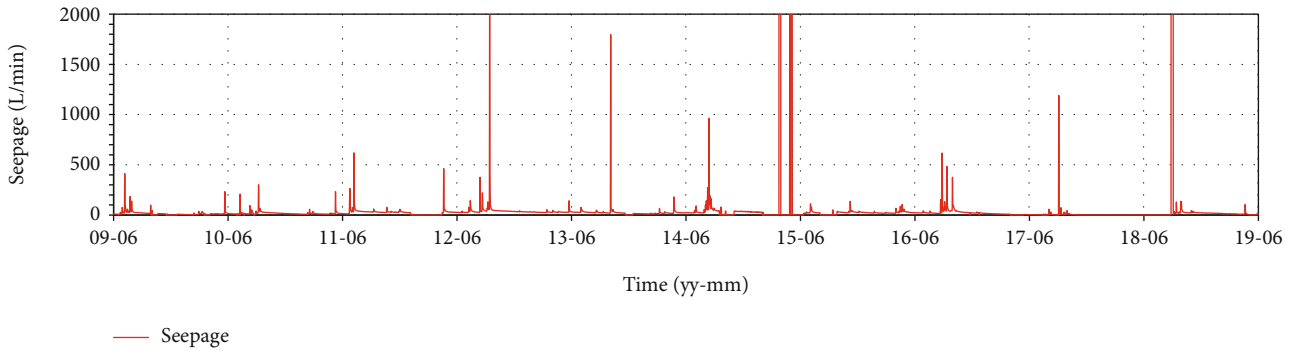

Figure 6: Seepage data.

dam increases rapidly when rainfall occurs as the direct inflow of rainfall from the downstream slope and the left and right sides occurs. As shown in Figure 6, potential upper bound outliers are distributed throughout the data, and seepage quantities above 1000 L/min may be measured during rainfall.

3.3. Removal of Outliers of Seepage. Statistical analysis of seepage shows an extreme asymmetric distribution with an average observed value of 178.74 L/min, a median of 18.4 L/min, and a standard deviation of 2,950 L/min. In the case of seepage water meters, it is deemed impossible to remove outliers effectively by searching for outliers based on univariate such as z-score, since they are measured in one place. Therefore, in this study, a data analysis-based outlier removal method using rainfall and water level data is applied for quantitative analysis of seepage data. The maximum capacity of the V-notch measuring seepage is applied by the Kindsvater-Shen equation presented by the International Organization for Standardization ISO [13], and the calculated maximum possible observation was found to be approximately 1,500 L/min [16]. As illustrated in Figure 7(a), it can be seen that seepage data exceeding the maximum possible observations are distributed throughout the time series data. In addition, Figures 7(b)–7(d), which illustrate the relationship between seepage, rainfall, and water level, show that no extreme values

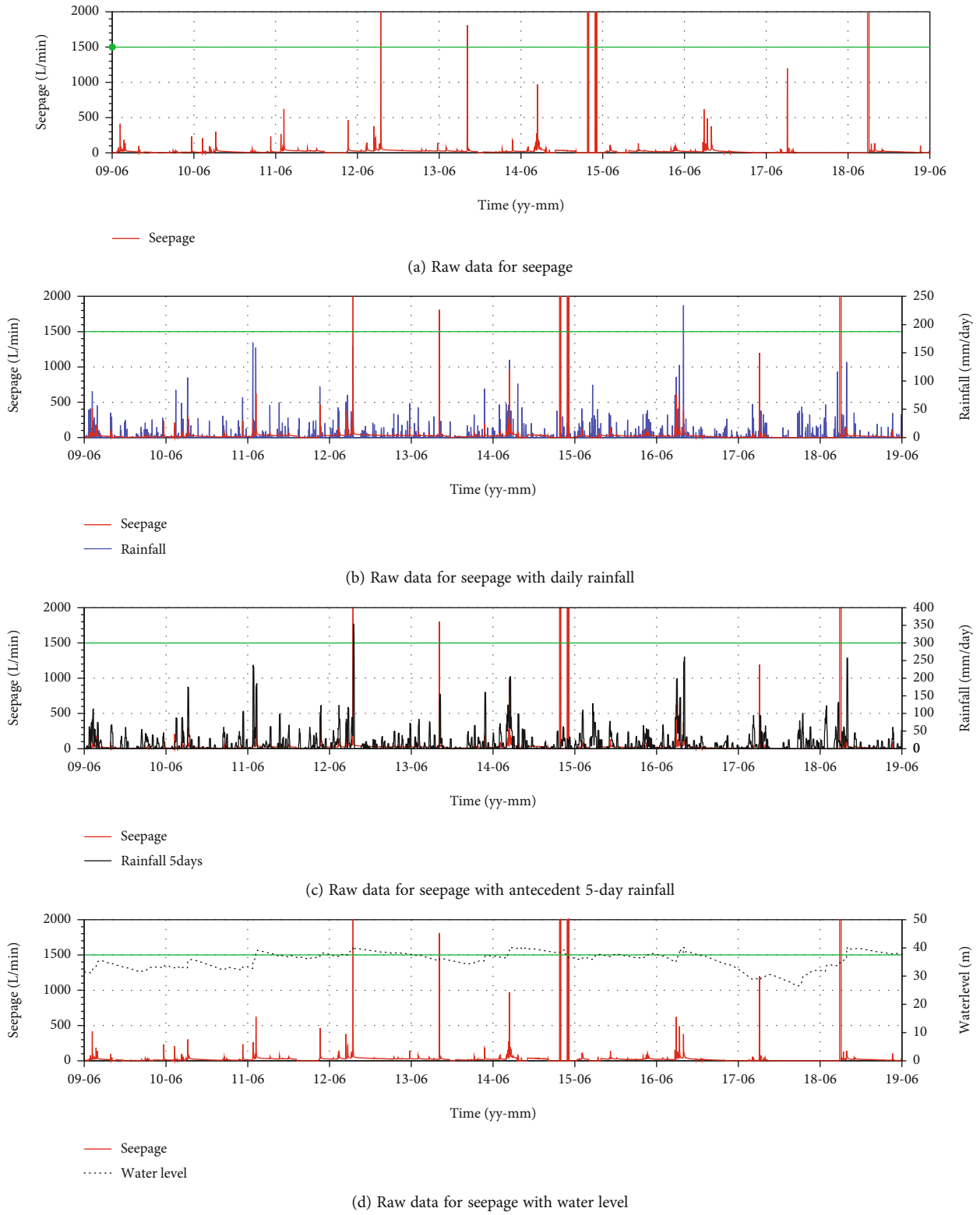

(a) Raw data for seepage

(b) Raw data for seepage with daily rainfall

(c) Raw data for seepage with antecedent 5-day rainfall

(d) Raw data for seepage with water level

Figure 7: Comparisons among seepage, rainfall, and water level.

of rainfall and water level occur when the maximum possible observations of seepage are exceeded. Therefore, considering the relationship between the maximum possible observations of seepage, rainfall, and water level, observations exceeding 1,500 L/min were judged as simple outliers and eliminated.

The seepage data contains approximately 22% (missing rate) of observations recorded as "0(zero)" indicating the missing. It was compared to rainfall and water level data to distinguish whether the observation was missing or actual. Figure 8(a) below illustrates the relationship between the

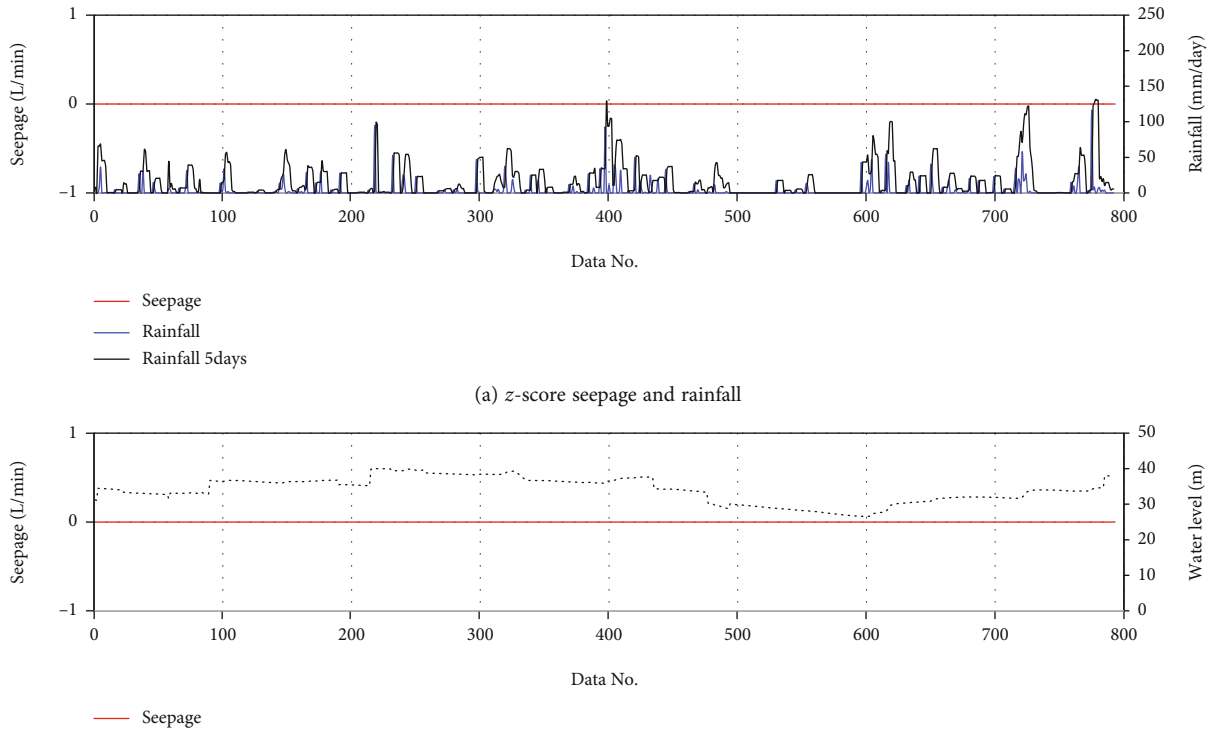

(a) z-score seepage and rainfall

(b) z-score seepage and water level

Figure 8: Time histories for no data.

time recorded as "0," and Figure 8(b) illustrates the relationship with the water level. The observation was eliminated by considering that the actual rainfall occurred when the seepage was recorded as "0(zero)" in Figure 8, and that the change in the water level was distributed above and below the average.

Figure 9 compares the seepage-rainfall and seepage-water level after removing the measurement of seepage water measurements determined to be outliers. In Figures 9(a) and 9(b), which illustrate the seepage and rainfall, the seepage is shown to increase when the rainfall increases significantly. In Figure 9(c), which illustrates the relationship between seepage and water level, it can be seen that seepage increases and decreases with changes in water level as well as rainfall. In other words, the seepage of the dam subject to research is shown to be sensitive to rainfall and water level as response variables.

3.4. Removal of Outliers of Seepage. To closely analyze the effects of rainfall on seepage, the data to be analyzed were classified into two groups consisting of a rainfall-free group (group A) and a rainfall-occurring group (group B). In the case of rainfall, the daily rainfall and antecedent 5-day rainfall in net unit were generated and applied in consideration of the hydrologic response time of the dam basin. The detailed AMC conditions according to the antecedent 5-day rainfall are as shown in Table 2 below [15].

Figures 10 and 11 show the classification into rainfall-occurring group and rainfall-free group, respectively, after removing the seepage outliers and missing values from the raw data. Of 2854 data excluding 792 missing data and 15 outliers from total measured data of 3,662 data (June 1st, 2009~June 10th, 2019), group A, a rainfall-free group, has 2133 data, while group B, a rainfall-occurring group, has 721 data.

4. Decision Tree Analysis

4.1. Purpose and Process of Decision Tree Analysis. Decision tree analysis is more applicable because it is easy to understand the classification structure of the data and can explain the reasons for the decision, unlike the Neural Network Analysis which is a similar type. Algorithms for tree structure formation in decision tree analysis are currently being developed in various ways. Decision trees start from the roots and are formed by dividing the segmented joints until each branch becomes the end joint. Like this, in order to complete the decision tree, several steps must be performed on the selection of a splitting rule, the selection of a stopping rule to stop the splits, the selection of a pruning method, and, if there is a defect within the input variable value, imputation method [16]. Mainly known algorithms include CART (Classification and Regression Trees), CHAID (Chi-squared Automatic Interaction Detection), C5.0 [17], and C4.5 [18], and this study conducted the seepage analysis using the most commonly used CART algorithm [19].

The CART algorithm is a methodology for generating multiple subset trees of the data and finding the optimal subset tree among them. The CART algorithm is applicable to nominal, ordinal, and continuous variables and is

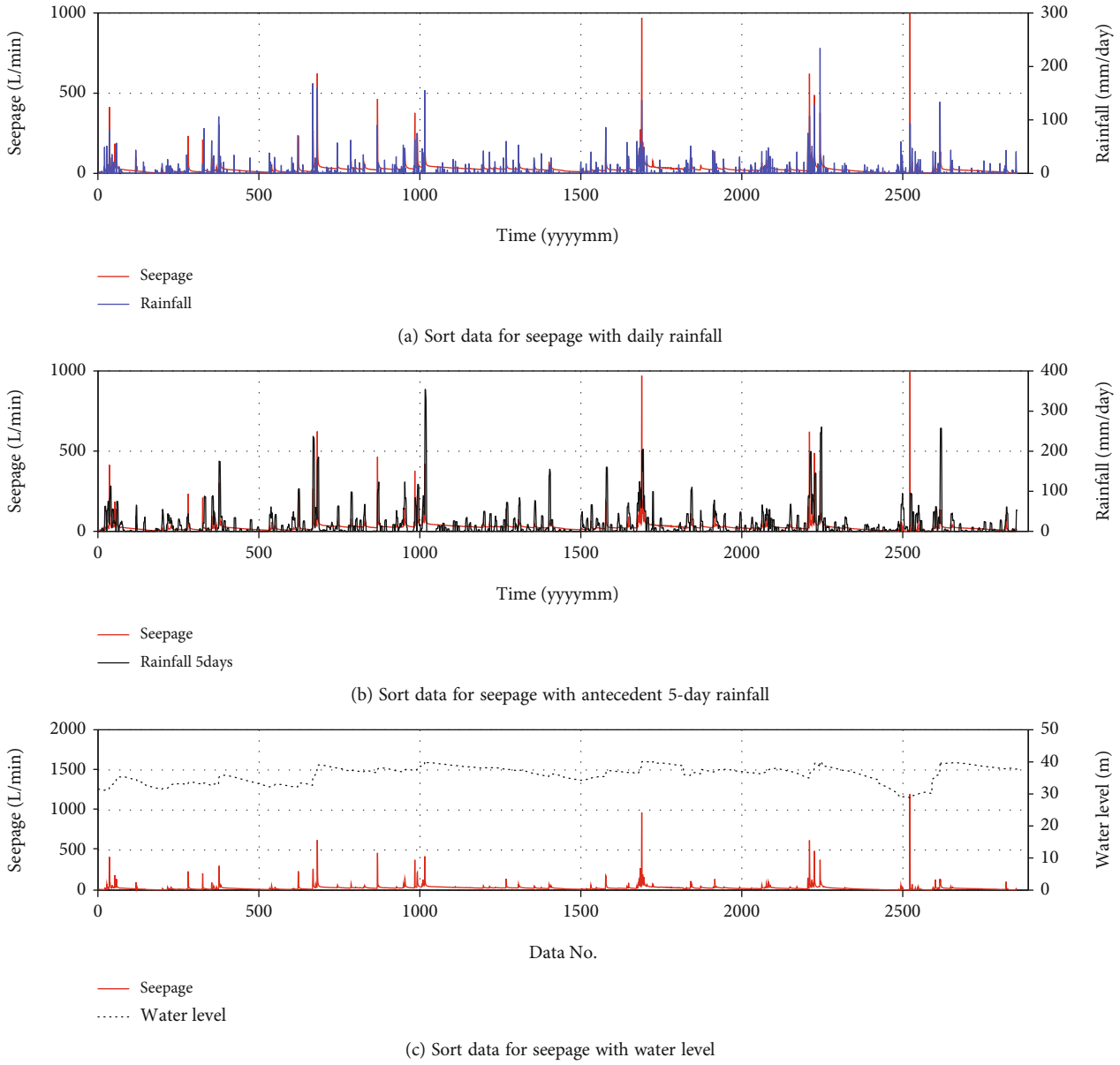

(a) Sort data for seepage with daily rainfall

(b) Sort data for seepage with antecedent 5-day rainfall

(c) Sort data for seepage with water level

Figure 9: Relationship after removal of outliers and missing data.

Table 2: AMC conditions according to antecedent 5-day rainfall [15].

AMC condition	Antecedent 5-day rainfall P_5 (mm)	
	Dormant season	Growing season
I	$P_5 < 12.70$	$P_5 < 35.56$
II	$12.70 < P_5 < 27.94$	$35.56 < P_5 < 53.34$
III	$P_5 > 27.94$	$P_5 > 53.34$

characterized by structuring the model's composition according to the conditions of explanatory variables in the order of root nodes, child nodes, and branches, as shown in Figure 12. The root node has the most influential variable among the explanatory variables describing the change in the response variable, and it constructs a binary branch according to the conditions of the corresponding variable. The branch node includes the first explanatory variable or other explanatory variables, and the leaf node is the final-stage node divaricated from the root and each joint, with one leaf node representing clusters according to classified rules. Then, the regression equations estimated from classified cluster units are aggregated to produce a model that can predict the behavior of the response variable.

In particular, the CART algorithm can be proposed as an alternative to regression analysis for the cases such as the presence of interactions of independent variables or the presence of multicollinearity problems. In the CART algorithm, a separation criterion is a criterion for determining the choice of explanatory variables and the merging of

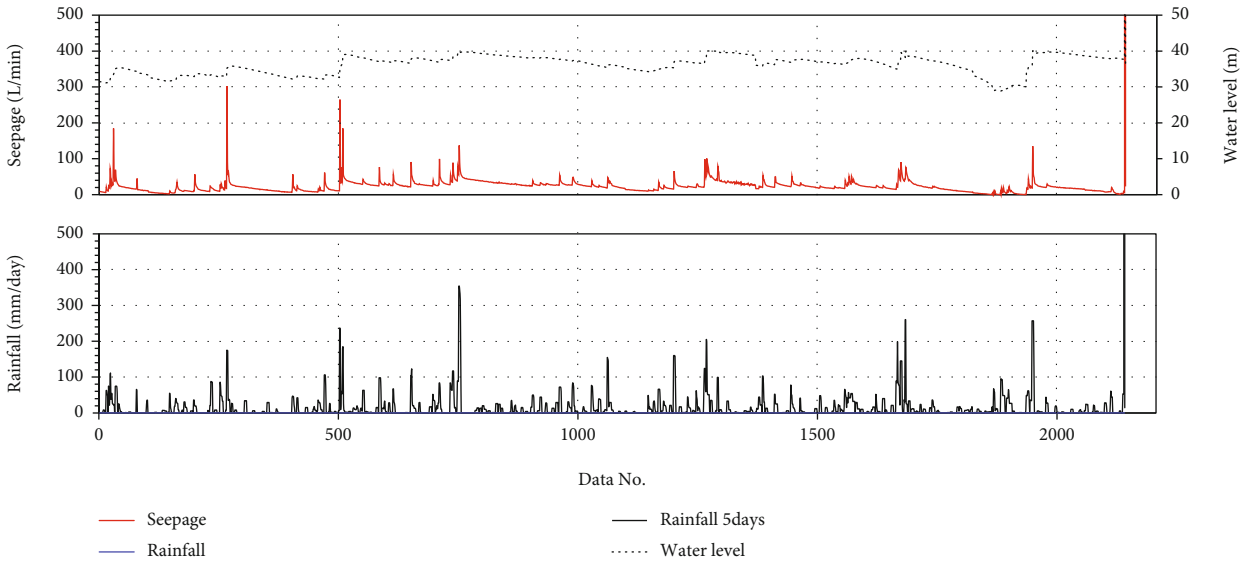

Figure 10: Seepage, rainfall, and water level for group A.

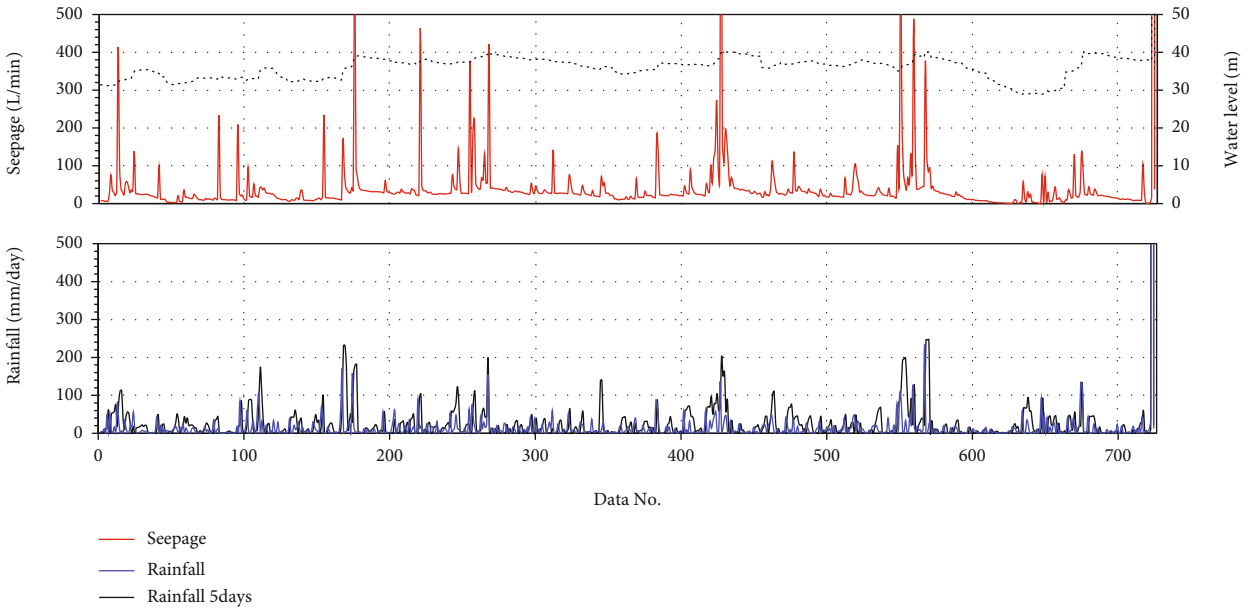

Figure 11: Seepage, rainfall, and water level for group B.

categories when child nodes are formed from parent nodes. Therefore, quantifying the separation criteria requires quantification of explanatory variable selection and separation conditions that best distinguish the distribution of the response variables. For discrete data, the separation occurs based on the frequency of each category of response variables, while the separation of joints occurs based on the mean and standard deviation of the target variables for continuous data [20]. Detailed separation criteria and conditions for each data type are summarized in Table 3.

In this paper, Matlab R2020a was utilized as a tool for decision tree analysis, and the variance reduction was applied as a separation criterion as the target data is continuous. Variable reduction, $R(t)$, is defined as shown in equation (1) for each separation node for the data set of N -explanatory variable $x_1 = (x_1 \cdots x_d)$ and response variable $y_1 = (y_1 \cdots y_n)$.

$$R(t) = \frac{1}{n} \sum_{y_i, x_i \in_t} (y_i - \bar{y}(t))^2, \tag{1}$$

Here, $\bar{y} = 1/n(t) \sum_{y_i, x_i \in_t} y_i$.

When the set of all possible branch conditions in each separation step is called S, and each branch condition is

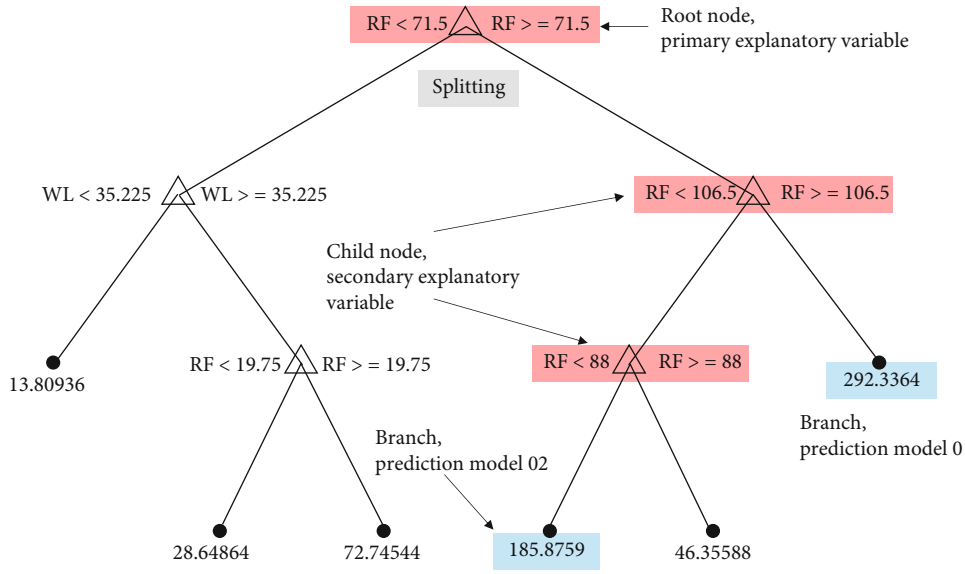

Figure 12: CART algorithm.

Table 3: Splitting rules for decision trees.

Categories	Splitting rules	Splitting conditions
Discrete distribution	p value for χ^2	Under the condition that p value is minimized
	Gini index	Under the conditions that most reduce the Gini index
	Entropy index	Under conditions that reduce the most entropy index
Continuous distribution	p value for F	Under conditions where p value is minimized
	Decrements of variance	Under conditions that maximize the amount of variance reduction

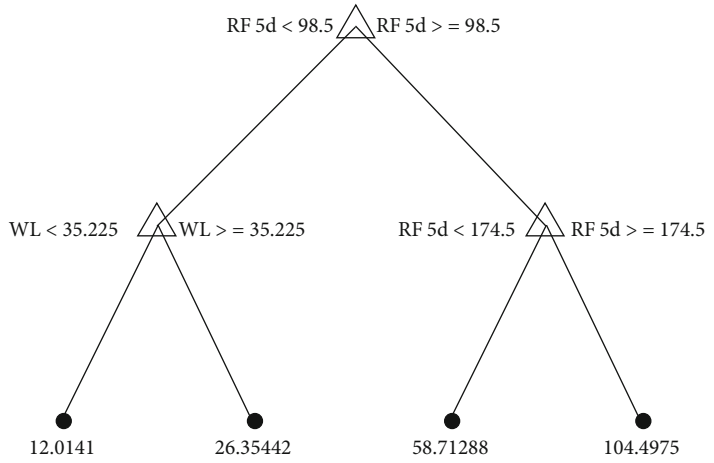

Figure 13: Decision tree for group A (seepage, antecedent 5-day rainfall, and water level).

called s, the optimal branch condition is s^*as shown in the following equation.

$$\Delta R(s,t) = R(t) - R(t_L) - R(t_R),$$
$$\Delta R(s^*,t) = \max \Delta R(s,t)\,; s \in S. \tag{2}$$

Here, $R(t_L)$ and $R(t_R)$ are the variance reduction of the left/right branches in each joint.

The predictor importance (PI) of the explanatory variables can be calculated by equation (3) through the explanatory variable (x_i) selected from the optimal branch condition of each joint, s^*, and variance reduction, $\Delta R(s^*,t)_{x_i}$. The

Table 4: Results of decision tress analysis for group A.

Primary explanatory variable	Second explanatory variable	Response variable	
Antecedent 5-day rainfall (RF_5 d, mm/day)	Water level (WL, m)	Seepage (LQ, L/min)	
		Mean	Subset *n*
RF_5 d ≥ 174.5		104.5	18 (0.8%)
98.5 ≤ RF_5 d < 174.5		58.72	32 (1.5%)
RF_5 d < 98.5		21.8	2,083 (97.7%)
	WL ≥ 35.23	26.35	1,421 (66.6%)
	WL < 35.23	12.01	662 (31.0%)

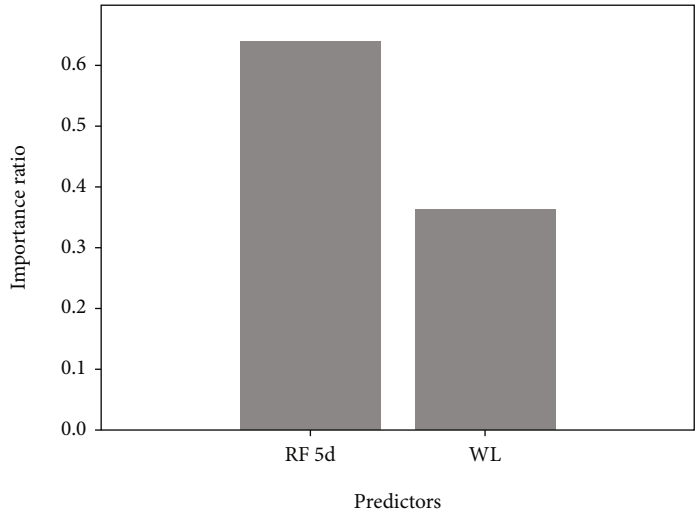

Figure 14: Predictor importance estimates for group A.

explanatory variable with larger PI means better explanation for the response variable.

$$\mathrm{PI}_{x_i} = \frac{1}{N_t}\left(\Delta R(s^*, t)_{x_i}\right). \quad (3)$$

4.2. Decision Tree Analysis of Seepage of Seepage. The analytical tree model is organized in the order of root (the primary explanatory variable), branch (other explanatory variables) division, and leaf (classification group/predictive model), which facilitates the analysis of multivariate factors with interactions. Therefore, an analytical tree analysis using the CART algorithm to analyze the effects of rainfall and water level on the causes of changes in seepage was conducted.

Figure 13 and Table 4 are the results of decision tree analysis of group A, representing the analytical tree results of the rainfall-free group performed by setting the seepage (LQ) as a response variable and antecedent 5-day rainfall (RF 5 d) and water level (WL) as explanatory variables. Figure 14 shows the dimensionless variable importance PI for the antecedent 5-day rainfall and water level applied as explanatory variables. Here, dimensionless PI presents the size of PI of each explanatory variable as a ratio to the total PI. As the explanatory variable antecedent 5-day rainfall was 0.64 and water level was 0.36, the antecedent 5-day rainfall

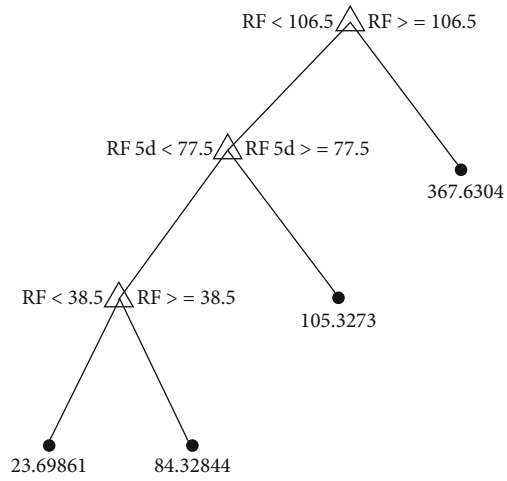

Figure 15: Decision tree for group B (seepage, rainfall, antecedent 5-day rainfall, and water level).

was selected as the primary explanatory variable. The statistics of the seepage group were calculated according to classified conditions to analyze the changes in seepage according to changes in rainfall and water level. As summarized in Table 4, the branch conditions of the antecedent 5-day

Table 5: Results of decision tress analysis for group B.

Primary explanatory variable	Second explanatory variable	Response variable Seepage (LQ, L/min)	
Rainfall (RF, mm/day)	Antecedent 5-day rainfall (RF_5 d, mm/day)	Mean	Subset *n*
RF ≥ 106.5		367.63	9 (1.2%)
	RF_5 d ≥ 77.5	105.33	48 (6.6%)
	RF_5 d < 77.5	27.9	664 (92.1%)
RF > 38.5		84.33	46 (6.4%)
RF < 38.5		23.7	618 (85.7%)

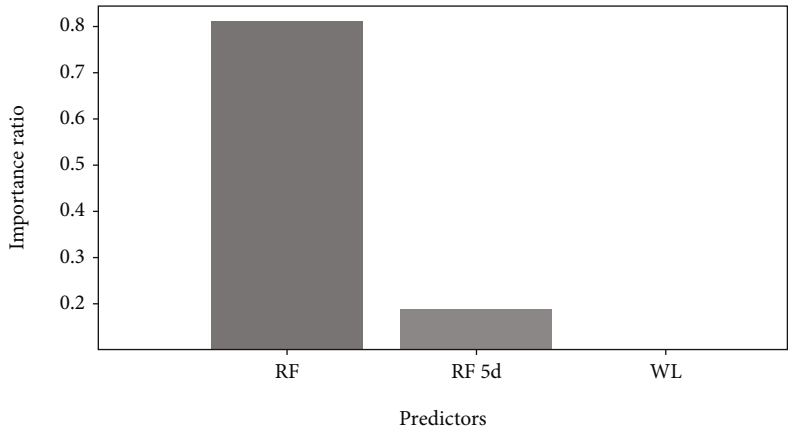

Figure 16: Predictor importance estimates for group B.

rainfall selected as the primary variable were 98.5 mm/day and 174.5 mm/day, with the water level acting as the explanatory variable under the conditions of antecedent 5-day rainfall below 98.5 mm/day. The branch condition of the water level was analyzed to be 35.23 m. In particular, 97.7% of the water leakage data are distributed under conditions of antecedent 5-day rainfall below 98.5 mm/day, with the average value of the group being 12.01 L/min~26.35 L/min, which is significantly lower than the average value of the relative group (58.72 L/min to 104.50 L/min). Therefore, it is determined that the antecedent 5-day rainfall can be considered as a major influence factor on the leakage at the point of no rainfall, and antecedent 5-day rainfall of 98.5 mm/day can be presented as the allowable seepage value for the increase in the amount of water leakage.

Figure 15 and Table 5 are the results of decision tree analysis of group B, representing the analytical tree results of the rainfall-occurring group performed by setting the seepage (LQ) as a response variable and antecedent 5-day rainfall (RF 5 d) and water level (WL) as explanatory variables. Figure 16 shows the dimensionless PI. As the explanatory variable daily rainfall (RF) was 0.81, the antecedent 5-day rainfall (RF 5 d) was 0.19, the water level (WL) was 0.00, and daily rainfall was selected as the primary explanatory variable. Group B, a rainfall-occurring group, was analyzed to have no effect of water level as an explanatory variable. To analyze the changes in seepage, the statistics of the seepage group were calculated according to the classified conditions. As summarized in Table 5, the branch conditions of daily rainfall selected as the first variable were 106.5 mm/day and 38.5 mm/day, while the antecedent 5-day rainfall only worked as an explanatory variable in the range of 38.5 mm/day to 106.5 mm/day. In other words, the effect of antecedent 5-day rainfall on the amount of leakage is determined to be significant only at the time of occurrence of daily rainfall bigger than medium-size. In addition, in group B, 85.7% of the water leakage data are distributed under the conditions of daily rainfall below 38.5 mm/day, and the average value of the group was 23.70 L/min, which is significantly lower than the average value of the relative group (84.33 L/min~367.63 L/min). Therefore, it is determined that the daily rainfall (RF) can be considered as a major influence factor on the amount of water leakage at the time of rainfall, and that the daily rainfall of 38.5 mm/day can be presented as the allowable seepage value for the increase in the amount of water leakage.

5. Conclusions

In this study, the following results were obtained by classifying the group into two groups consisting of a rainfall-free group and a rainfall-occurring group to conduct decision tree analysis considering the effects of dam water level, daily rainfall, and antecedent 5-day rainfall on the seepage, which is the primary measured item for prediction of leakage of fill dam and piping..

As a result of the decision-making tree analysis on rainfall-free group (group A), there were the most data (66.6%) with the antecedent 5-day rainfall, selected as the primary explanatory variable, of less than 98.5 mm/day and water level higher than EL.35.225 m, and the average seepage at this time was 26.35 L/min.

As a result of the decision-making tree analysis on rainfall-occurring group (group B), the branch conditions of the daily rainfall, selected as the primary explanatory variable, were 106.5 mm/day and 38.5 mm/day. In addition, it was analyzed that the change in seepage during rainfall is not related to the water level. 85.75% of seepage data was distributed under the conditions with the antecedent 5-day rainfall, the primary explanatory variable, of less than 77.5 mm/day and daily rainfall less than 38.5 mm/day, and the average seepage at this time was 23.70 L/min. Also, when daily rainfall was more than 38.5 mm/day under the same conditions, the average seepage was 84.33 L/min.

Therefore, the seepage of the dam subject to research was found to be more directly affected by rainfall than by water level. Rather than presenting a single value as the acceptable seepage of the fill dam, the acceptable seepage according to the explanatory variables determined by the decision tree analysis can be presented, respectively.

Data Availability

The data set used in this study is available through Water Energy & Infrastructure Research Center, K-water (http://www.kwater.or.kr/kiwe/main.do).

Conflicts of Interest

The authors declare no conflict of interest.

Acknowledgments

This research was supported by the Basic Science Research Program through the National Research Foundation of Korea (NRF) funded by the Ministry of Education (No. 2020R1I1A3067248).

References

[1] K-Water, *A Study on the Combined Analysis Method of Measurement Data for Dam Safety and Maintenance(2)*, (K-Water)16, 2019.

[2] korean geotechnical society, "Design, Construction and Safety Management for the Dam and Embankment," in *Goomi book*, KGS, 2010.

[3] H. K. Park and D. H. Shin, *Safety management of dams*, CIR, 2013.

[4] J. Lee, S. Yoon, E.-S. Im, and G. Kang, "A study on management criteria of seepage for fill dams considering rainfall effect," *Journal of the Korean Geotechnical Society*, vol. 36, no. 5, pp. 5–16, 2020.

[5] United States Cold Storage, *Lessons of Dam Incidents*, USCOLD, USA, 1975.

[6] B. D. Noh, *A study 314 on road slope safety investigation plan for disaster prevention*, 7th Seminar for Disaster Prevention Administration, 2002.

[7] S. Kuperman, M. Moretti, J. Pinfari, and E. Carneiro, "Placing limit values on instrument readings," *Hydro Review*, vol. 15, no. 3, pp. 24–31, 2007.

[8] J. Lee, "Application of statistical method for establishment of alert level for dam instrumentation," *Journal of the Korean Geotechnical Society, KSCE*, vol. 36, no. 5, pp. 283-284, 2014.

[9] P. T. Ryan, *Statistical Methods for Quality Improvement*, John Wiley and Sons, second edition, 2000.

[10] L. S. Lewis, C. D. Montgomery, and H. R. Myers, "Examples of designed experiments with nonnormal responses," *Journal of Quality Technology*, vol. 33, no. 3, pp. 265–278, 2001.

[11] R. Myers and D. Montgomery, *Response Surface Methodology: Product and Process Op-Timization Using Designed Experiments*, John Wiley & Sons, second edition edition, 2002.

[12] S. Park and H. Park, "A control chart method using quartiles for asymmetric distributed processes," *Journal of the Korean Statistical Society*, vol. 19, no. 1, pp. 81–96, 2006.

[13] International Organization for Standardization, *Water Flow Measurement in Open Channels Using Weirs and Venturi Flumes- Part1: Thin-Plate Weirs*, ISO, 1998.

[14] C. Jang and J. Lee, "Development of national standard technology and status of v-notch for measuring seepage of dam in Korean, water for future," *The KoreaWater Resources Association*, vol. 51, no. 5, pp. 57–63, 2018.

[15] Soil Conservation Service, *National Engineering Handbook, Section 4, Hydrology*, SCS, 1972.

[16] K-water, *(Field investigations and improvement plansfor for existing seepage instruments of 25 dams in Korea)*, (K-Water), 2017.

[17] Z. Guo, Y. Shi, F. Huang, X. Fan, and J. Huang, "Landslide susceptibility zonation method based on C5.0 decision tree and K-means cluster algorithms to improve the efficiency of risk management," *Geoscience Frontiers*, vol. 12, no. 6, article 101249, 2021.

[18] N. S. Park, Y. Lee, S. Chae, and S. Yoon, "A study on the statistical predictability of drinking water qualities for contamination warning system," *Journal of Korean Society of Water and Wastewater*, vol. 29, no. 4, pp. 469–479, 2015.

[19] L. Breiman, J. Friedman, C. J. Stone, and R. A. Olshen, *Classification and Egression Trees*, Taylor & Francis, 1984.

[20] H. Kang, S. Han, J. Choi, E. Kim, and I. Um, *Data Mining Methodology for Big Data Analysis*, Free Academy, 2014.

Hindawi
Geofluids
Volume 2022, Article ID 6006383, 17 pages
https://doi.org/10.1155/2022/6006383

Research Article

Numerical Research of Lightweight Foam Concrete Replacement Method of Deep Soft Foundation Treatment of Low-Filled Embankment

Fanfan Li,[1] **Zhifeng Zhang**,[1] **Xing Chen**,[1] **Zecheng Chi**,[2] **Jianbin Li**,[3] **and Wei Wang**[4]

[1]*Research and Development Center on Technology and Equipment for Energy Conservation and Environmental Protection of Highway Transport, Anhui Transport Consulting & Design Institute Co., Ltd, Hefei 230088, China*
[2]*Faculty of Engineering, China University of Geosciences, Wuhan 430074, China*
[3]*School of Civil Engineering, Guangzhou University, Guangzhou 510006, China*
[4]*Guangdong Research Institute of Water Resources and Hydropower, Guangzhou 510610, China*

Correspondence should be addressed to Zecheng Chi; chizecheng@cug.edu.cn

Received 7 March 2022; Accepted 19 May 2022; Published 13 June 2022

Academic Editor: Zizheng Guo

A new method of replacing soft soil with lightweight foam concrete (lightweight foam concrete replacement method, LFCRM) is carried out to treat deep soft foundation under the low-filled embankment. Two-dimensional models with different thicknesses of replacement are established by the finite element platform (MIDAS/GTS). Moreover, the deformation and stress distribution law of treated foundation is analyzed by numerical simulation with different models. The results are as follows: (1) LFCRM can offset part of dead load; (2) the transverse distribution of settlement presents an "arc" shape; (3) the replacement made of lightweight foam concrete can spread stress well; (4) increase of replacement thickness will cause the necking of the additional stress "bubble"; (5) initial excess pore water pressure is related to the additional stress, and its dissipation path is deduced; (6) preliminary analysis indicates the feasibility of LFCRM for treating deep soft foundation with the low-filled embankment.

1. Introduction

Soft foundation failure is one of the most common geotechnical problems [1–3]. Deep soft soil is widely distributed in the plains of China [4], and low-filled embankment is a common form of road construction in this region because of the conservation of land resources [5]. Conventionally, a deep soft foundation in road engineering can be treated by the composite foundation, rigid pile, and drainage consolidation method [6–8]. Related specifications suggest that the treating depth of the above methods should be greater than that of soft soil [9], which is, however, not economical for the low-filled embankment.

Improvements have been made on existing methods to improve economic benefits in treating deep soft foundation under the low-filled embankment, such as composite foundation by partial penetration of columns [10–12], silt extrusion by riprap dumping [13], and shallow drainage consolidation method [14–16].

Methods for deep soft foundation treatment with low-filled embankment are far more than above [17–19]. Interestingly, these methods share similar basic mechanisms: (1) changing the physical properties (increasing elasticity modulus) of the top layer of soft soil (area with the largest additional stress) by physical, chemical, or biological method [20, 21] to reduce the

deformation of top layer and (2) turning the foundation to the double-layered structure (the upper layer is harder than the lower layer) and accordingly changing the distribution of additional stress (a harder layer can effectively spread the upper load [22]).

In this paper, treating deep soft foundation with low-filled embankment is considered by replacing soft soil with lightweight foam concrete (lightweight foam concrete replacement method, LFCRM). Except for the above advantages, this method can also offset part of dead load by the density difference between the two materials.

Tam et al. [23] studied the physical property of foam concrete with different densities (1300-2250 kg/m^3) and concluded that the strength of moist-cured foam concrete depends on both water/cement ratio and air/cement ratio. Nambiar and Ramamurthy [24] measured the water absorption of foam concrete by complete immersion for various mixes with different fly ash replacement levels for sand and different foam volume. It was found that sorption values are lower than the corresponding base mix (without foam) and reduce with the increase in foam volume. Bing et al. [25] represented that foam concretes with a density of 800-1500 kg/m^3 and compressive strength of 10-50 MPa (28 days) can be made using silica fume, fly ash, and polypropylene fiber. Ranjani and Ramamurthy [26] examined the behavior of foam concrete produced with two synthetic surfactants under sodium and magnesium sulfate environment. They indicated that the expansion of foam concrete exposed to sodium sulfate is 28% higher than that exposed to magnesium sulfate environment, which can be attributed to the greater quantum of ettringite formed in sodium sulfate environment. Wan et al. [27] studied the full field drying shrinkage distributions of foam concrete by the expanded digital volume correlation method with a high precision of 0.01 voxel (about 0.6 μm) in displacement.

Zhang and Yang [28] focused on foam concrete aircraft arresting system, which provides an economical and nondestructive means for decelerating aircraft that overshoot runway, and also conducted a full-scale test to demonstrate the effectiveness of the system. Tan et al. [29] put forward a composite support system containing foam concrete damping layer in view of the large deformation in soft rock roadway, and related application has been carried out successfully. She et al. [30] implemented continuous field testing of settlement, lateral displacement, and soil pressure in the Hangzhou East Railway Station Project and identified the excellent loading and differential settlement reduction of foam concrete as a filling material. Cai et al. [31] studied the dynamic characteristics of lightweight foam concrete with different wet densities and water-bearing states under train loading. Huang et al. [32] established a large-scale model of a subgrade filled with lightweight foam concrete with target density of 650 kg/m^3 to determine its long-term performance under cyclic dynamic loads. The results show that the strength of lightweight foam concrete with target density of 500-800 kg/m^3 can meet the requirements of both the static and dynamic conditions of ballastless track subgrade, and the ballastless track subgrade filled by lightweight foam concrete with target density of 650 kg/m^3 has a good long-term dynamic stability under cyclic dynamic loads when a dynamic buffer layer with thickness of 0.5 m is set between lightweight foam concrete layer and foundation slab. Klomranok and Su [33] conducted numerical simulations based on basic physics experiments and claimed that the presence of foam concrete in high-speed railways could reduce the dynamic response that occurs more efficiently than the traditional track structure.

There has been a great deal of research on the properties and applications of foam concrete [31, 34–36], but few of them mention LFCRM directly. This paper sheds light on the LFCRM and explores the influence of the thickness of replacement on the deformation and stress distribution of reinforced foundation (treated by LFCRM) by numerical simulation. Finally, the feasibility of LFCRM is preliminarily identified based on the results of numerical simulation and the Chinese technical specification [9, 37].

This paper is organized as follows. Section 2 introduces a newly built expressway project and describes the design and mechanism of this project. In Section 3, the numerical simulation method and two-dimensional models are constructed by finite element platform. Sections 4 and 5 analyze the deformation and stress simulation results and discuss the preliminary feasibility of LFCRM. Conclusions are summarized in Section 6.

2. Project Profile

2.1. Background. Soft soil is exposed on the ground surface in one section of a newly built expressway project, reaching a maximum depth of 21.6 m. Below it lies the strongly weathered argillaceous sandstone. The longitudinal section of geology in this section is shown in Figure 1, and the recommended geological parameters are shown in Table 1.

2.2. Design and Mechanism. In this project, the soft foundation treatment by LFCRM is considered. As shown in Figure 2, the design and mechanism are described as follows:

2.2.1. Design. The thickness of replacement is 1.5-3.0 m; the width of replacement is equal to the bottom width of the embankment; the physical parameters are shown in Table 1.

2.2.2. Mechanisms. (1) The weight difference between soft soil and lightweight foam concrete can offset part of the dead load; (2) lightweight foam concrete has a larger elasticity modulus than soft soil, reducing the deformation of the area of replacement; (3) replacing soft soil with lightweight foam concrete to form a double-layer structure (upper layer is harder than the lower) can spread the upper load effectively.

3. Numerical Simulation Method and Models

MIDAS/GTS is a software program for the stress-strain analysis and design in the construction phase of geotechnical structures [38–42]. In this study, MIDAS/GTS was used for simulation analysis, and the geotechnical parameters and material properties used in the simulation were provided from the design file of the expressway project, so that the simulation results can reflect the characteristics of the treated foundation and better guide the design.

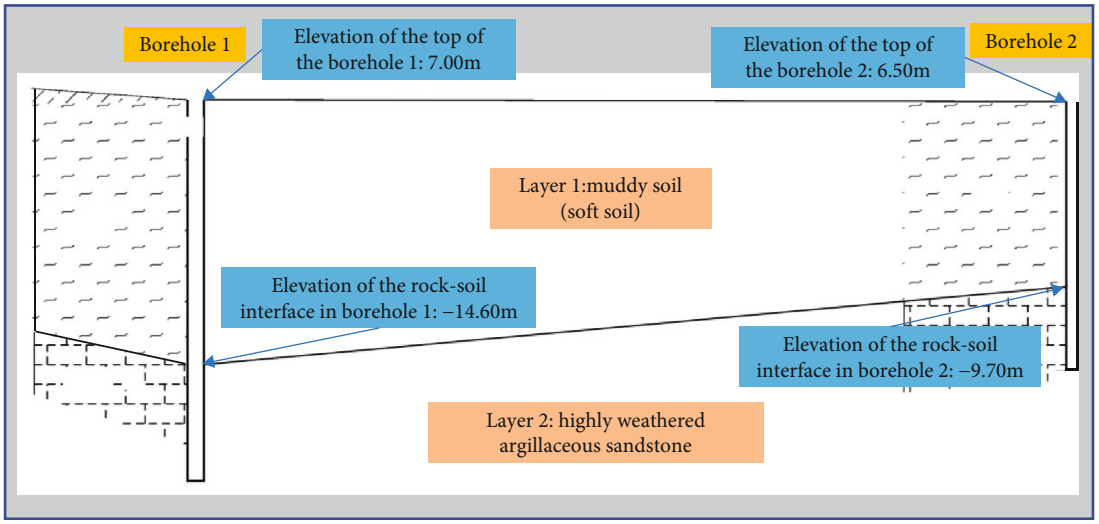

Figure 1: Longitudinal section of engineering geology.

Table 1: Parameter values of various materials.

Material	Elasticity modulus/MPa	Poisson ratio	Volume weight/ kN·m^{-3}	Permeability coefficient/m·s^{-1}	Cohesive force/kPa	Friction angle/°
Lightweight foam concrete	250	0.20	8.00	1.0×10^{-4}	120	4
Embankment	50	0.25	20.00	/	15	25
Soft soil	15	0.38	19.22	1.20×10^{-7}	12	10
Strongly weathered argillaceous sandstone	500	0.25	23.00	9.51×10^{-8}	32	30

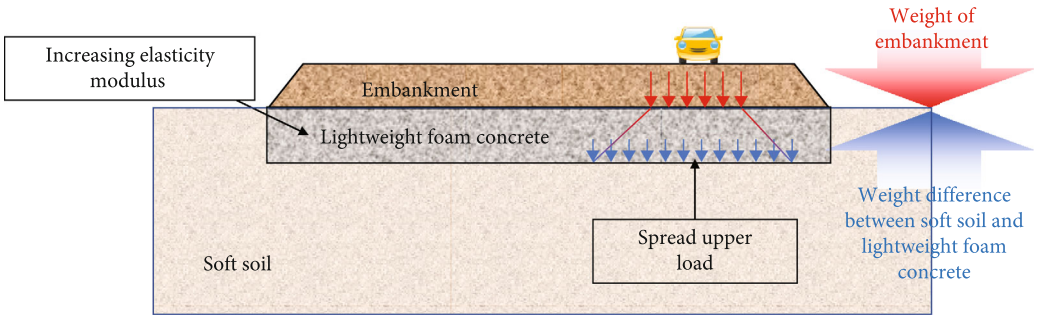

Figure 2: Scheme of the lightweight foam concrete replacement method.

3.1. Basic Theory of MIDAS/GTS

3.1.1. Finite Element Governing Equation. Based on the Hellinger-Reissner variational principle [43], the virtual work equation is obtained:

$$\delta G_{\text{ext}} = \int_{\Omega} (\nabla \delta \mathbf{u})^T \boldsymbol{\sigma} + \delta \boldsymbol{\sigma}^T (\nabla \mathbf{u} - \boldsymbol{\varepsilon}(\boldsymbol{\sigma})) d\Omega, \quad (1)$$

where G_{ext} is the virtual work generated by the external force; ∇ is the strain-displacement relational operator; $\mathbf{u}$ is the displacement; $\boldsymbol{\sigma}$ is the stress; $\boldsymbol{\varepsilon}$ is the strain; Ω is the integral area; and $\boldsymbol{\varepsilon}(\boldsymbol{\sigma})$ is the strain derived from stress.

If elements satisfy the compatibility equation of deformation, the following equation can be obtained from Equation (1):

$$\delta G_{\text{ext}} = \int_{\Omega} (\nabla \delta \mathbf{u})^T \boldsymbol{\sigma}(\mathbf{u}) d\Omega. \quad (2)$$

Equation (2) may be expressed as follows by utilizing the displacement-strain relationship:

$$\delta G_{\text{ext}} = \delta \mathbf{d}^{eT} \left[\sum \int_{\Omega} (\nabla \mathbf{N})^T \mathbf{D} (\nabla \mathbf{N}) d\Omega \right] \mathbf{d}^e, \quad (3)$$

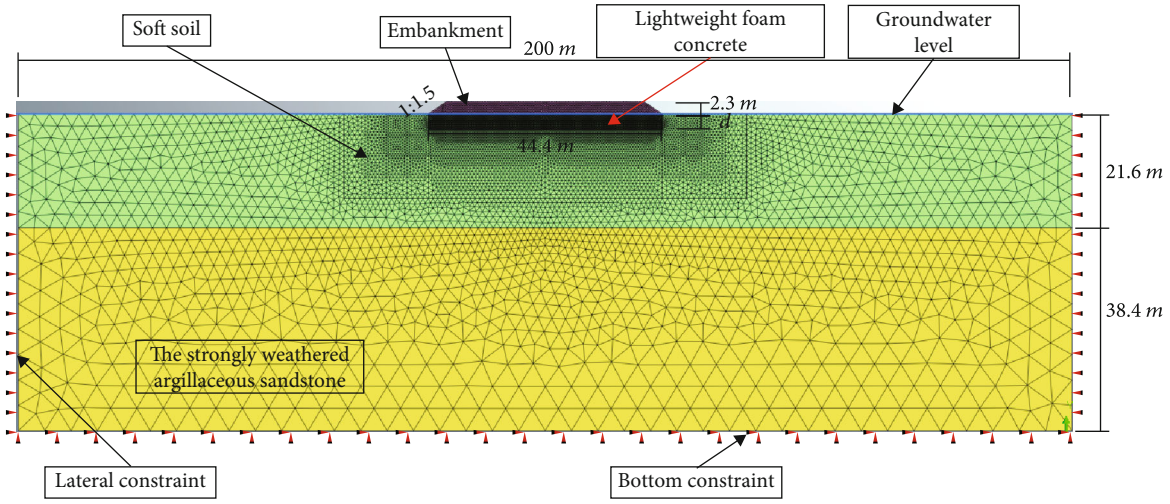

Figure 3: 2D finite element method model.

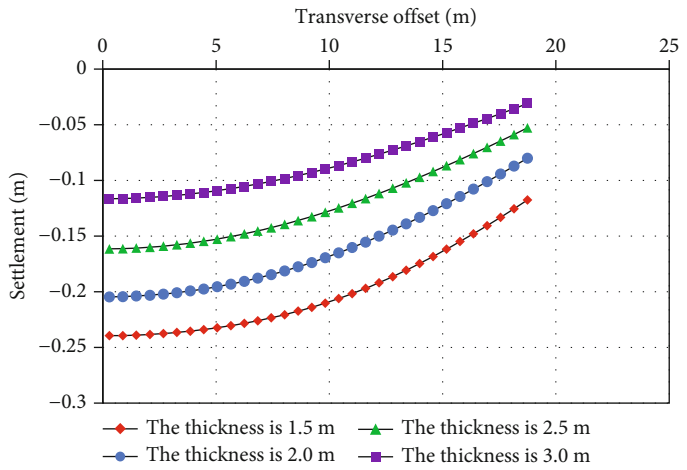

Figure 4: Settlement-transverse offset curves on the top of embankment with different thicknesses of replacement.

where **D** is the stress-strain relational matrix; $\mathbf{d}^e$ is the element node degree of freedom; and **N** is the shape function.

3.1.2. Seepage Analysis Theory. Unsteady-flow analysis was used in this study. The flow law used in MIDAS/GTS is Darcy's law, and the basic equation for flow is as follows [41]:

$$\frac{\partial}{\partial x}\left(k_x \frac{\partial H}{\partial x}\right) + \frac{\partial}{\partial y}\left(k_y \frac{\partial H}{\partial y}\right) + \frac{\partial}{\partial z}\left(k_z \frac{\partial H}{\partial z}\right) + Q = \frac{\partial \Theta}{\partial t}, \quad (4)$$

where H is the total head; k_x, k_y, and k_z are the permeability coefficient in the x-, y-, and z-directions, respectively; Q is the flow rate; Θ is the volumetric water content; and t is the time.

3.1.3. Mohr-Coulomb Strength Criterion. Mohr-Coulomb criterion is widely used, as the constitutive model can accurately reflect the characteristics of geotechnical materials. The equation of Mohr-Coulomb criterion is as follows [40]:

$$\frac{\sigma_1 - \sigma_3}{2 = -\sigma_1 + \sigma_3} \quad (5)$$
$$2 \sin \varphi + c \cos \varphi,$$

where σ_1 and σ_3 are the maximal and minimal principal stress, respectively; φ is the frictional angle; and c is the cohesion.

MIDAS/GTS assumes that the material satisfies the associative flow rule, and the yield criterion and plastic potential equations are as follows [44]:

$$\begin{cases} \frac{F(I_1, J_2, \theta_\sigma) = 1}{3} I_1 \sin \varphi + \sqrt{J_2}\left(\frac{\cos \theta_\sigma - 1}{\sqrt{3} \sin \theta_\sigma \sin \varphi}\right) - c \cos \varphi = 0, G(I_1, J_2, \theta_\sigma) = 1 \\ 3I_1 \sin \psi + \sqrt{J_2}\left(\frac{\cos \theta_\sigma - 1}{\sqrt{3} \sin \theta_\sigma \sin \psi}\right) - c \cos \psi = 0, \end{cases} \quad (6)$$

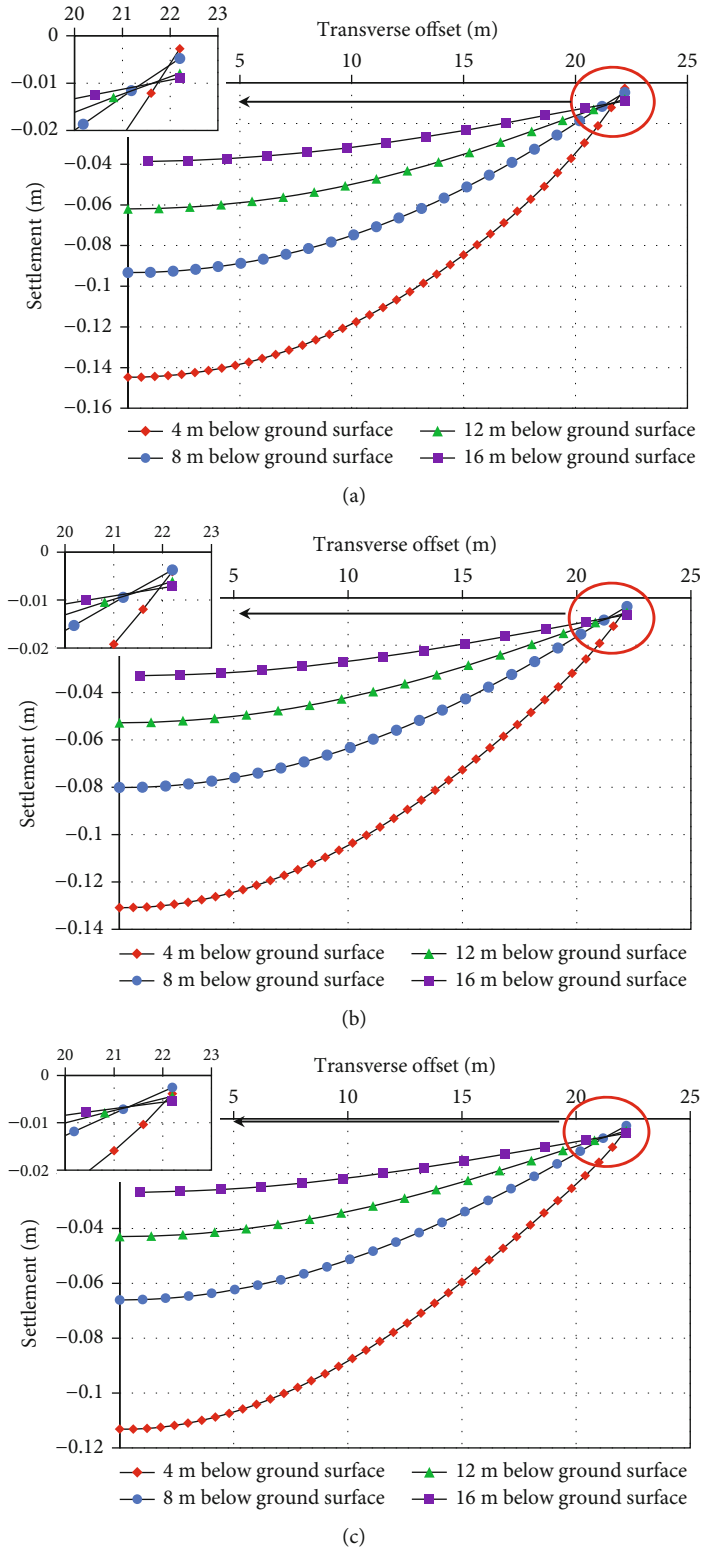

Figure 5: Continued.

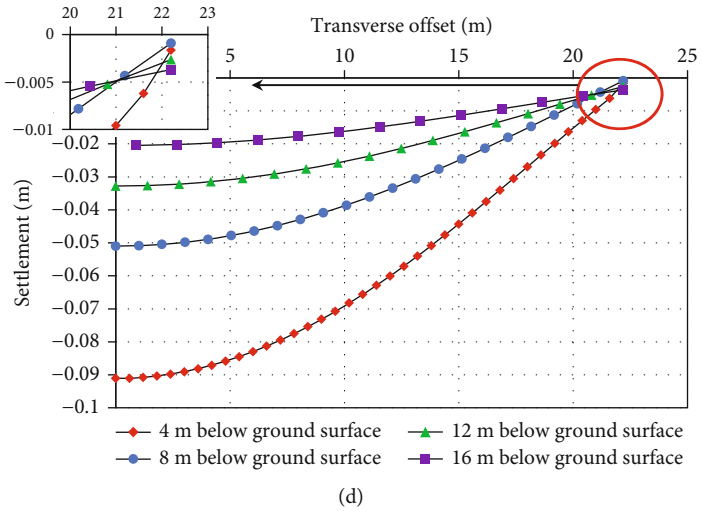

Figure 5: Settlement-transverse offset curve of different underground depths in the soft soil with the replacement thicknesses of (a) 1.5 m, (b) 2.0 m, (c) 2.5 m, and (d) 3.0 m.

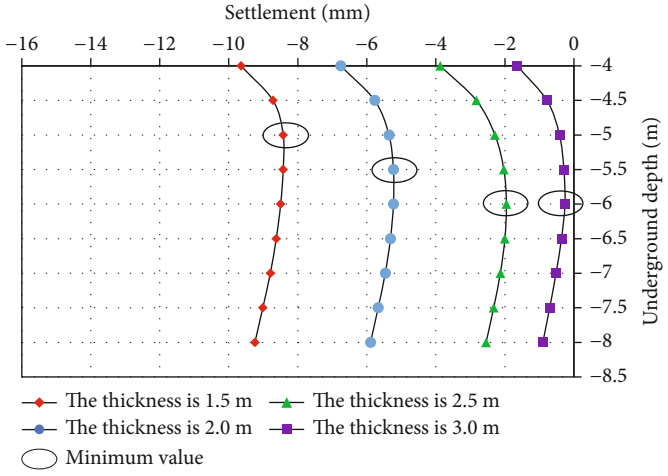

Figure 6: Settlements in the soft foundation of different underground depths under slope toe.

where I_1 is the first stress invariant; $J_2$is the second invariant of deviatoric stress; θ_σ is the Lode angle; and ψ is the dilatancy angle.

3.2. Models and Physical Parameters. Assuming that the transverse geology is invariant, the cross-sectional finite element model is established based on the geological interpretation of borehole 1 (Figure 3), with the width and height of 200 m and 60 m, respectively. The height and bottom width of the embankment are 2.3 m and 44.4 m, respectively. The thickness of the soft soil layer is 21.6 m, and the thicknesses of replacement are $d = 1.5, 2.0, 2.5, 3.0m$.

Element type: triangular plane strain element with six nodes

Initial conditions: in the present case, $\sigma_{zz} = \rho gz$ is the initial vertical stress in the z-direction; $\sigma_{xx} = \lambda_x \sigma_{zz}$ is the initial horizontal stresses in the x-direction. Moreover, the lateral total pressure coefficient is $\lambda_x = 1.0$

Boundary conditions: horizontal and vertical displacements are constrained at the bottom of the model, while horizontal displacements are constrained on both sides. A drainage boundary is set on the ground surface flush with the groundwater level. A total of 20 kPa traffic load is added on the top of the embankment uniformly after road completion.

Simulation steps include the geostress balance (steady-state analysis), construction of replacement and embankment, and 15-year opening to traffic.

The main parameters of materials are presented in Table 1. The parameters of soft soil and strongly weathered argillaceous sandstone are from the geological survey report, and the parameters of lightweight foam concrete and embankment are from the existing literature [9, 45–49].

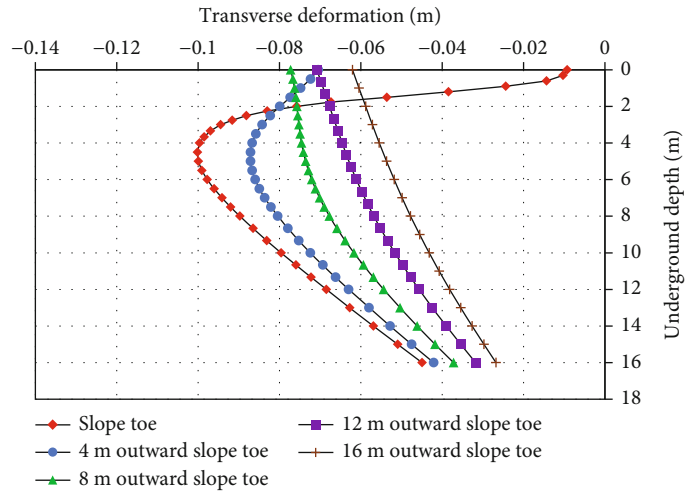

(a)

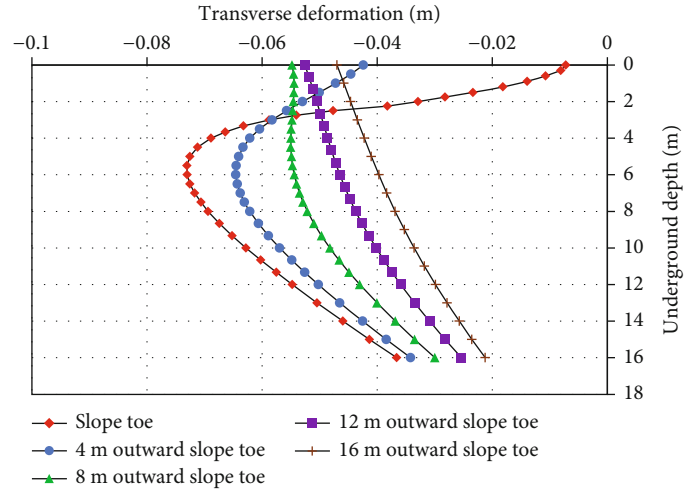

(b)

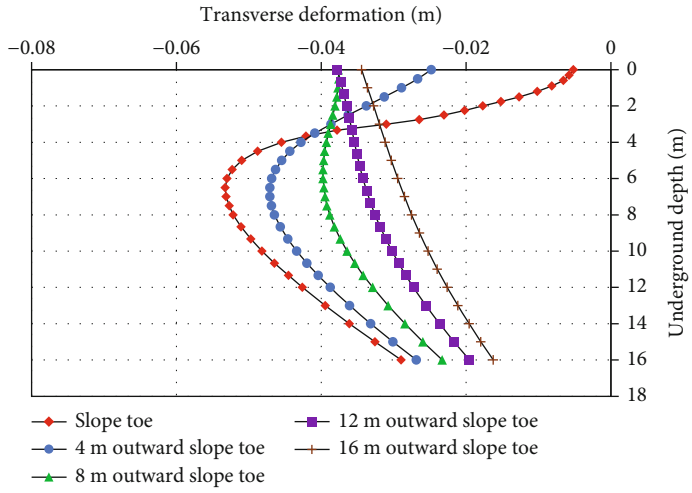

(c)

Figure 7: Continued.

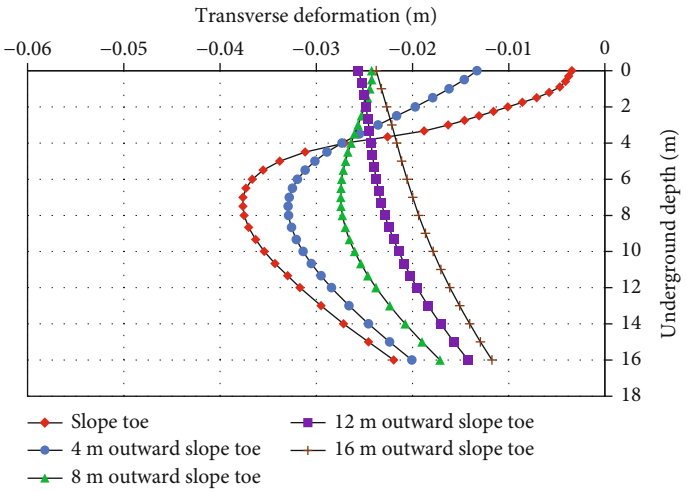

(d)

Figure 7: Transverse deformation-underground depth curves at different distances outside slope toe in soft soil with variable replacement thicknesses. (a) Replacement thickness = 1.5 m. (b) Replacement thickness = 2.0 m. (c) Replacement thickness = 2.5 m. (d) Replacement thickness = 3.0 m.

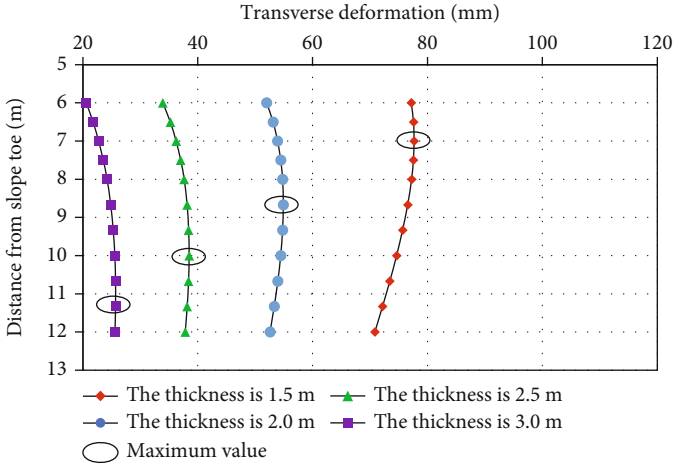

Figure 8: Transverse deformations at the ground surface with different distances from slope toe.

4. Result and Analysis

The simulation results of variables in this section are the final calculation results except for excess pore water pressure.

4.1. Deformation

4.1.1. Settlement. Figures 4 and 5 show the transverse settlement distribution on the embankment top and in the soft soil with different replacement thicknesses.

The following results are illustrated from Figure 4:

(1) The transverse settlement distribution of foundation and embankment presents an "arc" shape in cross-section, which is attributed to the closure effect [50] of replacement and flow deformation. Soft soil

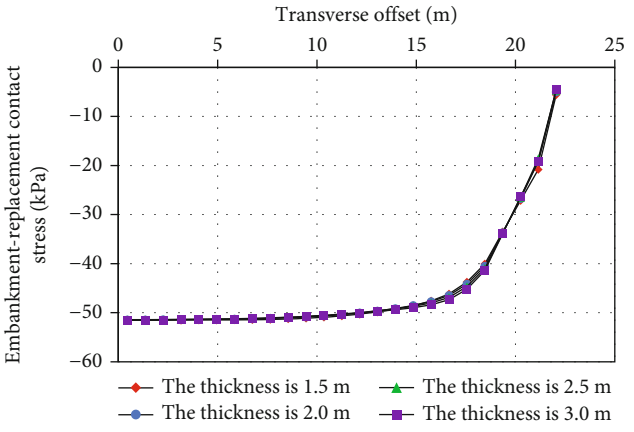

Figure 9: Transverse distribution of embankment-replacement contact stress with different thicknesses of replacement.

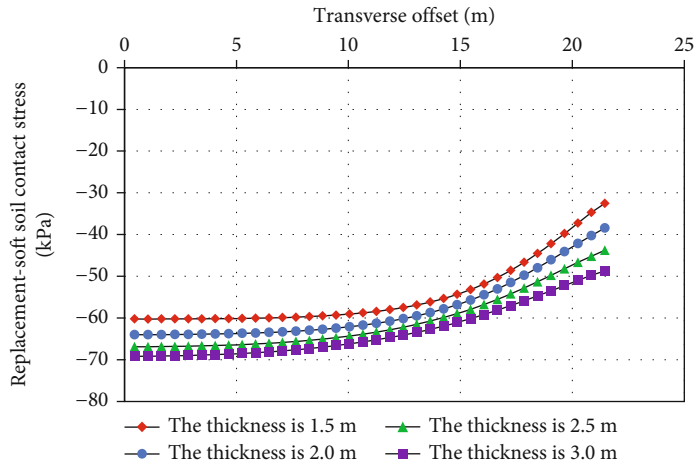

Figure 10: Transverse distribution of replacement-soft soil contact stress with different thicknesses of replacement.

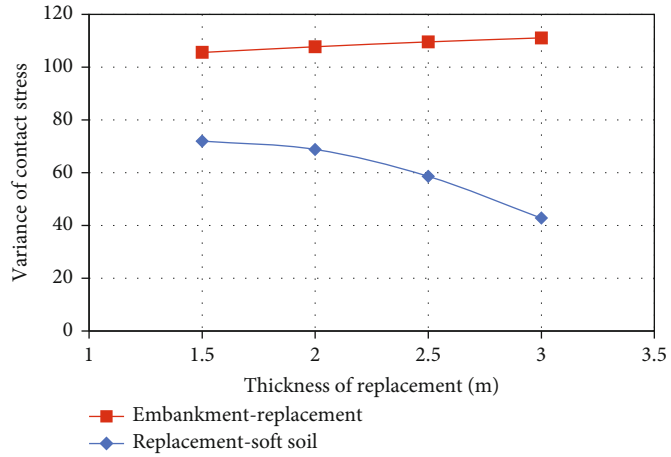

Figure 11: The variance of embankment-replacement and replacement-soft soil contact stresses with the increasing replacement thickness.

in the critical state will flow from the middle to both sides under the closure effect [50]

(2) The thicker the replacement, the smaller the settlement of embankment. When the thicknesses of replacement are 1.5, 2.0, 2.5, and 3.0 m, the maximum settlements on the top of the embankment are 23.95, 20.46, 16.20, and 11.64 cm, respectively. This is because the weight difference between soft soil and lightweight foam concrete is related to the replacement

The following result is illustrated from Figure 5:

(3) Generally, the settlement in the soft foundation under the embankment center decreases with the increasing underground depth, while that under slope toe performs differently (the results are extracted as shown in Figure 6)

It can be concluded from Figure 6 that an inflection point exists in the settlement-underground depth curve under the slope toe and gradually deepens with the increasing thickness of replacement. This is caused by the closure effect [50] of replacement and flow deformation of soft soil.

4.1.2. Transverse Deformation. Figure 7 shows the vertical distribution of transverse deformation in soft soil with different thicknesses of replacement.

The following results are illustrated from Figure 7:

(1) The transverse displacement in soft foundation decreases with the increasing thickness of replacement. When the thickness of replacement is 1.5, 2.0, 2.5, and 3.0 m, the maximum transverse displacement under slope toe is 10.02, 7.30, 5.32, and 3.76 cm, respectively. The same reason is depicted in Section 4.1.1 (2)

(2) The maximum transverse deformation moves downward as the thickness of the replacement increases. When the thicknesses are 1.5, 2.0, 2.5, and 3.0 m, the underground depths of the maximum transverse displacement under slope toe are 4.5, 5.5, 6.5, and 7.0 m, respectively. In addition, (3) the transverse

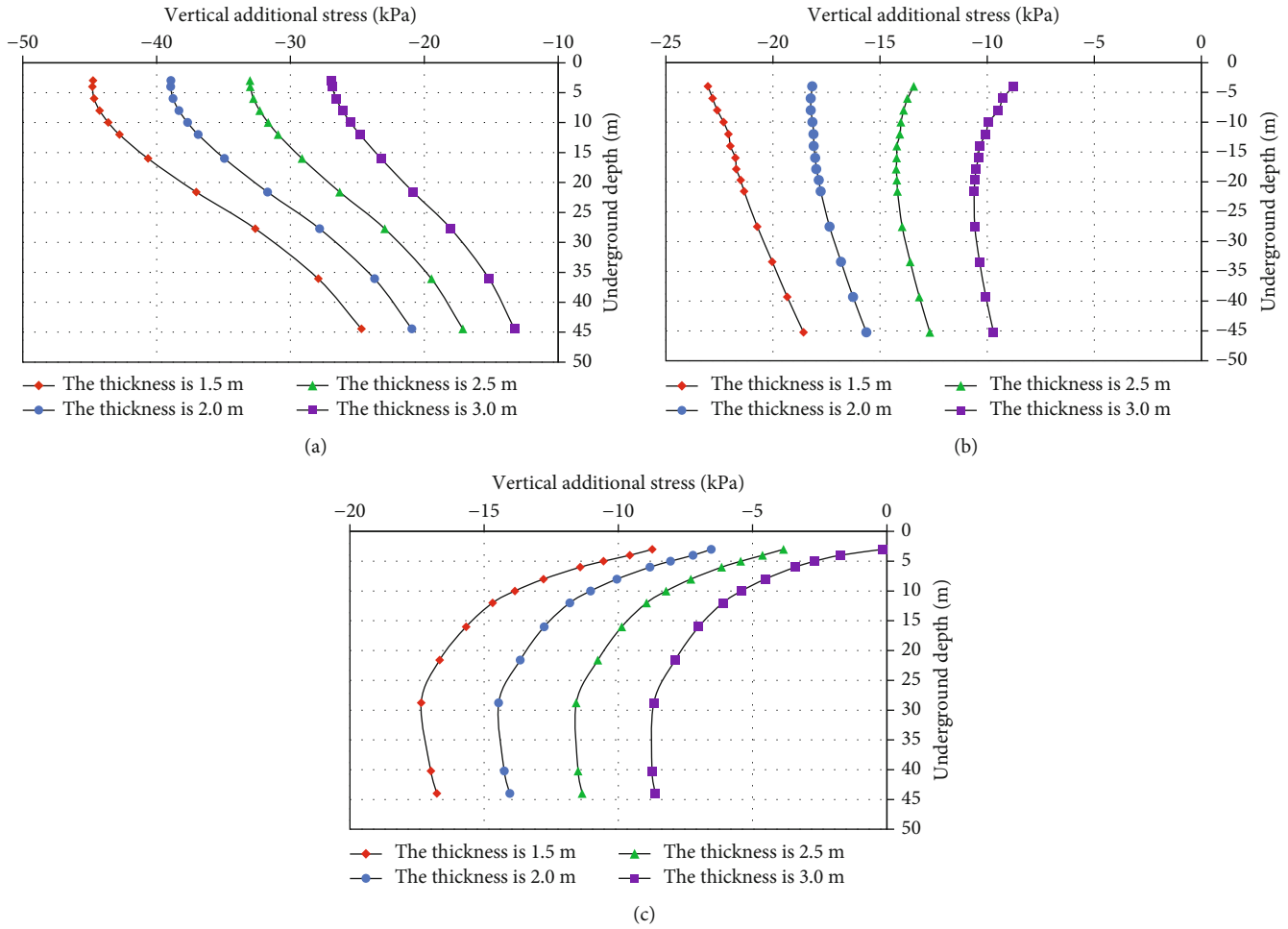

Figure 12: The vertical additional stress-underground depth curves with variable thickness of replacement under (a) embankment center, (b) embankment shoulder, and (c) slope toe.

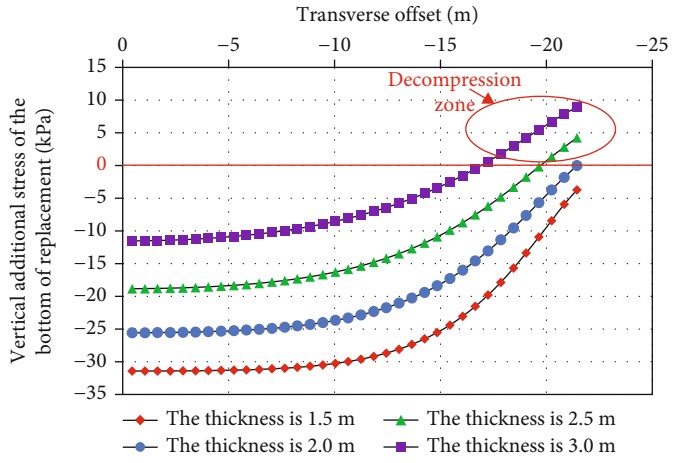

Figure 13: The transverse distribution of vertical additional stress on the bottom of replacement.

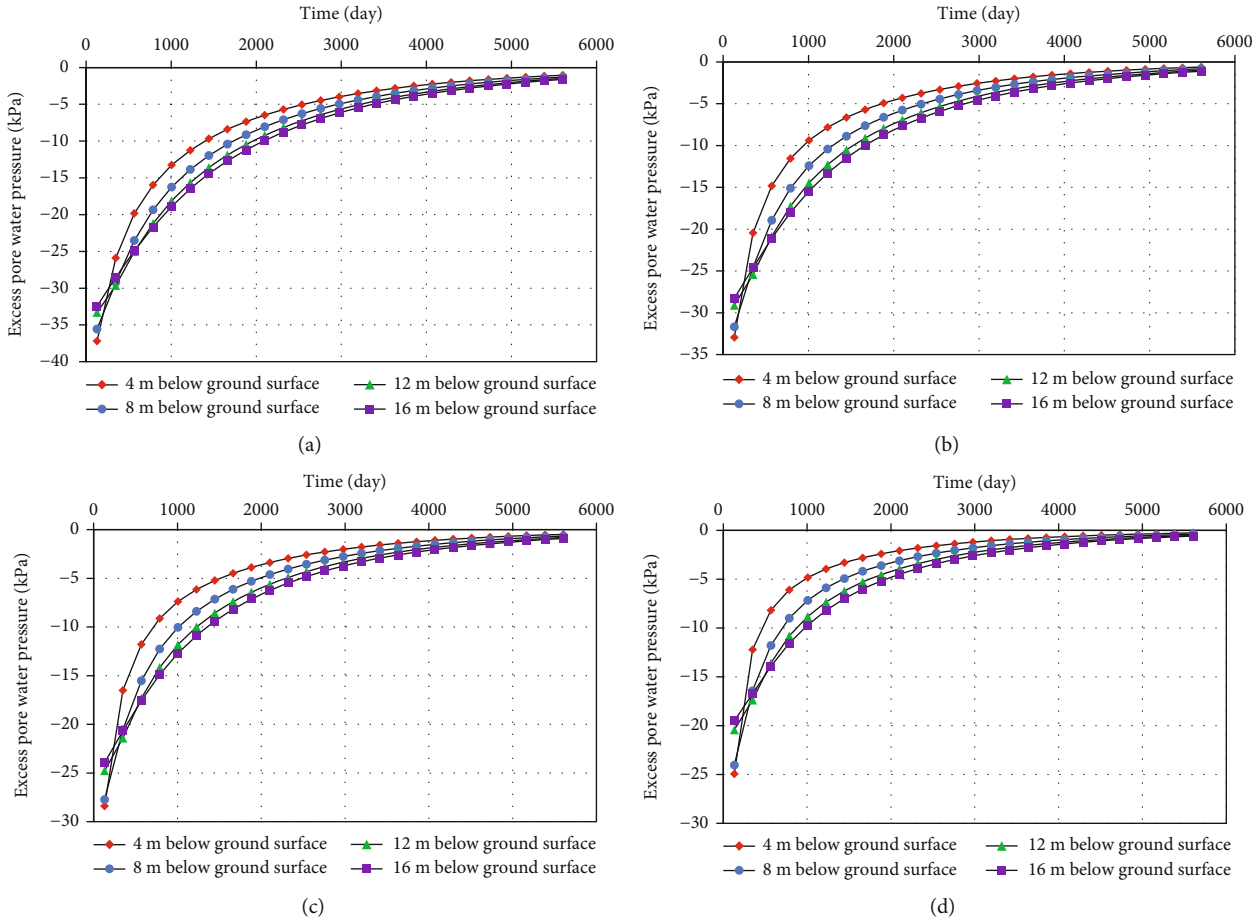

Figure 14: Excess pore water pressure-time curve in soft soil under embankment center with the replacement thicknesses of (a) 1.5 m, (b) 2.0 m, (c) 2.5 m, and (d) 3.0 m.

deformations at the ground surface outside slope toe are extracted, as shown in Figure 8

As shown in Figure 8, the maximum transverse displacement at the ground surface shifts outward with the increasing thickness of the replacement.

These phenomena (mentioned in viewpoints (2) and (3)) are relevant to the closure effect [50] of replacement and flow deformation.

4.2. Stress and Pressure

4.2.1. Contact Stress. Figures 9 and 10 show the transverse distributions of embankment-replacement and replacement-soft soil contact stress with different thicknesses of replacement, respectively.

The following results are illustrated from Figure 9:

(1) The transverse distribution of embankment-replacement contact stress presents a "trapezoid" shape, similar to the geometry of embankment. The centrifugal model test of Jiang et al. [51] verified this viewpoint. In addition, (2) the thickness of replacement is not the influencing factor of the embankment-replacement contact stress distribution.

The following results are illustrated from Figure 10:

(3) The distribution of replacement-soft soil contact stress gradually changes from the "trapezoid" to the "arc" shape with the increasing replacement thickness, implying the correlation between the spreading of the load and the thickness of replacement. The variance method is used to quantitatively analyze the influence of the replacement thickness on the stress diffusion. The variance of embankment-replacement and replacement-soft soil contact stresses are shown in Figure 11.

As shown in Figure 11, the uniformity of the distribution of replacement-soft soil contact stress increases with the rising thickness of replacement.

4.2.2. Vertical Additional Stress. Figure 12 shows the vertical distribution of vertical additional stress under embankment center, embankment shoulder, and slope toe with different thicknesses of replacement.

The following results are illustrated from Figure 12:

(1) The vertical additional stress in the soft soil decreases with the thickening replacement layer. For example, at 3 meters below the surface in Figure 12(a), when the thickness of replacement is 1.5, 2.0, 2.5, and 3.0 m, the vertical additional stress is 44.76, 38.94, 33.03, and

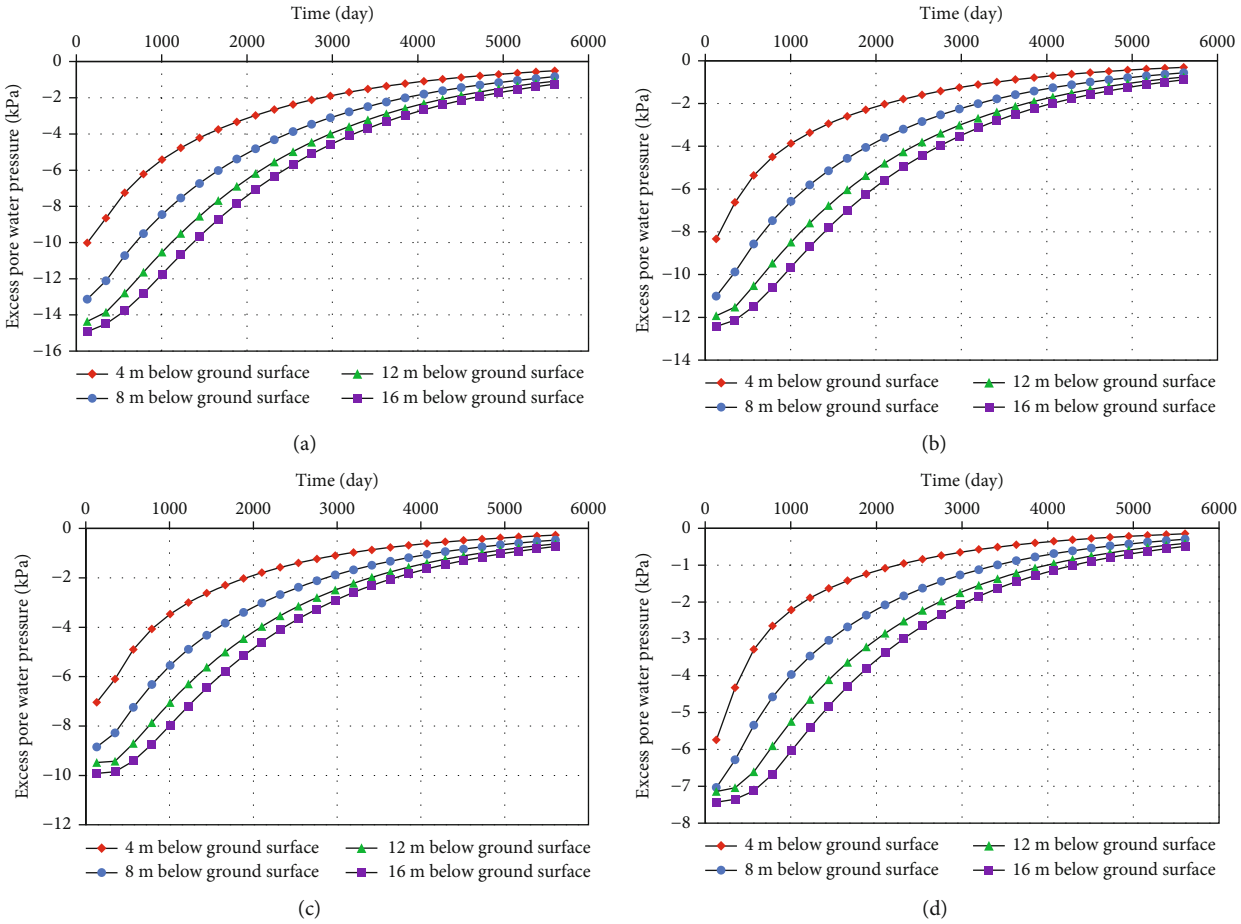

Figure 15: Excess pore water pressure-time curve in soft soil under slope toe with the replacement thicknesses of (a) 1.5 m, (b) 2.0 m, (c) 2.5 m, and (d) 3.0 m.

26.94 kPa, respectively. The reason is consistent with viewpoint (2) in Section 4.1.1

(2) The additional stress under the embankment center decreases with the deepened underground depth, and the gradient presents an increase firstly and then a decrease. The additional stress under the slope toe goes up and then down with the deepened underground depth. This is because the transverse shape of the additional stress contour is similar to a symmetrical "bubble" [52], and the axis of symmetry is at the embankment center

(3) When the replacement thickness is 1.5 and 2.0 m, the additional stress under the embankment shoulder decreases with the deepening of depth; when the thickness is 2.5 and 3.0 m, the additional stress under the embankment shoulder first increases and then decreases with the deepening of depth. This is because a decompression zone appears in the foundation (as shown in Figure 13, the new load on the bottom of replacement is less than the original load) when the replacement thickness is large, which results in the necking of the "bubble" around the bottom of replacement

4.2.3. Excess Pore Water Pressure. Figures 14 and 15 show the dissipation results of excess pore water pressure in soft soil under embankment center and slope toe, respectively, at the last calculation step.

The following results are illustrated from Figures 14 to 15:

(1) The greater the thickness of replacement, the lower the initial excess pore water pressure is. Taking the position 4 m below the surface in Figure 14 as an example: when the thicknesses of replacement are 1.5, 2.0, 2.5, and 3.0 m, the initial excess pore water pressures are 37.20, 32.94, 28.38, and 24.92 kPa, respectively. This is because the excess pore water pressure is caused by additional stress (the relationship between additional stress and thickness of replacement is depicted in viewpoint (1) of Section 4.2.2).

(2) The initial excess pore pressure under the embankment center gradually decreases with the deepening

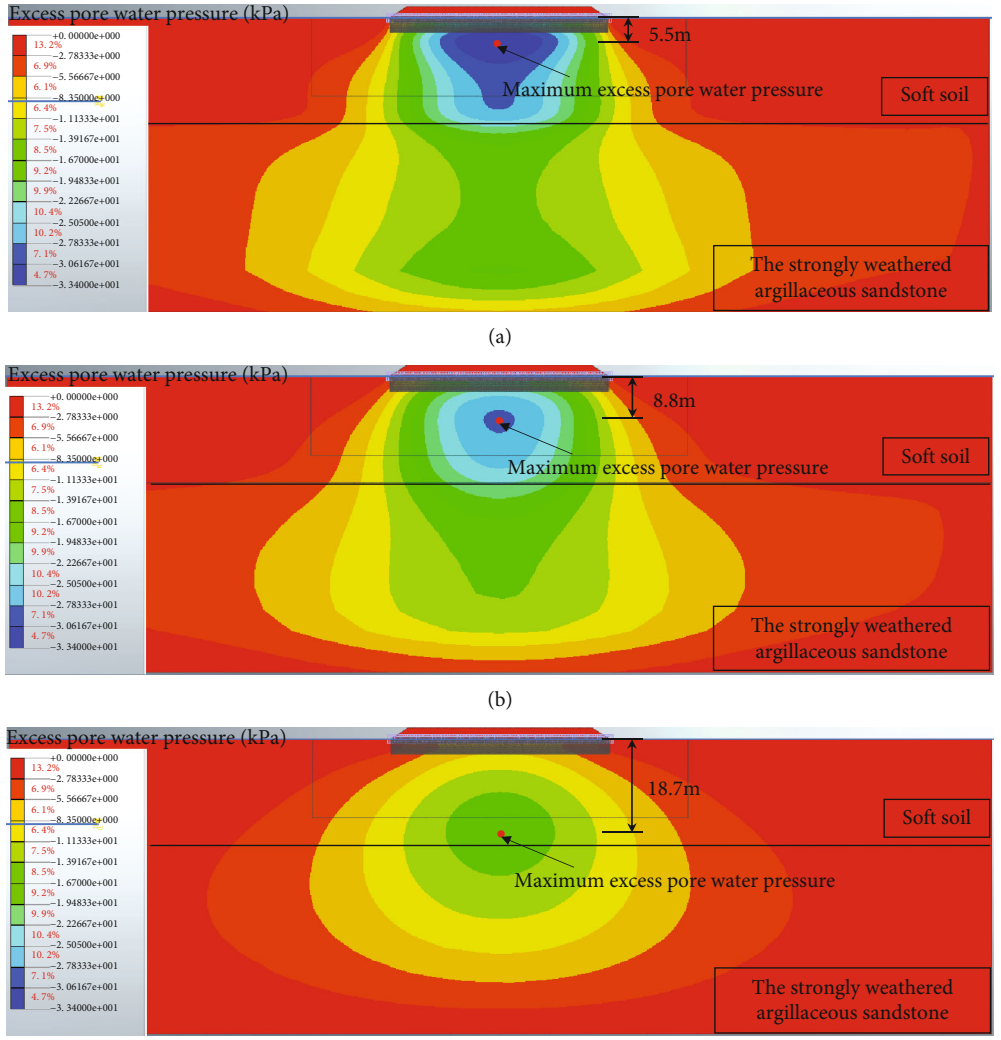

Figure 16: The colored nephogram of excess pore water pressure (a) four months, (b) seven months, and (c) twenty-nine months after road completion (the replacement thickness is 2 m).

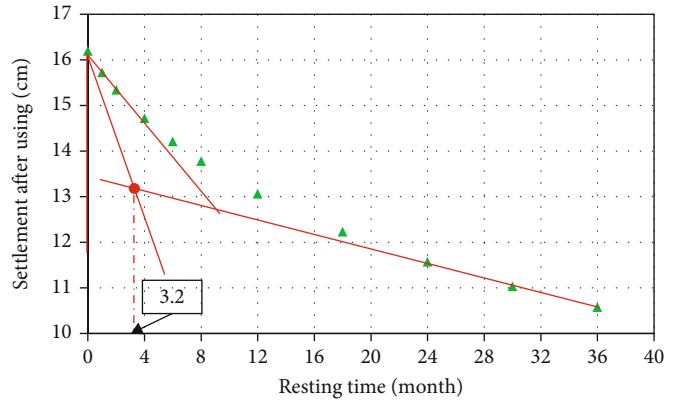

Figure 17: The relationship between settlement after 15 years of using and resting time.

of depth (4-16 m), while the initial excess pore pressure at the slope toe gradually increases with the deepening of depth (4-16 m). This phenomenon is related to the distribution of additional stress

(3) It can be concluded that the dissipation rate of excess pore water pressure is negatively correlated with underground depth by comparing the dissipation curves of excess pore water pressure of different underground depths. In addition, (4) the dissipation rate of excess pore water pressure under the embankment center is found greater than that under slope toe by comparing their dissipation curves. This may relate to dissipation path of excess pore water pressure

Figure 16 shows the colored nephogram of excess pore water pressure during the last calculation step (the replacement thickness is 2 m).

As shown in Figure 16, the position of the maximum excess pore water pressure gradually deepens with time. Considering the geometrically symmetric structure of the 2D model, the dissipation path of excess pore water pressure can be inferred to dissipate from the embankment center to both sides and downwards in the near field.

5. Preliminary Feasibility Analysis

The settlement, foundation bearing capacity, and stability of embankment slope are the main indicators for soft foundation reinforcement design in road engineering [9]. This paper focuses on the low-filled embankment, and thus, the instability of the embankment slope is unimportant. Furthermore, given that the volume weight of lightweight foam concrete is less than that of water, the antifloating stability is given additional consideration [37].

In this section, the calculation results of settlement, foundation bearing capacity, and antifloating stability are obtained for the final replacement thickness of this project (2.5 m, considering safety and construction factors), and the optimal resting time is suggested.

5.1. Settlement. The maximum settlement on the top of the embankment with different thicknesses of replacement is listed in Figure 4. When the replacement thickness is 2.5 m, the settlement meets the requirements of general highway sections in the existing technical specification (16.20 cm<30 cm) [9]. Therefore, the settlement of soft foundation handled by LFCRM accords with the existing technical specification.

5.2. Foundation Bearing Capacity. The maximum replacement-soft soil contact stress with a thickness of 2.5 m can be obtained from Figure 10, which is 66.90 kPa. The foundation bearing capacity is calculated according to Terzaghi's equation [53] (Equation (7)), and the result show the reasonability of the bearing capacity.

$$p_u = 1/2\gamma b N_\gamma + cN_c + qN_q, \tag{7}$$

where γ is soft soil weight; b is footing width; N_γ, N_c, and N_q are dimensionless coefficients; c is the cohesion of soft soil; and q is specific soil pressure above footing bottom. The footing width item in Equation (7) is not considered in this paper.

5.3. Antifloating Stability. Only the permanent load is considered in calculating antifloating stability (as shown in Equation (8)), and the safety factor is no less than 1.2 [37]. Taking an example for calculation (the thickness of replacement is 2.5 m and the groundwater level is flush with the top of the embankment), the calculation result meets the requirements [37].

$$\frac{F_s = 0.95\sum_{i=1}^{n}\gamma_i V_i}{\rho_w g V_w \geq 1.2,} \tag{8}$$

where γ_i is the volume weight of filling materials; V_i is the volume of filling materials; $\rho_w g$ is the volume weight of groundwater; and V_w is the volume of filling under the groundwater level.

According to above preliminary analysis, it is feasible to treat the deep soft foundation with the low-filled embankment by LFCRM.

5.4. Resting Time after Road Completion. Figure 17 shows the relationship between resting time (the time between completion and using of road) and the total settlement after 15 years of using. It can be seen from the figure that with the increase of resting time, the total settlement after using gradually decreases, and the rate of decrease is also slowing down. The abrupt change point of the curve, 3.2 months (about 96 days), is calculated by the Casagrande method [54] as the optimal resting time.

It should be pointed out that LFCRM is not suitable for all conditions. According to the existing research results, this paper believes that the following conditions may not be suitable: (1) high-filled embankment sections, (2) areas with obvious alternate cooling and heating (around 0 degrees Celsius) [55], and (3) saline land [56].

6. Conclusions

The result of deep soft foundation with low-filled embankment improved by LFCRM with different thicknesses of replacement is obtained using the finite element method, and the deformation and stress of the numerical results are analyzed in detail. Finally, the preliminary feasibility of LFCRM is demonstrated by combining the numerical results and the Chinese technical specification [9, 37]. The detailed conclusions are as follows:

(i) Replacing soft soil with lightweight foam concrete can offset part of dead load due to the weight difference between the two materials, reducing the deformation, additional stress, and initial excess pore water pressure accordingly. This feature will be enhanced by the increasing thickness of replacement

(ii) The transverse distribution of settlement of embankment and foundation presents an "arc" shape under the combined action of flow of soft soil and the closure effect of replacement

(iii) The uniformity of the replacement-soft soil contact stress is significantly better than that of the embankment-replacement contact stress due to the stress spreading

(iv) A decompression zone appears in the foundation with the replacement thickness increases and results in the necking of the "bubble" around the bottom of replacement

(v) The distribution of initial excess pore water pressure is relevant to additional stress, and excess pore water pressure will dissipate from the center to both sides of embarkment and downwards in the near field

(vi) LFCRM is preliminarily considered feasible by analyzing settlement, foundation bearing capacity, and antifloating stability based on numerical results and Chinese technical specification, and the optimal resting time is suggested

In the next step in the future, the feasibility of LFCRM will be further studied by field test.

Data Availability

The data used to support the findings of this study are available from the corresponding author upon request.

Additional Points

Featured Application. New method for treating deep soft foundation treatment with low-filled embankment. *Highlight*. (i) A new method, lightweight foam concrete replacement method (LFCRM), is carried out to treat deep soft foundations under the low-filled embankment; (ii) LFCRM can offset and spread the upper load effectively which is related to replacement thickness; (iii) the deformation of treated foundation is affected by flow of soft soil and closure effect of replacement; (iv) the excess pore water pressure will dissipate from the center to both sides of embarkment and downwards in the near field; (v) the potential feasibility of LFCRM is demonstrated by preliminary analysis.

Conflicts of Interest

The authors declare that they have no known competing financial interests or personal relationships that could have appeared to influence the work reported in this paper.

Authors' Contributions

Conceptualization was performed by Fanfan Li and Zecheng Chi; formal analysis was performed by Fanfan Li and Xing Chen; investigation was performed by Fanfan Li and Zhifeng Zhang; resources were contributed by Zhifeng Zhang; supervision was contributed by Zecheng Chi; visualization was performed by Fanfan Li; writing–original draft was contributed by Fanfan Li; writing–review and editing was contributed by Fanfan Li, Zhifeng Zhang, Xing Chen, Zecheng Chi, Jianbin Li, and Wei Wang.

Acknowledgments

This research is funded by the National Natural Science Foundation of China, grant numbers 52008122 and 52108366; the China Postdoctoral Science Foundation, grant number 51479190; and the Science and Technology Project of Housing Urban and Rural Construction in Anhui Province, grant number 2020-YF19;

References

[1] M. Zhou, F. Dang, Y. Li, J. Ding, J. Gao, and C. Wu, "Study on critical hydraulic gradient theory of flow soil failure in cohesive soil foundation," *Geofluids*, vol. 2021, Article ID 5599977, 13 pages, 2021.

[2] X. Fu, Q. Sheng, G. Li, Z. Zhang, Y. Zhou, and Y. Du, "Analysis of landslide stability under seismic action and subsequent rainfall: a case study on the Ganjiazhai giant landslide along the Zhaotong-Qiaojia road during the 2014 Ludian earthquake, Yunnan, China," *Bulletin of Engineering Geology and the Environment*, vol. 79, no. 10, pp. 5229–5248, 2020.

[3] Y. Zhou, Q. Sheng, N. Li, and X. Fu, "The dynamic mechanical properties of a hard rock under true triaxial damage-controlled dynamic cyclic loading with different loading rates: a case study," *Rock Mechanics and Rock Engineering*, vol. 55, no. 4, pp. 2471–2492, 2022.

[4] Y. Mei, D. Zhou, X. Wang et al., "Deformation law of the diaphragm wall during deep foundation pit construction on Lake and sea soft soil in the Yangtze River Delta," *Advances in Civil Engineering*, vol. 2021, 11 pages, 2021.

[5] L. Lou, *Study on Key Technologies of Deep Soft Soil Foundation Treatment and Low Embankment Design of Highway (in Chinese),. Master*, Southwest Jiaotong University, 2016.

[6] C. Lee, C. Lau, C. Ng et al., *Soft Soil Engineering. 1st Editon Ed*, Routledge, London, Greater London, United Kingdom, 2001.

[7] L. Miao, F. Wang, and W. Lv, "A simplified calculation method for stress concentration ratio of composite foundation with rigid piles," *KSCE Journal of Civil Engineering*, vol. 22, no. 9, pp. 3263–3270, 2018.

[8] Y. Wang, X. Zou, and J. Hu, "Bearing capacity of single pile-friction wheel composite foundation on sand-over-clay deposit under V-H-M combined loadings," *Applied Sciences*, vol. 11, no. 20, p. 9446, 2021.

[9] MOT, *Technical Guidelines for Design and Construction of Highway Embankment on Soft Ground (in Chinese) JTG/T D31-02-2013 General Office of Ministry of Transport*, Ministry of Transport of the People's Republic of China (MOT), Beijing, China, 2013.

[10] T. Yang, J. Z. Yang, and J. Ni, "Analytical solution for the consolidation of a composite ground reinforced by partially penetrated impervious columns," *Computers and Geotechnics*, vol. 57, pp. 30–36, 2014.

[11] Y. G. Zhang, M. Sun, and K. H. Xie, "Study of simplifying solution to consolidation of composite ground with partially penetrated granular columns (in Chinese)," *Rock and Soil Mechanics*, vol. 35, no. 5, 2014.

[12] S. Rajesh, "Time-dependent behaviour of fully and partially penetrated geosynthetic encased stone columns," *Geosynthetics International*, vol. 24, no. 1, pp. 60–71, 2017.

[13] S. Yan, J. Chen, L. Sun, H. Chen, and S. Lin, "Calculation method and model test on penetration depth of squeezing soft

clay (with stone) method (in Chinese)," *Rock and Soil Mechanics*, vol. 36, pp. 43–48, 2015.

[14] J. C. Chai, J. P. Carter, and S. Hayashi, "Vacuum consolidation and its combination with embankment loading," *Canadian Geotechnical Journal*, vol. 43, no. 10, pp. 985–996, 2006.

[15] J. Hu, X. Li, D. Zhang, J. Wang, X. Hu, and Y. Cai, "Experimental study on the effect of additives on drainage consolidation in vacuum preloading combined with electroosmosis," *KSCE Journal of Civil Engineering*, vol. 24, no. 9, pp. 2599–2609, 2020.

[16] Y. Huang, T. Li, and X. Fu, "Consolidation of unsaturated drainage well foundation with smear effect under time-dependent loading," *KSCE Journal of Civil Engineering*, vol. 25, no. 3, pp. 768–781, 2021.

[17] TRB, *Treatment of Soft Foundations for Highway Embankments*, Transportation Research Board (TRB), 1975, http://trb.org/Onlinepubs/nchrp/nchrp_syn_29.pdf.

[18] H. Y. Fang, *Foundation Engineering Handbook. 2nd Edition Ed*, Springer US, New York, NY, USA, 1991.

[19] Y. Wang, Y. Chen, W. Qiao, D. Zuo, Z. Hu, and Q. Feng, "Road engineering field tests on an artificial crust layer combined with pre-stressed pipe piles over soft ground," *Soil Mechanics and Foundation Engineering*, vol. 54, no. 6, pp. 402–408, 2018.

[20] M. B. Burbank, T. J. Weaver, T. L. Green, B. C. Williams, and R. L. Crawford, "Precipitation of calcite by indigenous microorganisms to strengthen liquefiable soils," *Geomicrobiology Journal*, vol. 28, no. 4, pp. 301–312, 2011.

[21] S. L. Zhan, S. S. Gao, and J. Y. Lai, "Research about the effect of polypropylene fiber on mechanical properties of curing sludge," *Advanced Materials Research*, vol. 250-253, pp. 788–794, 2011.

[22] D. M. Burmister, "The general theory of stresses and displacements in layered systems. I," *Journal of Applied Physics*, vol. 16, no. 2, pp. 89–94, 1945.

[23] C. T. Tam, T. Y. Lim, R. S. Ravindrarajah, and S. L. Lee, "Relationship between strength and volumetric composition of moist-cured cellular concrete," *Magazine of Concrete Research*, vol. 39, no. 139, pp. 115–115, 1987.

[24] E. K. K. Nambiar and K. Ramamurthy, "Sorption characteristics of foam concrete," *Cement and Concrete Research*, vol. 37, no. 9, pp. 1341–1347, 2007.

[25] C. Bing, W. Zhen, and L. Ning, "Experimental research on properties of high-strength foamed concrete," *Journal of Materials in Civil Engineering*, vol. 24, no. 1, pp. 113–118, 2012.

[26] G. I. S. Ranjani and K. Ramamurthy, "Behaviour of foam concrete under sulphate environments," *Cement and Concrete Composites*, vol. 34, no. 7, pp. 825–834, 2012.

[27] K. Wan, G. Li, S. Wang, and C. Pang, "3D full field study of drying shrinkage of foam concrete," *Cement and Concrete Composites*, vol. 82, pp. 217–226, 2017.

[28] Z. Q. Zhang and J. L. Yang, "Improving safety of runway overrun through foamed concrete aircraft arresting system: an experimental study," *International Journal of Crashworthiness*, vol. 20, no. 5, pp. 448–463, 2015.

[29] X. Tan, W. Chen, H. Liu et al., "A combined supporting system based on foamed concrete and U-shaped steel for underground coal mine roadways undergoing large deformations," *Tunnelling and Underground Space Technology*, vol. 68, pp. 196–210, 2017.

[30] W. She, Y. Du, G. Zhao, P. Feng, Y. Zhang, and X. Cao, "Influence of coarse fly ash on the performance of foam concrete and its application in high-speed railway roadbeds," *Construction and Building Materials*, vol. 170, pp. 153–166, 2018.

[31] D. G. Cai, S. W. Wei, Y. S. Ye, Q. L. Zhang, Z. G. Li, and S. Li, "Mechanical properties of lightweight foam concrete filler for roadbed of high-speed railway," *Arabian Journal of Geosciences*, vol. 14, no. 10, 2021.

[32] J. Huang, Q. Su, W. Zhao, T. Li, and X. Zhang, "Experimental study on use of lightweight foam concrete as subgrade bed filler of ballastless track," *Construction and Building Materials*, vol. 149, pp. 911–920, 2017.

[33] T. Klomranok and Q. Su, "Assessment of the use of polypropylene fiber reinforced foam concrete as a subgrade material for the China Railway Track System (CRTS) III slab ballastless tracks," *Transportation Research Record: Journal of the Transportation Research Board*, vol. 2675, no. 11, pp. 641–654, 2021.

[34] A. Hajimohammadi, T. Ngo, and P. Mendis, "Enhancing the strength of pre-made foams for foam concrete applications," *Cement and Concrete Composites*, vol. 87, pp. 164–171, 2018.

[35] A. Raj, D. Sathyan, and K. M. Mini, "Physical and functional characteristics of foam concrete: a review," *Construction and Building Materials*, vol. 221, pp. 787–799, 2019.

[36] E. Eltayeb, X. Ma, Y. Zhuge, O. Youssf, and J. E. Mills, "Influence of rubber particles on the properties of foam concrete," *Journal of Building Engineering*, vol. 30, p. 101217, 2020.

[37] MOHURD, "Technical Specification for Foamed Mixture Lightweight Soil Filling Engineering (in Chinese) CJJ/T 177-2012 Ministry of Housing and Urban Rural Development of the People's Republic of China (MOHURD) Beijing, China," in *China Architecture and Building Press*, 2012.

[38] J. H. Hu, T. Lei, K. P. Zhou, X. W. Luo, and N. G. Yang, "Mechanical response of roof rock mass unloading during continuous mining process in underground mine," *Transactions of Nonferrous Metals Society of China*, vol. 21, no. 12, pp. 2727–2733, 2011.

[39] L. Duris and E. Hrubesova, "Numerical simulation of the interaction between fibre concrete slab and subsoil—the impact of selected determining factors," *Sustainability*, vol. 12, no. 23, 2020.

[40] X. Gao, W. Tian, and Z. Zhang, "Analysis of deformation characteristics of foundation-pit excavation and circular wall," *Sustainability*, vol. 12, no. 8, 2020.

[41] C. Yuan, Z. Hu, Z. Zhu et al., "Numerical simulation of seepage and deformation in excavation of a deep foundation pit under water-rich fractured intrusive rock," *Geofluids*, vol. 2021, Article ID 6628882, 10 pages, 2021.

[42] J. Xue, J. Lin, B. Briseghella, H. Tabatabai, and B. Chen, "Solar radiation parameters for assessing temperature distributions on bridge cross-sections," *Applied Sciences*, vol. 8, no. 4, 2018.

[43] H. Stolarski and T. Belytschko, "On the equivalence of mode decomposition and mixed finite elements based on the hellinger-reissner principle. Part I: theory," *Computer Methods in Applied Mechanics and Engineering*, vol. 58, no. 3, pp. 249–263, 1986.

[44] H. S. Yu, *Plasticity and Geotechnics*, Springer US, New York, NY, USA, 2006.

[45] R. W. Crossley and G. H. Beckwith, *Subgrade Elastic Modulus for Arizona Pavements*, 1978.

[46] W. Wei, W. Qin, and X. Fan, "Testing method of elastic modulus of foamed concrete (in Chinese)," *Concrete*, vol. 9, pp. 4–

6, 2008, http://www.cnki.com.cn/Article/CJFDTotal-HLTF200809002.htm.

[47] S. Meena, L. Choudhary, and A. Dey, "Quasi-static analysis of geotextile reinforced unpaved road resting on _c-φ_ subgrade," *Procedia-Social and Behavioral Sciences*, vol. 104, pp. 235–244, 2013.

[48] N. Sutmoller, M. Gomez, and J. Kevern, "Soft soil remediation with permeable low-density cellular concrete (PLDCC)," *MATEC Web of Conferences*, vol. 271, p. 02002, 2019.

[49] MOT, *Specifications for Design of Highway Subgrades (in Chinese) JTG D30-2015 General Office of Ministry of Transport*, Ministry of Transport of the People's Republic of China (MOT), Beijing, China, 2015.

[50] Y. X. Wen and J. Zhou, "Critical edge pressure analysis of two-layered ground considering closure effect (in Chinese)," *Chinese Journal of Geotechnical Engineering*, vol. 30, pp. 685–689, 2008.

[51] L. Jiang, H. Wang, A. Li, and C. Zhang, "Experimental study on ground reaction under loading of soil subgrade (in Chinese)," *Journal of the China Railway Society*, vol. 34, pp. 69–74, 2012.

[52] G. L. Wang, S. Y. Qu, X. M. Hou, F. F. Zhu, and J. Zhang, "Preliminary study on vertical subsoil participating mass," *Advanced Materials Research*, vol. 199-200, pp. 1429–1434, 2011.

[53] V. G. Fedorovskii, "A correction term in the Terzaghi equation for subsoil bearing capacity analysis," *Soil Mechanics and Foundation Engineering*, vol. 53, no. 6, pp. 365–369, 2017.

[54] A. O. Eberemu, "Consolidation properties of compacted lateritic soil treated with rice husk ash," *Geomaterials*, vol. 1, no. 3, pp. 70–78, 2011.

[55] X. Tan, W. Chen, H. Tian, and J. Yuan, "Degradation characteristics of foamed concrete with lightweight aggregate and polypropylene fibre under freeze–thaw cycles," *Magazine of Concrete Research*, vol. 65, no. 12, pp. 720–730, 2013.

[56] Y. Lei, *Experimental Study on Salt Corrosion Resistance of Lightweight Cement Fly Ash Subgrade Filler (in Chinese)*, Taiyuan University of Technology, 2020.

Hindawi
Geofluids
Volume 2022, Article ID 4015303, 8 pages
https://doi.org/10.1155/2022/4015303

Research Article

Reinforcement Mechanism and Engineering Application of Weak Tailing Pond Beach by Soilbag Method

Cui Xuan,[1,2] Li Shuang,[3] Zhou Han-min,[2] and Cao Hui[1]

[1]*School of Civil and Resources Engineering, University of Science and Technology Beijing, Beijing 100083, China*
[2]*BGRIMM Technology Group, Beijing 100160, China*
[3]*Tourism College of Beijing Union University, Beijing 100101, China*

Correspondence should be addressed to Cao Hui; cao_h@ustb.edu.cn

Received 25 March 2022; Revised 24 April 2022; Accepted 16 May 2022; Published 8 June 2022

Academic Editor: Zizheng Guo

In light of the engineering characteristics of fine-grained tailings, such as their high moisture content, high compressibility, difficult deposition, and difficult consolidation, and based on the summary and analysis of the experience of tailing dam construction in China and abroad, a new comprehensive treatment technology suitable for dam construction on a weak beach, which is composed of strengthening foundation with the soilbag, subdam stabilization, and collaborative drainage, is proposed. Taking a dam construction project on the weak beach of a tailing pond in China as the research object and through the study of the reinforcement mechanism of the soft beach treated using the soilbag method, it can be seen that the soilbag body has the mechanism of strength growth by sand fixation and water permeability and constraint formation and can achieve an overall stable effect of extrusion and silt replacement, stacking and surcharge, and flexible embedding in a weak beach. Using this method, combined with relevant monitoring technology, a good demonstration of dam construction speed of up to 30 m/a and a safe dam construction height of up to 60 m on a weak beach surface is achieved in a tailing dam construction project, which provides a good reference for the design and construction of fine tailing dam engineering and the cooperative disposal of adverse geological conditions.

1. Introduction

A tailing pond is used to store the tailings of metal and nonmetal mines after mineral processing. Fine tailing storage is a difficult problem that must be managed in tailing treatment technology, and this exits in the fields of gold, copper, lead–zinc, and other materials. Martin and McRoberts [1] pointed out that the stability of tailing dams constructed using the upstream method is a challenging problem due to the great uncertainty of the shear strength of fine tailings or cement. Fine tailings have the following engineering characteristics: high moisture content, high compressibility, difficult deposition, and difficult consolidation. Sedimentary beaches formed by tailings after storage have the characteristics of low bearing and poor drainage capacities. It is difficult for these to directly serve as a dam body in the later stage of dam foundation bearing, which restricts the large-scale production of mining enterprises.

With the continuous and rapid development of mineral resources, tailing dam construction is developing in the direction of using fine-grained and building high dam. Rapid dam constructions on weak beaches caused by a high clay content, high rise rate, and large service scale have become new challenges for the safe operation of tailing reservoirs. Regarding the study of the storage and disposal of fine tailings, foreign countries have mainly focused on improving the performance of fine tailings and improving dam construction technology. To improve the performance of fine-grained tailings, natural drying, cyclone, thickener, filter press, and other types of technical equipment are used to remove the moisture of multiple particles, or flocculant and coagulant is added to promote the polymerization of fine-grained tailings, improve the overall particle size and dehydration effect, and improve the dam performance of tailings [2–4]. In terms of improving dam construction technology, the midline and downstream methods are often used. In recent years, relevant studies have been

Figure 1: Tailing beach surface in the initial dam.

carried out in the context of bag dewatering dam construction and waste rock dam construction [5, 6]. Ferdosi et al. [7, 8] studied the beneficial effects of the combined storage of waste rock mixed with tailings on tailing seepage, consolidation, and seismic liquefaction resistance. Domestic research on fine tailing dam construction has mainly focused on paste/dry tailing storage, seepage reinforcement, and waste rock dam construction. Yang and Ai and Zhang [9, 10] studied the paste characteristics of fine tailings and the stability of dam construction; Zhou [11] proposed a comprehensive dam construction strategy based on the soilbag method; Wei [12] carried out a study on tailing dam technology based on the improved upstream method, seepage control, and reinforcement; Cui and Zhou and Zhao [13, 14] studied and applied waste rock dam construction techniques such as the waste rock midline and waste rock downstream methods, while the strategy of dam constructions with fine tailings has achieved some promising results, but the height of the dam is mostly 20–30 m, and there is little available experience to use as reference for the continuous increase in the dam body. In addition, the existence of a weak beach, thick layer, and insufficient bearing capacity in the process of fine tailing discharge further aggravates the difficulty of dam construction, and similar dam construction projects have not been reported at home or abroad. Therefore, based on summaries of previous experiments, this paper proposes a rapid dam construction technique for a fine-grained tailing dam based on the soft beach bag method, having conducted field dam construction for nearly three years in a domestic tailing dam. The height of the tailing dam is over 60 m, and the operating parameters of the dam body are stable. Relevant engineering experience can provide a reference for dam construction design and the construction of fine tailing reservoirs in the future.

2. Engineering Background

The tailing pond studied is located in southwestern China. It is a valley-type tailing pond with an average slope of about 11% at the bottom of the ditch and a depth of about 2.2 km. On two sides, it is surrounded by high steep mountains, with a slope angle between 20° and 40°. The width of the valley bottom is 260 m~700 m, and the valley has a "U" shape. The strata at the dam site are mainly composed of pebbles, silty clay with gravel, strongly weathered quartz sandstone, and moderately weathered quartz sandstone. To save water resources significantly and reduce transportation costs, the tailing pond was designed as a paste upstream tailing pond, as shown in Figure 1.

Affected by the production process of the concentrator, the actual operation of the tailing pond has three characteristics:

(1) The clay content of the tailings is high, and the amount of particles with a size of $d < 20\,\mu$m is within the range of 49.3–53.09%, whereas the amount of particles with a size of $d < 5\,\mu$m is within the range of 17.87–20.06%. The beach surface is in a state of plastic flow

(2) The actual tailing concentration is 55~60%, the beach tailings are not graded, the permeability coefficient is low, and the tailings are difficult to consolidate

(3) The tailing dam rises fast, and the maximum rise speed can reach 30 m/a. The tailing deposition consolidation time is limited, which makes it difficult to meet the requirements of the dam

In addition, to meet the production requirements of the concentrator, the tailing dam height was designed to be 175 m. How to build dams safely and reliably has become the key concern of tailing dam operations.

3. Analysis of the Mechanism of Reinforcement of a Weak Beach Using the Soilbag Method

A large number of application cases show that [15] the soilbag method has the advantages of having a strong adaptability to a soft soil foundation, good overall continuity, and fast construction speed, and it is widely used in the construction of soft foundation dams, such as beaches and reclamation areas. The application of the soilbag method in tailing dam construction refers to the formation of a soilbag subdam by filling the soilbag with tailings, forming a consolidated filling body through the drainage of pressure, and using the filling body for continuous staggered stacking. The following principles are mainly applied to the reinforcement of weak beach surfaces using the soilbag method:

3.1. The Treatment of Fine Tailings Using the Soilbag Method Has the Mechanism of Strength Growth by Sand Fixation and Permeability, Extrusion and Drainage Consolidation, and Constraint Molding

(1) A soilbag is a bag-like structural material that is constructed by stitching woven geotextiles to encapsulate and filter grouted tailings. According to the distribution of the particle size of the grouted tailings, the appropriate mold bag material can be selected according to relevant criteria, such as soil conservation and permeability, to achieve the purpose of water and sand permeability

(2) After filling the soilbag with the tailings, the soilbag produces tension along the bag by the action of self-weight and external force. The tension produces additional stress extrusion drainage along the long axis and short axis of the soilbag to accelerate the consolidation of the tailings in the bag, as shown in Figure 2

(3) Sihong and Yisen [16] analyzed the constraint-forming effect of the soilbag on the fine tailings and proposed the equivalent additional cohesion theory for soilbag constraint. This theory states that the reinforcement effect of the soilbag originates from the comprehensive mechanism of action of three factors—the bag tension T, the bag shape (B, H), and the internal friction angle of the bag material—and points out that the additional cohesion caused by the tension of the soilbag increases the shear strength of the dam body. Based on the above theory, Cui and Zhou [17] carried out an unconfined compression test on a tailing mold bag. According to the test results, the compressive strength of the soilbag can reach 2.92 MPa, which can meet the needs of the dam materials

3.2. Mechanism of Action of the Replacement of Silt and the Stacking Static Pressure Caused by Bag Dams on the Soft Beach. The settlement of silt occurs when a soilbag is located on a weak beach. The settlement of the foundation is mainly caused by the lateral deformation of the soil and the compression deformation of the soil itself. The mold bag limits the lateral deformation of the soil well, thus effectively inhibiting the settlement of the dam foundation. When the extrusion is stable, the self-weight of the bag body is balanced with the bearing capacity of the soft clay, and the settlement of the bag is basically stable. The height of the single-stage model bag dam in the field test was 5 m. After the test, the top surface of the model bag was about 5 m higher than that of the weak beach. The height of the model bag below the weak beach was 2.4 m, and the bottom width of the model bag was 42 m, as shown in Figure 3.

When the soilbag compresses and replaces the soft fine tailings and fills the extruded space, it can be equivalent to a foundation with buried depth D (as shown in Figure 4). The shear strength of the soft foundation is $C = 2.3$ kPa, the weight is 17.5 kN/m^3, and the weight of the soilbag is 20 kN/m^3. We adopt the Meyerhof formula to analyze the bearing capacity of the soft foundation.

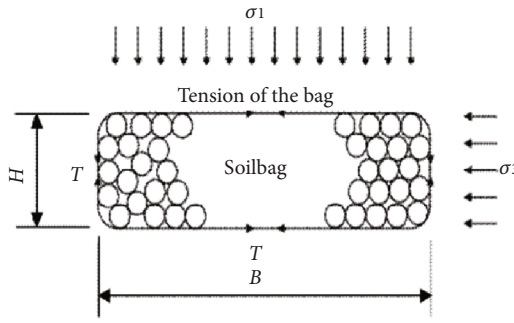

Figure 2: Schematic of the bag tension.

Figure 3: Effect of squeezing silt and replacement by soilbag.

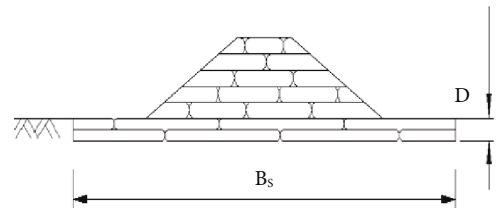

Figure 4: Schematic diagram of the reinforcement of the soft foundation using soilbags.

$$q_f = \frac{cN_c + \gamma DN_q + \gamma B_S N_\gamma}{2}, \quad (1)$$

where q_f is soil-bearing capacity; N_c, N_q, and N_γ are bearing capacity factors; D is soil-bearing capacity; B_S is soil-bearing capacity.

After the calculations, the bearing capacity of the foundation is increased from 11.82 KPa to 59.82 KPa when the thickness of the soilbag reaches 2.4 m, and these values meet the loading requirement of the 5 m bag dam. With the layer-by-layer construction and superimposed compressive load of the soilbag, the underlying soft beach is gradually compacted and consolidated with the multiple generations, development, and dissipation of excess pore water pressure, and the strength of soft foundation materials improves, which can further increase the bearing capacity of the foundation.

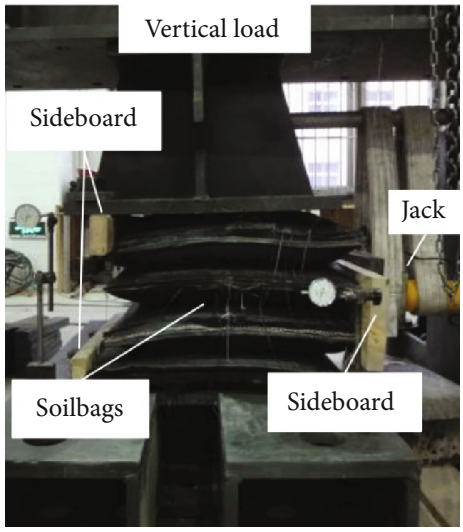

Figure 5: Shearing experiment of the soilbags.

3.3. Mechanical Properties of Formwork Dams with Lateral Force Reduction and Flexible Embedded Reinforcement of the Interlayer. Due to the tensile properties of the molded bag fabric, the horizontal force generated by the tailings in the bag is mostly offset by the tensile effect of the geotextile during the transfer process from the multilayer molded bag to the foundation. Only a small part of the horizontal force is transferred to the foundation soil, thus improving the stability of the molded bag dam. Pan [18] studied the law of distribution of the horizontal earth pressure between mold bags filled with Tongji sand; the coefficient of the horizontal earth pressure between mold bags was 0.035, which was much smaller than the coefficient of static earth pressure of Tongji sand. Fu [19] considered that, as long as the bag cannot be broken, the stability of the bag body will not pass through the bag. If instability occurs, the foundation between or below the bag layer will be destroyed. Liu et al. [20] applied the Fellenius method to check the overall stability of an expansive soil slope reinforced by soilbags. This method treats the soilbag part as the overall compressive load and considers the antislide effect caused by the friction between the soilbag layers at the arcing exit; it has achieved good results in engineering applications.

The interlaminar friction characteristics of the soilbag are affected by the friction performance between the mold bag materials, the particle size of the material in the bag, and the arrangement of the soilbag [21]. In this paper, a direct shear stress apparatus for large soilbags was designed and it was composed of a rigid pad, jack, and baffle, as shown in Figure 5. Vertical normal stress and shear stress were created by a hydraulic jack. Four groups of bag samples ($25 \times 25 \times 10$ cm) were placed horizontally in each test, in which the upper and lower bags prevented the limit deformation and the middle two bags bore the horizontal shear stress.

The raw material of the test bag was a polypropylene woven fabric of 150 g/m^2. The particle size of the filling tailings in the bag was $-74\,\mu$m, whose overall content was 42.8%, and the moisture content was 14–16%. The maximum vertical normal stress applied in the test was 1.2 MPa, and the soilbag was not damaged during the process. The coefficient of the measured interlaminar friction was 0.53. Fan et al. [22] considered that the occlusal and imbedding effect formed on the contact surface of the soilbag during the stacking process had a great influence on the shear strength and failure mode of the soilbag. The shear force of the staggered soilbag was increased by an average of 1.09 times compared with that of the nonstaggered mold bag.

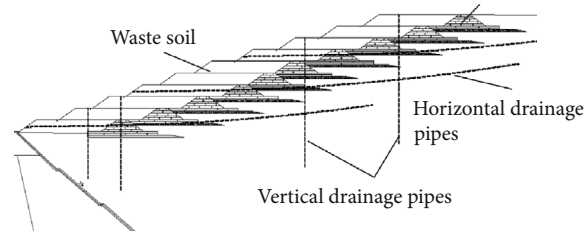

Figure 6: Design profile of the dam body.

4. Application of the Formwork Bag Method in Dam Construction on a Weak Beach

Given the problems regarding the dam construction arising from the weak beach surface, low strength, and slow consolidation of fine tailings in this project, based on the comprehensive analysis of the abovementioned mechanism of dam construction using the soilbag and combined with the rich slag and soil material sources in the reservoir area, this paper proposes a dam construction scheme based on using the formwork bag method for strengthening the foundation of the dam, increasing the stability of the wide-top subdam of the slag and soil, and coordinating the seepage discharge of the dam foundation, as shown in Figure 6.

(1) *Dam Design*. The height of the single-stage subdam was 5 m, the top width was 54 m, and the bottom width was 82 m. It was composed of a soilbag dam and a slag dam, and the slope ratio was 1 : 5.0. The dam section was trapezoidal, the top width was 6 m, the internal to external slope ratio was 1 : 2, and the bottom was 2.4 m high and 42 m wide. The requirements for the geobag materials are shown in Table 1. The requirements for the particle size of the tailings to fill the soilbag were as follows: $d \geq 0.045$ mm; the content of tailing particles should be not less than 50% when $d \leq 0.005$ mm; the content of tailing particles should be less than 10% when the filling concentration is 50-55%; the filling pressure should be controlled at 0.1-0.2 MPa. The dam body of the slag was a parallelogram section with a top width of 48 m and a height of 5 m. The wide slope formed by the soilbag dam and the slag dam could resist an unconsolidated tailing load in advance

(2) *Reinforcement Measures*. A layer of 82 m long TGDG80 unidirectional geogrid was laid at the bottom of each subdam perpendicular to the dam axis

Table 1: Main parameters of the soilbag materials.

Material	Mass per unit area/g/m^2	Tensile strength/kN/m		Elongation/%		Permeability coefficient/cm/s	Equivalent aperture O_{90}/mm
		Warp direction	Latitudinal direction	Warp direction	Latitudinal direction		
Polypropylene	150	28.2	21.6	21.5	20.9	3.45×10^{-3}	0.08-0.15

(a) Present situation of the dam construction (b) Drainage facility of the dam

Figure 7: Field dam construction.

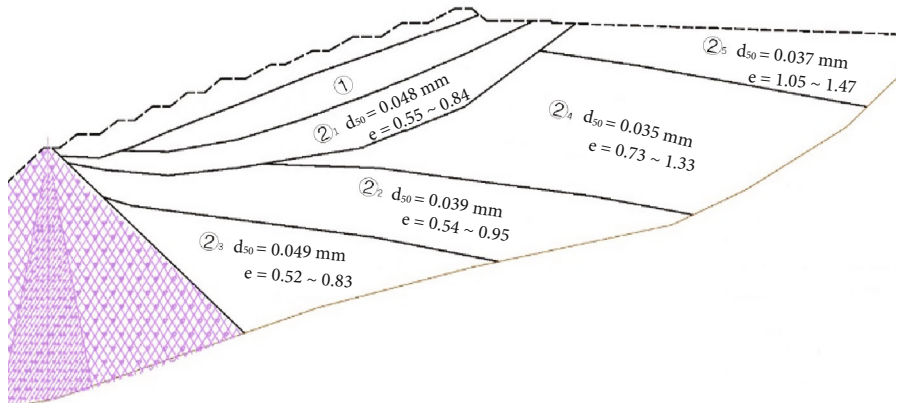

Figure 8: Geological profile of the tailing pond.

(3) *Drainage Measures*. After the formation of the dam slope, vertical and horizontal drainage pipes were arranged on the dam slope to accelerate the consolidation of the tailings. The vertical drainage pipes were arranged in rows every 20 m of the height of the dam, with a hole depth of 50-55 m and spacing of 10 m; the horizontal drainage pipes were arranged in rows every 15 m of the height of the dam. The length of a single pipe was 230 m, and the pipe spacing was 10 m

In this paper, the author used the above scheme to carry out dam construction in the field for nearly three years, as shown in Figure 7.

Since the dam construction project started, the height of the dam in the upstream method of the tailing pond has exceeded 60 m, with a production scale of the mine dressing plant of 40 000 t/d and a maximum rise speed of the dam body of 30 m/a. Through multiple borehole sampling verifications, it can be seen that the consolidation performance and mechanical properties of the tailings in the entire tailing pond are developing in a good direction, the monitoring indexes are stable, and the dam safety meets the operational requirements.

5. Analysis of the Borehole Sampling and Monitoring Data

5.1. Analysis of the Borehole Sampling in the Dam Body. Three typical sections were selected along the dam slope and the soft beach area of the tailing pond, and nine boreholes were arranged on each section for the sampling analysis. Along with the coring situation of each borehole and the results of the static penetration test, the geological section of the tailing pond is shown in Figure 8. The material of tailing silt is represented by layer ②. According to the consolidation of the tailings, layer ② is divided into zone $②_1$, zone $②_2$, zone $②_3$, zone $②_4$, and zone $②_5$. The average particle size and pore ratio of each tailing zone is also shown in the figure.

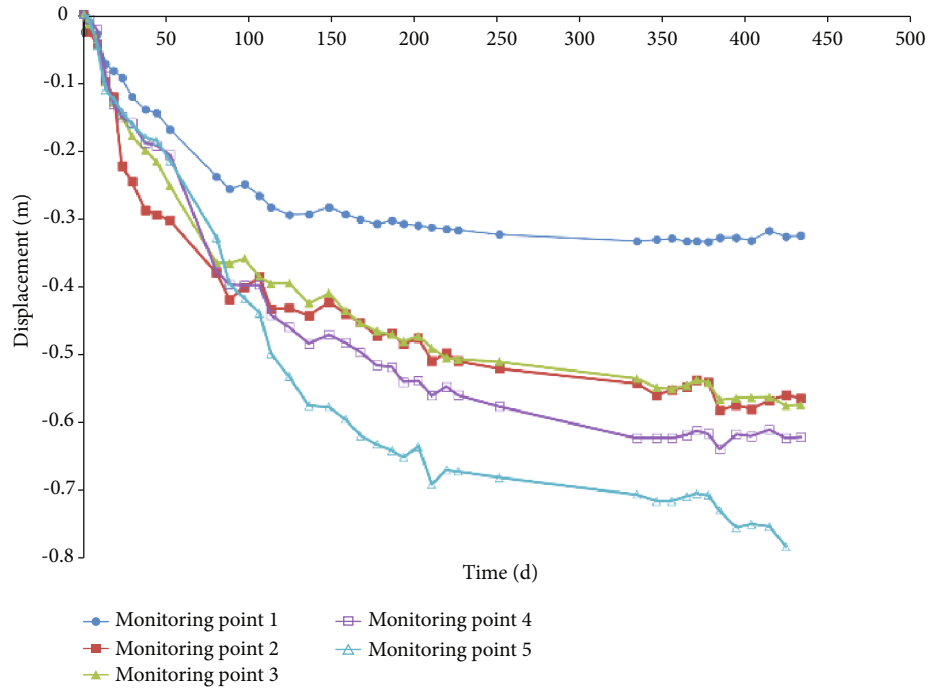

Figure 9: Curves of the time and displacement of the dam surface.

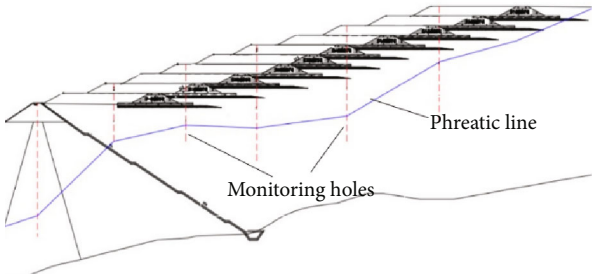

Figure 10: Monitoring hole and buried depth of the dam infiltration line.

From Figure 8, the following can be observed:

(1) High-concentration fine tailings have sorting features on a horizontal beach surface, but the effect is not obvious, and the average particle size is 0.035-0.049 mm

(2) The tailing depth in the weak area of the reservoir, which has the shape of scissor's mouth, is 40 m. The comprehensive shear strength of the cross plate shear test is 3.4–28.6 kPa

(3) Under the action of self-weight and drainage consolidations, with the increase in the accumulation dam, the weak zones are gradually transformed from zone ②$_4$ to zone ②$_1$ and zone ②$_2$. The performance of the weak zones is gradually transformed in a good direction

5.2. Analysis of Displacement Monitoring of the Dam. The relation curves of the time and displacement of the dam surface are shown in Figure 9. The monitoring points are arranged at the subdam platform per 10 m of the height of the dam, and the monitoring begins after the synchronous construction of the dam body is completed. A comparative analysis of the same time interval was performed according to the increase in the monitoring points from low to high, numbered 1-5.

It can be seen from Figure 9 that, after the completion of each subdam construction, the surface displacement of the dam body shows a large settlement at the early stage, gradually decreasing and tending towards stability at the later stage. With the continuous increase in the dam, the settlement of the dam gradually increases. According to the long-term monitoring of the data, the maximum cumulative settlement of the first ten subdams is 78.6 cm. In the construction process, the settlement deformation can be rolled and repaired in a timely manner.

5.3. Monitoring and Analysis of the Dam Phreatic Line. The monitoring hole and buried depth of typical dam phreatic lines are shown in Figure 10. The dotted line in the figure represents the monitoring hole of the phreatic line, and the blue line indicates the location of the dam phreatic line. With the long-term operation of drainage facilities, the water discharge of the single pipe of the vertical drainage pipes changed from 5.81 m^3/d to 0.31 m^3/d, and the water discharge of the single pipe of the horizontal drainage pipes changed from 15.55 m^3/d to 1.88 m^3/d.

It can be seen from Figure 10 that, under the combined action of the vertical and horizontal drainage pipes, the buried depth of the dam phreatic line is controlled between 25 m and 39 m. However, the drainage pipe of the fine tailing reservoir is clogged, and the horizontal drainage pipe performs better than the vertical drainage pipe in anticlogging. The reason for this is that the hydraulic gradient around the vertical drainage pipe is much larger than that of the

horizontal drainage pipe, and the tailings around the vertical drainage pipe hinder the entry of the seepage due to the rapid consolidation of the tailings. Additionally, frequent air exchange in the process of vertical drainage pipe drainage can easily lead to chemical congestion. Therefore, attention should be paid to this in the subsequent research and application of fine tailing drainage technology.

According to the above drilling conditions and the distribution of the phreatic line, the Bishop method was used to analyze the stability of the operation status of the tailing dam. The safety coefficient of the dam under normal conditions is 1.951–1.980, and the safety coefficient of the dam under seismic conditions is 1.287–1.295, values which meet the normal operation requirements of a tailing dam.

6. Conclusion

In light of the practical problems of fine tailing particles, the difficult consolidation of tailing discharge, and the low efficiency of dam construction in a mining concentrator, this study proposed an efficient dam construction process based on the fine tailing soilbag method for the cooperative reinforcement and disposal of a weak beach, having carried out field dam construction for nearly three years and the monitoring and analysis of dam safety for more than one year. The research and analysis show that the application effect of this technology is good, which is beneficial to ensure the safe and efficient construction and operation management of mine tailing dam. Based on the above research and practice, the results can be summarized as follows:

(1) The fine tailing soilbag has the mechanism of strength growth by solid sand permeability, extrusion and drainage consolidation, and constraint molding. This method was applied to the construction of a dam on a weak beach with the principles of silt replacement, stacking static pressure, and the flexible embedded reinforcement of the interlayer, which can help to achieve rapid dam construction on a weak beach

(2) With the new dam construction technique proposed in this paper, which includes the strong foundation of the dam using the soilbag method, the enhancement of the stability of the wide-top subdam with slag soil, and the synergistic drainage of the dam foundation, the rise speed of the fine tailing reservoirs reached 30 m/a in the project, and the height of the dam construction has exceeded 60 m

(3) From the field drilling and monitoring data, under the action of self-weight and drainage consolidation, the weak area gradually moved to the reservoir, taking the form of scissors. The maximum surface displacement was 78.6 cm, and the depth of the infiltration line was 25-39 m. In practice, the analysis of drilling information and monitoring data should be performed thoroughly, and relevant measures should be implemented in time to find abnormalities

(4) Although this technique has a good applicability in the construction of dams with a complex foundation environment and the effective utilization of fine tailings, there are also shortcomings, such as high cost compared with the traditional dam construction techniques and the materials of the soilbag being predisposed to aging when exposed for a long time. Therefore, further research should be carried out on the development of rapid filling equipment and mold bag materials to improve the efficiency and universality of the technology

Data Availability

All data, models, and code generated or used during the study appear in the submitted article.

Conflicts of Interest

The authors declare that they have no conflicts of interest.

References

[1] T. E. Martin and E. C. Mcroberts, "Some considerations in the stability analysis of upstream tailings dams," in *Proceedings of the sixth international conference on tailings and mine waste*, pp. 287–302, Rotterdam, Netherlands, 1999.

[2] S. Masala and N. Dhadli, "Correlations of shear strengths of soft oil sands tailings assessed by different in situ methods," in *Proceedings from 3rd International Oil Sand Tailings Conference*, Edmonton, Alberta, Canada, January 2013, https://sites.google.com/a/ualberta.ca/iostc2012.

[3] A. H. Watson, P. G. Corser, E. E. Garces Pardo, T. E. Lopez Christian, and J. Vandekeybus, "Comparison of alternative tailings disposal methods-the promises and realities," in *Mine Waste 2010: Proceedings of the First International Seminar on the Reduction of Risk in the Management of Tailings and Mine Waste*, pp. 499–514, Perth, Australia, 2010.

[4] N. Alam, O. Ozdemir, M. A. Hampton, and A. V. Nguyen, "Dewatering of coal plant tailings: flocculation followed by filtration," *Fuel*, vol. 90, no. 1, pp. 26–35, 2011.

[5] P. J. Assinder, M. Breytenbach, J. Wiemers, and F. Hörtkorn, "Utilizing geotextile tubes to extend the life of a tailings storage facility," in *Proceeding of the First Southern African Geotechnical Conference*, pp. 373–379, London, 2016.

[6] M. T. Van Kessel, M. Breytenbach, and M. Wilke, "Common practice and innovations in tailings dams using geosynthetic tubes," in *84TH ICOLD general meeting*, pp. 29–37, Johannesburg, 2016.

[7] B. E. Wickland, G. W. Wilson, and D. Wijewickreme, "Hydraulic conductivity and consolidation response of mixtures of mine waste rock and tailings," *Canadian Geotechnical Journal*, vol. 47, no. 4, pp. 472–485, 2010.

[8] B. Ferdosi, M. James, and M. Aubertin, "Effect of waste rock inclusions on the seismic stability of an upstream raised tailings impoundment: a numerical investigation," *Canadian Geotechnical Journal*, vol. 52, no. 12, pp. 1930–1944, 2015.

[9] Y. Lingyun and A. Chunming, "Dam stability analysis of tailing paste stockpiling in a Chinese mine," *China Mine Engineering*, vol. 42, no. 6, pp. 67–71, 2013.

[10] Z. Dezhou, "Development and application of paste tailings stacking technology," *China Mine Engineering*, vol. 39, no. 2, pp. 49–53, 2010.

[11] Z. Hanmin, "New technology and development of partial fine-grained tailings dam," *Nonferrous Metals (Mining Section)*, vol. 63, no. 5, pp. 1–5, 2011.

[12] W. Zuoan, *Research on the Characteristics and Dam Stability of Fine Grained Tailings*, Chongqing University, 2004.

[13] C. Xuan and Z. Hanmin, "Application of centerline embankment by using waste rock in tailings dam located in strong earthquake area," *Nonferrous Metals (Mining Section)*, vol. 67, no. 6, pp. 104–106, 2015.

[14] Z. Yongzhi, "Study and application of super-huge type high density fine particle tailings and waste rock for damming," *Mining Engineering*, vol. 12, no. 4, pp. 54–57, 2014.

[15] Z. Lili, *Research on mechanism, technology and calculation for constructing roads on very soft subsoil using large scale silt-filled geotubes*, Tianjin University, 2010.

[16] L. Sihong and Y. Wang, "Reinforcement mechanism of soilbag and its applications," *Geotechnical Engineering Technique*, vol. 21, no. 5, pp. 221–225, 2007.

[17] C. Xuan and Z. Hanmin, "Experimental study on the characteristics of geofabriform filling body with fine tailings," *Nonferrous Metals (Mineral Processing Section)*, vol. 1, pp. 60–64, 2016.

[18] Y. Pan, *Mechanical Analysis for Embankment Reinforced with Soilbags*, Shanghai Jiao Tong University, 2007.

[19] F. Haifeng, *Research on the Construction Method of the Marine Cofferdams with Geotextile Bags Filled with Solidified Soil[D]*, Tianjin University, 2006.

[20] S. Liu, F. Bai, Y. Wang, S. Wang, and Z. Li, "Treatment for expansive soil channel slope with soilbags," *Journal of Aerospace Engineering*, vol. 26, no. 4, pp. 657–666, 2013.

[21] S. H. Liu, K. W. Fan, X. L. Chen, F. Jia, H. Y. Mao, and Y. W. Lin, "Experimental studies on interface friction characteristics of soilbags," *Chinese Journal of Geotechnical Engineering*, vol. 38, no. 10, pp. 1874–1880, 2016.

[22] F. Kewei, L. Sihong, J. Liao, F. Binxin, and W. Jianlei, "Experimental study on shearing characteristics of pebbles-filled soilbags," *Rock and Soil Mechanics*, vol. 41, no. 2, pp. 477–484, 2020.

Hindawi
Geofluids
Volume 2022, Article ID 3800053, 13 pages
https://doi.org/10.1155/2022/3800053

Research Article

Numerical Investigation of the Landslide and Its Surge: A Case Study of the Gongjiafang Landslide in the Three Gorges Reservoir Area

Yunyun Fan, Dongyang Ma, and Xu Sun

School of Resource and Civil Engineering, Northeastern University, Shenyang 110004, China

Correspondence should be addressed to Yunyun Fan; yunyunfan@126.com

Received 28 February 2022; Revised 26 April 2022; Accepted 9 May 2022; Published 30 May 2022

Academic Editor: Danqing Song

Once the slope in the near bank area enters the state of failure, a geological disaster chain caused by landslide and its generated surge occurs very likely. In this study, a two-layer depth-averaged model was used to describe the disaster chain. The HLL (Harten-Lax-van Leer) finite volume method was used for numerical simulation and analysis. Meanwhile, the linear interpolation technique was employed to obtain second-order accuracy. The numerical results of the analytical examples reflect the movement characteristics of the two-layer fluid and verify the correctness of the numerical model. On the basis of numerical verification, the Gongjiafang landslide and its surge were simulated and analyzed. In the early stage, the deformation of the underwater geomaterials disturbed the water, forming the prototype of the surge, and then the landslide movement promoted the rapid development of the surge. After the landslide was deposited, the surge continued to travel forward and formed the largest form near the opposite bank. The numerical simulation is applicable to complex terrain and reveals some mechanisms and characteristics of the disaster chain. Compared with empirical methods, the numerical model adopted could reproduce the process of disasters chain more accurately and effectively and then improve the understanding of the disaster chain. It is feasible that the proposed numerical model can be applied under approximate plane strain conditions but is no longer applicable under 3D conditions. This work can provide reference for further research on disaster chain caused by landslide.

1. Introduction

The landslide and generated surge caused by earthquakes, rainfall, and reservoir filling are devastating geological disasters. A large landslide in the Vajont reservoir in Italy in 1963 is a representative case of this kind. A dam break and about 2,000 casualties were caused by the landslide and its surge [1, 2]. These disasters threaten the navigation of vessels, the stability of dams, and the life and property safety along the banks [3, 4]. This kind of disasters with great destructiveness has aroused great concern of scholars and has become a hot issue in the field of geological disaster research in recent years.

To deeply study the mechanism and characteristics of landslide and its surge, a lot of research have been carried out in the field observation [5], model experiment [6], theoretical analysis [7], empirical method [8], and numerical simulation [9–11]. Among them, the field observation provides the most reliable data, but due to the unpredictability of disasters and the limitations of field data, it cannot provide sufficient support for research. Experiments can be designed for specific research goals, and the observation and experimental data provided by them are important references for research but limited by experimental conditions and testing methods; so, the experiment methods cannot meet all the needs of research. Theoretical analysis is the foundation of research, but the analytical analysis cannot be applied to complex situations. Empirical methods are simple and easy to apply, but their applicability is often limited. The numerical simulation can realize the back analysis and prediction of the disaster process under complex conditions. Through numerical simulation, the mode of slope failure [12, 13] and the effect of protective structure [14] can be studied. The numerical simulation can further solve complex problems such as energy transfer in disasters [9] and the

impact of surge on protective structures [10]. The discussion of "drag along," "lift up," and "push ahead" effects in the disaster chain has deepened the understanding of the interaction between landslide and water [11]. With the development of modern computing science, numerical simulation has become one of the indispensable means to study the geological disaster. Nonetheless, it must be noted that the numerical investigation should be verified by field observations, experimental data, and analytical solutions.

In the existing numerical simulation of landslide and its surge, the movement model of landslide is mainly divided into two types: rigid body model and deformed body model [15]. For the rigid body model, the landslide is considered as a rigid body or a bottom boundary varying with time, and the actual deformation of the landslide during motion process is generally ignored. For the rigid model, the kinematics and semiempirical formulas need to be combined to define the motion of the rigid body, with the consideration of the effects of gravity, buoyancy, friction, flow resistance and inertial force, etc. [16, 17]. The rigid body models are generally suitable for the landslides with higher stiffness. Numerical and experimental studies have shown that the deformation of landslide has a great impact on the landslide and its surge [18, 19]. Therefore, to make a more accurate calculation of landslide and its surge, the effects of deformation and rheological properties should be considered in the numerical simulation. The landslide can be regarded as a deformed body, and a fluid is commonly used to describe the landslide. For the deformed body model, the landslide and the surrounding water can be regarded as two-phase fluid, which is distinguished by the volume fraction [20]. It is also possible to treat the landslide body in the lower layer and the water body in the upper layer as two separate layers, each layer having its own rheological properties. It is worth mentioning that due to the complexity of material composition and motion, the landslide generally adopts the depth-averaged models. The main difference of these models is that different rheological models are used [21–24].

The models currently used to simulate the surge process are mainly the depth-averaged models and the models based on *N-S* (Navier-Stokes) equations. The depth-averaged models are mainly represented by shallow water equation and Boussinesq equation, which has three main forms, namely, typical Boussinesq equation [25], extended Boussinesq equation [26–29], and multilayer Boussinesq equation [30]. The shallow water equation is currently the main choice for most scholars to simulate the surge process because of its strong applicability and high computational efficiency [25]. Boussinesq equation can obtain higher order precision, mainly focusing on the nonlinearity and dispersivity of surge wave [29], but the calculation cost is relatively high. For more complex surge process, it is necessary to solve the *N-S* equations [31]. Since the *N-S* equations require large storage, it also needs to cooperate with the corresponding interface tracking technology. As these solution methods of $N-S$ equations are computationally inefficient, it is difficult to solve the *N-S* equations for large-scale engineering. The landslide and its surge models are coupled by phase-to-phase coordination and forces. The meshing methods such as finite difference method [32], finite element method [33], and finite volume method [15], as well as the meshless methods such as smoothed particle hydrodynamics method [34], moving particle semi-implicit method [35], and discrete element method [31, 36], are used for the numerical solution of the model of landslide and its surge. These numerical methods have their own advantages and are widely used in the numerical simulation of landslide and its surge.

The goal of this study is to achieve an effective simulation of the landslide and its surge, so as to analyze the mechanism and characteristics of the disaster chain combining with typical case. For the purpose of this study, a numerical investigation of the Gongjiafang landslide and its surge in the Three Gorges region, China, was carried out using the depth-averaged theoretical model and the finite volume method. The main contribution of this work is to fully demonstrate the feasibility and reliability of the proposed numerical scheme for simulating the disaster chain, thus providing a good numerical scheme option for the numerical investigations of similar disasters. At the same time, some understanding of the disaster chain is also helpful for future research.

In the study of this case, the applicability of numerical and empirical methods was analyzed through comparison, so as to provide reference for further research of similar disasters.

2. Numerical Model

Since the density of the landslide is relatively large, it moves under the water, and the following subscript $m = 1, 2$ indicates the variables of the water and the landslide, respectively, as shown in Figure 1.

The mass and momentum equations of incompressible medium can be expressed as Equation (1):

$$\begin{aligned} \nabla \bullet \mathbf{u} &= 0, \\ \rho(\partial_t \mathbf{u} + \mathbf{u} \bullet \nabla \mathbf{u}) &= -\nabla \bullet \mathbf{T}, \end{aligned} \tag{1}$$

where t represents the time, ρ is the density of the medium, $\mathbf{u}$ is the velocity vector, and $\mathbf{T}$ is the Cauchy stress tensor.

The water and the landslide are, respectively, subjected to averaging processing in the depth direction, and the variables are defined as averages along the depth, which can be expressed by Equation (2):

$$\begin{cases} \bar{u}_{i,m} = \dfrac{1}{h_m} \displaystyle\int_{z_{\mathrm{bm}}}^{z_{\mathrm{bm}}+h_m} u_{i,m} dz \,; (m = 1, 2), \\ \bar{\sigma}_{ij,m} = \dfrac{1}{h_m} \displaystyle\int_{z_{\mathrm{bm}}}^{z_{\mathrm{bm}}+h_m} \sigma_{i,m} dz \,; (m = 1, 2), \end{cases} \tag{2}$$

where h_m is the depth of flow, $u_{i,m}$ is the flow velocity, $\sigma_{ij,m}$ is the stress component, and $\bar{u}_{i,m}$ and $\bar{\sigma}_{ij,m}$ represent the velocity and the stress component after average along the depth, respectively.

By depth-averaging the mass and momentum equations of incompressible continuous medium, the model equation used to simulate the landslide and its surge can be expressed by Equation (3) [21]:

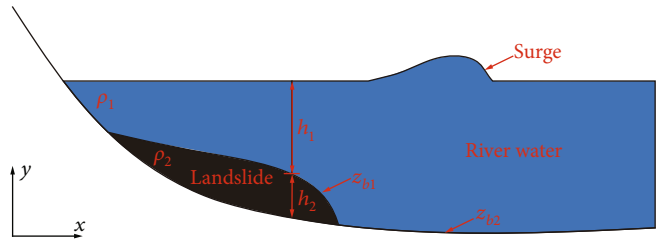

Figure 1: Sketch of the numerical model.

$$\begin{cases} \dfrac{\partial \mathbf{U}}{\partial t} + \dfrac{\partial \mathbf{F}}{\partial x} = \mathbf{S}, \\ \mathbf{U} = \begin{pmatrix} h_1 \\ h_1\bar{u}_1 \\ h_2 \\ h_2\bar{u}_2 \end{pmatrix}, \mathbf{F} = \begin{pmatrix} h_1\bar{u}_1 \\ h_1\bar{u}_1^2 + \dfrac{1}{2}gh_1^2 \\ h_2\bar{u}_2 \\ h_2\bar{u}_2^2 + \dfrac{1}{2}kgh_2^2 \end{pmatrix}, \mathbf{S} = \begin{pmatrix} 0 \\ -h_1 g\dfrac{\partial(z_{b2}+h_2)}{\partial x} + \dfrac{\tau_{xz}(z_{b1})}{\rho_1} \\ 0 \\ -krh_2 g\dfrac{\partial h_1}{\partial x} - kh_2 g\dfrac{\partial z_b}{\partial x} + \dfrac{\tau_{xz}(z_{b2}) - \tau_{xz}(z_{b1})}{\rho_2} \end{pmatrix}, \end{cases} \tag{3}$$

where g is the gravitational acceleration, k is the lateral stress coefficient, z_{b2} and z_{b1} represent the elevation of the sliding surface and the two-phase interface, respectively, $r = \rho_1/\rho_2$ is the density ratio, and τ_{xz} is the shear stress.

The shear stress $\tau_{xz}(z_{b1})$ between the two layers in Equation (3) can be expressed as Equation (4):

$$\tau_{xz}(z_{b1}) = \rho_1 \kappa(\bar{u}_2 - \bar{u}_1)|\bar{u}_2 - \bar{u}_1|, \tag{4}$$

where κ is a positive constant.

The bottom shear stress $\tau_{xz}(z_{b2})$ of the landslide is affected by the pore pressure and can be expressed as Equation (5):

$$\tau_{xz}(z_{b2}) = -gh_2(\rho_2 - \rho_1)\tan\varphi_b = -gh_2\rho_2(1-r)\tan\varphi_b = -\mu_b gh_2\rho_2, \tag{5}$$

where φ_b is the bottom friction angle, and μ_b is the underwater friction coefficient.

In this study, Equation (3) was discretized by the finite volume method of the HLL scheme (see the appendix for the scheme). The HLL scheme used in this study to calculate the interface flux is relatively simple in solving the Riemann approximation problem. In order to improve the accuracy of the numerical solution, the second-order linear interpolation technique is needed to reconstruct the variables on the left and right sides of the interface. The code was originally developed based on the model theory and numerical methods described above and used in the numerical investigation of landslide-induced disaster chain in this study. The appendix provides a detailed introduction to the numerical scheme.

3. Numerical Results and Analysis

3.1. Dam-Break Flow. In order to verify the effectiveness of the numerical scheme in calculating the discontinuous transient flow, the numerical simulation of dam-break flow was carried out. The initial condition of the two-layer dam-break flow is shown in Figure 2.

In order to facilitate the comparison with the analytical solution, the same density was applied to the two-layer fluid in the numerical simulation (this means that the density ratio r is equal to 1), and the two cases shown in Table 1 were calculated and compared. The dam break is located at $x = 10$ m. Under the condition that the upstream and downstream water depths are determined, the analytical solution can obtain a free surface at a certain moment [37]. In order to be consistent with the assumptions of the analytical solution, the numerical calculation does not consider the resistances, and the lateral stress coefficient k is set to 1.

The numerical results of case 1 and case 2 at 0.8 s are shown in Figure 3.

In the calculations of case 1 and case 2, since the total water depths in the upstream and downstream are identical (i.e., $h_L = h_R$), the free surface of the calculated dam-break wave should be theoretically the same. It can be seen from the results of the dam-break flow that the transient free surfaces of the two cases both have good consistency with the analytical solution. This difference does not seem obvious, indicating that the numerical scheme used is correct and effective. At the same time, since the upper and lower layers have the same density in the two cases, a consistent contact discontinuity obtained after exchanging the initial depths of the upper and lower layers can confirm that the calculation is reasonable. The results show that the contact discontinuity obtained by the two cases has almost the same profile. In despite of some differences from the analytical solution, they are generally consistent with the analytical solution and show good numerical stability, without numerical oscillation. Due to the limitation of space, only the two-layer dam-break flow with the same density was simulated in this study, while the dam-break flow with different densities in the upper and lower layers have not been fully discussed. This is because the numerical solution under the condition that the two layers have the same density can facilitate the comparison with the analytical solution and then verify the correctness. Obviously, in the case of two layers with different densities, the advantages of the two-layer fluid model can be fully exploited. To deeply apply the two-layer fluid model, it is necessary to further study the engineering cases under the condition that the upper and lower layers have different physical properties. Nevertheless, the numerical simulation of the dam-break flow show that the two-layer flow can be transformed into a single-layer flow with the same density, and the calculation can capture the flow characteristics of the two-layer dam-break flow, which can be further applied to the study of the landslide and its surge.

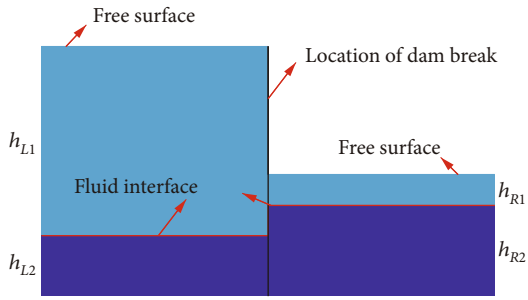

Figure 2: Initial condition of the two-layer dam-break flow.

Table 1: Initial conditions of the dam-break flow.

Case	h_{L1} (m)	h_{L2} (m)	h_{R1} (m)	h_{R2} (m)	h_L (m)	h_R (m)
Case 1	5	0	0	1	5	1
Case 2	0	5	1	0	5	1

3.2. The Gongjiafang Landslide and Its Surge. The Gongjiafang landslide is located in the Wu Gorge section of the Three Gorges reservoir, China, on the north bank of the Yangtze River, about 4.5 km upstream of the new Wushan county. The mountain where the landslide is located is steep, and the relative height is about 600 m. The slope is generally east-south, with an original average incline of 53°. The landslide is bounded by two gullies, and the rear edge elevation is about 400 m. The rock of the landslide has a fragmented layer structure. The landslide occurred on November 23, 2008. On that day, the Three Gorges Reservoir was in the storage stage. In the Gongjiafang section, the water level was 172 m, the width of the Yangtze River was about 480 m, and the minimum elevation of the riverbed was about 40 m. After the landslide occurred, the investigation revealed that the exposed fresh rock surface appeared as an isosceles trapezoid with an upper width of 45 m and a width of 194 m at the water surface [8]. The longitudinal length of the landslide was 293 m, the height was 210 m, the upper slope was 64°, and the lower slope was 44°. The water entry angle of the landslide was about 40°. The comparative analysis of the topography before and after the landslide shows that the average thickness was 15 m, and the volume was 380,000m^3. According to the image at the time of the slope failure and the underwater measurement analysis made by the Chongqing Three Gorges Geological Disaster Office, the depth of the landslide after entry into the water was about 50 m. According to the field investigation, the surge caused the cables of several ships docked to be broken and the bottom of the ships to be damaged [38]. Fortunately, no ships have been overturned, and no casualties have been caused. The regional location map and site pictures of the Gongjiafang landslide are shown in Figure 4, and the main information of the Gongjiafang landslide is shown in Table 2.

The Gongjiafang landslide occurred when the water level of the Three Gorges Reservoir reached 172 m. For the internal induced factors related to the geological structure, the mountain where the Gongjiafang landslide is located was cut by two structural planes, and the rock on the slope surface was broken as a fragmented and scattered structure [8]. These are the internal controlling factors of the collapse. At the same time, the left and right parts of the landslide are topographically bounded by the gullies without lateral constraints, and the slide along joint surface was caused by the level uplift of groundwater. As for the external cause, the water level of the Three Gorges Reservoir rose, the front edge of the landslide was hollowed out with the entrainment, and then the support at the slope foot was lost. At the same time, the groundwater level in the landslide rose rapidly, resulting in the continuous decrease of the strength of the slip zone, and the landslide eventually occurred under the influence of internal and external factors. The surge caused by the rapid impact on the water after the slope failure is an important secondary disaster. As the spreading scope of the surges continued to expand, sometimes, the consequences of disasters are much more serious than the landslides themselves. Therefore, it is necessary to conduct a more in-depth study on the generation and propagation of surge in combination with landslide movement.

According to the actual situation of the disaster, the range of the horizontal distance was 0-1200 m, and the elevation was 0-450 m in the numerical simulation. In this model, the elevation of the rear edge of the landslide was 403 m, the maximum elevation of the opposite bank of the landslide was 397 m, and the initial water level of the river was 172 m, as shown in Figure 5.

The calculation parameters must be calibrated first in order to better represent the propagation process of the Gongjiafang landslide and its surge. In consideration of unavailability of enough information, final deposition of the landslide, and the maximum surge height, the two pieces of the most important known information about disaster were used for back analysis of the calculated parameters. According to the existing data, the density ratio r was 0.4 (the specific gravity of water and geomaterials was 1 and 2.65, respectively) in calculation. Considering the movement characteristics of Gongjiafang landslide fluidization, the lateral stress coefficient k was 1, so that the underwater friction coefficient μ_b became the most important parameter for back calculation. After back calculation and analysis, the final result obtained at $\mu_b = 0.42$ complies with the actualities. See Figure 6 for the landslide deposition and the maximum surge height obtained by the numerical calculation.

It can be concluded from Figure 5 that the deposition obtained by numerical simulation is basically consistent with actualities under the given calculation parameters. Since the deposition of actual landslide expands along the river in the deceleration zone, the deposition calculated on the vertical section is larger than that in actualities, which also leads to certain difference between the numerical results of the front and rear edges of the depositions and those in actualities, even if the overall deposition obtained by the numerical simulation is consistent with that in actualities. All these differences also exert certain influence on the formation and spread of surge (mainly on the front edge of landslide). To be specific, the maximum surge height calculated is 32.65 m (the result of $t = 15.1$ s), slightly higher than the actual maximum surge height 31.8 m (the front edge of the landslide obtained by numerical calculation moves longer, which pushes water more

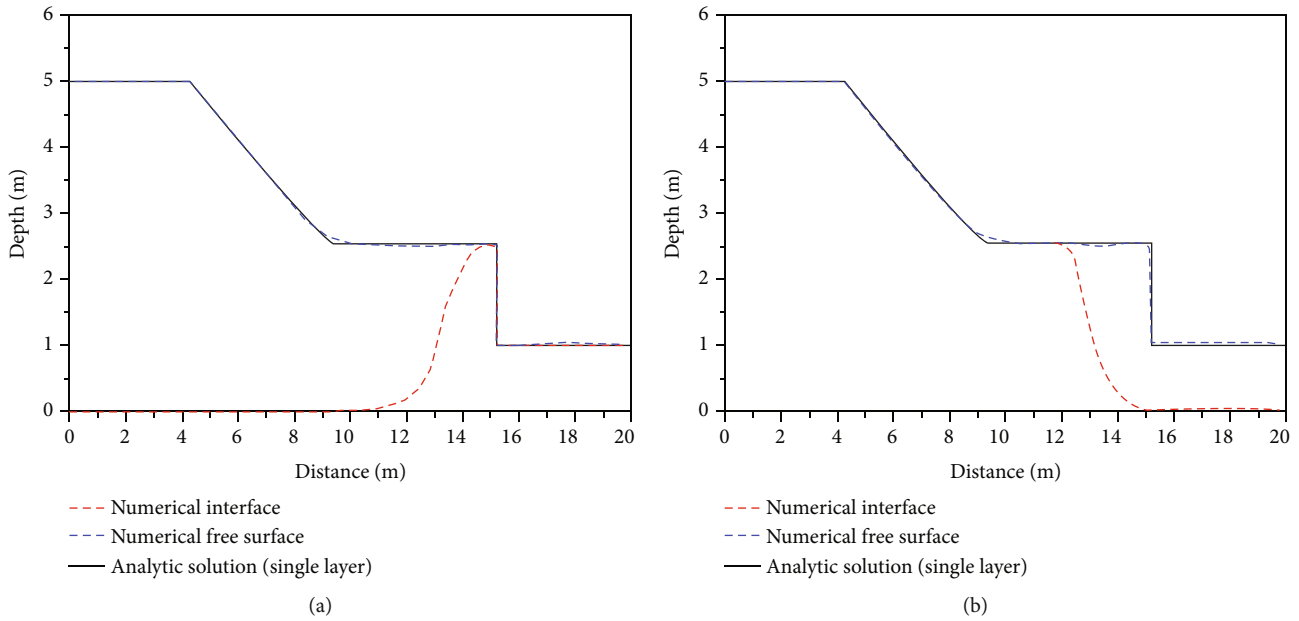

Figure 3: Numerical results of the dam-break flow at 0.8 s. (a) Case1. (b) Case2.

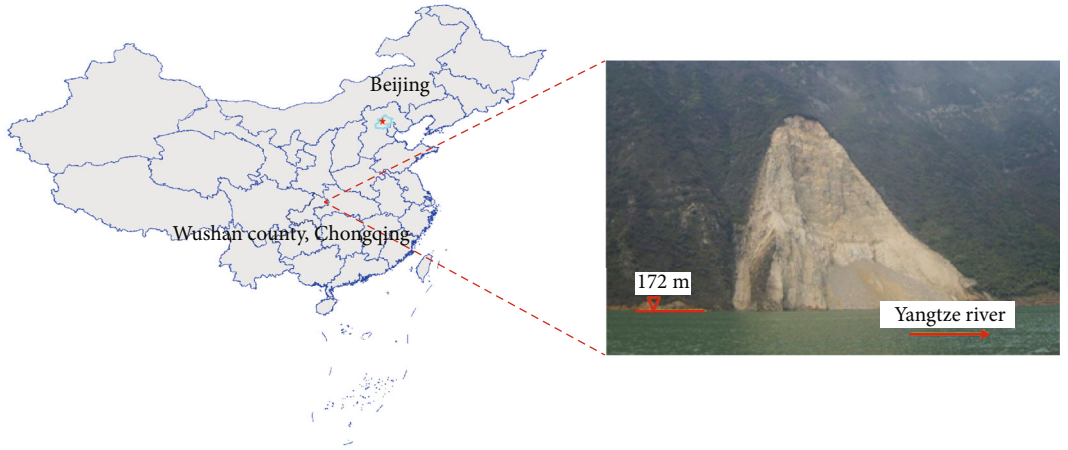

Figure 4: The regional location map and site pictures of the Gongjiafang landslide [39].

Table 2: The main information of the Gongjiafang landslide [8].

Information	Scale	Information	Scale
Volume of the landslide	380,000 m^3	Average incline	53°
Average thickness of the landslide	15 m	Upper slope of the landslide	64°
Longitudinal length of the landslide	293 m	Lower slope of the landslide	44°
Height was of the landslide	210 m	Width of the landslide at the water surface	194 m
Rear edge elevation	About 400 m	Upper width of the landslide	45 m

significantly). The differences can be ignored for the calculation of a large scale; so, the differences between the numerical result and the actual maximum surge height are believed limit and acceptable. Based on the comparison between numerical calculation and actual disaster, the numerical simulation is indeed correct and effective.

The characteristics of the Gongjiafang landslide and its surge were further studied through numerical simulation on the basis of verifying the correctness and effectiveness, as shown in Figures 7 and 8.

The occurrence and development process of the disaster chain caused by the landslide are shown in Figure 6, where

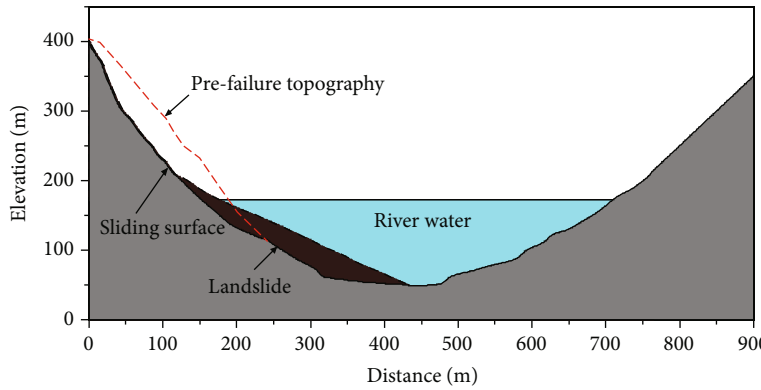

Figure 5: Numerical model of the Gongjiafang landslide.

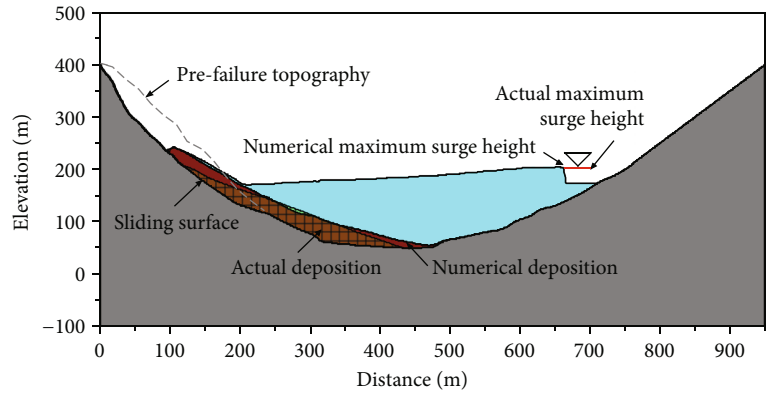

Figure 6: Comparison of numerical results and actualities.

some characteristics of the process are also fully demonstrated. The overall forward movement of landslide is insignificant when the slope becomes unstable but a few waves form on the water surface, which is caused by the deformation of unstable geomaterials. At this time, no obvious displacement of landslide front edge can be found. This indicates that the formation of the surge is closely related to the deformation of the landslide; although, the landslide movement may be the more dominant cause of the formation of the surge (Figure 7(a)). Subsequently, the unstable geomaterials moved downward along the sliding surface under gravity, and the front edge of the landslide moves with a faster speed. The landslide pushes the water to move towards the opposite bank, and several waves spread to the opposite bank under the pushing effect of the geomaterials. During this period, the movement of the front and rear edges of the landslide is similar, and the movement is mainly in the form of a whole (Figure 7(b)). The landslide moves slower after the front edge of the landslide enters the bottom of the river bed, and the waves caused by the landslide continue to spread forward and will enter the shallow water area. The shape of the landslide changed significantly during this period, and it became longer due to the much slower movement of the rear edge. (Figure 7(c)). Wave height increases along with the spreading of the surge to shallow water area. The difference in the velocities of several waves causes the spacing between the wave crests to gradually decrease. Although the front edge of the landslide moves forward at a slow speed, its overall impact on the surge has been weakened (Figure 7(d)). The front edge of the landslide reaches its final position along with time passing by, but the geomaterials have not yet reached the balance state, and the main movement occurs at the rear edge of the landslide. Meanwhile, several waves superimpose in the shallow water area, which boosts the formation of a higher surge gradually. At this time, the impact of the landslide on the surge is negligible (Figure 7(e)), when the surge will start run-up movement upon its arrival at the opposite bank. Meanwhile, the landslide almost does not move any longer, and the deposition adjusts its final shape mainly by deformation (Figure 7(f)). Figure 8 shows the results of several critical moments on the same figure, which clearly shows the dynamic process of maximum surge formation. The results of surge run-up under vertical section calculation are inaccurate (in the numerical model, the resistance of the surge in the run-up process is much greater than the resistance along the river. Therefore, the surge spreads to upstream and downstream after reaching the opposite bank but its run-up to the opposite bank is extremely limited). Therefore, the run-up and the possible further back spread process of surge were not simulated in the study. Nevertheless, it could be seen from the above analysis

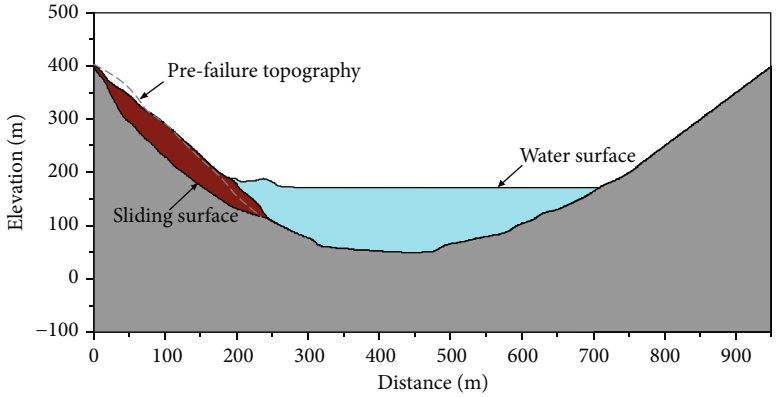

(a)

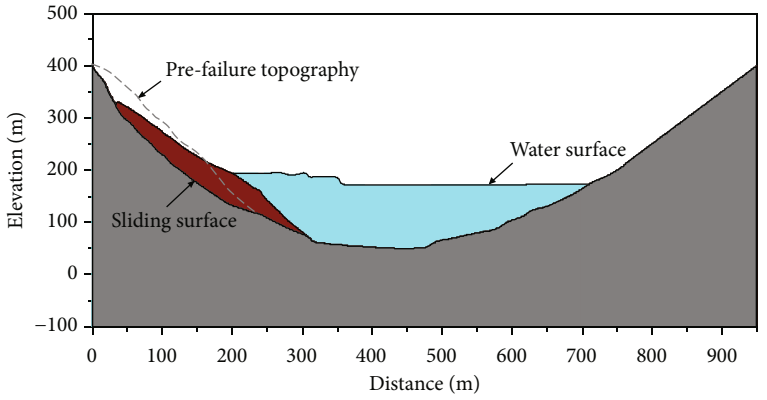

(b)

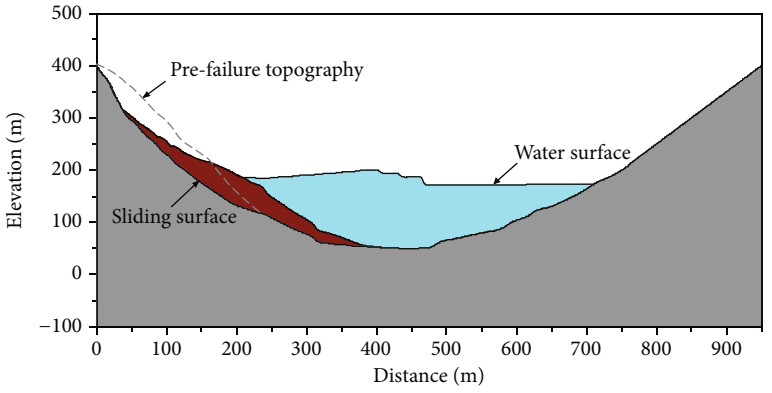

(c)

Figure 7: Continued.

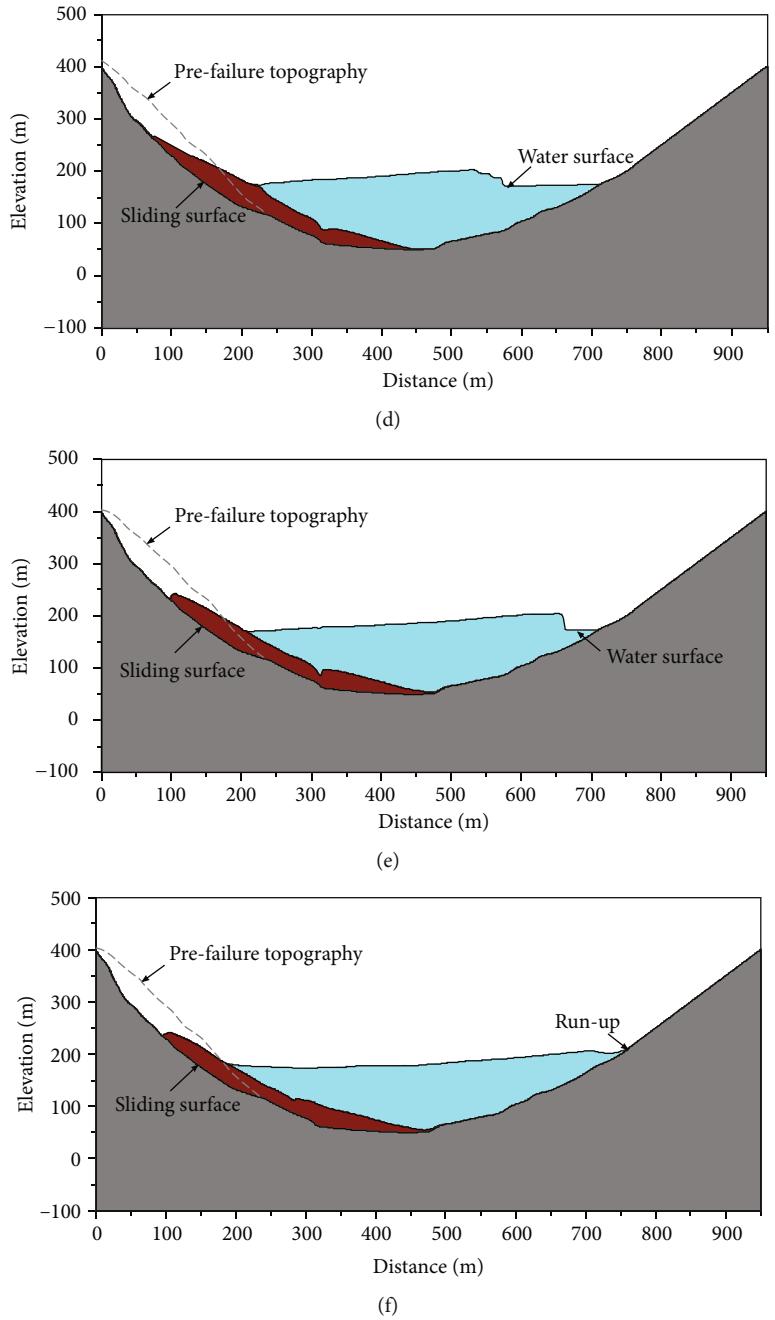

Figure 7: Numerical results of the disaster chain caused by the Gongjiafang landslide. (a) $t = 3$ s. (b) $t = 6$ s. (c) $t = 9$ s. (d) $t = 12$ s. (e) $t = 15$ s. (f) $t = 18$ s.

of numerical simulation that the numerical model in the study could obtain the main characteristics of the disaster chain caused by the landslide accurately.

There are indeed some studies based on landslide and its surge, which have played a huge role in promoting the study of disaster chains. However, the author did not use experiments to verify the numerical model because the experimental data and information we can obtain are not enough, or some experiments are not suitable for the numerical model of this study. The model equations in this study can simulate landslides with fluidized motion, which is significantly different from the disaster chain caused by landslides that move in rigid body form as a whole. The HLL finite volume scheme was used to numerically discretize the model equation, and this numerical method has good conservation. Since the linear reconstruction technique was also used, the second-order accuracy can be achieved, which is sufficient for large-scale disasters. The numerical scheme used also has the advantage that the method can handle discontinuities as well as wet and dry interfaces. Through case analysis, it is confirmed that the adopted method is effective and feasible, thus providing an applicable choice for the study of landslide and its surge.

To verify validity of the existing empirical formula, the results obtained by the empirical formula were further

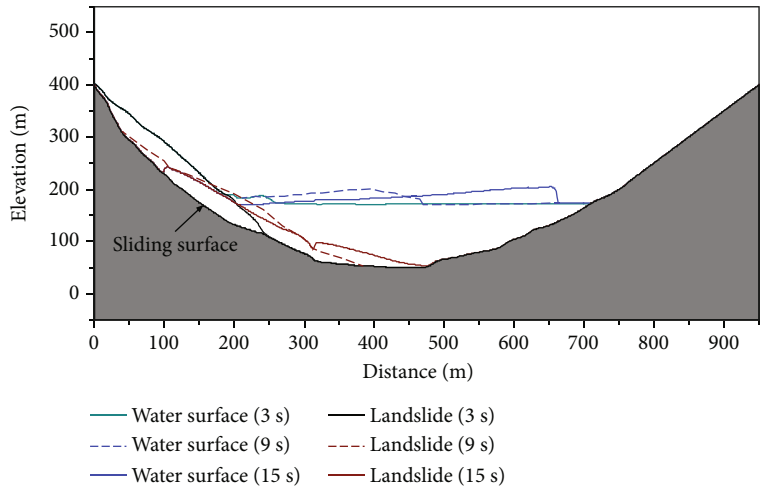

Figure 8: Formation process of maximum surge.

Table 3: Empirical formulas for the maximum surge height caused by the landslide.

Method	Formula form	Variable description
S&V	$\mathrm{Log}\,(a_{\max}/h) = -1.25 + 0.71\ \log\ (\mathrm{KE})$ $\mathrm{KE} = 0.5\left(l \bullet s \bullet b/h^3\right)(\rho/\rho_w)\left(u^2/(g \bullet h)\right)$	l is the length of the landslide, s is the thickness of the landslide, b is the average width of the landslide, h is the water depth, ρ is the density of the landslide, ρ_w is the density of water, u is the sliding velocity, and a is the surge height.
IWHR	$a_{\max} = ku^{1.85}v^{0.5}/2\,\mathrm{g}$	k is the comprehensive influence coefficient, which takes the average value 0.12; v is the volume of the landslide, and u is the velocity of the landslide when entering the water.
Noda	$a_{\max} = 1.32hu/\sqrt{gh}$	$a_{\max}$ is the maximum surge height, u is the sliding velocity of the landslide, and h is the water depth.
Pan	When the landslide enters the water mainly in horizontal motion: $\xi_0 = 1.17hu/\sqrt{gh}$ When the landslide enters the water mainly in vertical motion: $\xi_0 = h \bullet f\left(u'/\sqrt{gh}\right)$ The ξ_0 function relationship can be expressed in sections as follows: (i) When $0 < u'/\sqrt{gh} \le 0.5$, $\xi_0 = hu'/\sqrt{gh}$ (ii) When $0.5 < u'/\sqrt{gh} \le 2$, $f\left(u'/\sqrt{gh}\right)$ changes in a curve (iii) When $u'/\sqrt{gh} > 2$, $\xi_0 = h$	ξ_0 is the surge height, u is the horizontal sliding velocity, u' is the vertical sliding velocity, and h is the water depth.

compared with that in actualities and analyzed. In the disaster chain caused by the landslide, the maximum surge height plays a key role in evaluating the scale of the disaster chain, which may be affected by factors such as geomaterials volume, landslide speed, and water depth. At present, some formulas for calculating the maximum surge height have been proposed [8, 40, 41], as shown in Table 3:

Using the above empirical formulas to calculate the surge caused by the Gongjiafang landslide, in addition to the coefficients contained in the formulas, the calculation parameters of the Gongjiafang landslide and water used in the formula calculation are the same as the numerical simulation. The calculation results of the maximum surge height caused by the Gongjiafang landslide using the above empirical formulas are shown in Table 3. The results of the empirical formulas in Table 4 are provided by the literature [8].

The calculation results show that the calculated values of the S&V method and the IWHR method are relatively small, and the calculation errors are the largest; so, these two methods are not suitable for the calculation of the surge caused by the Gongjiafang landslide. The formulas of the Noda method and Pan method have similar expressions, and the calculated results range from 17.90 m to 23.80 m, which are closer to the actual situation. Compared with the formula calculation method, the maximum surge height obtained by numerical simulation is the most consistent with the actual situation, which is 32.65 m. However, since the numerical simulation does not consider the surge propagation out of the plane

Table 4: Maximum surge height using various methods.

Method	S&V	IWHR	Noda	Pan		Numerical simulation	Field observation
				Horizontal motion	Vertical Motion		
Maximum surge height (m)	3.94	3.54	23.80	20.95	17.90	32.65	31.80

direction, the obtained result is larger than the field observation value. The results in Table 3 show that the actual surge process caused by landslides has certain complexity. Using empirical formulas to calculate the maximum surge height does not yield very reliable results, because these formulas are obtained under various theoretical assumptions and simplifications, as well as empirical summaries, with limited applicability. Compared with the formula method, numerical simulation has stronger applicability, and reliable results can still be obtained under complicated conditions.

4. Discussion

The analytical example used in this study is simple, which not only verifies the correctness and effectiveness of the numerical model but also confirms the ability of the method to handle discontinuous problems. Obviously, the two-layer model can be reduced to a single-layer model under certain conditions; so, it is an effective extension of the single-layer model.

During the numerical investigation of the case, some mechanisms were revealed. The front edge of the landslide was first deformed significantly, and the deformation disturbed the water, thus forming the prototype of the surge. When the landslide moved downward under gravity, the landslide pushed the water forward and promoted the development of the surge. At this time, the landslide movement became the main reason for the promotion of the surge. Affected by the irregular shape and complex movement process of the landslide, several waves with different frequencies were formed. After the landslide movement stopped, the waves continued to propagate forward, and several waves superimpose and form the largest surge in the shallow water area close to the opposite bank. In the case, the above mechanism is representative to a certain extent, but due to the extremely complex process of surge caused by landslide, the disaster chain mechanism in more complex situations still needs to be further studied.

In the investigated case, the numerical deposition is in good agreement with the actual situation, but because the numerical method cannot consider the lateral movement of the mass on the riverbed, the numerical deposition is larger than the actual situation. Although the lateral movement is only a minor factor in this case, ignoring it makes the landslide move further distances and also makes the numerical maximum surge larger than the actual one, which is not a significant difference. Based on the above analysis, the numerical model can make numerical deposition and maximum surge larger than actual ones. The calculation in this study does not discuss more about the maximum run-up but focuses on the maximum surge height. This is because when the surge approaches the opposite bank, it must not only make a run-up movement towards the bank but also spread to the upstream and downstream of the river. The relatively high resistance to the run-up movement forces the surge to spread in the direction along the river when approaching the bank. As a result, the calculated run-up height is obviously larger, which is also a major shortcoming of the vertical section model. However, the maximum surge does not generally occur in the near bank area; so, the calculation of the maximum surge height is not much influenced by the numerical model, and the calculation of the maximum surge is more in line with the actual situation.

In addition, the model used in this study still cannot effectively simulate some special phenomena in the process of landslide and its surge, such as the process of mixing geomaterials with water under high-speed motion on top surface of the landslide and the " hydroplaning" [42] caused by water wedging into the bottom of the landslide (which greatly enhances the sportiness of landslides). Obviously, the study of these complex processes is our future work. However, in order to simulate these phenomena, it is necessary to add experiments and theoretical research on the basis of existing ones and build more complex and accurate 3D models to complete the further expansion of the theoretical and numerical models.

Based on the above discussion, the method in this study is mainly limited by the application environment. For complex disaster processes with obvious three-dimensional effects or special mechanisms, this method is no longer applicable. In future research, the method can be extended to three dimensions, and the equations and solutions for special mechanisms can be supplemented to better cope with the application limitations of the current work. Although the numerical model in this study cannot solve all the problems in the disaster chain, it has the advantages of simple numerical scheme and high efficiency, can still effectively simulate the disaster with plane strain, and quickly realize the back analysis and prediction. Therefore, it is an important and effective numerical model for studying the characteristics and development of disasters.

5. Conclusions

In this study, a two-layer depth-averaged continuous fluid model and a HLL finite volume method were used to simulate the landslide and generated surge. The main conclusions are as follows:

(1) Numerical results of analytical and practical examples show that the adopted numerical model can reflect the deformation and deceleration of the lower layer due to the blockage of the upper layer and also reflect the fluctuation of the upper layer driven by the lower layer. The abovementioned movement characteristics of the two-layer fluid correspond to the landslide and its surge process; so, the effective

simulation of the disaster chain can be realized. For similar disaster chain investigations, the numerical model in this study is a reliable option

(2) The numerical simulation revealed that the landslide movement on the irregular terrain changes the bottom boundary of the water and pushes the water to generate multiple waves. These waves are superimposed to the maximum surge when they propagate to the shallow water area close to the opposite bank, which is extremely harmful to shipping. Compared with empirical formulas, the numerical simulation can better adapt to complex terrain. The numerical results such as the maximum surge height are more consistent with the actual disaster

(3) Due to the simplifications of the model and the limitations of theoretical assumptions, the numerical model in this study is mainly applicable to approximate plane strain conditions. The numerical results are conservative for disaster assessment. The numerical model is no longer applicable to the cases more sensitive to three-dimensional effects such as surge run-up height. At the same time, the corresponding equations need to be supplemented by further research to deal with more complex phenomena

Appendix

The elevation of the sliding surface and the conservation variable U were both defined in the center of the grid. This treatment avoids the creation of semidry and semiwet element, and Green's theorem was applied to obtain the discrete equation as Equation (A.1):

$$\mathbf{U}_i^{n+1} = \mathbf{U}_i^n - \frac{\Delta t}{\Delta x}\left(\mathbf{F}_{i+1/2} - \mathbf{F}_{i-1/2}\right) + \Delta t \mathbf{S}_i, \tag{A.1}$$

where Δt is the time step, Δx is the space step, $F_{i+1/2}$ and $F_{i-1/2}$ are the numerical fluxes at the interface of $x_{i+1/2}$ and $x_{i-1/2}$, respectively, and $\mathbf{S}_i$ is the source term.

The HLL scheme is suitable when dealing with dry and wet elements. The scheme for flux can be expressed as Equation (A.2):

$$\mathbf{F}_{\mathrm{HLL}} = \begin{cases} \mathbf{F}_{L,m}, s_{L,m} \geq 0, \\ \mathbf{F}_{\boldsymbol{m}}^*, s_{L,m} < 0 < s_{R,m}, \\ \mathbf{F}_{R,m}, s_{R,m} \leq 0, \end{cases} \tag{A.2}$$

where $\mathbf{F}_{\boldsymbol{m}}^* = (s_{R,m}\mathbf{F}_{L,m} - s_{L,m}\mathbf{F}_{R,m} + s_{L,m}s_{R,m}(\mathbf{U}_{R,m} - \mathbf{U}_{L,m}))/(s_{R,m} - s_{L,m})$,

where $\mathbf{F}_{L,m}$ and $\mathbf{F}_{R,m}$ are, respectively, the numerical fluxes on the left and right sides of the interface, $s_{L,m}$ and $s_{R,m}$ are, respectively, the wave velocity on the left and right sides of the interface, $\mathbf{F}_m^*$ is the numerical flux value on the interface, and $\mathbf{U}_{L,m}$ and $\mathbf{U}_{R,m}$ are, respectively, the variables on the left and right sides of the interface.

For the calculation of the flux, $s_{L,m}$ and $s_{R,m}$ can be calculated using Equation (A.3):

$$\begin{cases} s_{L,m} = \min\left(u_{L,m} - \sqrt{gh_{L,m}}, u_m^* - \sqrt{gh_m^*}\right), \\ s_{R,m} = \max\left(u_{R,m} - \sqrt{gh_{R,m}}, u_m^* - \sqrt{gh_m^*}\right), \end{cases} \tag{A.3}$$

where $h_{L,m}$ and $h_{R,m}$ are, respectively, the flow depths on the left and right sides of the interface, and u_m^* and $\sqrt{gh_m^*}$ can be calculated as Equations (A.4) and (A.5):

$$u_m^* = \frac{1}{2}\left(u_{L,m} + u_{R,m}\right) + \sqrt{gh_{L,m}} - \sqrt{gh_{R,m}}, \tag{A.4}$$

$$\sqrt{gh_m^*} = \frac{1}{2}\left(\sqrt{gh_{L,m}} + \sqrt{gh_{R,m}}\right) + \frac{1}{4}\left(u_{L,m} - u_{R,m}\right). \tag{A.5}$$

The wave velocity on the wet and dry interface can be calculated using Equations (A.6) and (A.7):

$$s_{L,m} = u_{L,m} - 2\sqrt{gh_{L,m}}, s_{R,m} = u_{L,m} + 2\sqrt{gh_{L,m}}, \tag{A.6}$$

where the dry element is on the right.

$$s_{L,m} = u_{R,m} - 2\sqrt{gh_{R,m}}, s_{R,m} = u_{R,m} + 2\sqrt{gh_{R,m}}, \tag{A.7}$$

where the dry element is on the left.

The second-order linear reconstruction is shown in Equations (A.8) and (A.9):

$$\mathbf{U}_{i+1/2}^L = \mathbf{U}_i + \frac{\Delta x_i}{2}\left(\frac{\partial \mathbf{U}}{\partial x}\right)_i, \tag{A.8}$$

$$\mathbf{U}_{i+1/2}^R = \mathbf{U}_{i+1} + \frac{\Delta x_{i+1}}{2}\left(\frac{\partial \mathbf{U}}{\partial x}\right)_{i+1}, \tag{A.9}$$

where $\partial \mathrm{U}/\partial x$ is the intraelement variable gradient. The minmod limiter was used to avoid nonphysical numerical fluctuations, as shown in Equation (A.10) [43]:

$$\frac{\partial \mathbf{U}}{\partial x} = \mathrm{minmod}\left(\frac{\mathbf{U}_i - \mathbf{U}_{i-1}}{x_i - x_{i-1}}, \frac{\mathbf{U}_{i+1} - \mathbf{U}_i}{x_{i+1} - x_i}\right). \tag{A.10}$$

Data Availability

The numerical calculation data used to support the findings of this study are available from the corresponding author upon request.

Conflicts of Interest

The authors declare that there are no conflicts of interest regarding the publication of this paper.

Acknowledgments

This work is supported by the Fundamental Research Funds for the Central Universities of China (Grant No. N2201021), the National Key Research and Development Program of China (Grant Nos. 2016YFC0801603 and 2017YFC1503101), the National Natural Science Foundation of China (Grant No. 41201007), the Key Science and Technology Projects of Liaoning Province, China (Grant No. 2019JH2-10100035), and the Research Fund for General Science Project of Department of Education of Liaoning Province (Grant No. L2013103).

References

[1] R. Vacondio, P. Mignosa, and S. Pagani, "3D SPH numerical simulation of the wave generated by the Vajont rockslide," *Advances in Water Resources*, vol. 59, pp. 146–156, 2013.

[2] G. B. Crosta, S. Imposimato, and D. Roddeman, "Landslide spreading, impulse water waves and modelling of the vajont rockslide," *Rock Mechanics and Rock Engineering*, vol. 49, no. 6, pp. 2413–2436, 2016.

[3] P. Cui and X. H. Zhu, "SURGE generation in reservoirs by landslides triggered by the wenchuan earthquake," *Journal of Earthquake and Tsunami*, vol. 5, no. 5, pp. 461–474, 2011.

[4] B. L. Huang, Y. P. Yin, X. T. Chen, G. N. Liu, S. C. Wang, and Z. B. Jiang, "Experimental modeling of tsunamis generated by subaerial landslides: two case studies of the three gorges reservoir, China," *Environmental Earth Sciences*, vol. 71, no. 9, pp. 3813–3825, 2014.

[5] S. T. Grilli, C. Zhang, and J. T. Kirby, "Modeling of the Dec. 22nd 2018 Anak Krakatau volcano lateral collapse and tsunami based on recent field surveys: Comparison with observed tsunami impact," *Marine Geology*, vol. 440, article 106566, 2021.

[6] A. Mahallem, M. Roudane, A. Krimi, and S. A. Gouri, "Smoothed Particle Hydrodynamics for modelling landslide–water interaction problems," *Landslides*, vol. 19, no. 5, pp. 1249–1263, 2022.

[7] S. Michele, E. Renzi, A. G. L. Borthwick, C. Whittaker, and A. C. Raby, "Weakly nonlinear theory for dispersive waves generated by moving seabed deformation," *Journal of Fluid Mechanics*, vol. 937, article ???, 2022.

[8] B. L. Huang, *Water Wave Dynamic Analysis Method Study on Landslide-Generated Impulse Wave Hazard in Reservoirs*, Ph D Thesis, China University of Geosciences, Wuhan, China, 2014.

[9] Y. Qi, Q. Xu, J. Chen, G. Zhang, and J. Li, "Study on solid block landslide generated tsunami using a modified δ-les-SPH model," *Ocean Engineering*, vol. 245, article ???, 2022.

[10] T. Attili, V. Heller, and S. Triantafyllou, "A numerical investigation of tsunamis impacting dams," *Coastal Engineering*, vol. 169, article ???, 2021.

[11] J. J. Wang, L. L. Xiao, and S. N. Ward, "Tsunami Squares modeling of landslide tsunami generation considering the 'Push Ahead' effects in slide/water interactions: theory, experimental validation, and sensitivity analyses," *Engineering Geology*, vol. 288, article ???, 2021.

[12] D. Song, Z. Chen, H. Chao, Y. Ke, and W. Nie, "Numerical study on seismic response of a rock slope with discontinuities based on the time-frequency joint analysis method," *Soil Dynamics and Earthquake Engineering*, vol. 133, article 106112, 2020.

[13] D. Song, Z. Chen, Y. Ke, and W. Nie, "Seismic response analysis of a bedding rock slope based on the time-frequency joint analysis method: a case study from the middle reach of the Jinsha River, China," *Engineering Geology*, vol. 274, article 105731, 2020.

[14] Z. Chen, D. Song, and L. Dong, "Characteristics and emergency mitigation of the 2018 Laochang landslide in Tianquan County, Sichuan Province, China," *Scientific Reports*, vol. 11, no. 1, 2021.

[15] S. Yavari-Ramshe and B. Ataie-Ashtiani, "Numerical modeling of subaerial and submarine landslide-generated tsunami waves-recent advances and future challenges," *Landslides*, vol. 13, no. 6, pp. 1325–1368, 2016.

[16] P. Watts, "Wavemaker curves for tsunamis generated by underwater landslides," *Journal of Waterway, Port, Coastal, and Ocean Engineering*, vol. 124, no. 3, pp. 127–137, 1998.

[17] P. Lynett and P. L. F. Liu, "A two-layer approach to wave modelling," *Series A: Mathematical, Physical and Engineering Sciences*, vol. 460, no. 2049, pp. 2637–2669, 2004.

[18] F. M. Evers and W. H. Hager, "Impulse wave generation: comparison of free granular with mesh-packed slides," *Journal of Marine Science and Engineering*, vol. 3, no. 1, pp. 100–110, 2015.

[19] F. Løvholt, G. Pedersen, C. B. Harbitz, S. Glimsdal, and J. Kim, "On the characteristics of landslide tsunamis," *Philosophical Transactions of the Royal Society A: Mathematical, Physical and Engineering Sciences*, vol. 373, no. 2053, article 20140376, 2015.

[20] S. M. Abadie, J. C. Harris, S. T. Grilli, and R. Fabre, "Numerical modeling of tsunami waves generated by the flank collapse of the cumbre vieja volcano (La Palma, Canary Islands): tsunami source and near field effects," *Journal of Geophysical Research-Oceans*, vol. 117, no. C5, article C050530, 2012.

[21] E. D. Fernández-Nieto, F. Bouchut, D. Bresch, M. J. C. Díaz, and A. Mangeney, "A new Savage-Hutter type model for submarine avalanches and generated tsunami," *Journal of Computational Physics*, vol. 227, no. 16, pp. 7720–7754, 2008.

[22] J. Kafle, P. Kattel, P. R. Pokhrel, K. B. Khattri, D. B. Gurung, and S. P. Pudasaini, "Dynamic interaction between a two-phase submarine landslide and a fluid reservoir," *International Journal of Landslide and Environment*, vol. 1, no. 1, pp. 35-36, 2013.

[23] Y. Shigihara, D. Goto, F. Imamura et al., "Hydraulic and numerical study on the generation of a subaqueous landslide-induced tsunami along the coast," *Natural Hazards*, vol. 39, no. 2, pp. 159–177, 2006.

[24] G. Ma, J. T. Kirby, T. J. Hsu, and F. Y. Shi, "A two-layer granular landslide model for tsunami wave generation: theory and computation," *Ocean Model*, vol. 93, pp. 40–55, 2015.

[25] P. Lynett and P. L. F. Liu, "A numerical study of submarine landslide generated waves and run-up," *Proceedings of the Royal Society of London Series A: Mathematical, Physical and Engineering Sciences*, vol. 458, no. 2028, pp. 2885–2910, 2002.

[26] M. F. Gobbi, J. T. Kirby, and G. E. Wei, "A fully nonlinear boussinesq model for surface waves. Part 2. Extension to O (kh)4," *Journal of Fluid Mechanics*, vol. 405, pp. 181–210, 2000.

[27] E. Pelinovsky, T. Talipova, A. Kurkin, and C. Kharif, "Nonlinear mechanism of tsunami wave generation by atmospheric

disturbances," *Natural Hazards and Earth System Sciences*, vol. 1, no. 4, pp. 243–250, 2001.

[28] B. Ataie-Ashtiani and A. N. Najafi-Jilani, "A higher-order Boussinesq-type model with moving bottom boundary: applications to submarine landslide tsunami waves," *International Journal for Numerical Methods in Fluids*, vol. 53, no. 6, pp. 1019–1048, 2007.

[29] B. Ataie-Ashtiani and S. Yavari-Ramshe, "Numerical simulation of wave generated by landslide incidents in dam reservoirs," *Landslides*, vol. 8, no. 4, pp. 417–432, 2011.

[30] P. Lynett and P. L. F. Liu, "A numerical study of the run-up generated by three-dimensional landslides," *Journal of Geophysical Research-Oceans*, vol. 110, no. C3, article C03006, 2005.

[31] J. Mao, L. H. Zhao, Y. T. Di, X. N. Liu, and W. Y. Xu, "A resolved CFD-DEM approach for the simulation of landslides and impulse waves," *Computer Methods in Applied Mechanics and Engineering*, vol. 359, article 112750, 2021.

[32] R. Keiser, *Meshless Lagrangian Methods for Physics-Based Animations of Solids and Fluids*, Ph D thesis, Swiss Federal Institute of Technology, ETH Zürich, Switzerland, 2006.

[33] R. A. Walters, "A semi-implicit finite element model for non-hydrostatic (dispersive) surface waves," *International Journal for Numerical Methods in Fluids*, vol. 49, no. 7, pp. 721–737, 2005.

[34] A. Ghaitanellis, D. Violeau, P. L. F. Liu, and T. Viard, "SPH simulation of the 2007 Chehalis lake landslide and subsequent tsunami," *Journal of Hydraulic Research*, vol. 59, no. 6, pp. 863–887, 2021.

[35] J. Xie, Y. C. Tai, and Y. C. Jin, "Study of the free surface flow of water-kaolinite mixture by moving particle semi-implicit (mps) method," *International Journal for Numerical and Analytical Methods in Geomechanics*, vol. 38, no. 8, pp. 811–827, 2013.

[36] Z. Chen and D. Song, "Numerical investigation of the recent Chenhecun landslide (Gansu, China) using the discrete element method," *Natural Hazards*, vol. 105, no. 1, pp. 717–733, 2021.

[37] B. Spinewine, V. Guinot, S. Soares-Frazão, and Y. Zech, "Solution properties and approximate Riemann solvers for two-layer shallow flow models," *Computers & Fluids*, vol. 44, no. 1, pp. 202–220, 2011.

[38] P. Si, J. Aaron, S. McDougall et al., "A non-hydrostatic model for the numerical study of landslide-generated waves," *Landslides*, vol. 15, no. 4, pp. 711–726, 2018.

[39] Y. Wang, J. Liu, D. Li, and S. Yan, "Optimization model for maximum tsunami amplitude generated by riverfront landslides based on laboratory investigations," *Ocean Engineering*, vol. 142, no. 15, pp. 433–440, 2017.

[40] R. L. Slingerland and B. Voight, "Occurrences, properties, and predictive models of landslide-generated water waves," *Developments in Geotechnical Engineering*, vol. 14, pp. 317–394, 1979.

[41] E. Noda, "Water waves generated by landslides," *Journal of waterways, Harbors and Coastal Engineering Division*, vol. 96, no. 4, pp. 835–855, 1970.

[42] D. Mohrig, K. X. Whipple, M. Hondzo, C. Ellis, and G. Parker, "Hydroplaning of subaqueous debris flows," *Geological Society of America Bulletin*, vol. 110, no. 3, pp. 387–394, 1998.

[43] D. Dummy, S. T. Grilli, and P. Watts, "Modeling of waves generated by a moving submerged body. Applications to underwater landslides," *Engineering Analysis with Boundary Elements*, vol. 23, no. 8, pp. 645–656, 1999.